ISSN 1949-8470 (online)

World Journal of *Radiology*

World J Radiol 2016 March 28; 8(3): 226-330

Published by Baishideng Publishing Group Inc

WJR World Journal of Radiology

A peer-reviewed, online, open-access journal of Radiology

Editorial Board

2014-2017

The *World Journal of Radiology* Editorial Board consists of 365 members, representing a team of worldwide experts in radiology. They are from 36 countries, including Afghanistan (1), Argentina (2), Australia (5), Austria (7), Belgium (2), Brazil (8), Canada (6), Chile (1), China (43), Croatia (1), Denmark (4), Egypt (6), France (5), Germany (22), Greece (10), India (12), Iran (6), Ireland (2), Israel (3), Italy (47), Japan (13), Netherlands (1), New Zealand (1), Pakistan (1), Poland (2), Portugal (1), Serbia (1), Singapore (3), Slovakia (1), South Korea (18), Spain (4), Sweden (2), Switzerland (4), Thailand (1), Turkey (26), United Kingdom (11), and United States (82).

Yue-Qi Zhu, *Shanghai*

Croatia

Goran Kusec, Osijek

Denmark

Poul E Andersen, *Odense*
Lars J Petersen, *Aalborg*
Thomas Z Ramsoy, *Frederiksberg*
Morten Ziebell, *Copenhagen*

Egypt

Mohamed F Bazeed, *Mansoura*
Mohamed Abou El-Ghar, *Mansoura*
Reem HA Mohamed, *Cairo*
Mohamed R Nouh, *Alexandria*
Ahmed AKA Razek, *Mansoura*
Ashraf A Zytoon, *Shebin El-Koom*

France

Sabine F Bensamoun, *Compiègne*
Romaric Loffroy, *Dijon*
Stephanie Nougaret, *Montpellier*
Hassane Oudadesse, *Rennes*
Vincent Vinh-Hung, *Fort-de-France*

Germany

Henryk Barthel, *Leipzig*
Peter Bannas, *Hamburg*
Martin Beeres, *Frankfurt*
Ilja F Ciernik, *Dessau*
A Dimitrakopoulou-Strauss, *Heidelberg*
Peter A Fasching, *Erlanegn*
Andreas G Schreyer, *Regensburg*
Philipp Heusch, *Duesseldorf*
Sonja M Kirchhoff, *Munich*
Sebastian Ley, *Munich*
Adel Maataoui, *Frankfurt am Main*
Stephan M Meckel, *Freiburg*
Hans W Muller, *Duesseldorf*
Kay Raum, *Berlin*
Dirk Rades, *Luebeck*
Marc-Ulrich Regier, *Hamburg*
Alexey Surov, *Halle*
Martin Walter, *Magdeburg*
Axel Wetter, *Essen*
Christoph Zilkens, *Düsseldorf*

Greece

Panagiotis Antoniou, *Thessaloniki*
Nikos Efthimiou, *Athens*
Dimitris Karnabatidis, *Patras*
George Latsios, *Athens*
Stylianos Megremis, *Iraklion*
Alexander D Rapidis, *Athens*
Kiki Theodorou, *Larissa*
Ioannis A Tsalafoutas, *Athens*
Evanthia E Tripoliti, *Ioannina*
Athina C Tsili, *Ioannina*

India

Ritesh Agarwal, *Chandigarh*
Chandan J Das, *New Delhi*
Prathamesh V Joshi, *Mumbai*
Naveen Kalra, *Chandigarh*
Chandrasekharan Kesavadas, *Trivandrum*
Jyoti Kumar, *New Delhi*
Atin Kumar, *New Delhi*
Kaushala P Mishra, *Allahabad*
Daya N Sharma, *New Delhi*
Binit Sureka, *New Delhi*
Sanjay Sharma, *New Delhi*
Raja R Yadav, *Allahabad*

Iran

Majid Assadi, *Bushehr*
SeyedReza Najafizadeh, *Tehran*
Mohammad Ali Oghabian, *Tehran*
Amir Reza Radmard, *Tehran*
Ramin Sadeghi, *Mashhad*
Hadi Rokni Yazdi, *Tehran*

Ireland

Tadhg Gleeson, *Wexford*
Frederik JAI Vernimmen, *Cork*

Israel

Dafna Ben Bashat, *Tel Aviv*
Amit Gefen, *Tel Aviv*
Tamar Sella, *Jerusalem*

Italy

Adriano Alippi, *Rome*
Dante Amelio, *Trento*
Michele Anzidei, *Rome*
Filippo F Angileri, *Messinas*
Stefano Arcangeli, *Rome*
Roberto Azzoni, *San Donato milanese*
Tommaso V Bartolotta, *Palermo*
Tommaso Bartalena, *Imola*
Livia Bernardin, *San Bonifacio*
Federico Boschi, *Verona*
Sergio Casciaro, *Lecce*
Emanuele Casciani, *Rome*
Musa M Can, *Napoli*
Alberto Cuocolo, *Napoli*
Michele Ferrara, *Coppito*
Mauro Feola, *Fossano*
Giampiero Francica, *Castel Volturno*
Luigi De Gennaro, *Rome*
Giulio Giovannetti, *Pisa*
Francesca Iacobellis, *Napoli*
Formato Invernizzi, *Monza Brianza*
Francesco Lassandro, *Naples*
Lorenzo Livi, *Florence*
Pier P Mainenti, *Napoli*
Laura Marzetti, *Chieti*
Giuseppe Malinverni, *Crescentino*
Enrica Milanesi, *Turin*
Giovanni Morana, *Treviso*
Lorenzo Monti, *Milan*
Silvia D Morbelli, *Genoa*
Barbara Palumbo, *Perugia*
Cecilia Parazzini, *Milan*
Stefano Pergolizzi, *Messina*
Antonio Pinto, *Naples*
Camillo Porcaro, *Rome*
Carlo C Quattrocchi, *Rome*
Alberto Rebonato, *Perugia*
Giuseppe Rizzo, *Rome*
Roberto De Rosa, *Naples*
Domenico Rubello, *Rovigo*
Andrea Salvati, *Bari*
Sergio Sartori, *Ferrara*
Luca M Sconfienza, *Milano*
Giovanni Storto, *Rionero*
Nicola Sverzellati, *Parma*
Alberto S Tagliafico, *Genova*
Nicola Troisi, *Florence*

Japan

Yasuhiko Hori, *Chiba*
Hidetoshi Ikeda, *Koriyama*
Masahito Kawabori, *Sapporo*
Tamotsu Kamishima, *Sapporo*
Hiro Kiyosue, *Yufu*
Yasunori Minami, *Osaka-sayama*
Yasuhiro Morimoto, *Kitakyushu*
Satoru Murata, *Tokyo*
Shigeki Nagamachi, *Miyazaki*
Hiroshi Onishi, *Yamanashi*
Morio Sato, *Wakayama Shi*
Yoshito Tsushima, *Maebashi*
Masahiro Yanagawa, *Suita*

Netherlands

Willem Jan van Rooij, *Tilburg*

New Zealand

W Howell Round, *Hamilton*

Pakistan

Wazir Muhammad, *Abbottabad*

Poland

Maciej S Baglaj, *Wroclaw*

Piotr Czauderna, *Gdansk*

Portugal

Joao Manuel RS Tavares, *Porto*

Serbia

Olivera Ciraj-Bjelac, *Belgrade*

Singapore

Gopinathan Anil, *Singapore*
Terence KB Teo, *Singapore*
Cher Heng Tan, *Singapore*

Slovakia

Stefan Sivak, *Martin*

South Korea

Ki Seok Choo, *Busan*
Seung Hong Choi, *Seoul*
Dae-Seob Choi, *Jinju*
Hong-Seok Jang, *Seoul*
Yong Jeong, *Daejeon*
Chan Kyo Kim, *Seoul*
Se Hyung Kim, *Seoul*
Joong-Seok Kim, *Seoul*
Sang Eun Kim, *Seongnam*
Sung Joon Kwon, *Seoul*
Jeong Min Lee, *Seoul*
In Sook Lee, *Busan*
Noh Park, *Goyang*
Chang Min Park, *Seoul*
Sung Bin Park, *Seoul*
Deuk Jae Sung, *Seoul*
Choongsoo Shin, *Seoul*
Kwon-Ha Yoon, *Iksan*

Spain

Miguel A De Gregorio, *Zaragoza*
Antonio Luna, *Jaén*
Enrique Marco de Lucas, *Santander*
Fernando Ruiz Santiago, *Granada*

Sweden

Dmitry Grishenkov, *Stockholm*
Tie-Qiang Li, *Stockholm*

Switzerland

Nicolau Beckmann, *Basel*
Christian Boy, *Bern*
Giorgio Treglia, *Bellinzona*

Stephan Ulmer, *Kiel*

Thailand

Sirianong Namwongprom, *Chiang Mai*

Turkey

Kubilay Aydin, *Istanbul*
Ramazan Akdemir, *Sakarya*
Serhat Avcu, *Ankara*
Ayse Aralasmak, *Istanbul*
Oktay Algin, *Ankara*
Nevbahar Akcar, *Meselik*
Bilal Battal, *Ankara*
Zulkif Bozgeyik, *Elazig*
Nazan Ciledag, Aakara
Fuldem Y Donmez, *Ankara*
Gulgun Engin, *Istanbul*
Ahmet Y Goktay, *Izmir*
Oguzhan G Gumustas, *Bursa*
Kaan Gunduz, *Ankara*
Pelin Ozcan Kara, *Mersin*
Kivanc Kamburoglu, *Ankara*
Ozgur Kilickesmez, *Istanbul*
Furuzan Numan, *Istanbul*
Cem Onal, *Adana*
Ozgur Oztekin, *Izmir*
Seda Ozbek (Boruban), *Konya*
Selda Sarikaya, *Zonguldak*
Figen Taser, *Kutahya*
Baran Tokar, *Eskisehir*
Ender Uysal, *Istanbul*
Ensar Yekeler, *Istanbul*

United Kingdom

Indran Davagnanam, *London*
M DC Valdés Hernández, *Edinburgh*
Alan Jackson, *Manchester*
Suneil Jain, *Belfast*
Long R Jiao, *London*
Miltiadis Krokidis, *Cambridge*
Pradesh Kumar, *Liverpool*
Peter D Kuzmich, *Derby*
Georgios Plataniotis, *Brighton*
Vanessa Sluming, *Liverpool*

United States

Garima Agrawal, *Saint Louis*
James R Brasic, *Baltimore*
Rajendra D Badgaiyan, *Buffalo*
Ulas Bagci, *Bethesda*
Anat Biegon, *Stony Brook*
Ramon Casanova, *Winston Salem*
Wenli Cai, *Boston*
Zheng Chang, *Durham*
Corey J Chakarun, *Long Beach*
Kai Chen, *Los Angeles*
Hyun-Soon Chong, *Chicago*
Marco Cura, *Dallas*
Ravi R Desai, *Bensalem*
Delia DeBuc, *Miami*
Carlo N De Cecco, *Charleston*
Timm-Michael L Dickfeld, *Baltimore*
Subba R Digumarthy, *Boston*
Huy M Do, *Stanford*
Todd A Faasse, *Grand Rapids*
Salomao Faintuch, *Boston*
Girish M Fatterpekar, *New York*
Dhakshinamoorthy Ganeshan, *Houston*
Robert J Griffin, *Little Rock*
Andrew J Gunn, *Boston*
Sandeep S Hedgire, *Boston*
Timothy J Hoffman, *Columbia*
Mai-Lan Ho, *San Francisco*
Juebin Huang, *Jackson*
Abid Irshad, *Charleston*
Matilde Inglese, *New York*
El-Sayed H Ibrahim, *Jacksonville*
Paul R Julsrud, *Rochester*
Pamela T Johnson, *Baltimore*
Ming-Hung Kao, *Tempe*
Sunil Krishnan, *Houston*
Richard A Komoroski, *Cincinnati*
Sandi A Kwee, *Honolulu*
King Kim, *Ft. Lauderdale*
Guozheng Liu, *Worcester*
Yiyan Liu, *Newark*
Venkatesh Mani, *New York*
Lian-Sheng Ma, *Pleasanton*
Rachna Madan, *Boston*
Zeyad A Metwalli, *Houston*
Yilong Ma, *Manhasset*
Hui Mao, *Atlanta*
Feroze B Mohamed, *Philadelphia*
Gul Moonis, *Boston*
John L Nosher, *New Brunswick*
Rahmi Oklu, *Boston*
Aytekin Oto, *Chicago*
Bishnuhari Paudyal, *Philadelphia*
Rajul Pandya, *Youngstown*
Chong-Xian Pan, *Sacramento*
Jay J Pillai, *Baltimore*
Neal Prakash, *Duarte*
Reza Rahbar, *Boston*
Ali S Raja, *Boston*
Gustavo J Rodriguez, *El Paso*
David J Sahn, *Portlsand*
Steven Schild, *Scottsdale*
Ali R Sepahdari, *Los Angeles*
Li Shen, *Indianapolis*
JP Sheehan, *Charlottesville*
Atul B Shinagare, *Boston*
Sarabjeet Singh, *Boston*
Charles J Smith, *Columbia*
Kenji Suzuki, *Chicago*
Monvadi Srichai-Parsia, *Washington*
Sree H Tirumani, *Boston*
Hebert A Vargas, *New York*
Sachit Verma, *Philadelphia*
Yoichi Watanabe, *Minneapolis*
Li Wang, *Chapel Hill*
Carol C Wu, *Boston*
Shoujun Xu, *Houston*
Min Yao, *Cleveland*
Xiaofeng Yang, *Atlanta*
Qingbao Yu, *Albuquerque*
Aifeng Zhang, *Chicago*
Chao Zhou, *Bethlehem*
Hongming Zhuang, *Philadelphia*

WJR World Journal of Radiology

Contents

Monthly Volume 8 Number 3 March 28, 2016

Observational Study

World Journal of Radiology
Volume 8 Number 3 March 28, 2016

Contents

NAME OF JOURNAL
World Journal of Radiology

ISSN
ISSN 1949-8470 (online)

LAUNCH DATE
January 31, 2009

FREQUENCY
Monthly

EDITORIAL OFFICE
Jin-Lei Wang, Director
Xiu-Xia Song, Vice Director
World Journal of Radiology
Room 903, Building D, Ocean International Center,
No. 62 Dongsihuan Zhonglu, Chaoyang District,
Beijing 100025, China
Telephone: +86-10-59080039
Fax: +86-10-85381893
E-mail: editorialoffice@wjgnet.com
Help Desk: http://www.wjgnet.com/esps/helpdesk.aspx
http://www.wjgnet.com

PUBLISHER
Baishideng Publishing Group Inc
8226 Regency Drive,
Pleasanton, CA 94588, USA
Telephone: +1-925-223-8242
Fax: +1-925-223-8243
E-mail: bpgoffice@wjgnet.com
Help Desk: http://www.wjgnet.com/esps/helpdesk.aspx
http://www.wjgnet.com

PUBLICATION DATE
March 28, 2016

INSTRUCTIONS TO AUTHORS
Full instructions are available online at http://www.wjgnet.com/bpg/g_info_20160116143427.htm

ONLINE SUBMISSION
http://www.wjgnet.com/esps/

World Journal of Radiology

Submit a Manuscript: http://www.wjgnet.com/esps/
Help Desk: http://www.wjgnet.com/esps/helpdesk.aspx
DOI: 10.4329/wjr.v8.i3.226

World J Radiol 2016 March 28; 8(3): 226-239
ISSN 1949-8470 (online)

REVIEW

Molecular imaging of movement disorders

Karlo J Lizarraga, Alessandra Gorgulho, Wei Chen, Antonio A De Salles

Karlo J Lizarraga, Department of Neurology, Jackson Memorial Hospital, University of Miami Miller School of Medicine, Miami, FL 33136, United States

Alessandra Gorgulho, Antonio A De Salles, Department of Neurosurgery, David Geffen School of Medicine, University of California Los Angeles, Los Angeles, CA 90095, United States

Wei Chen, Department of Molecular and Medical Pharmacology, David Geffen School of Medicine, University of California Los Angeles, Los Angeles, CA 90095, United States

Author contributions: Lizarraga KJ conceptualized and designed the manuscript, reviewed the literature and drafted all article versions; Gorgulho A, Chen W and De Salles AA interpreted data and critically revised all manuscript versions; all authors approved the final version of the article to be published.

Conflict-of-interest statement: The authors declare no potential conflict of interest for this review.

Correspondence to: Karlo J Lizarraga, MD, MS, Department of Neurology, Jackson Memorial Hospital, University of Miami Miller School of Medicine, 1120 N.W. 14th Street, Suite 1383, Miami, FL 33136, United States. klizarraga@med.miami.edu
Telephone: +1-305-2432742
Fax: +1-305-2438108

Received: September 30, 2015
Peer-review started: October 3, 2015
First decision: November 4, 2015
Revised: November 19, 2015
Accepted: January 5, 2016
Article in press: January 7, 2016
Published online: March 28, 2016

Abstract

Positron emission tomography measures the activity of radioactively labeled compounds which distribute and accumulate in central nervous system regions in proportion to their metabolic rate or blood flow. Specific circuits such as the dopaminergic nigrostriatal projection can be studied with ligands that bind to the pre-synaptic dopamine transporter or post-synaptic dopamine receptors (D1 and D2). Single photon emission computerized tomography (SPECT) measures the activity of similar tracers labeled with heavy radioactive species such as technetium and iodine. In essential tremor, there is cerebellar hypermetabolism and abnormal GABAergic function in premotor cortices, dentate nuclei and ventral thalami, without significant abnormalities in dopaminergic transmission. In Huntington's disease, there is hypometabolism in the striatum, frontal and temporal cortices. Disease progression is accompanied by reduction in striatal D1 and D2 binding that correlates with trinucleotide repeat length, disease duration and severity. In dystonia, there is hypermetabolism in the basal ganglia, supplementary motor areas and cerebellum at rest. Thalamic and cerebellar hypermetabolism is seen during dystonic movements, which can be modulated by globus pallidus deep brain stimulation (DBS). Additionally, GABA-A receptor activity is reduced in motor, premotor and somatosensory cortices. In Tourette's syndrome, there is hypermetabolism in premotor and sensorimotor cortices, as well as hypometabolism in the striatum, thalamus and limbic regions at rest. During tics, multiple areas related to cognitive, sensory and motor functions become hypermetabolic. Also, there is abnormal serotoninergic transmission in prefrontal cortices and bilateral thalami, as well as hyperactivity in the striatal dopaminergic system which can be modulated with thalamic DBS. In Parkinson's disease (PD), there is asymmetric progressive decline in striatal dopaminergic tracer accumulation, which follows a caudal-to-rostral direction. Uptake declines prior to symptom presentation and progresses from contralateral to the most symptomatic side to bilateral, correlating with symptom severity. In progressive supranuclear

palsy (PSP) and multiple system atrophy (MSA), striatal activity is symmetrically and diffusely decreased. The caudal-to-rostral pattern is lost in PSP, but could be present in MSA. In corticobasal degeneration (CBD), there is asymmetric, diffuse reduction of striatal activity, contralateral to the most symptomatic side. Additionally, there is hypometabolism in contralateral parieto-occipital and frontal cortices in PD; bilateral putamen and cerebellum in MSA; caudate, thalamus, midbrain, mesial frontal and prefrontal cortices in PSP; and contralateral cortices in CBD. Finally, cardiac sympathetic SPECT signal is decreased in PD. The capacity of molecular imaging to provide *in vivo* time courses of gene expression, protein synthesis, receptor and transporter binding, could facilitate the development and evaluation of novel medical, surgical and genetic therapies in movement disorders.

Key words: Positron emission tomography; Single photon emission computerized tomography; Movement disorders; Essential tremor; Huntington's disease; Dystonia; Tourette's syndrome; Parkinson's disease; Parkinsonism

Core tip: By evaluating changes in regional brain perfusion, glucose metabolism and neurotransmitter systems, molecular imaging has shed light onto the etiology, pathophysiology, diagnosis, progression and therapeutic options of movement disorders, including the identification and individualization of potential neuromodulation targets. Continuing progress in the design of positron emission tomography and single photon emission computerized tomography systems, such as new detector materials and image reconstruction algorithms, higher performance technology, and improved availability will contribute to a wider range of applications. In particular, the combined use of genetic therapy and molecular imaging could provide opportunities for the design and evaluation of novel therapies at early stages of the disease.

Lizarraga KJ, Gorgulho A, Chen W, De Salles AA. Molecular imaging of movement disorders. *World J Radiol* 2016; 8(3): 226-239 Available from: URL: http://www.wjgnet.com/1949-8470/full/v8/i3/226.htm DOI: http://dx.doi.org/10.4329/wjr.v8.i3.226

INTRODUCTION

Movement disorders manifest with excess or paucity of movements (*i.e.,* hyper- or hypokinetic disorders). The most common hyperkinetic disorders are tremor, chorea, dystonia, tics and myoclonus. In the hypokinetic group, the parkinsonian syndromes are the most frequent. Many of these conditions are related to dysfunction of the basal ganglia, the cerebellum and/or their connections with primary or associative motor cortices. In these regions, neuronal alterations usually begin at the genetic, molecular and cellular levels, later progressing to neurotransmitter and network dysfunction.

Structural imaging with techniques such as magnetic resonance imaging (MRI) could demonstrate anatomical abnormalities in motor circuits. These defects are usually identified at advanced stages when continued neurodegeneration has led to volume loss (atrophy). MRI can also identify ischemia, neoplasm, infection, demyelination or abnormal substance deposition as the etiology of abnormal movements.

In contrast, molecular imaging techniques could provide neurochemical information useful to learn about the pathophysiology of the disorder, to diagnose the conditions at early stages, to monitor disease progression, as well as to plan and assess the response to medical and surgical interventions, including the identification of potential targets for neuromodulation. In this review, we describe the use of positron emission tomography (PET) and single-photon emission computerized tomography (SPECT) in movement disorders.

BASICS OF PET AND SPECT

PET evaluates neurobiological processes at the molecular level by using nanomolar concentrations of radioactively labeled compounds without producing significant disturbances in the biological system being assessed. The essential components of PET are: (1) the production of positron-emitting species in a cyclotron such as fluorine [^{18}F] (half-life = 109.8 min), carbon [^{11}C] (half-life = 20.3 min) and oxygen [^{15}O] (half-life = 2 min); (2) the radiopharmaceutical procedure to attach the positron-emitting species to a physiological substrate such as glucose or amino acids; (3) the introduction of this tracer into the human body and its distribution in central nervous system (CNS) regions based on uptake and metabolic characteristics; (4) the detection and indirect measurement of its positron-emitting activity (high-energy gamma-rays) in a positron tomograph camera; (5) the construction of the corresponding images; and (6) the tracer-kinetic model for the interpretation of temporal changes in the regional distribution, accumulation and clearance of that positron-emitting activity[1-3].

2-[^{18}F]-fluoro-2-deoxy-D-glucose (FDG) is the most widely used tracer in human PET studies. The same carrier transports both FDG and glucose across the blood-brain barrier (BBB) into the CNS. Both compounds then enter the glycolysis cycle and are phosphorylated by hexokinase. Unlike glucose-6-phosphate, FDG-6-phosphate is not a substrate for further metabolism and remains trapped in the tissue for at least 1 h. Accordingly, FDG-6-phosphate will accumulate in the tissue proportionally to its metabolic rate[1-3]. Additionally, PET can estimate regional cerebral blood flow (CBF) with the use of [^{15}O]-labeled tracers such as [^{15}O]H_2O. Consequently, several "metabolic signatures" corresponding to different movement disorders have been obtained with PET.

Neurotransmitter systems can also be evaluated with PET. Particularly, the dopaminergic nigrostriatal

circuit has been extensively studied using [^{18}F]-labeled L-3,4-dihydroxiphenylalanine (FDOPA) and ligands that selectively bind to the pre-synaptic dopamine transporter (DAT) or the post-synaptic dopamine receptors (D_1 and D_2)[4-6]. With these PET techniques, neurochemical deficits have been identified that uniquely characterize a wide variety of movement disorders.

In SPECT, low-energy gamma-rays emitted by probes labeled with heavy radioactive species such as technetium [^{99m}Tc] (half-life = 6 h) and iodine [^{123}I] (half-life = 13.3 h) are directly detected in a gamma camera, which has reduced sensitivity as compared with PET. However, the longer half-lives of SPECT tracers enable transportation from distance and even performance of several studies, in contrast to PET studies, which usually depend on an adjacent cyclotron. Thus, SPECT is usually more available than PET. For example, regional brain perfusion has been investigated extensively with the SPECT tracer [^{99m}Tc]hexamethyl propylene amine oxime (HMPAO).

MOLECULAR IMAGING OF TREMOR

Essential tremor (ET) is a common disorder characterized by bilateral, symmetric postural and kinetic tremor, more pronounced in the hands. It is thought to be related to abnormalities in the connections between the inferior olive, dentate nucleus, red nucleus, thalamus and motor cortices ("tremor-network"). However, there is controversy between neurodegeneration, dysfunction of GABAergic systems and/or abnormal tremor-network oscillations to explain the origin of ET. In fact, PET studies have demonstrated increased bilateral cerebellar metabolic activity during both tremor and at rest, as well as its suppression with ethanol consumption[7,8]. Also, PET has shown abnormal GABAergic function in premotor cortices, dentate nuclei and ventral thalami with the use of the GABA-A receptor antagonist [^{11}C]flumazenil[9] (Table 1). Interestingly, a PET study has shown increased CBF in the supplementary motor area (SMA) ipsilateral to ventral intermediate thalamic deep brain stimulation (DBS), suggesting a stimulating rather than inactivating effect[10]. Further investigation with PET will likely continue increasing our understanding of ET.

In addition, molecular imaging including FDOPA PET and DAT SPECT studies have not shown abnormalities in dopamine striatal neurotransmission in ET[11,12]. Thus, evaluation of the dopaminergic system with PET or SPECT could aid in the distinction between ET and tremor-predominant parkinsonism when the clinical diagnosis is equivocal.

MOLECULAR IMAGING OF CHOREA

Huntington's disease (HD) is a fatal neurodegenerative condition caused by an abnormally increased number of CAG repeats in the huntingtin gene located in chromosome 4p. Usually between the age of 40-50 years, a significant loss of medium spiny GABAergic neurons in the caudate, putamen and cerebral cortices results in progressive behavioral symptoms, chorea and cognitive dysfunction. The pathological processes underlying this degeneration likely precede symptom-onset by several years.

As the affected GABAergic striatal neurons contain the majority of dopamine receptors in the striatum, decreases in D_1 and D_2 receptors accompany the extent of cell loss[13]. Actually, initial PET imaging in HD focused on alterations of these receptors using the D_1 receptor ligand [^{11}C]SCH 23390 and the D_2 receptor ligand [^{11}C]raclopride. These studies have demonstrated that HD progression is accompanied by significant reductions in both D_1 and D_2 binding[14]. Striatal D_2 binding decreases by approximately 5% per year, and this reduction correlates with trinucleotide repeat length, disease duration and severity[15-18]. In patients with HD, dopaminergic uptake is also reduced in pre-synaptic striatal and extrastriatal neurons[16,17].

FDG PET studies have shown hypometabolism in striatum, frontal and temporal cortices in HD patients and asymptomatic carriers preceding neuronal loss[19] (Table 1). In fact, HD carriers who became symptomatic had lower caudate metabolism compared to those who remained asymptomatic after 5 years[20]. PET imaging has also demonstrated increased levels of activated microglia in the striatum of HD carriers, which correlated with the probability of disease-onset and clinical severity[21].

MOLECULAR IMAGING OF DYSTONIA

Dystonia is characterized by sustained or intermittent involuntary contractions of agonist and antagonist muscles resulting in abnormal, repetitive movements and postures that are typically patterned and twisting. Dystonia is associated with abnormal inhibition, processing and plasticity in basal ganglia and sensorimotor networks.

FDG PET studies of large cohorts of patients comparing movement-related and movement-free images obtained during wake and sleep states respectively, have allowed for the development of "metabolic signatures" of dystonia. In *DYT1* dystonia, a generalized dystonia caused by a GAG deletion in chromosome 9, hypermetabolism was found in the premotor cortices, basal ganglia, pons and midbrain[22]. The movement-free hypermetabolic network was identified in the basal ganglia, SMA and cerebellum, whereas movement-related hypermetabolism was found in the cerebellum and thalamus (Table 1). In addition, asymptomatic gene carriers were found to have the movement-free but not the movement-related abnormalities[23]. Afterwards, patients with focal dystonia (blepharospasm)[24] and *DYT6* dystonia[25] were surprisingly found to have similar movement-free metabolic patterns, suggesting that this topography is not genotype-specific. In another study, *DYT1* and *DYT6* patients manifesting dystonia were found to have hypermetabolism in the bilateral SMAs and parietal association cortices. In

Table 1 Summary of molecular imaging findings in common movement disorders

Movement disorder	Metabolism and/or perfusion		Nigrostriatal dopaminergic activity		Other abnormal systems
	Increased	Decreased	Pre-synaptic	Post-synaptic	
Tremor: Essential tremor	Cerebellar, brainstem, thalamic, motor cortices ("tremor-network")	-	Normal	Normal	GABAergic: Reduced in cerebellum, thalami and premotor
Chorea: Huntington's disease	-	Striatum, frontal and temporal	Reduced	Reduced	-
Dystonia	Rest: Basal ganglia, cerebellar, sensorimotor Dystonia: Thalamic, cerebellar	Focal dystonia: Contralateral primary motor cortex	Focal and dopa-responsive dystonia: Normal DAT	Reduced D_2 Dopa-responsive dystonia: Increased D_2, normal D_1	GABA-A: Reduced in motor, premotor and somatosensory cortices
Tics: Tourette's syndrome	Rest: Premotor, sensorimotor Tic: Multiple cognitive and sensorimotor regions	Rest: Striatum, thalamus, limbic	Hyper responsive, correlates with decreased serotonin	Hyper responsive, correlates with decreased serotonin	Serotoninergic: Prefrontal and thalamic GABA-A: Reduced in amygdala and ventral striatum
Parkinsonism: Parkinson's disease	Basal ganglia, thalamus, contralateral to initial/worse symptoms, ipsilateral cerebellum	Parieto-occipital, frontal premotor, contralateral to initial/worse symptoms	Reduced in striatum contralateral to initial/worse symptoms, caudal-to-rostral (putamen-to-caudate)	Normal or increased putaminal D_2 if untreated, could normalize with therapy	Cholinergic: Reduced early Noradrenergic, locus coeruleus: Increased early, reduced later Cardiac sympathetic: Reduced
Multiple system atrophy	-	Bilateral striatal (putamen) and cerebellum	Diffuse reduction in bilateral striatum, variable caudal-to-rostral	Reduced D_2	-
Progressive supranuclear palsy	-	Bilateral mesial frontal, prefrontal, striatal, thalamic, midbrain	Diffuse reduction in bilateral striatum, not caudal-to-rostral	Reduced D_2	-
Corticobasal degeneration	-	Cortices contralateral to symptoms	Diffuse striatal reduction contralateral to symptoms, not caudal-to-rostral	-	-

contrast, *DYT1* asymptomatic carriers were found to have hypermetabolism in the putamen, anterior cingulate and cerebellum, whereas *DYT6* carriers had hypometabolism in the putamen and hypermetabolism in the temporal cortices[26]. Additionally, PET studies with [^{11}C]raclopride have demonstrated that symptomatic and asymptomatic *DYT1* and *DYT6* individuals have decreased D_2 striatal uptake[27,28]. Abnormalities of GABAergic networks have also been postulated in the pathophysiology of dystonia. Particularly, the inhibitory modulation of afferent signals arriving to the somatosensory regions is dysfunctional. In fact, reductions in GABA-A receptor activity in motor, premotor, primary and secondary somatosensory cortices has been revealed in an [^{11}C]flumazenil PET study of patients with dystonia[29]. These results suggest that hereditary dystonia is a neurodevelopmental disorder of sensorimotor integration ("motor preparation") networks, with resulting excessive output of existing postural control systems[30-32].

The effects of globus pallidus (GP) DBS in patients with dystonia have been assessed by measuring regional cerebral blood flow with [^{15}O]H_2O PET. These studies have shown hyperactivity in the thalamus, dorsolateral prefrontal cortex, medial and superior frontal gyri, which could be modulated with GP-DBS[33,34]. Remarkably, long-term GP-DBS may correct these abnormalities, such that continued stimulation may ultimately prove unnecessary[35]. Finally, FDG PET could also be used to monitor and even individualize treatment with other neuromodulation techniques in patients with dystonia[36,37].

DOPA-responsive dystonia (DRD) is a childhood-onset dystonia related to mutations in genes that encode enzymes important for the production of dopamine. DRD patients have been found to have increased [^{11}C]raclopride D_2 binding in the striatum as compared to PD patients and healthy controls[38]. In addition, increased striatal dopamine D_2 availability with unchanged D_1 and DAT binding have been found in patients with DRD[39] (Table 1). The results of these studies might reflect reduced competition and tracer displacement by lack of endogenous dopamine and/or a compensatory response to the dopamine deficiency.

In focal dystonias, post-synaptic striatal D_2 binding reduction along with normal pre-synaptic DAT binding have been evidenced in PET and SPECT studies[40,41] (Table 1). Furthermore, patients with focal limb dystonia ("writer's cramp") were found to have different patterns of striatal dopamine release during motor tasks involving

the dystonic limb as compared to asymptomatic tasks[42]. Botulinum toxin injection, currently considered the first-line treatment of focal dystonia, failed to improve the abnormal activation of the contralateral primary motor cortex in patients with "writer's cramp" despite clinical improvement[43]. Yet, it may induce central plasticity through modulation of afferent muscle spindle inputs[44].

MOLECULAR IMAGING OF TICS

Tourette's syndrome (TS) is a childhood-onset neuropsychiatric disorder defined by persistence of motor and phonic tics, as well as complex behavioral disturbances usually including obsessive-compulsive disorder (OCD).

Molecular imaging techniques have suggested abnormal function of cortico-striatal-thalamo-cortical circuits in TS. FDG PET has demonstrated hypermetabolism in premotor and sensorimotor cortices, as well as hypometabolism in the striatum, thalamus and limbic cortices including orbitofrontal and hippocampal regions in the resting state. During the tics, there is hypermetabolism in the anterior cingulate, inferior parietal, medial and lateral premotor cortices, primary motor cortices including Broca's area, cerebellum, insula, thalamus and the striatum[45,46] (Table 1). Moreover, OCD symptoms correlated with a different pattern characterized by hypometabolism in anterior cingulate and dorsolateral prefrontal cortices, and hypermetabolism in primary motor cortices and precuneus[46]. These results support abnormal hyperactivity of the systems involved in processing sensory information and motor planning in TS.

Given the clinical improvement observed with the use of D_2 antagonists, TS has been linked to dysregulation of dopaminergic transmission. In fact, striatal pre-synaptic dopamine release after amphetamine administration was studied in adult TS patients using [^{11}C]raclopride PET. Finally, abnormal regulation of phasic dopamine responses resulted in hyper responsive dopaminergic system activation in TS, suggesting an imbalance between tonic and phasic dopaminergic responses[47].

Anomalies in serotoninergic transmission in the dorsolateral prefrontal cortices and bilateral thalami were evidenced in a study using alpha-[^{11}C]methyl-L-tryptophan ([^{11}C]AMT) PET to study tryptophan metabolism in children with TS[48]. Increased caudate serotonin synthesis has been shown in another study[49]. Furthermore, a strong correlation between phasic dopamine release and low levels of serotonin was found after evaluating patients with TS using [^{11}C]radopride (D_2 ligand), [^{11}C]WIN (DAT antagonist), [^{11}C]McN (5-HT_{2a} receptor antagonist) and [^{11}C]MDL (SERT antagonist) as tracers[50]. The modulating effects of thalamic DBS in the hyperactive basal ganglia dopaminergic system of patients with TS have been evidenced by [^{18}F]Fallypride PET[51,52]. In addition, the GABAergic system of patients with TS has been studied with [^{11}C]flumazenil PET. A consistent decrease of GABA-A receptor activity was found in the amygdala, ventral striatum, insula and thalamus; with increased activity in the cerebellum, substantia nigra and periaqueductal gray[53].

MOLECULAR IMAGING OF PARKINSONISM

Most CNS dopaminergic neurons are located in the hypothalamus, substantia nigra and ventral tegmental area. They project to the hypophysis (tubero-hypophyseal pathway), striatum (nigrostriatal pathway), frontal, limbic and olfactory regions (mesocortical and mesolimbic pathways). The main dopaminergic system involved in motor control arises from the substantia nigra, a midbrain structure divided into a dorsolateral pars compacta (SNc) that projects mostly to the putamen, and a ventromedial pars reticulata (SNr) that projects mainly to the thalamus.

Parkinsonism is a syndrome characterized by bradykinesia plus rigidity, resting tremor or postural instability. It encompasses several conditions with overlapping clinical features including secondary parkinsonism, alpha-synucleinopathies such as Parkinson's disease (PD) and multiple systems atrophy (MSA), as well as tauopathies such as progressive supranuclear palsy (PSP) and corticobasal degeneration (CBD). The most common parkinsonian syndrome is PD, a progressive neurodegenerative condition in which there is abnormal accumulation of alpha-synuclein in SNc neurons and subsequent dopamine deficiency in the nigrostriatal system. In addition to parkinsonism, PD has important non-motor manifestations including cognitive, behavioral and autonomic disturbances.

Unlike many other neurotransmitters, dopamine has biological attributes that make it amenable to imaging with PET. Given that it cannot cross the BBB, dopaminergic neurons normally synthesize dopamine by decarboxylation of its immediate precursor, LDOPA, which can cross the BBB but is typically synthesized in situ by hydroxylation of tyrosine.

The first approach to imaging of the nigrostriatal dopaminergic system integrity was based on the assessment of pre-synaptic striatal dopamine synthesis capacity. Given the short half-life (20 min) and rapid procedures needed for [^{11}C]DOPA synthesis, LDOPA was labeled with [^{18}F][54]. After several studies, [^{18}F]6-fluoro-L-DOPA (FDOPA) became the preferred tracer for measurements of LDOPA distribution and uptake in the CNS[55,56].

FDOPA is transported across the BBB into the brain by the large neutral amino acid transporter, with similar kinetics to LDOPA[57]. Yet, the rate of FDOPA metabolism by peripheral catechol-O-methyl transferase (COMT) is about one fourth of that of LDOPA[58], which is favorable for brain PET studies, but should be considered during studies aiming to measure or monitor treatment with LDOPA. Once localized in the pre-synaptic terminals of striatal dopaminergic neurons, FDOPA is converted to [^{18}F]fluorodopamine (FDA) by the cerebral aromatic amino acid decarboxylase (AAAD) and subsequently stored in synaptic vesicles. Striatal FDOPA activity is increased if preceded by the administration of a peripheral decarboxylase inhibitor and is decreased after treatment with reserpine, a drug that releases catecholamines from pre-synaptic vesicles. This was the first time the regional

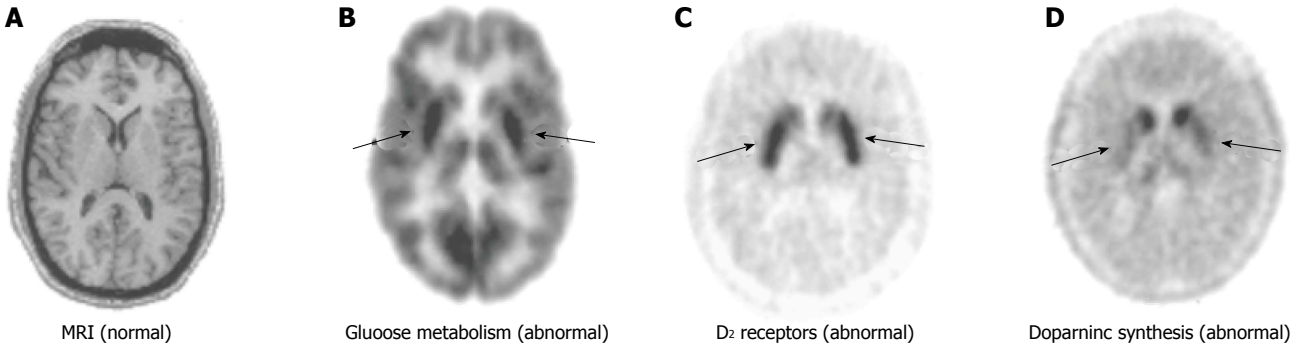

Figure 1 Imaging of early Parkinson's disease. A: MRI of the striatum does not indicate any significant anatomical abnormalities; B: PET reveals selective regional alterations in diverse neurochemical processes: FDG PET shows putaminal hypermetabolism relative to the caudate (approximately 10%); C: [^{18}F]fluoroethylspiperone PET shows approximately 15% greater D_2 receptor density in the putamen as compared to the caudate; D: FDOPA PET shows significant reduction in dopamine synthetic capacity (80%) in the putamen but not in the caudate. Arrows in B, C, and D indicate putamen. MRI: Magnetic resonance imaging; PET: Positron emission tomography; FDG: 2-[^{18}F]-fluoro-2-deoxy-D-glucose; FDOPA: [^{18}F]-labeled L-3,4-dihydroxiphenylalanine. (Originally published in the JNM. Phelps ME. PET: the merging of biology and imaging into molecular imaging. *J Nucl Med* 2000; **41**: 661-681. © by the Society of Nuclear Medicine and Molecular Imaging, Inc.)

distribution, localization and pharmacological manipulation of a neurotransmitter were imaged[59]. Later, the first human FDOPA PET study demonstrated a similar pattern of dopaminergic localization[60]. Although FDOPA can be taken up by noradrenergic and serotoninergic neurons, the striatal uptake of FDOPA has been used as a correlate of nigrostriatal dopaminergic pre-synaptic integrity (Figure 1).

Another approach is to evaluate dopamine terminal density with tracers that bind to the DAT, a pre-synaptic membrane protein responsible for the reuptake of released dopamine. The cocaine congener, *N*-[3-[^{18}F]fluoropropyl]-2β-carbomethoxy-3β-(4-iodophenyl)nortropane [^{18}F]FPCIT, which has high binding affinity for the DAT, is the most common PET tracer used for this purpose (Figure 2). Several other tracers have been synthesized for SPECT, such as [^{99m}Tc]TRODAT-1, beta-[^{123}I]CIT and [^{123}I]FPCIT (DaTScan™) (Figure 3). Although kinetic properties and DAT selectivity vary between tracers, they all provide similar information about pre-synaptic dopaminergic function. Of note, DATs can undergo compensatory or pharmacological regulation, thus the use of DAT ligands is controversial particularly when used to monitor disease progression or the effect of medical therapy. The pre-synaptic vesicular monoamine transporter type 2 (VMAT-2) is less subject to these regulatory changes but is expressed in all monoaminergic neurons. Since most striatal VMAT-2 activity occurs in dopamine terminals, PET studies labeling VMAT-2 with [^{11}C]dihydrotetrabenazine (DTBZ) or [^{18}F]fluoropropyl-DTBZ might also help evaluate dopaminergic nerve terminal function[61].

Post-synaptic striatal dopaminergic function can be assessed with tracers that bind to D_1 and D_2. For example, [^{18}F]Fluoroethylspiperone is a PET tracer (Figure 1) and [^{123}I]IBZM is a SPECT tracer (Figure 3), both of which can bind to D_2 receptors. D_1 and D_2 receptors have different functions based on their mechanisms of adenylyl cyclase stimulation and inhibition, respectively[62]. Since receptor binding is subject to competition with endogenous dopamine, molecular tracers with low D_2 affinity can be used to estimate the amount of dopamine (*i.e.,* increased synaptic dopamine leads to decreased D_2 activity). Furthermore, changes after therapeutic interventions can be assessed with these low receptor affinity ligands. Lastly, high affinity probes can help evaluate extrastriatal D_2 binding[63].

The capability to detect localized subregional biochemical deficits in the nigrostriatal system has provided insights into the etiology, pathophysiology, differential diagnosis and therapy for patients with parkinsonian syndromes, particularly PD.

Etiology and diagnosis

The cause of PD is still unclear. The combination of genetic susceptibility with environmental factors probably plays a significant role. A longitudinal FDOPA PET study of PD monozygotic twins showed that many unaffected twins had decreased tracer uptake, concordant with their affected siblings. When followed for several years, 75% of the twin pairs were clinically or radiologically concordant[64]. This study helped stimulate debate on the genetics of PD. A digenic genotype with complete penetrance was even theorized to explain the pattern of PD inheritance rather than multiple genes or a single gene with incomplete penetrance[65].

PD is characterized by asymmetrical progressive decline in tracer accumulation in the striatum contralateral to the most symptomatic side of the body (Figures 1-3). The reduction of striatal dopaminergic pre-synaptic activity follows a caudal-to-rostral direction, being initially more severe in the posterior striatum (Figure 2). This pattern corresponds with the lateral-to-medial pattern of neurodegeneration in the substantia nigra, with earlier and more severe involvement of the ventrolateral aspect of the SNc[66]. Regional striatal alterations showing larger increases in D_2 receptor binding in the putamen than in the caudate can also been detected (Figure 1). As expected, neuropsychologically normal patients with PD can have reduced FDOPA PET activity in the putamen but not in the caudate contralateral to their major motor

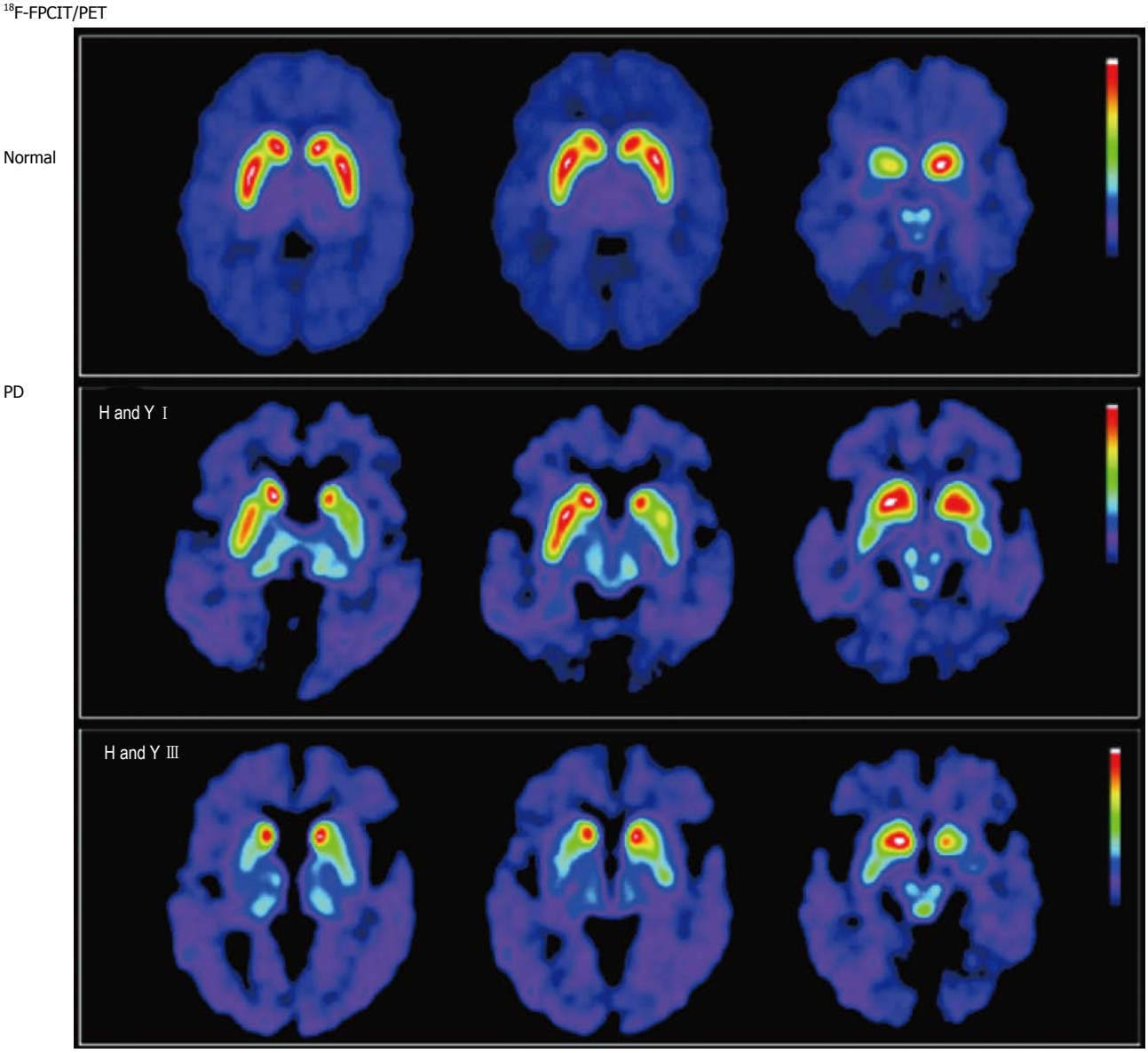

Figure 2 Nigrostriatal dopaminergic system degeneration in Parkinson's disease. PET images show striatal uptake of [^{18}F]FPCIT, a ligand with high affinity for pre-synaptic dopamine transporters, for a normal volunteer (top row), and 2 patients with Parkinson's disease (PD) [middle row: Hoehn and Yahr (H and Y) stage Ⅰ; bottom row: H and Y stage Ⅲ]. Striatal [^{18}F]FPCIT uptake is mainly reduced in the putamen contralateral to the most symptomatic side in early PD (middle row), progressing to bilateral reduction in a caudal-to-rostral pattern (bottom row). (Originally published in the JNM. Katzumata K, Dhawan V, Chaly T, *et al*. Dopamine transporter imaging with fluorine-18-FPCIT and PET. *J Nucl Med* 1998; **39**: 1521-1530. © by the Society of Nuclear Medicine and Molecular Imaging, Inc.)

signs. This reduction can be similar between tremor-predominant and akinetic-rigid patients. To explain these findings, it has been postulated that the putamen is mainly involved in motor control, whereas the caudate participates mostly in cognitive functions[67]. However, most patients in these initial studies had early PD, perhaps before involvement of the caudate could be appreciated. In addition, FDOPA activity can be increased relative to the degree of denervation in early disease, possibly due to compensatory upregulation of AAAD. Moreover, FDG PET studies have shown hypermetabolism in the same areas with decreased FDOPA uptake[68] (Figure 4). Although characteristic, this appearance is not completely specific for PD and might be noted in other parkinsonian syndromes, particularly MSA (Figure 3).

Differential diagnosis

PSP is an atypical parkinsonism associated with reduction of vertical gaze and axial rather than appendicular rigidity manifesting with premature falls. MSA is defined by autonomic failure and either poor LDOPA-responsive parkinsonism (MSA-P, striatonigral degeneration) or cerebellar dysfunction (MSA-C, olivopontocerebellar atrophy). CBD presents with asymmetric onset of limb bradykinesia, rigidity, dystonia or myoclonus; plus apraxia, cortical sensory deficits or alien limb phenomenon.

The direction of pathologic changes in the substantia nigra of patients with PSP is from medial-to-lateral, corresponding with their early truncal rigidity, but opposite to the direction seen in PD[66,69]. In PSP and MSA, pre-synaptic striatal activity is usually symmetrically and

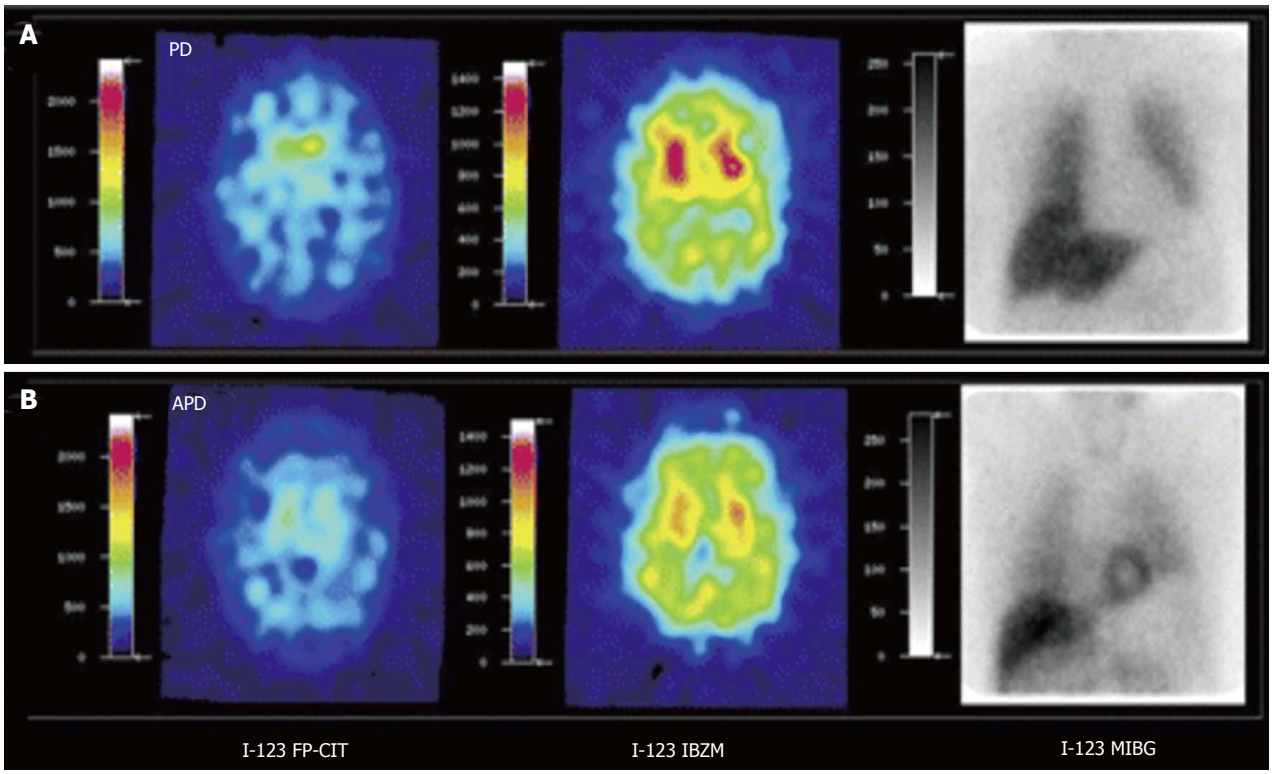

Figure 3 [^{123}I]FPCIT, [^{123}I]IBZM and cardiac SPECT imaging [[^{123}I]MIBG] of Parkinson's disease (A) and atypical parkinsonism (B). Striatal [^{123}I]FPCIT is decreased in both PD and APD. Striatal D_2 receptor binding is normal in PD but decreased in APD. Myocardial sympathetic SPECT signal is decreased in PD but normal in APD. PD: Parkinson's disease; APD: Atypical parkinsonism; SPECT: Single photon emission computerized tomography. (Originally published in the JNM. Südmeyer M, Antke C, Zizek T, et al. *J Nucl Med* 2011; **52**: 733-740. © by the Society of Nuclear Medicine and Molecular Imaging, Inc.)

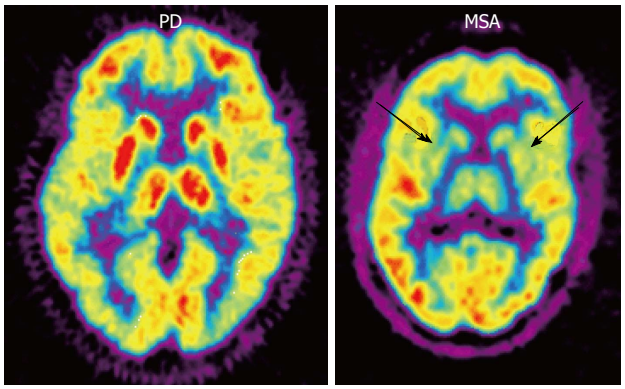

Figure 4 2-[^{18}F]-fluoro-2-deoxy-D-glucose positron emission tomography (FDG PET) in Parkinson's disease (PD) and multiple system atrophy (MSA). FDG PET shows hypometabolism in bilateral parieto-occipital and prefrontal cortices, as well as hypermetabolism in the basal ganglia and thalamus in PD, as opposed to bilateral striatal and thalamic hypometabolism in MSA (arrows). (Originally published in the JNM. Brooks DJ. *J Nucl Med* 2010; **51**: 596-609. © by the Society of Nuclear Medicine and Molecular Imaging, Inc.)

diffusely decreased. The caudal-to-rostral pattern seen in PD is lost in PSP, but could be variably present in MSA (Figure 3). In CBD, there is asymmetric reduction of FDOPA accumulation in the striatum contralateral to the most symptomatic side. Additionally, increased post-synaptic putamen D_2 binding that can be normalized with therapy is seen in PD. D_2 binding is reduced in PSP and MSA[61] (Table 1, Figure 3).

Although not specific, FDG PET or HMPAO SPECT patterns might also help differentiate between the parkinsonian syndromes. In fact, characteristic hypometabolism has been demonstrated in contralateral parieto-occipital and frontal cortices in PD; bilateral putamen and cerebellum in MSA (Figure 4); caudate, thalami, midbrain, mesial frontal and prefrontal cortices in PSP; and contralateral cortical regions in CBD. In addition, PD patients have hypermetabolism in the basal ganglia, thalami, pons and cerebellum[70] (Table 1, Figure 4). Furthermore, SPECT studies have shown decreased cardiac sympathetic terminals signal indicating denervation in PD as opposed to the atypical parkinsonisms[71] (Figure 3).

Remarkably, up to 20% of patients with a clinical diagnosis of PD can have normal molecular imaging of the nigrostriatal dopaminergic system. This phenomenon has been labeled "symptoms without evidence for dopamine deficiency" (SWEDD)[72]. Most cases of SWEDD are due to clinical misdiagnosis. Yet, a small proportion of SWEDD patients may actually have PD based on clinical progression, LDOPA responsiveness and/or repeated imaging[73]. Although still controversial, these findings imply that normal functional imaging cannot completely exclude early PD[74]. Clearly, additional studies comparing PET and/or SPECT with neuropathology for the diagnosis of PD are needed.

Pathophysiology and disease progression

Molecular imaging studies evaluate dopaminergic activity rather than the number of neurons. Moreover,

disability in PD is related to deficiencies in multiple other neurotransmitter systems. Nonetheless, imaging of the nigrostriatal dopaminergic system is one of the best markers to assess PD progression.

Neuroinflammation might precede neuronal death in neurodegenerative disorders. PET studies targeting specific molecules expressed by activated microglia have provided controversial results in PD[75,76]. More consistent findings have been reported in MSA[77], PSP[78], CBD[79] and HD[80]. The challenging imaging of the usual small amounts of intracellular-predominant alpha-synuclein deposits could lead to exciting advances in the future[81].

In PD, the loss of nigrostriatal neurons eventually exceeds an asymptomatic threshold. In fact, striatal uptake prior to symptom presentation has been measured to decline at an annual rate of 9%-12%[82]. Interestingly, molecular studies have demonstrated subclinical dopamine deficits in people exposed to nigral toxins, individuals with family history of dominant or recessive PD, twins of PD patients[64], and patients with non-motor symptoms of PD such as hyposmia, autonomic dysfunction and/or REM sleep behavior disorder (RBD)[83]. In fact, people with these non-motor symptoms and dopaminergic deficits on functional imaging have a higher risk of developing PD[83]. Early identification and long-term clinico-radiological follow-up of these patients could be of great value to study the natural history of PD and to evaluate if, when and how strongly molecular imaging can predict the conversion from prodromal to clinically-evident PD.

FDOPA uptake is increased in the noradrenergic locus coeruleus in early PD but decreases to abnormal levels with disease progression, suggesting early compensatory upregulation. PET studies have also shown early cholinergic dysfunction in PD patients with impaired olfactory function or RBD with or without cognitive dysfunction[84].

[^{18}F]FPCIT PET studies have demonstrated how the pathology in PD progresses from unilateral to bilateral striatal dopamine deficits, and that its magnitude correlates with the severity of symptoms[85] (Figure 2). Interestingly, decreased striatal dopaminergic uptake correlates with metabolic hyperactivity in the STN and GP[86].

Assessment of disease progression requires objective markers to overcome the confounding effects of symptomatic benefit. The evaluation of PD progression with molecular imaging should be carefully interpreted, since tracer metabolism can be altered by compensatory regulation and/or therapeutic interventions.

Treatment

Deprenyl (Selegiline), an irreversible monoamine oxidase type B (MAO-B) inhibitor employed in the treatment of PD, was used to determine that CNS MAO-B distribution is approximately 60% higher in the thalamus and basal ganglia relative to cortical regions and cerebellum. In further studies, 5 mg of deprenyl were administered daily for 7 d in order to obtain maximal binding to MAO-B. Then, the subjects were evaluated with [^{11}C]deprenyl PET. Relative to pre-treatment values, [^{11}C]deprenyl binding after deprenyl administration was reduced by 90%, indicating near complete inactivation of the enzyme. Multiple PET scans during the next two months revealed that MAO-B binding capacity could be restored only by synthesis of new enzyme. It was calculated that the half-time for MAO-B synthesis was approximately 40 d. These results provided the first *in vivo* measurement of the synthesis rate of a specific protein in the brain. Furthermore, it was demonstrated that the recommended daily dose of deprenyl (5 mg twice daily) exceeded that necessary for therapeutic efficacy, illustrating how PET can be used to determine drug dosage for optimal efficacy in movement disorders[87].

FDOPA PET has been used in several studies to evaluate the effects of potential neuroprotective agents on dopaminergic function[72]. For example, the relative rates of progression of early PD in patients started on ropinirole or LDOPA were compared in a double-blind, randomized study in which FDOPA PET studies were obtained at baseline and 2 years later. The mean reduction in putamen FDOPA uptake was not significantly different for both groups[88].

Molecular studies have shown that LDOPA-induced dopamine release in the striatum increases with the severity and duration of PD, and is of larger magnitude in patients with LDOPA-induced dyskinesias[89,90]. Moreover, greater magnitude but shorter duration of LDOPA-induced dopamine release in responsive patients could predict the future development of motor fluctuations[91]. In addition, changes in D_2 receptor density of PD patients have been measured with PET after exposure to dopaminergic pharmacotherapy and/or the compensatory reactions to the ongoing disease process, showing normal or increased D_2 binding potential in untreated PD patients, and reduced potential in PD patients with fluctuating responses to LDOPA[92].

Impulse control disorders have a higher incidence in patients with PD treated with dopamine agonists. [^{11}C]raclopride PET was used to compare D_2 receptor availability during a gambling task in PD patients with and without pathological gambling. It was found that those with pathological gambling had lower D_2 binding at baseline but increased release of dopamine in the ventral striatum during the gambling task, as is seen in those with chemical addictions in response to the drug to which they are addicted[93]. Later, increased release of dopamine in the ventral striatum during reward cues was also demonstrated, implying that PD patients who develop impulse control disorders could represent a susceptible group of individuals unmasked by dopaminergic agonists[94]. Pharmacokinetic and pharmacodynamic studies with PET will likely continue increasing our understanding of the mechanisms of action, efficacy and complications of medical interventions in patients with PD.

Molecular imaging has also been used to evaluate efficacy of different surgical interventions. For example, in PD patients who received a striatal fetal nigral tissue transplant, a significant increase in FDOPA PET activity was observed. Unfortunately, clinical improvement was

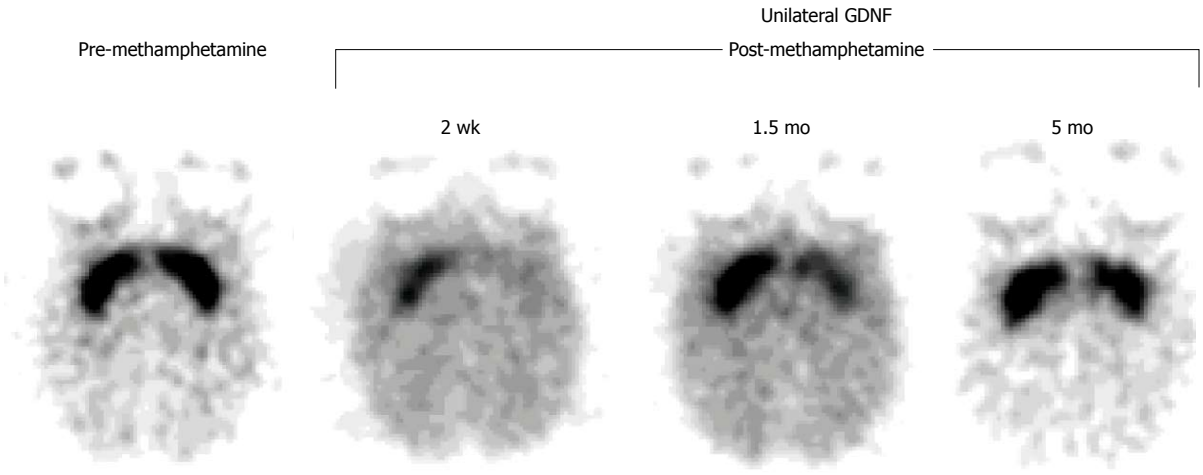

Figure 5 Positron emission tomography assessment of a neuroprotective strategy for methamphetamine-induced neurotoxicity with [^{11}C]WIN 35,428, a selective dopamine transporter ligand. Prior to drug treatment, symmetrical and selective striatal uptake was demonstrated (left, pre-methamphetamine). Glial cell-line derived growth factor (GDNF) was then unilaterally injected into the striatum (left-sided striatum on the images shown). One week later, a neurotoxic methamphetamine (METH) dosage was systemically administered. Subsequent studies showed that the GDNF-pretreated striatum was partially protected from the METH-induced neurotoxicity and that it recovered at a faster rate relative to the contralateral striatum (right, post-methamphetamine). (Originally published in Synapse. Melega WP, Lacan G, Desalles AA, Phelps ME. Long-term methamphetamine-induced decreases of [(11)C]WIN 35,428 binding in striatum are reduced by GDNF: PET studies in the vervet monkey. *Synapse* 2000; **35**: 243-249. © by John Wiley & Sons publications, Inc.)

dismal, suggesting implant survival without enough or adequate post-synaptic connections[95]. Later, PET imaging has provided evidence that PD patients benefit from surgical interventions such as STN or GP DBS, which reduce the abnormally increased inhibitory output from the basal ganglia to the ventral thalamus[96]. In fact, FDG PET studies have demonstrated that STN DBS suppresses hypermetabolism in the rostral cerebellum, and partly reverses reductions of cortical glucose consumption in limbic and associative regions where basal ganglia connections project, including frontal cortices[97,98].

FUTURE DIRECTIONS

The mission of first defining the impaired molecular mechanisms leading to abnormal motor network dysfunction and movements disorders, and then designing therapies to restore their normal function requires a tremendous effort and integration of different specialties. A fundamental technology in this quest is molecular imaging with PET and SPECT.

In addition to established neuromodulation techniques such as DBS, the use of genetic therapy to alter neurotransmitter activity might be incorporated into therapeutic options in the coming years. These therapies can be quantitatively assessed with specific tracers as mentioned in this review. In fact, the gene for AAAD was inserted into an adeno-associated virus that had been stripped of its replicative functions but was still capable of infecting cells. It was hypothesized that upon injection of the virus into the striatum, the subsequent expression of AAAD in the infected striatal cells would provide a local source of AAAD that could selectively convert LDOPA to dopamine. For the experiment, the subjects first received an intracarotid injection of 1-methyl-4-phenyl-1,2,3,6-tetrahydropyridine (MPTP), a neurotoxin that specifically targets dopaminergic nigral neurons. Afterwards, 6-[^{18}F]fluoro-L-metatyrosine (FMT), an analog of LDOPA, was used as a PET tracer to show unilateral reduction in AAAD activity, indicating that MPTP had produced a unilateral striatal dopamine deficit. Subsequently, the AAAD gene-viral vector was stereotactically injected into the lesioned striatum. Two months later, a robust FMT PET uptake was detected in the striatum that had been injected with the virus containing AAAD[99].

Based on prior studies showing neuroprotective effects of the glial cell-line derived growth factor (GDNF) against MPTP, a solution containing GDNF was stereotactically and unilaterally delivered into the caudate and putamen of vervet monkeys one week prior to systemic administration of methamphetamine. The potential neuroprotective effects of GDNF were then evaluated by PET imaging of the striatum in multiple studies with the tracer [^{11}C]WIN 35428, a selective DAT ligand. The results showed that GDNF pretreatment provided partial neuroprotection from methamphetamine-induced loss of DATs. These results provided evidence that exogenously administered GDNF could provide neuroprotection in the adult non-human primate brain and that a corresponding pharmacotherapy approach could be monitored with PET[100] (Figure 5).

The capacity of molecular imaging, in particular PET, to provide an *in vivo* time course of gene expression, protein synthesis, receptor and transporter binding, could enable researchers and clinicians to develop novel therapeutic approaches in humans with movement disorders. These methods should first be evaluated in non-human primate models to validate and optimize drug dosages, targets for injection or modulation, evaluation of treatment safety and efficacy, and more.

CONCLUSION

Molecular imaging has evaluated changes in regional

brain perfusion, glucose metabolism and neurotransmitter systems in movement disorders, shedding light into their etiology, pathophysiology, diagnosis, disease progression and therapeutic options, including the identification and individualization of potential neuromodulation targets.

The recognition of asymptomatic and progressive disease by molecular imaging in contrast to the unremarkable data from structural imaging illustrates that significant neurochemical alterations precede and are not necessarily paralleled by morphological changes. In this context, PET and SPECT have provided disease-specific biomarkers that could help determine which individuals are more likely to benefit from different therapeutic modalities.

Continuing progress in the design of PET and SPECT systems, as reflected by new detector materials and image reconstruction algorithms, higher performance computer technology and improved availability of radiopharmaceuticals will all contribute to a wider range of applications in movement disorders. In particular, the combined use of genetic therapy and molecular imaging could provide opportunities for the design and evaluation of novel therapies at early stages of the disease.

REFERENCES

1 **Sokoloff L**. Cerebral circulation, energy metabolism, and protein synthesis: general characteristics and principles of measurement. In: Phelps M, Mazziotta JC, Heinrich R, Schelbert HR, editors. Positron emission tomography and autoradiography: principles and applications for the brain and heart. New York: Raven Press, 1986: 1-71

2 **Sokoloff L**, Reivich M, Kennedy C, Des Rosiers MH, Patlak CS, Pettigrew KD, Sakurada O, Shinohara M. The [14C]deoxyglucose method for the measurement of local cerebral glucose utilization: theory, procedure, and normal values in the conscious and anesthetized albino rat. *J Neurochem* 1977; **28**: 897-916 [PMID: 864466 DOI: 10.1111/j.1471-4159.1977.tb10649.x]

3 **Melega WP**, De Salles AAF. Molecular Imaging of the Brain with Positron Emission Tomography. In: Youmans JR, Winn HR, editors. Youmans Neurological Surgery. 6th ed. USA: El Sevier, 2011: 376-392

4 **Volkow ND**, Fowler JS, Gatley SJ, Logan J, Wang GJ, Ding YS, Dewey S. PET evaluation of the dopamine system of the human brain. *J Nucl Med* 1996; **37**: 1242-1256 [PMID: 8965206]

5 **Blomqvist G**, Pauli S, Farde L, Eriksson L, Persson A, Halldin C. Maps of receptor binding parameters in the human brain--a kinetic analysis of PET measurements. *Eur J Nucl Med* 1990; **16**: 257-265 [PMID: 2112470 DOI: 10.1007/BF00842777]

6 **Mazière B**, Mazière M. Where have we got to with neuroreceptor mapping of the human brain? *Eur J Nucl Med* 1990; **16**: 817-835 [PMID: 2170141 DOI: 10.1007/BF00833018]

7 **Wills AJ**, Jenkins IH, Thompson PD, Findley LJ, Brooks DJ. Red nuclear and cerebellar but no olivary activation associated with essential tremor: a positron emission tomographic study. *Ann Neurol* 1994; **36**: 636-642 [PMID: 7944296]

8 **Boecker H**, Wills AJ, Ceballos-Baumann A, Samuel M, Thompson PD, Findley LJ, Brooks DJ. The effect of ethanol on alcohol-responsive essential tremor: a positron emission tomography study. *Ann Neurol* 1996; **39**: 650-658 [PMID: 8619551 DOI: 10.1002/ana.410390515]

9 **Boecker H**, Weindl A, Brooks DJ, Ceballos-Baumann AO, Liedtke C, Miederer M, Sprenger T, Wagner KJ, Miederer I. GABAergic dysfunction in essential tremor: an 11C-flumazenil PET study. *J Nucl Med* 2010; **51**: 1030-1035 [PMID: 20554735 DOI: 10.2967/jnumed.109.074120]

10 **Perlmutter JS**, Mink JW, Bastian AJ, Zackowski K, Hershey T, Miyawaki E, Koller W, Videen TO. Blood flow responses to deep brain stimulation of thalamus. *Neurology* 2002; **58**: 1388-1394 [PMID: 12011286 DOI: 10.1212/WNL.58.9.1388]

11 **Antonini A**, Moresco RM, Gobbo C, De Notaris R, Panzacchi A, Barone P, Calzetti S, Negrotti A, Pezzoli G, Fazio F. The status of dopamine nerve terminals in Parkinson's disease and essential tremor: a PET study with the tracer [11-C]FE-CIT. *Neurol Sci* 2001; **22**: 47-48 [PMID: 11487195]

12 **Isaias IU**, Marotta G, Hirano S, Canesi M, Benti R, Righini A, Tang C, Cilia R, Pezzoli G, Eidelberg D, Antonini A. Imaging essential tremor. *Mov Disord* 2010; **25**: 679-686 [PMID: 20437537]

13 **Cross A**, Rossor M. Dopamine D-1 and D-2 receptors in Huntington's disease. *Eur J Pharmacol* 1983; **88**: 223-229 [PMID: 6221936]

14 **Andrews TC**, Weeks RA, Turjanski N, Gunn RN, Watkins LH, Sahakian B, Hodges JR, Rosser AE, Wood NW, Brooks DJ. Huntington's disease progression. PET and clinical observations. *Brain* 1999; **122** (Pt 12): 2353-2363 [PMID: 10581228]

15 **Antonini A**, Leenders KL, Eidelberg D. [11C]raclopride-PET studies of the Huntington's disease rate of progression: relevance of the trinucleotide repeat length. *Ann Neurol* 1998; **43**: 253-255 [PMID: 9485067]

16 **Pavese N**, Andrews TC, Brooks DJ, Ho AK, Rosser AE, Barker RA, Robbins TW, Sahakian BJ, Dunnett SB, Piccini P. Progressive striatal and cortical dopamine receptor dysfunction in Huntington's disease: a PET study. *Brain* 2003; **126**: 1127-1135 [PMID: 12690052]

17 **Ginovart N**, Lundin A, Farde L, Halldin C, Bäckman L, Swahn CG, Pauli S, Sedvall G. PET study of the pre- and post-synaptic dopaminergic markers for the neurodegenerative process in Huntington's disease. *Brain* 1997; **120** (Pt 3): 503-514 [PMID: 9126061]

18 **Antonini A**, Leenders KL, Spiegel R, Meier D, Vontobel P, Weigell-Weber M, Sanchez-Pernaute R, de Yébenez JG, Boesiger P, Weindl A, Maguire RP. Striatal glucose metabolism and dopamine D2 receptor binding in asymptomatic gene carriers and patients with Huntington's disease. *Brain* 1996; **119** (Pt 6): 2085-2095 [PMID: 9010012]

19 **Ciarmiello A**, Cannella M, Lastoria S, Simonelli M, Frati L, Rubinsztein DC, Squitieri F. Brain white-matter volume loss and glucose hypometabolism precede the clinical symptoms of Huntington's disease. *J Nucl Med* 2006; **47**: 215-222 [PMID: 16455626]

20 **Ciarmiello A**, Giovacchini G, Orobello S, Bruselli L, Elifani F, Squitieri F. 18F-FDG PET uptake in the pre-Huntington disease caudate affects the time-to-onset independently of CAG expansion size. *Eur J Nucl Med Mol Imaging* 2012; **39**: 1030-1036 [PMID: 22526956]

21 **Politis M**, Pavese N, Tai YF, Kiferle L, Mason SL, Brooks DJ, Tabrizi SJ, Barker RA, Piccini P. Microglial activation in regions related to cognitive function predicts disease onset in Huntington's disease: a multimodal imaging study. *Hum Brain Mapp* 2011; **32**: 258-270 [PMID: 21229614 DOI: 10.1002/hbm.21008]

22 **Eidelberg D**, Moeller JR, Ishikawa T, Dhawan V, Spetsieris P, Przedborski S, Fahn S. The metabolic topography of idiopathic torsion dystonia. *Brain* 1995; **118** (Pt 6): 1473-1484 [PMID: 8595478 DOI: 10.1093/brain/118.6.1473]

23 **Eidelberg D**, Moeller JR, Antonini A, Kazumata K, Nakamura T, Dhawan V, Spetsieris P, deLeon D, Bressman SB, Fahn S. Functional brain networks in DYT1 dystonia. *Ann Neurol* 1998; **44**: 303-312 [PMID: 9749595 DOI: 10.1002/ana.410440304]

24 **Hutchinson M**, Nakamura T, Moeller JR, Antonini A, Belakhlef A, Dhawan V, Eidelberg D. The metabolic topography of essential blepharospasm: a focal dystonia with general implications. *Neurology* 2000; **55**: 673-677 [PMID: 10980732 DOI: 10.1212/WNL.55.5.673]

25 **Trost M**, Carbon M, Edwards C, Ma Y, Raymond D, Mentis MJ, Moeller JR, Bressman SB, Eidelberg D. Primary dystonia: is abnormal functional brain architecture linked to genotype?

Ann Neurol 2002; **52**: 853-856 [PMID: 12447944 DOI: 10.1002/ana.10418]

26 **Carbon M**, Su S, Dhawan V, Raymond D, Bressman S, Eidelberg D. Regional metabolism in primary torsion dystonia: effects of penetrance and genotype. *Neurology* 2004; **62**: 1384-1390 [PMID: 15111678 DOI: 10.1212/01.WNL.0000120541.97467.FE]

27 **Asanuma K**, Ma Y, Okulski J, Dhawan V, Chaly T, Carbon M, Bressman SB, Eidelberg D. Decreased striatal D2 receptor binding in non-manifesting carriers of the DYT1 dystonia mutation. *Neurology* 2005; **64**: 347-349 [PMID: 15668438 DOI: 10.1212/01.WNL.0000149764.34953.BF]

28 **Carbon M**, Niethammer M, Peng S, Raymond D, Dhawan V, Chaly T, Ma Y, Bressman S, Eidelberg D. Abnormal striatal and thalamic dopamine neurotransmission: Genotype-related features of dystonia. *Neurology* 2009; **72**: 2097-2103 [PMID: 19528516]

29 **Garibotto V**, Romito LM, Elia AE, Soliveri P, Panzacchi A, Carpinelli A, Tinazzi M, Albanese A, Perani D. In vivo evidence for GABA(A) receptor changes in the sensorimotor system in primary dystonia. *Mov Disord* 2011; **26**: 852-857 [PMID: 21370265 DOI: 10.1002/mds.23553]

30 **Marsden CD**. The mysterious motor function of the basal ganglia: the Robert Wartenberg Lecture. *Neurology* 1982; **32**: 514-539 [PMID: 7200209 DOI: 10.1212/WNL.32.5.514]

31 **Carbon M**, Argyelan M, Habeck C, Ghilardi MF, Fitzpatrick T, Dhawan V, Pourfar M, Bressman SB, Eidelberg D. Increased sensorimotor network activity in DYT1 dystonia: a functional imaging study. *Brain* 2010; **133**: 690-700 [PMID: 20207699]

32 **Niethammer M**, Carbon M, Argyelan M, Eidelberg D. Hereditary dystonia as a neurodevelopmental circuit disorder: Evidence from neuroimaging. *Neurobiol Dis* 2011; **42**: 202-209 [PMID: 20965251 DOI: 10.1016/j.nbd.2010.10.010]

33 **Detante O**, Vercueil L, Thobois S, Broussolle E, Costes N, Lavenne F, Chabardes S, Lebars D, Vidailhet M, Benabid AL, Pollak P. Globus pallidus internus stimulation in primary generalized dystonia: a H215O PET study. *Brain* 2004; **127**: 1899-1908 [PMID: 15231585 DOI: 10.1093/brain/awh213]

34 **Thobois S**, Ballanger B, Xie-Brustolin J, Damier P, Durif F, Azulay JP, Derost P, Witjas T, Raoul S, Le Bars D, Broussolle E. Globus pallidus stimulation reduces frontal hyperactivity in tardive dystonia. *J Cereb Blood Flow Metab* 2008; **28**: 1127-1138 [PMID: 18231115 DOI: 10.1038/sj.jcbfm.9600610]

35 **Hebb MO**, Chiasson P, Lang AE, Brownstone RM, Mendez I. Sustained relief of dystonia following cessation of deep brain stimulation. *Mov Disord* 2007; **22**: 1958-1962 [PMID: 17674409 DOI: 10.1002/mds.21616]

36 **Lalli S**, Piacentini S, Franzini A, Panzacchi A, Cerami C, Messina G, Ferré F, Perani D, Albanese A. Epidural premotor cortical stimulation in primary focal dystonia: clinical and 18F-fluoro deoxyglucose positron emission tomography open study. *Mov Disord* 2012; **27**: 533-538 [PMID: 22344674 DOI: 10.1002/mds.24949]

37 **Romito LM**, Franzini A, Perani D, Carella F, Marras C, Capus L, Garibotto V, Broggi G, Albanese A. Fixed dystonia unresponsive to pallidal stimulation improved by motor cortex stimulation. *Neurology* 2007; **68**: 875-876 [PMID: 17353483 DOI: 10.1212/01.wnl.0000256816.83036.c9]

38 **Styczyńska B**, Krzemińska A, Mańkowska H, Sereda B. [Kelevan used as poisoned nutrition in the destruction of Pharaoh's ants (Monomorium pharaonis L.)]. *Rocz Panstw Zakl Hig* 1976; **27**: 577-585 [PMID: 981893 DOI: 10.1002/ana.410440509]

39 **Rinne JO**, Iivanainen M, Metsähonkala L, Vainionpää L, Pääkkönen L, Nagren K, Helenius H. Striatal dopaminergic system in dopa-responsive dystonia: a multi-tracer PET study shows increased D2 receptors. *J Neural Transm* 2004; **111**: 59-67 [PMID: 14714216 DOI: 10.1007/s00702-003-0053-3]

40 **Perlmutter JS**, Stambuk MK, Markham J, Black KJ, McGee-Minnich L, Jankovic J, Moerlein SM. Decreased [18F]spiperone binding in putamen in idiopathic focal dystonia. *J Neurosci* 1997; **17**: 843-850 [PMID: 8987805]

41 **Naumann M**, Pirker W, Reiners K, Lange KW, Becker G, Brücke T. Imaging the pre- and postsynaptic side of striatal dopaminergic synapses in idiopathic cervical dystonia: a SPECT study using [123I] epidepride and [123I] beta-CIT. *Mov Disord* 1998; **13**: 319-323 [PMID: 9539347 DOI: 10.1002/mds.870130219]

42 **Berman BD**, Hallett M, Herscovitch P, Simonyan K. Striatal dopaminergic dysfunction at rest and during task performance in writer's cramp. *Brain* 2013; **136** (Pt 12): 3645-3658 [PMID: 24148273 DOI: 10.1093/brain/awt282]

43 **Ceballos-Baumann AO**, Sheean G, Passingham RE, Marsden CD, Brooks DJ. Botulinum toxin does not reverse the cortical dysfunction associated with writer's cramp. A PET study. *Brain* 1997; **120** (Pt 4): 571-582 [PMID: 9153120 DOI: 10.1093/brain/120.4.571]

44 **Walsh R**, Hutchinson M. Molding the sensory cortex: spatial acuity improves after botulinum toxin treatment for cervical dystonia. *Mov Disord* 2007; **22**: 2443-2446 [PMID: 17960812 DOI: 10.1002/mds.21759]

45 **Jeffries KJ**, Schooler C, Schoenbach C, Herscovitch P, Chase TN, Braun AR. The functional neuroanatomy of Tourette's syndrome: an FDG PET study III: functional coupling of regional cerebral metabolic rates. *Neuropsychopharmacology* 2002; **27**: 92-104 [PMID: 12062910 DOI: 10.1016/S0893-133X(01)00428-6]

46 **Pourfar M**, Feigin A, Tang CC, Carbon-Correll M, Bussa M, Budman C, Dhawan V, Eidelberg D. Abnormal metabolic brain networks in Tourette syndrome. *Neurology* 2011; **76**: 944-952 [PMID: 21307354 DOI: 10.1212/WNL.0b013e3182104106]

47 **Singer HS**, Szymanski S, Giuliano J, Yokoi F, Dogan AS, Brasic JR, Zhou Y, Grace AA, Wong DF. Elevated intrasynaptic dopamine release in Tourette's syndrome measured by PET. *Am J Psychiatry* 2002; **159**: 1329-1336 [PMID: 12153825 DOI: 10.1176/appi.ajp.159.8.1329]

48 **Behen M**, Chugani HT, Juhász C, Helder E, Ho A, Maqbool M, Rothermel RD, Perry J, Muzik O. Abnormal brain tryptophan metabolism and clinical correlates in Tourette syndrome. *Mov Disord* 2007; **22**: 2256-2262 [PMID: 17708557 DOI: 10.1002/mds.21712]

49 **Saporta AS**, Chugani HT, Juhász C, Makki MI, Muzik O, Wilson BJ, Behen ME. Multimodality neuroimaging in Tourette syndrome: alpha-[11C] methyl-L-tryptophan positron emission tomography and diffusion tensor imaging studies. *J Child Neurol* 2010; **25**: 336-342 [PMID: 19749182 DOI: 10.1177/0883073809339394]

50 **Wong DF**, Brasić JR, Singer HS, Schretlen DJ, Kuwabara H, Zhou Y, Nandi A, Maris MA, Alexander M, Ye W, Rousset O, Kumar A, Szabo Z, Gjedde A, Grace AA. Mechanisms of dopaminergic and serotonergic neurotransmission in Tourette syndrome: clues from an in vivo neurochemistry study with PET. *Neuropsychopharmacology* 2008; **33**: 1239-1251 [PMID: 17987065 DOI: 10.1038/sj.npp.1301528]

51 **Vernaleken I**, Kuhn J, Lenartz D, Raptis M, Huff W, Janouschek H, Neuner I, Schaefer WM, Gründer G, Sturm V. Bithalamical deep brain stimulation in tourette syndrome is associated with reduction in dopaminergic transmission. *Biol Psychiatry* 2009; **66**: e15-e17 [PMID: 19709645 DOI: 10.1016/j.biopsych.2009.06.025]

52 **Kuhn J**, Janouschek H, Raptis M, Rex S, Lenartz D, Neuner I, Mottaghy FM, Schneider F, Schaefer WM, Sturm V, Gründer G, Vernaleken I. In vivo evidence of deep brain stimulation-induced dopaminergic modulation in Tourette's syndrome. *Biol Psychiatry* 2012; **71**: e11-e13 [PMID: 22129758 DOI: 10.1016/j.biopsych.2011.09.035]

53 **Lerner A**, Bagic A, Simmons JM, Mari Z, Bonne O, Xu B, Kazuba D, Herscovitch P, Carson RE, Murphy DL, Drevets WC, Hallett M. Widespread abnormality of the γ-aminobutyric acid-ergic system in Tourette syndrome. *Brain* 2012; **135**: 1926-1936 [PMID: 22577221 DOI: 10.1093/brain/aws104]

54 **Reiffers S**, Beerling-van der Molen HD, Vaalburg W, Ten Hoeve W, Paans AM, Korf J, Woldring MG, Wynberg H. Rapid synthesis and purification of carbon-11 labelled DOPA: a potential agent for brain studies. *Int J Appl Radiat Isot* 1977; **28**: 955-958 [PMID: 608780]

55 **Garnett ES**, Firnau G, Nahmias C, Sood S, Belbeck L. Blood-brain barrier transport and cerebral utilization of dopa in living monkeys.

Am J Physiol 1980; **238**: R318-R327 [PMID: 6769344]
56 **Firnau G**, Sood S, Pantel R, Garnett S. Phenol ionization in dopa determines the site of methylation by catechol-O-methyltransferase. *Mol Pharmacol* 1981; **19**: 130-133 [PMID: 6782443]
57 **Barrio JR**, Huang SC, Melega WP, Yu DC, Hoffman JM, Schneider JS, Satyamurthy N, Mazziotta JC, Phelps ME. 6-[18F]fluoro-L-dopa probes dopamine turnover rates in central dopaminergic structures. *J Neurosci Res* 1990; **27**: 487-493 [PMID: 2127807 DOI: 10.1002/jnr.490270408]
58 **Firnau G**, Garnett ES, Chirakal R, Sood S, Nahmias C, Schrobilgen G. [18F]fluoro-L-dopa for the in vivo study of intracerebral dopamine. *Int J Rad Appl Instrum A* 1986; **37**: 669-675 [PMID: 3021668 DOI: 10.1016/0883-2889(86)90260-1]
59 **Garnett S**, Firnau G, Nahmias C, Chirakal R. Striatal dopamine metabolism in living monkeys examined by positron emission tomography. *Brain Res* 1983; **280**: 169-171 [PMID: 6418330 DOI: 10.1016/0006-8993(83)91187-3]
60 **Garnett ES**, Firnau G, Nahmias C. Dopamine visualized in the basal ganglia of living man. *Nature* 1983; **305**: 137-138 [PMID: 6604227 DOI: 10.1038/305137a0]
61 **Stoessl AJ**, Lehericy S, Strafella AP. Imaging insights into basal ganglia function, Parkinson's disease, and dystonia. *Lancet* 2014; **384**: 532-544 [PMID: 24954673 DOI: 10.1016/S0140-6736(14)60041-6]
62 **Robertson HA**. Dopamine receptor interactions: some implications for the treatment of Parkinson's disease. *Trends Neurosci* 1992; **15**: 201-206 [PMID: 1378662 DOI: 10.1016/0166-2236(92)90034-6]
63 **Farde L**. The advantage of using positron emission tomography in drug research. *Trends Neurosci* 1996; **19**: 211-214 [PMID: 8761953 DOI: 10.1016/0166-2236(96)40002-9]
64 **Piccini P**, Burn DJ, Ceravolo R, Maraganore D, Brooks DJ. The role of inheritance in sporadic Parkinson's disease: evidence from a longitudinal study of dopaminergic function in twins. *Ann Neurol* 1999; **45**: 577-582 [PMID: 10319879 DOI: 10.1002/1531-8249(199905)45: 5<577: : AID-ANA5>3.0.CO; 2-O]
65 **Hutchinson M**, Spanaki C, Lebedev S, Plaitakis A. Genetic basis of common diseases: the general theory of Mendelian recessive genetics. *Med Hypotheses* 2005; **65**: 282-286 [PMID: 15922101 DOI: 10.1016/j.mehy.2005.02.034]
66 **Kish SJ**, Shannak K, Hornykiewicz O. Uneven pattern of dopamine loss in the striatum of patients with idiopathic Parkinson's disease. Pathophysiologic and clinical implications. *N Engl J Med* 1988; **318**: 876-880 [PMID: 3352672 DOI: 10.1056/NEJM198804073181402]
67 **Nahmias C**, Garnett ES, Firnau G, Lang A. Striatal dopamine distribution in parkinsonian patients during life. *J Neurol Sci* 1985; **69**: 223-230 [PMID: 3928823 DOI: 10.1016/0022-510X(85)90135-2]
68 **Brooks DJ**. PET studies on the early and differential diagnosis of Parkinson's disease. *Neurology* 1993; **43**: S6-16 [PMID: 8264913]
69 **Fearnley JM**, Lees AJ. Ageing and Parkinson's disease: substantia nigra regional selectivity. *Brain* 1991; **114** (Pt 5): 2283-2301 [PMID: 1933245 DOI: 10.1093/brain/114.5.2283]
70 **Teune LK**, Bartels AL, de Jong BM, Willemsen AT, Eshuis SA, de Vries JJ, van Oostrom JC, Leenders KL. Typical cerebral metabolic patterns in neurodegenerative brain diseases. *Mov Disord* 2010; **25**: 2395-2404 [PMID: 20669302 DOI: 10.1002/mds.23291]
71 **Rascol O**, Schelosky L. 123I-metaiodobenzylguanidine scintigraphy in Parkinson's disease and related disorders. *Mov Disord* 2009; **24** Suppl 2: S732-S741 [PMID: 19877202 DOI: 10.1002/mds.22499]
72 **Marek K**, Jennings D, Seibyl J. Imaging the dopamine system to assess disease-modifying drugs: studies comparing dopamine agonists and levodopa. *Neurology* 2003; **61**: S43-S48 [PMID: 14504379 DOI: 10.1212/WNL.61.6_suppl_3.S43]
73 **Stoessl AJ**. Scans without evidence of dopamine deficiency: the triumph of careful clinical assessment. *Mov Disord* 2010; **25**: 529-530 [PMID: 20425792 DOI: 10.1002/mds.23138]
74 **Vlaar AM**, van Kroonenburgh MJ, Kessels AG, Weber WE. Meta-analysis of the literature on diagnostic accuracy of SPECT in parkinsonian syndromes. *BMC Neurol* 2007; **7**: 27 [PMID: 17764571 DOI: 10.1186/1471-2377-7-27]
75 **Gerhard A**, Pavese N, Hotton G, Turkheimer F, Es M, Hammers A, Eggert K, Oertel W, Banati RB, Brooks DJ. In vivo imaging of microglial activation with [11C](R)-PK11195 PET in idiopathic Parkinson's disease. *Neurobiol Dis* 2006; **21**: 404-412 [PMID: 16182554 DOI: 10.1016/j.nbd.2005.08.002]
76 **Bartels AL**, Willemsen AT, Doorduin J, de Vries EF, Dierckx RA, Leenders KL. [11C]-PK11195 PET: quantification of neuroinflammation and a monitor of anti-inflammatory treatment in Parkinson's disease? *Parkinsonism Relat Disord* 2010; **16**: 57-59 [PMID: 19487152 DOI: 10.1016/j.parkreldis.2009.05.005]
77 **Gerhard A**, Banati RB, Goerres GB, Cagnin A, Myers R, Gunn RN, Turkheimer F, Good CD, Mathias CJ, Quinn N, Schwarz J, Brooks DJ. [11C](R)-PK11195 PET imaging of microglial activation in multiple system atrophy. *Neurology* 2003; **61**: 686-689 [PMID: 12963764 DOI: 10.1212/01.WNL.0000078192.95645.E6]
78 **Gerhard A**, Trender-Gerhard I, Turkheimer F, Quinn NP, Bhatia KP, Brooks DJ. In vivo imaging of microglial activation with [11C](R)-PK11195 PET in progressive supranuclear palsy. *Mov Disord* 2006; **21**: 89-93 [PMID: 16108021 DOI: 10.1002/mds.20668]
79 **Gerhard A**, Watts J, Trender-Gerhard I, Turkheimer F, Banati RB, Bhatia K, Brooks DJ. In vivo imaging of microglial activation with [11C](R)-PK11195 PET in corticobasal degeneration. *Mov Disord* 2004; **19**: 1221-1226 [PMID: 15390000 DOI: 10.1002/mds.20162]
80 **Pavese N**, Gerhard A, Tai YF, Ho AK, Turkheimer F, Barker RA, Brooks DJ, Piccini P. Microglial activation correlates with severity in Huntington disease: a clinical and PET study. *Neurology* 2006; **66**: 1638-1643 [PMID: 16769933 DOI: 10.1212/01.wnl.0000222734.56412.17]
81 **Bagchi DP**, Yu L, Perlmutter JS, Xu J, Mach RH, Tu Z, Kotzbauer PT. Binding of the radioligand SIL23 to α-synuclein fibrils in Parkinson disease brain tissue establishes feasibility and screening approaches for developing a Parkinson disease imaging agent. *PLoS One* 2013; **8**: e55031 [PMID: 23405108 DOI: 10.1371/journal.pone.0055031]
82 **Morrish PK**, Sawle GV, Brooks DJ. An [18F]dopa-PET and clinical study of the rate of progression in Parkinson's disease. *Brain* 1996; **119** (Pt 2): 585-591 [PMID: 8800950 DOI: 10.1093/brain/119.2.585]
83 **Stoessl AJ**. Positron emission tomography in premotor Parkinson's disease. *Parkinsonism Relat Disord* 2007; **13** Suppl 3: S421-S424 [PMID: 18267275 DOI: 10.1016/S1353-8020(08)70041-5]
84 **Müller ML**, Bohnen NI. Cholinergic dysfunction in Parkinson's disease. *Curr Neurol Neurosci Rep* 2013; **13**: 377 [PMID: 23943367 DOI: 10.1007/s11910-013-0377-9]
85 **Kazumata K**, Dhawan V, Chaly T, Antonini A, Margouleff C, Belakhlef A, Neumeyer J, Eidelberg D. Dopamine transporter imaging with fluorine-18-FPCIT and PET. *J Nucl Med* 1998; **39**: 1521-1530 [PMID: 9744335]
86 **Ma Y**, Eidelberg D. Functional imaging of cerebral blood flow and glucose metabolism in Parkinson's disease and Huntington's disease. *Mol Imaging Biol* 2007; **9**: 223-233 [PMID: 17334854 DOI: 10.1007/s11307-007-0085-4]
87 **Fowler JS**, Volkow ND, Logan J, Wang GJ, MacGregor RR, Schyler D, Wolf AP, Pappas N, Alexoff D, Shea C. Slow recovery of human brain MAO B after L-deprenyl (Selegeline) withdrawal. *Synapse* 1994; **18**: 86-93 [PMID: 7839316 DOI: 10.1002/syn.890180203]
88 **Rakshi JS**, Pavese N, Uema T, Ito K, Morrish PK, Bailey DL, Brooks DJ. A comparison of the progression of early Parkinson's disease in patients started on ropinirole or L-dopa: an 18F-dopa PET study. *J Neural Transm* (Vienna) 2002; **109**: 1433-1443 [PMID: 12486484 DOI: 10.1007/s00702-002-0753-0]
89 **Tedroff J**, Pedersen M, Aquilonius SM, Hartvig P, Jacobsson G, Långström B. Levodopa-induced changes in synaptic dopamine in patients with Parkinson's disease as measured by [11C]raclopride displacement and PET. *Neurology* 1996; **46**: 1430-1436 [PMID: 8628494 DOI: 10.1212/WNL.46.5.1430]
90 **de la Fuente-Fernández R**, Sossi V, Huang Z, Furtado S, Lu JQ, Calne DB, Ruth TJ, Stoessl AJ. Levodopa-induced changes in synaptic dopamine levels increase with progression of Parkinson's disease: implications for dyskinesias. *Brain* 2004; **127**: 2747-2754 [PMID: 15329355 DOI: 10.1093/brain/awh290]
91 **de la Fuente-Fernández R**, Lu JQ, Sossi V, Jivan S, Schulzer M, Holden JE, Lee CS, Ruth TJ, Calne DB, Stoessl AJ. Biochemical variations in the synaptic level of dopamine precede motor

fluctuations in Parkinson's disease: PET evidence of increased dopamine turnover. *Ann Neurol* 2001; **49**: 298-303 [PMID: 11261503 DOI: 10.1002/ana.65]

92 **Brooks DJ**, Ibanez V, Sawle GV, Playford ED, Quinn N, Mathias CJ, Lees AJ, Marsden CD, Bannister R, Frackowiak RS. Striatal D2 receptor status in patients with Parkinson's disease, striatonigral degeneration, and progressive supranuclear palsy, measured with 11C-raclopride and positron emission tomography. *Ann Neurol* 1992; **31**: 184-192 [PMID: 1575457 DOI: 10.1002/ana.410310209]

93 **Steeves TD**, Miyasaki J, Zurowski M, Lang AE, Pellecchia G, Van Eimeren T, Rusjan P, Houle S, Strafella AP. Increased striatal dopamine release in Parkinsonian patients with pathological gambling: a [11C] raclopride PET study. *Brain* 2009; **132**: 1376-1385 [PMID: 19346328 DOI: 10.1093/brain/awp054]

94 **O'Sullivan SS**, Wu K, Politis M, Lawrence AD, Evans AH, Bose SK, Djamshidian A, Lees AJ, Piccini P. Cue-induced striatal dopamine release in Parkinson's disease-associated impulsive-compulsive behaviours. *Brain* 2011; **134**: 969-978 [PMID: 21349901 DOI: 10.1093/brain/awr003]

95 **Freed CR**, Greene PE, Breeze RE, Tsai WY, DuMouchel W, Kao R, Dillon S, Winfield H, Culver S, Trojanowski JQ, Eidelberg D, Fahn S. Transplantation of embryonic dopamine neurons for severe Parkinson's disease. *N Engl J Med* 2001; **344**: 710-719 [PMID: 11236774 DOI: 10.1056/NEJM200103083441002]

96 **Ceballos-Baumann AO**, Boecker H, Bartenstein P, von Falkenhayn I, Riescher H, Conrad B, Moringlane JR, Alesch F. A positron emission tomographic study of subthalamic nucleus stimulation in Parkinson disease: enhanced movement-related activity of motor-association cortex and decreased motor cortex resting activity. *Arch Neurol* 1999; **56**: 997-1003 [PMID: 10448806 DOI: 10.1001/archneur.56.8.997]

97 **Hilker R**, Voges J, Weisenbach S, Kalbe E, Burghaus L, Ghaemi M, Lehrke R, Koulousakis A, Herholz K, Sturm V, Heiss WD. Subthalamic nucleus stimulation restores glucose metabolism in associative and limbic cortices and in cerebellum: evidence from a FDG-PET study in advanced Parkinson's disease. *J Cereb Blood Flow Metab* 2004; **24**: 7-16 [PMID: 14688612 DOI: 10.1097/01.WCB.0000092831.44769.09]

98 **Hilker R**. [Functional imaging of deep brain stimulation in idiopathic Parkinson's disease]. *Nervenarzt* 2010; **81**: 1204-1207 [PMID: 20798917 DOI: 10.1007/s00115-010-3027-3]

99 **Bankiewicz KS**, Eberling JL, Kohutnicka M, Jagust W, Pivirotto P, Bringas J, Cunningham J, Budinger TF, Harvey-White J. Convection-enhanced delivery of AAV vector in parkinsonian monkeys; in vivo detection of gene expression and restoration of dopaminergic function using pro-drug approach. *Exp Neurol* 2000; **164**: 2-14 [PMID: 10877910 DOI: 10.1006/exnr.2000.7408]

100 **Melega WP**, Lacan G, Desalles AA, Phelps ME. Long-term methamphetamine-induced decreases of [(11)C]WIN 35,428 binding in striatum are reduced by GDNF: PET studies in the vervet monkey. *Synapse* 2000; **35**: 243-249 [PMID: 10657033 DOI: 10.1002/(SICI)1098-2396(20000315)35: 4<243: : AID-SYN1>3.3.CO; 2-E]

P- Reviewer: Lin WY, Storto G **S- Editor**: Qiu S **L- Editor**: A **E- Editor**: Lu YJ

World Journal of Radiology

Submit a Manuscript: http://www.wjgnet.com/esps/
Help Desk: http://www.wjgnet.com/esps/helpdesk.aspx
DOI: 10.4329/wjr.v8.i3.240

World J Radiol 2016 March 28; 8(3): 240-254
ISSN 1949-8470 (online)

REVIEW

What can imaging tell us about cognitive impairment and dementia?

Leela Narayanan, Alison Dorothy Murray

Leela Narayanan, Department of Clinical Radiology, NHS Grampian Health Board, NHS Foresterhill Health Site, Aberdeen AB25 2ZD, United Kingdom

Leela Narayanan, Aberdeen Biomedical Imaging Centre, Division of Applied Medicine, University of Aberdeen, Aberdeen AB25 2ZD, United Kingdom

Alison Dorothy Murray, Aberdeen Biomedical Imaging Centre, Division of Applied Medicine, School of Medicine, University of Aberdeen, Aberdeen AB25 2ZD, United Kingdom

Author contributions: This review was written by Narayanan L and the manuscript revised by Murray AD.

Conflict-of-interest statement: No conflicts of interest or financial support.

Correspondence to: Alison Dorothy Murray, PhD, MBChB(Hons), FRCR, FRCP, Roland Sutton Chair of Radiology, Aberdeen Biomedical Imaging Centre, Division of Applied Medicine, School of Medicine, University of Aberdeen, Lilian Sutton Building, Foresterhill, Aberdeen AB25 2ZD,
United Kingdom. a.d.murray@abdn.ac.uk
Telephone: +44-1224-438362

Received: August 24, 2015
Peer-review started: August 26, 2015
First decision: October 27, 2015
Revised: November 28, 2015
Accepted: January 5, 2016
Article in press: January 7, 2016
Published online: March 28, 2016

Abstract

Dementia is a contemporary global health issue with far reaching consequences, not only for affected individuals and their families, but for national and global socio-economic conditions. The hallmark feature of dementia is that of irreversible cognitive decline, usually affecting memory, and impaired activities of daily living. Advances in healthcare worldwide have facilitated longer life spans, increasing the risks of developing cognitive decline and dementia in late life. Dementia remains a clinical diagnosis. The role of structural and molecular neuroimaging in patients with dementia is primarily supportive role rather than diagnostic, American and European guidelines recommending imaging to exclude treatable causes of dementia, such as tumor, hydrocephalus or intracranial haemorrhage, but also to distinguish between different dementia subtypes, the commonest of which is Alzheimer's disease. However, this depends on the availability of these imaging techniques at individual centres. Advanced magnetic resonance imaging (MRI) techniques, such as functional connectivity MRI, diffusion tensor imaging and magnetic resonance spectroscopy, and molecular imaging techniques, such as 18F fluoro-deoxy glucose positron emission tomography (PET), amyloid PET, tau PET, are currently within the realm of dementia research but are available for clinical use. Increasingly the research focus is on earlier identification of at risk preclinical individuals, for example due to family history. Intervention at the preclinical stages before irreversible brain damage occurs is currently the best hope of reducing the impact of dementia.

Key words: Dementia; Alzheimer's disease; Magnetic resonance imaging; Molecular imaging; Frontotemporal dementia; Lewy body dementia; Vascular dementia

Core tip: Dementia is a clinical diagnosis that cannot

be made on imaging. Structural and molecular imaging techniques are useful to identify the likely underlying neuropathology. Neuroimaging techniques, such as computed tomography (CT) and blood flow single photon emission computed tomography (SPECT) are routinely used in clinical practice in all newly diagnosed dementia patients. Structural imaging with CT or magnetic resonance imaging is useful in suspected frontotemporal dementia. Amyloid positron emission tomography imaging has recently been introduced into clinical practice and is likely to be most useful in early onset Alzheimer's disease. Dopamine transporter imaging with iodine-123-b-carbo-methoxy-3-b-(4-iodophenyltropane) fluropropyl SPECT has been firmly established in clinical practice to support a diagnosis of Lewy body disease. This article is a review of the imaging techniques not only currently in clinical use but also the emerging imaging techniques in research.

Narayanan L, Murray AD. What can imaging tell us about cognitive impairment and dementia? *World J Radiol* 2016; 8(3): 240-254 Available from: URL: http://www.wjgnet.com/1949-8470/full/v8/i3/240.htm DOI: http://dx.doi.org/10.4329/wjr.v8.i3.240

INTRODUCTION

Dementia is a syndrome of progressive memory and cognitive decline affecting an individual in his activities of daily life, secondary to irreversible neuronal damage. With 2%-10% of those affected younger than 65 years, this condition is primarily a disease of the aging population[1]. Dementia is not an inevitable consequence of aging and the predicted rise in dementia as a result of an aging population is not as great as predicted, perhaps because the current definition of old-age dependency is too simplistic[2]. However, the published prevalence of dementia doubles with every 5 years increment in age, according to the World Alzheimer Report 2014 by Alzheimer Disease International[1]. Worldwide prevalence is estimated at 47.5 million with just over half living in middle and low income countries, expected to double by 2030 and treble by 2050 (World Health Organization fact sheet No.362, March 2015). The annual global cost of medical care, social support and informal care was estimated to be US$ 604 billion in 2010, which is only set to increase with the world population of over age 65 years outnumbering the under age 5 years by two-three fold by 2050[3].

On the other hand, delaying the onset of dementia by 5 years would reduce the population prevalence by 50%, greatly reducing its impact in the general population[1]. Currently there is no cure for dementia. Medical and non-medical interventions have had limited success in altering the course of the disease especially as neuropathology is usually extensive by the time the patient has presented with symptoms (Alzheimer's Disease International 2014 report).

Table 1 Causes of dementia and dementia syndromes

Types of dementia
Primary dementias
Alzheimer's disease
Late-onset Alzheimer's disease - most common form 60%-70% of all dementias
Early-onset Alzheimer's disease - under 65 yr of age, chromosome 14 implicated, Down's syndrome
Familial AD - inheritable form present in at least 2 generations within families
Dementia with Lewy bodies
Frontotemporal dementia
Mixed dementia - more than one form of pathology for, *e.g.*, Lewy bodies with Alzheimer's disease
Less common forms
Parkinson's disease
Progressive supranuclear palsy
Huntington's disease
Secondary dementias
Vascular/multi infarct dementia
Vascular with Alzheimer's disease
Creutzfeldt-Jakob disease
Intracranial mass lesions
Normal pressure hydrocephalus
Subdural haematomas
Trauma
Infections - primarily human immunodeficiency virus
Alcohol
Other documented causes
Vitamin deficiencies - vitamins E, B and folic acid are implicated
Medications
Other causes like depression

The diagnosis of dementia remains a clinical diagnosis and post-mortem examination of the brain tissue is the only definitive method to establish and confirm the diagnosis. *In vivo*, various invasive and non-invasive methods are available to support the diagnosis of different sub-types, due to different brain pathology.

Dementia has various causes (Table 1). By far the most important type is Alzheimer's disease (AD) accounting for 60%-70% of all dementias. Primary dementing conditions have in common abnormal protein or peptide accumulation in the brain: τ and β amyloid in AD; α synuclein in Lewy body dementia (LBD) and τ, Transactive DNA-binding protein (TDP) or Fused in Sarcoma (FUS) in fronto-temporal dementia (FTD). But these conditions can and do often co-exist with other pathologies of aging, most commonly cerebral small vessel disease (CSVD)[4]. Dementia secondary to cerebrovascular disease is the second most common form of dementia.

North American, European and United Kingdom National Institute of Health and Care Excellence (NICE) guidelines recommend neuroimaging in all patients at the time of initial diagnosis of dementia[5-8]. Structural and molecular imaging are both useful to support the diagnosis of a dementia-related neuropathology *in vivo*. Molecular imaging, for example, positron emission tomography (PET) using tracers for amyloid or tau and invasive methods like cerebrospinal fluid (CSF) analysis of amyloid β and τ are also available to support the diagnosis of AD *in*

vivo. However, many of these tools apart from structural neuroimaging remain elusive to regular clinical practice and are confined to specialised centres and to research. Therapeutic interventions in dementia, in particular in AD, have had mixed success, none achieving significant alteration in disease progression. This is largely due to the fact that the process of neuronal damage is quite advanced at the time of clinical presentation. It is widely recognised that early intervention before irreversible neuronal damage occurs is our best hope of delaying the onset and perhaps preventing dementia[9]. Inevitably then it becomes imperative that we learn to identify those individuals who are on the trajectory to develop AD, 15-20 years before clinical dementia. Confusing the picture is the fact that many of these neuronal changes including amyloid deposition occur within the spectrum of normal aging without ever causing dementia. So do we expose these individuals to an intervention that they may never need? Would it be cost effective to do so[10]?

Research has inevitably widened its scope with emphasis now on the pre-clinical stage of the disease so that we could precisely identify those vulnerable individuals with the greatest level of confidence. Individuals affected could potentially be identified for future trials. This has heralded a new era of collaborative global endeavour. Multicentre, collaborative large datasets like the Alzheimer's Disease Neuroimaging Initiative (ADNI) provide free access to multi-modality data to researchers worldwide, considerably reducing the cost of such research[11]. Molecular imaging and advanced MRI techniques are at the cutting edge of dementia research, primarily in the pre-clinical stage, helping us understand the early life of this devastating condition.

Here, we aim to discuss and provide an overview of imaging in common diseases that cause dementia, both in the clinical setting and within the realm of research. Imaging in dementia has moved away from just ruling out treatable causes of dementia like space occupying lesions or hydrocephalus, to characterising the different types of dementia-related neuropathology with increasing specificity.

AD

A primary neurodegenerative condition, AD is the most common form of late onset dementia (> 65)[12]. Neuropathologically it is characterised by extracellular amyloid plaques and intracellular tau aggregates[13]. Amyloid plaques are aggregates of insoluble fibrillary β-amyloid (Aβ) peptide mostly 40-42 amino acids in length, Aβ42 being the most prevalent[14]. The accumulation of Aβ in turn is thought to trigger a cascade of neurodegenerative events including intracellular aggregation of hyperphosphorylated tau[15] and neuroinflammation[16,17]. Accumulation of Aβ correlates with cognitive decline in some studies, as demonstrated on amyloid PET imaging[18,19]. Lately this is being challenged as there appears to be a certain disconnect between the time of amyloid deposition, which plateaus in late mid-life and progressive cognitive decline. The intracellular tau related neurofibrillary tangles, on the other hand, do correlate with disease severity and cognition at different stages of AD[20,21].

The evolution of AD is a continuum progressing from the asymptomatic pre-clinical stage, decades before the clinical onset of the disease, to the pro-dromal stage where there is onset of cognitive impairment but below the levels of formal dementia diagnosis and eventually to dementia. In the rare autosomal dominant early onset AD, abnormal accumulation of amyloid has been attributed to mutations in the genes regulating amyloid precursor protein (APP) and the presenilins (PSEN 1 and 2)[22]. In sporadic AD, apolipoprotein E gene (*APOE4*) has been implicated in earlier onset, greater cognitive impairment and more rapid progression[23], but this is not exclusive to AD and is found in other neurodegenerative conditions, such as Parkinson's disease (PD)[24].

The diagnostic criteria for AD have been recently updated for use in clinical practice as well as research[25]. Endeavours to recognise the disease in the earlier stages have also prompted standardisation of criteria for defining preclinical[26] and pro-dromal [amnestic mild cognitive impairment (MCI)] stages[27] for both clinical and research purposes.

Structural imaging

The evolution of neuropathological changes begins at the entorhinal cortex in the medial temporal lobe which plays an important role in laying down new memory by virtue of its connections to hippocampus. Subsequent hippocampal involvement results in episodic memory loss and, as the disease progresses to involve neocortex, impacts on cognition, language, attention and executive function, affecting the activities of daily life[28]. The typical imaging appearance is that of global brain atrophy with early disproportionate atrophy of medial temporal lobes (MTA), including the hippocampi[29] (Figure 1). MTA can differentiate AD from ageing with a sensitivity and specificity of 80%-85% and is a risk factor for cognitive decline and dementia in normal aging[30] and predicts AD in those with amnestic MCI with a sensitivity and specificity of 73% and 81%[31,32]. Progressive atrophy of posterior temporal and parietal lobes differentiates AD from FTD.

More advanced MRI imaging techniques such as diffusion weighted and diffusion tensor imaging (DWI and DTI), magnetic resonance spectroscopy (MRS) and perfusion imaging are also used in the research context. DWI and DTI techniques measure the integrity of tissue using two different measures, fractional anisotrophy (FA) and mean diffusivity (MD) or apparent diffusion coefficient (ADC). Increased MD/ADC and decreased FA are considered to be markers of neuronal fibre loss and reduced gray matter and white matter integrity (Figure 2)[33]. MRS is a technique to measure the biological metabolites in the target tissue, specifically the metabolites N-acetylaspartate (NAA), a marker of neuronal integrity, which decreases and myo-inositol, a marker of glial proliferation and neuronal damage, which increases. These changes are seen typically in the posterior cingulate gyrus, mesial temporal lobe, parieto-occipital lobes and the fronto-parietal lobes[34]. Cerebral perfusion is imaged using blood

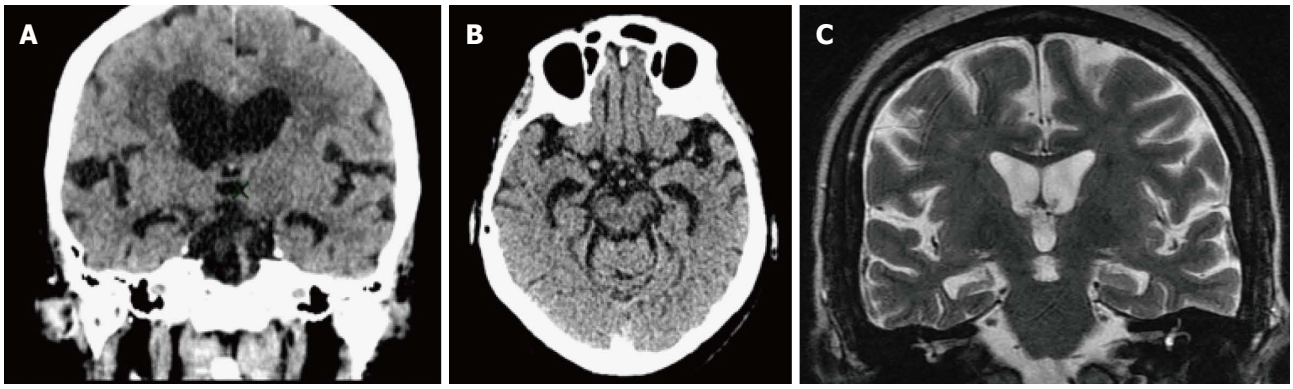

Figure 1 Hippocampal atrophy in an Alzheimer's disease patient. A: Computed tomography axial; B: Coronal images; C: Medial temporal lobe atrophy on magnetic resonance imaging (not the same patient).

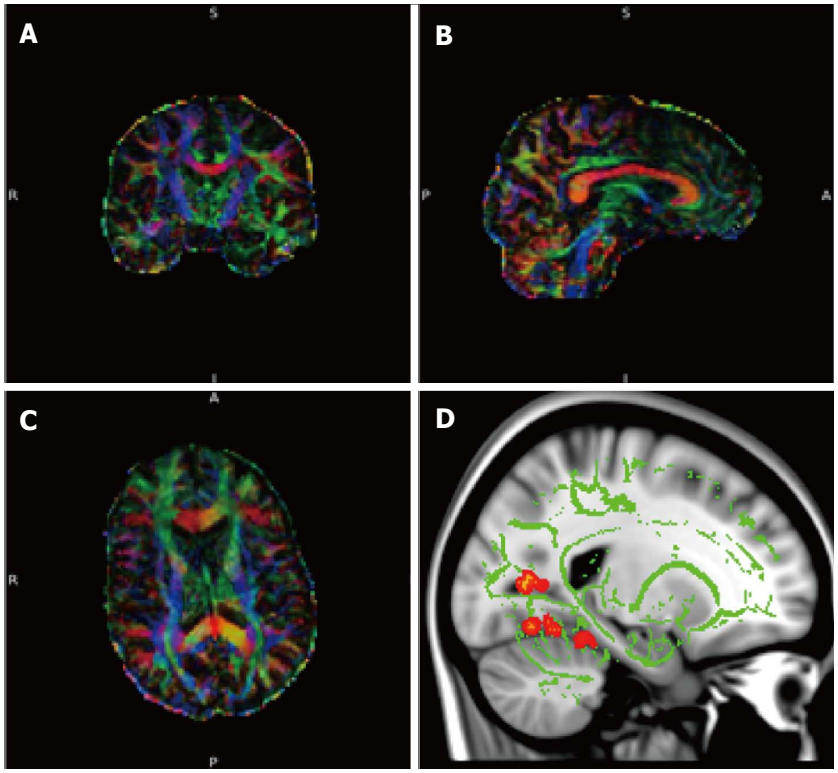

Figure 2 Diffusion tensor imaging. A-C: Diffusion tensor imaging (DTI) data set superimposed on structural image of the brain in 3 orthogonal planes demonstrating colour coded white matter tracts. Blue colour correlate to the tracts in the cranio-caudal direction, red in the transverse direction and green in the antero-posterior direction. (Images kindly prepared by Dr. Gordon D Waiter); D: DTI data of white matter tracts (green) superimposed on T1 image demonstrating statistically significant difference in fractional anisotropy in the fornix (orange areas) compared to the rest of the brain in a subgroup of patients. (Images kindly prepared by Dr. Gordon D Waiter).

flow SPECT, dynamic susceptibility contrast enhanced MRI or arterial spin labelling (ASL) techniques[35,36]. Functional MRI (fMRI) measures brain activity using blood oxygenation level dependent (BOLD) technique demonstrating areas of brain activity by demonstrating the greatest influx of oxygen into the region to compensate increased utilisation. This can be performed in the resting state or during a task[37].

A recent review of fMRI studies in dementia demonstrated decreased functional connectivity between precuneus, medial prefrontal cortex, posterior cingulate cortex, anterior cingulate cortex and hippocampus in the resting state, centres which are part of the default mode network (Figure 3) and more than can be accounted for by atrophy. The severity and distribution of decreased functional connectivity at rest is postulated to potentially distinguish MCI patients from AD and AD from other neurodegenerative dementias[38].

Molecular imaging

Molecular imaging aims to measure the pathophysiological change within the brain using either tracer that demonstrate normal physiology (non-specific tracers) or that bind to pathological targets (specific tracers). The two main modalities include single photon emission computed tomography (SPECT) and positron emission tomography (PET).

SPECT is used to measure regional cerebral blood flow (rCBF) by intravenously injecting technetium-labelled hexamethylpropylene amine oxime (^{99}Tc-HMPAO). In AD characteristic deficits in posterior temporoparietal, posterior cingulate and inferior frontal regions, reflect underlying neuronal dysfunction and neurodegeneration (Figure 4). Often images demonstrate features secondary to a combination of both Alzheimer's and vascular pathology

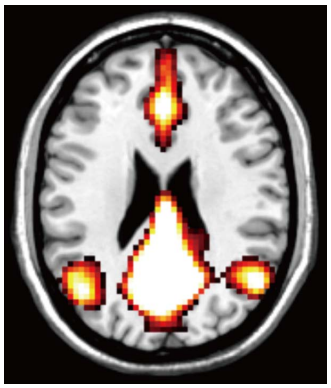

Figure 3 Default mode network, areas active during resting wakeful state. Resting state functional magnetic resonance imaging images using blood oxygenation level dependent technique. Typical areas involved include the medial prefrontal cortices, posterior cingulate, ventral precuneus and parts of parietal lobes (Images kindly prepared by Dr. Michael Stringer).

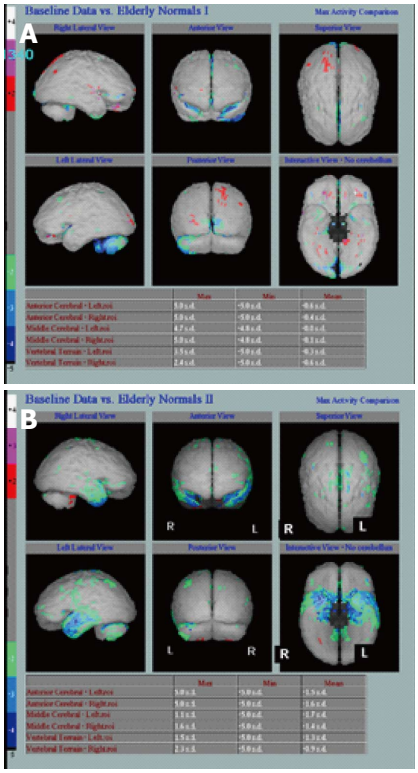

Figure 4 Underlying neuronal dysfunction and neurodegeneration. A: Hexamethylpropylene amine oxime (HMPAO) single photon emission computed tomography (SPECT) in normal control subject demonstrating normal almost symmetrical perfusion pattern; B: HMPAO SPECT in Alzheimer's disease parametric images demonstrate bilateral reduction in perfusion in the temporal lobes especially in the medial temporal regions up to 2 (green) and 3 (blue) standard deviation (Images kindly prepared by Ms Lesley Lovell, Senior technician).

(Figure 5).

Like HMPAO SPECT, 18 Fluorodeoxyglucose PET (FDG PET) demonstrates decrease in regional uptake reflecting decreased metabolism in a distribution similar to rCBF. In amnestic MCI, there is bilateral glucose hypometabolism in the limbic system, posterior cingulate cortex, parahippocampal gyri and temporal lobes (inferior temporal gyrus)[39,40], compared to AD patients who had additional profound hypometabolism in precuneus, inferior parietal lobule and middle temporal gyrus along with posterior cingulate cortex[39,41].

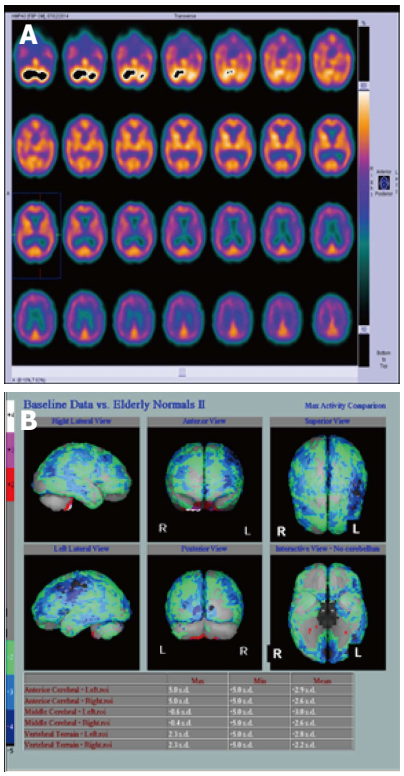

Figure 5 Hexamethylpropylene amine oxime single photon emission computed tomography in a patient with mixed vascular disease and Alzheimer's disease. A: Shows reduced perfusion in both the frontal and parietal lobes, especially on the left; B: Parametric images providing an overall view. There was hippocampal atrophy on computed tomography (Images kindly prepared by Dr. Fergus McKiddie).

Amyloid PET imaging has started new chapters in both clinical and research practice. Amyloid specific ligands such as ^{11}C-Pittsburg compound B (^{11}CPIB), ^{18}F Florbetapir, ^{18}F Flutemetamol, demonstrate amyloid deposition *in vivo* and show good correlation with autopsy measurements[42]. They show increased uptake in typical locations such as precuneus, posterior cingulate cortex, temporal, parietal and occipital lobes[19,43,44]. A recent review of amyloid imaging studies revealed that even though there was high sensitivity to amyloid across the board with increased uptake in healthy controls, AD, MCI and other dementias like FTD, the sensitivity and specificity to identify AD cases was high and there was a high conversion rate of amyloid positive MCI to AD compared to amyloid negative MCI[3]. Amyloid imaging is now included in the criteria for the diagnosis of AD[25,45]. Both FDA and EMA have approved ^{18}F florbetapir, ^{18}F florbetaben and ^{18}F flutemetamol[46] for clinical use. However, the role of amyloid PET is likely to be greater in early onset AD, than in late onset AD, where neuropathology is more heterogeneous[47]. However, structural MRI and FDG PET are more accurate than amyloid imaging in predicting cognitive status[48].

Ligands targeting the paired helical filament form (PHF) of tau, specific to AD have been developed and are currently close to market[49-51].

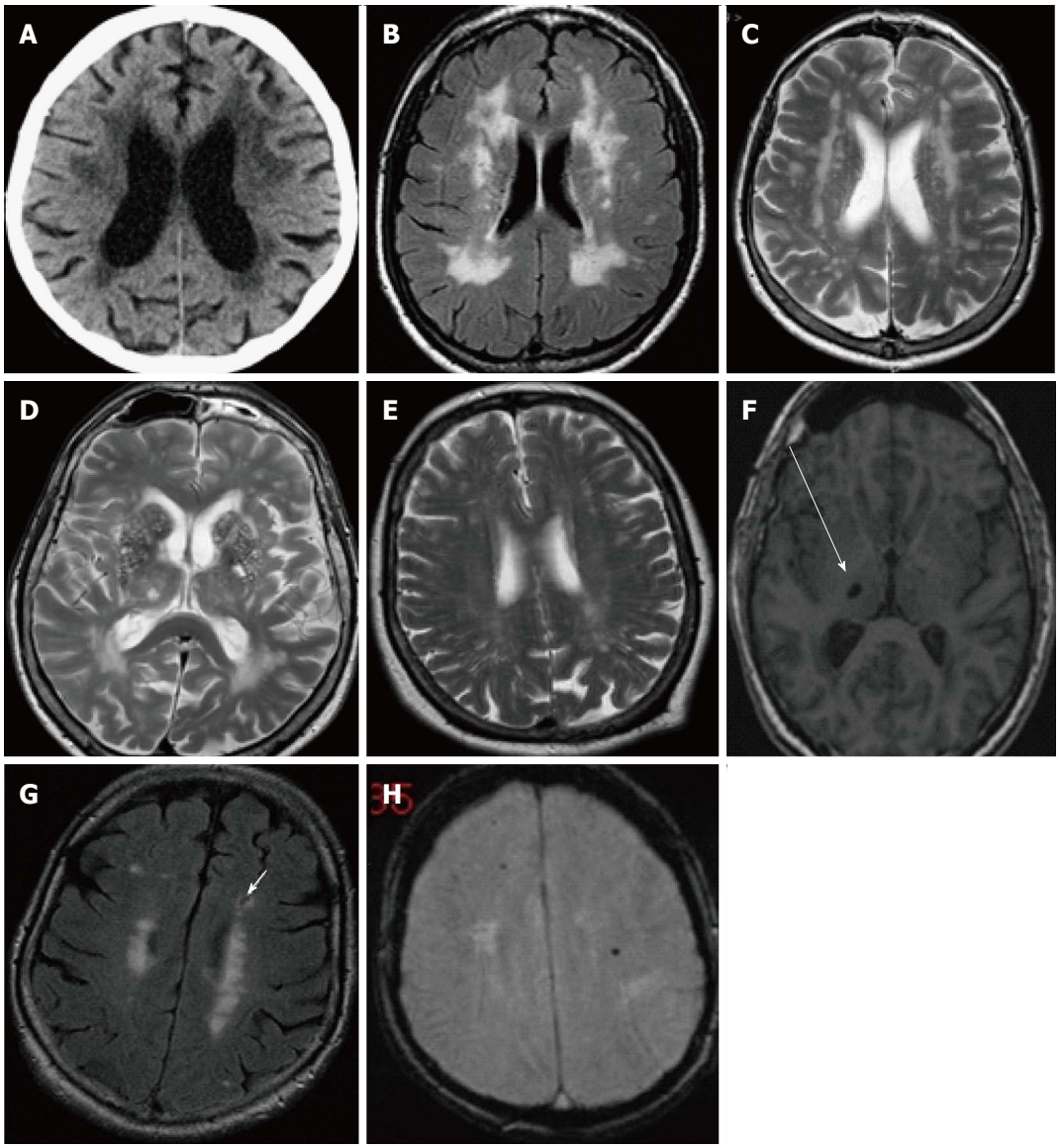

Figure 6 Computed tomography and magnetic resonance imaging images demonstrating structural changes secondary to cerebral small vessel disease. A: Axial image of CT brain demonstrating periventricular white matter low attenuation changes; B and C: The same seen as periventricular white matter high signal areas on FLAIR and T2 MRI; D: Prominent perivascular spaces typically seen in the basal ganglia; E: Centrum semiovale; F: Focal lacune, a cerebrospinal fluid filled space, sequelae of an old lacunar infarct in the right thalamus seen here (arrow) on an axial T1 image; G: Lacune (arrow) in the left frontal lobe on a FLAIR image, usually with a rim of high signal differentiating from a PVS; H: Cerebral microhaemorrhages, seen here as focal rounded black/low signal foci in the white matter of both frontal lobes on T2* gradient echo MRI. MRI: Magnetic resonance imaging; CT: Computed tomography.

Neuroinflammation is also thought to play a role in the neuropathogenesis of AD[52]. PET imaging of neuroinflammatory processes such as microglial activation, reactive astrocytosis and increased phospholipase activity is possible using specific agents[53-56]. Tau imaging and neuro inflammation imaging are out of the realm of clinical practice at present. PET tracers specific for acetylcholinesterase as a proxy measure of acetylcholine synaptic density have been used in a few studies[57-59].

In summary, a multiphase model of neuroimaging corresponding to the stage of evolving neuropathology[60], is most likely with amyloid PET imaging positive during βamyloid accumulation, followed by tau accumulation with reduced rCBF on SPECT and decreased metabolism on FDG PET due to neuronal dysfunction and atrophy on CT and structural MRI following neuronal death.

VASCULAR COGNITIVE IMPAIRMENT AND DEMENTIA

Vascular cognitive impairment (VCI) is the second most common form of late onset dementia and the most common form of secondary dementia. VCI is a heterogenous disease and is due to a number of vascular causes[61] both small and large vessel related. Larger vessel involvement result in cortical infarcts and primary haemorrhages, while small vessel disease manifests as lacunar infarcts, lacunes, white matter hyperintensities (WMH), enlarged perivascular spaces and cerebral microhaemorrhages[62-67] (Figure 6).

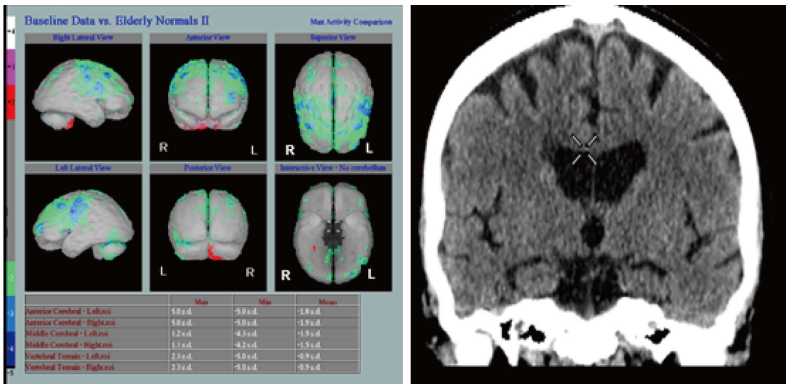

Figure 7 Hexamethylpropylene amine oxime single photon emission computed tomography in a pure cerebral vascular disease patient without Alzheimer's disease. Note normal hippocampal volumes in the pure cerebral vascular disease patient on computed tomography (Images kindly prepared by Ms Lesley Lovell and Dr Fergus Mckiddie, clinical scientist).

The term subcortical ischaemic vascular disease (SIVD) is also used, often synonymous with WMH, the biomarker most significantly correlated with vascular risk factors such as hypertension and impaired glycaemic control[68]. WMH are age related and moderate amounts of WMH is seen up to 30% of normal older population with no significant cognitive dysfunction[69]. WHM in the VCI population on the other hand are significantly associated with not only vascular risk factors, but with cognitive impairment especially executive dysfunction, rapid global functional decline and decline of psychomotor speed and executive control[70,71]. Areas vulnerable to hypoxia, especially in the deep white matter watershed areas when affected are thought to trigger a series of events leading to tissue injury with neuroinflammation, blood-brain barrier (BBB) disruption and axonal damage resulting in white matter loss[72].

Structural imaging

WMH are best seen on structural MRI as bright signal areas on T2 and FLAIR images (Figure 6) in subcortical and periventricular distribution. They are quantified using visual rating scales or automated segmentation methods[73-75]. They are predominantly supratentorial in distribution, although are also common in the pons, and have a predilection for the frontal lobes.

Advanced MRI techniques like DTI, MRS and dynamic contrast enhanced (DCE) MRI demonstrate reduced white matter integrity, evidence of neuronal damage with decrease in NAA and enhancement secondary to BBB breakdown. Techniques to image neuroinflammation demonstrate microglia and macrophages around blood vessels[72]. Abnormal permeability also results in an increase in CSF albumin ratio in patients with vascular dementia[76]. This process repeated over time eventually results in quite significant white matter damage and cognitive impairment.

Diagnosis of VCI is dependent on a combination of the presence of vascular risk factors including hypertension, impaired glycaemic control, renal impairment, WMH on imaging, absence of an AD pattern of atrophy and executive dysfunction on psychometric testing. Memory is less involved[77,78]. Montreal Cognitive Assessment tests executive function and is a more useful tool than MMSE in this group of patients. An attempt is being made to define a set of features that are characteristic of the progressive form of VCI, termed the Binswanger Disease scale score[72].

Molecular imaging

HMPAO SPECT demonstrates decreased perfusion typically distributed in a vascular territory, often bilateral and usually involving the frontal lobes (Figure 7), seen either in combination with AD and in pure vascular dementia.

FDG PET and rCBF SPECT demonstrate areas of decreased metabolism and perfusion respectively which may be bilateral, and/or arterial territory in distribution. Rarer causes of vascular dementia include hypercoaguable states (antiphospholipid antibodies), hereditary forms such as congenital autosomal dominant arteriopathy with subcortical infarcts and leucoencephalopathy (CADASIL), with a temporal lobe distribution of WMH, and leucodystrophies.

In routine clinical practice though, multidetector CT of the brain is the most common, and in most centres the only, imaging performed when a vascular cause is suspected for cognitive impairment.

LEWY BODY DEMENTIA

This is the second most common primary neurodegenerative dementia and accounts for 15% of all dementia in the population and is clinically characterised by cognitive impairment with executive dysfunction, visuospatial impairment, visual, motor parkinsonian features, disordered (rapid eye movement) REM sleep and fluctuation in cognition and arousal[79]. Neuropsychometric tests demonstrate deficits in attention, executive function and visuospatial ability[79].

Pathologically lewy body dementia (LBD) overlaps with PD and is characterised by dopaminergic cell loss and accumulation of α-synuclein particles in presynaptic terminals that aggregate to form intracellular Lewy bodies. Similar to β amyloid pathology, α synuclein can be present as oligomers, fibrils and aggregates, the small oligomers likely being the most neurotoxic. These mainly occur in the cerebral cortex and limbic system, while in PD they exist in the substantia nigra, pars compacta and nigrostriatal projections. Recent work has increased understanding of genetic associations of LBD and PD[80]. Parkinson's disease dementia (PDD) is pathologically and clinically indistinguishable to LBD, apart from the fact that in PDD, motor symptoms predate cognitive decline by up to 12 mo[79,81]. While the diagnosis

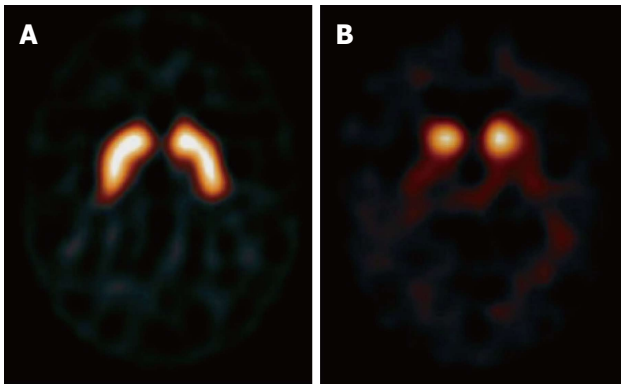

Figure 8 Iodine-123-b-carbo-methoxy-3-b-(4-iodophenyltropane) fluropropyl. A: Normal example symmetrical uptake in the caudate heads and putamen bilaterally; B: Absent uptake in the putamen in a patient with Lewy body dementia.

of LBD will often be obvious clinically, it may be unclear in a substantial minority of patients, where neuroimaging play a role.

Structural imaging

Structural MRI using Voxel Based Morphometry has demonstrated variable regional brain atrophy in LBD with some studies reporting cortical atrophy in the insula, frontal, inferior parietal, temporal and occipital cortices[82,83] while a larger study has differentiated LBD from AD with more atrophy of hypothalamus, basal forebrain, midbrain, caudate and the putamen with relative preservation of the medial temporal lobe and the hippocampi[84]. The rate of progressive atrophy is increased when compared to normal controls, exaggerated if AD co-exists, but much lower compared to AD. Visual hallucinations and visuo-perceptual deficits, a characteristic feature of LBD do not seem to correlate with occipital lobe involvement[85]. However, correlation with other regions involved in visual processing (visual association areas) and executive functions (inferior frontal lobe) have been reported. If present, hippocampal atrophy is seen in the anterior subfield (CA1)[86], while in AD, CA2 and CA3 are more affected on high resolution MRI.

DTI, ASL and MRS techniques have been used to compare LBD with AD. In general these demonstrate abnormalities in the visual association cortex and posterior putamen in LBD compared with medial temporal lobe and precuneus in AD. The best discrimination will be a result of cumulative data from more than one sequence or imaging modality[86].

Molecular imaging

Increased β amyloid is commonly seen in LBD but not in PD dementia[87]. Amyloid PET imaging demonstrates similar uptake in AD and LBD (apart from occipital lobes which are spared in AD), making it difficult to differentiate between these two conditions. Similarly they are indistinguishable on rCBF SPECT and FDG PET, however involvement of the visual cortex would favour LBD[88-90].

A dopaminergic presynaptic ligand, iodine-123-b-carbo-methoxy-3-b-(4-iodophenyltropane) fluoropropyl (FP-CIT) or ioflupane, is used in SPECT studies. Neuronal loss in the dopaminergic zones are demonstrated by decreased uptake in the posterior putamen and then caudate nuclei when compared to normal controls (Figure 8) and AD patients. Visual image analysis is adequate to make the distinction between normal *vs* 3 grades of reduced uptake in the striatum, justifying routine use in clinical practice[91] as recommended by both NICE in United Kingdom and European Federation of Neurological Sciences in Europe. Quantitative analysis of FP-CIT images using shape analysis is as accurate as expert observer assessment and more reproducible[92]. Low dopamine transporter uptake in basal ganglia demonstrated by SPECT or PET imaging is the only imaging feature in the diagnostic criteria for LBD[79]. However, FP-CIT SPECT is not indicated to distinguish between different parkinsonian syndromes[93]. FP-CIT SPECT scan has a sensitivity of 78% and a specificity of 90% with an overall accuracy of 80% to distinguish between normal (or AD) and a parkinsonian syndrome (LBD)[94].

Cholinergic neuronal loss and reduced presynaptic choline acetyltransferace activity is seen in both LBD and AD. There is however differential uptake with reductions in medical occipital cortex in LBD and temporal lobe in AD[95]. Cardiac sympathetic denervation in LBD and PD predates neuronal loss can be measured using 123I MIGB, an analogue of noradrenaline in myocardial scintigraphy. Yoshita *et al*[96] demonstrated that the cut-off value of heart-to-mediastinum ratio of 1.68 yielded a sensitivity of 100% and a specificity of 100% for differentiating LBD from AD.

FRONTOTEMPORAL DEMENTIA

Frontotemporal dementia is a heterogenous group of diseases that account for approximately 5% of late onset dementia but is the second commonest cause of early onset dementia after AD[97]. Clinical presentation is often in the 5th and 6th decade, at least 10 years younger than AD and patients have a family history in about 50% of the cases[98].

The two main clinical syndromes of frontotemporal dementia (FTD) are behavioural variant FTD (bvFTD) characterised by deterioration in social function and personality and primary progressive aphasia (PPA) where there is an insidious decline in language skills. There are various subtypes of PPA such as semantic dementia (svPPA), progressive non-fluent aphasia (nfvPPA), logopenic aphasia (LPA - an AD variant) and progressive apraxia of speech, based on speech pattern involved[99]. Pathologically, based on the protein involved, they are divided into the following three categories: (1) FTLD-tau: Including tauopathies such as progressive supranuclear palsy (PSP), corticobasal degeneration (CBD), multisystem tauopathy with dementia and Pick's disease; (2) FTLD-TDP43: Transactive DNA-binding protein (TDP) 43 related abnormalities, a subgroup may also have motor neuron disease (MND)[100]; and (3) FTLD-FUS: Fused in sarcoma (FUS) protein[101].

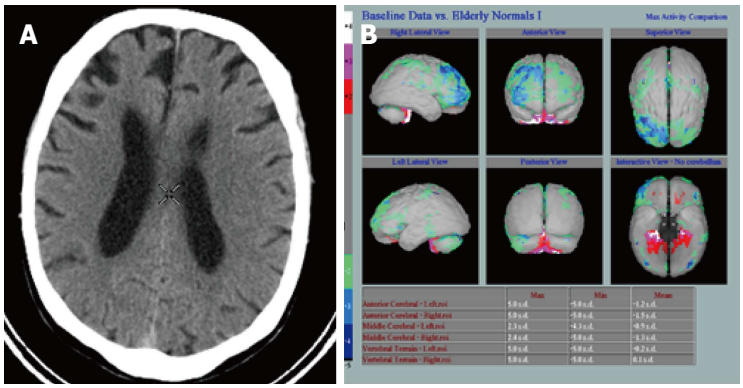

Figure 9 Computed tomography showing atrophy. A: Asymmetric right frontal lobe atrophy in fronto-temporal dementia; B: Hexamethylpropylene amine oxime single photon emission computed tomography in the same patient (Images kindly prepared by Ms Lewley Lovell, and Dr. Fergus Mckiddie).

As above FTD may be associated with overlap syndromes of MND or PSP, if so indicating likely molecular pathologies of TDP43 or tau respectively.

Structural imaging

Varying patterns of regional brain atrophy is the hallmark of these conditions depending on the clinical phenotype and the reporting radiologist may be the first to suggest FTD as the diagnosis in these patients.

bvFTD: Bilateral mesial frontal, orbitofrontal, anterior insular cortices and anterior cingulate cortex atrophy with more involvement on the right[102,103]. The frontal-insula-anterior cingulate are suggested to be part of a structurally and functionally connected neural network (a salience network) which demonstrates decreased functional connectivity during resting state fMRI[102,103] (Figure 9).

svPPA: Bilateral, typically highly asymmetrical, usually left sided, atrophy of the anterior temporal lobes. As disease progresses the atrophy extends inferiorly to involve the posterior temporal lobes and superiorly to involve the inferior frontal lobes.

nfvPPA: Anterior perisylvian especially the dominant hemisphere, in particular the left frontal operculum - Broca's areas 44, 45 and 47.

Quantification of regional atrophy rates on MRI could potentially be a useful biomarker of progression in FTD[49]. DTI has shown decreased white matter integrity in the respective regions affected depending on the clinical phenotype[104]. On fMRI FTD can be differentiated from AD by reduced connectivity in the salience network and increased connectivity in the DMN, opposite to that of AD[105,106].

Molecular imaging

FDG PET demonstrates frontal and anterior temporal lobe hypometabolism, which is useful in differentiating FTD from AD especially in the heterogenous group of progressive aphasias and in CBD[107]. However, PET imaging is not usually required as the diagnosis of FTD as frontal atrophy is usually obvious on structural imaging.

IMAGING IN OTHER DEMENTIAS

There are numerous less common causes of dementia. All these types of dementias can occur in people younger than 65 years but more often have a genetic cause and those affected generally tend to have accelerated progression. Dementias in people younger than 35 years are rare and more unusual causes such as infection or autoimmune encephalopathies need to be considered[108]. Imaging in this group and two other unusual causes of dementia will be discussed here.

AUTOIMMUNE DEMENTIAS

Previously termed as "limbic encephalitis", these are a heterogeneous group of disorders that include various encephalopathies with specific clinical, electroencephalographic or CSF features[109]. They may present with cognitive impairment, seizures and are responsive to steroids. Imaging features are variable, MRI may show high signal intensity on T2 weighted and FLAIR images in the areas involved, typically in the limbic system. About 50% of autoimmune dementia patients, who have neuron-specific CSF autoantibodies, will have a paraneoplastic syndrome and whole body FDG-PET CT is appropriate to identify an underlying tumor[110].

PRION PROTEIN DISEASES

Accumulation of abnormal prion proteins can occur sporadically [sporadic Creutzfeld Jakob disease (CJD)], due to exposure to food (variant CJD) or infected tissues (iatrogenic CJD) due to genetic variation in the prion protein gene (*PrnP*), fatal familial insomnia. sCJD and vCJD typically present as rapidly progressive dementia with an earlier age at onset in vCJD. Other features at presentation could be hemiparesis, myoclonus in sCJD and painful sensory symptoms in vCJD supplemented by typical abnormal complexes on EEG. On MRI typical T2 and FLAIR hyperintensity is seen in the pulvinar of the thalami in vCJD, which is virtualy pathognomonic, and in the caudate heads and cortices ("cortical ribboning") in sCJD which can be asymmetrical[111]. These abnormalities are best seen on DWI where they demonstrate diffusion

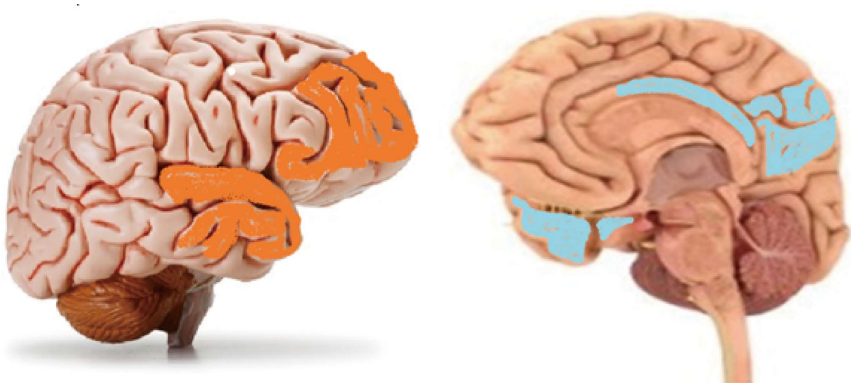

Figure 10 Regions of atrophy in fronto-temporal dementia (shaded orange) and Alzheimer's disease (shaded light blue).

Table 2 Summary

Dementia	Pathological feature	Structural imaging CT/MRI	Molecular imaging (non-specific)	Molecular imaging (specific)	Research
Alzheimer's disease	Primary neurodegenerative, extracellular amyloid plaques (Aβ42), intracellular tau aggregates[13], Autosomal dominant early onset inherited form - presenelins are also implicated[22]	Hippocampal-medial temporal lobe (CA2 and CA3 hippocampal subregions are more affected), posterior cingulate gyrus and postero-medial parietal lobe atrophy on MRI and CT	SPECT[1]- ↓perfusion FDG PET[2]- ↓glucose uptake in medial temporal lobe and hippocampi[39-41]	^{11}C PIB, Florbetapir[3] uptake in amyloid plaques[42]	Tau specific ligands -PET, MRI-BOLD, fMRI- ↓connectivity in DMN, MR perfusion[38], MR spectroscopy, DTI -↓ medial temporal lobe and precuneus[34], VBM
LBD	Intracellular Lewy bodies- aggregates of α-synuclein particles in pre-synaptic terminals Overlaps with Parkinson's disease	Atrophy in inferior frontal lobe, visual cortex, insula, hypothalamus, midbrain, caudate, putamen and anterior hippocampi (CA1 subregion)[86]	SPECT -↓in putamen and caudate, visual cortex[88,89] FDG PET -↓in visual cortices[88-90]	FP-CIT-↓uptake in putamen and caudate[79] Cholinergic PET/ SPECT- ↓in medial occipital lobe[95] ^{123}I MIBG-↓cardiac uptake[96]	Diffusion weighted MR-DTI, ↓ in visual association cortex and posterior putamen MRS, fMRI ASL-MR
FTD	Various proteins including tauopathies, TDP43, FUS- clinically can overlap with PSP, MSA, MND[100,101]	Variable-predominantly anterior frontal, temporal and insular atrophy[102,103]	FDG PET and SPECT-↓anterior, frontal and temporal uptake[107]	-	fMRI, DTI-↓ in WM of affected regions[104] fMRI-↓"salient" network' but ↑DMN connectivity on resting fMRI- unlike AD[105,106]
Vascular dementia	Small and large vessel disease - vascular risk factors like HT, smoking and DM implicated[61] CADASIL- hereditary form	CT-cortical infarct, macrohaemorrhage, frontal subcortical and periventricular WMH, lacunes[62-67] MRI-CT features as above and PVS, CMB	FDG PET and rCBF SPECT-↓ frontal and periventricular regions	-	-
CJD sCJD vCJD	Prion protein - sources include food, tissues, genetic variation	MRI-↑signal on T2W and DWI in the caudate and cortex ("cortical ribboning") MRI-↑ on T2W and DWI in the pulvinar of thalami			
Autoimmune encephalitis related dementia	Previously limbic encephalitis -neuron specific CSF autoantibodies Paraneoplastic syndrome	MRI-↑ signal on T2W and FLAIR in the mesial temporal lobe	FDG PET -↑ uptake in the medial temporal lobe Whole body PET to identify underlying primary malignancy[110]		

[1]SPECT-radiotracer is ^{99m}Tc hexamethylpropylene amine oxime; [2]FDG PET-radiotracer is ^{18}F-FDG; [3]Recently approved by FDA for clinical use in specific cases, primarily to exclude Alzheimer's disease.↑: Increased; ↓: Decreased; Aβ42: Beta amyloid protein with 42 amino acids; CA1, CA2, CA3: Subfields of hippocampus; ASL-MR: Arterial spin labelling MR; BOLD: Blood oxygenation level dependent; CADASIL: Congenital autosomal dominant arteriopathy with subcortical infarcts and leukoencephalopathy; CMB: Cerebral microbleeds; CSF: Cerebrospinal fluid; DM: Diabetes mellitus; DTI: Diffusion tensor imaging; FDG: Fludeoxyglucose; FLAIR: Fluid-attenuated inversion–recovery; fMRI: Functional MRI; DMN: Default mode network; FP-CIT: Dopaminergic presynaptic ligand iodine-123-b-carbo-methoxy-3 b-(4-iodophenyltropane) fluoropropyl; FUS: Fused in sarcoma protein; HT: Hypertension; LBD: Lewy body dementia; MSA: Multisystem atrophy; MND: Motor neuron disease; MRS: MR spectroscopy; PET: Positron emission tomography; PIB: Pittsburgh compound B; PSP: Progressive supranuclear palsy; PVS: Perivascular spaces; rCBF SPECT: Regional cerebral blood flow SPECT; sCJD: Sporadic form of Creutzfeldt–Jacob disease; vCJD: Variant form of Creutzfeldt–Jacob disease; SPECT: Single photon emission computed tomography; T2W: T2 weighted; TDP43: Transactive DNA-binding protein; VBM: Voxel-based morphometry; WMH: White matter hyperintensities.

restriction.

HUMAN IMMUNODEFICIENCY VIRUS ASSOCIATED NEUROCOGNITIVE DISORDER

HIV associated dementia is the most severe HIV associated neurocognitive disorder and presents as impairment in executive function, motor activities and memory. On structural MRI global cortical atrophy is seen with predilection for the anterior cingulate, lateral temporal, primary motor and sensory cortices. White matter hyperintensities too are seen, some presenting as progressive multifocal leukoencephalopathy characterised by focal white matter lesions typically in subcortical regions[112,113]. DTI studies demonstrate reduced white matter integrity in the cortical white matter, corona radiata and the corpus callosum are associated with cognitive impairment[114-116]. Other imaging modalities include MRS, fMRI, FDG PET and dopamine transporter imaging and demonstrate evidence of neuronal loss, impaired functional connectivity, hypometabolism and decreased uptake in the putamina and ventral striatum respectively.

Some studies suggest these imaging abnormalities are reversible following retroviral therapies, however additional research is needed[104].

CONCLUSION

Imaging in neurodegenerative disorders that cause dementia has evolved from the days of ruling out other pathologies to diagnosis of specific likely underlying neuropathologies. MRI studies, without doubt, are far superior to MDCT in providing information on the structural and functional changes corresponding to the pathological evolution of the disease. Newer techniques in MRI and PET are readily embraced by researchers in the quest for earlier detection of the disease before irreversible neuronal damage occurs, now believed to be the best current approach the global community can adopt to tackle these devastating conditions. Current and future interventions need to target individuals who are most at risk before the manifestation of dementia. Large multicentre datasets like ADNI, which are freely available, are invaluable for providing new research opportunities are important for future progress.

Future PET tracers for specific proteinopathies (tau, TDP-43, α synuclein) would provide more information and offer more challenges. Development of specific imaging correlates of different proteinopathies is a research goal that will offer an opportunity to observe the disease processes in their earliest of stages and do not wait for clinical manifestation. The clinical challenge will be to identify those at risk at the earliest opportunity.

Large longitudinal cohort studies are a necessity to explore the influence of cognitive reserve and early life factors, which are increasingly gaining importance and attention.

Table 2 summarises the pathophysiology and the imaging features of all the dementias discussed (Figure 10). Demonstrates the regional atrophy in FTD and AD.

REFERENCES

1 World Alzheimer Report 2014. Available from: URL: https://www.alz.co.uk/research/WorldAlzheimerReport2014.pdf

2 **Spijker J**, MacInnes J. Population ageing: the timebomb that isn't? *BMJ* 2013; **347**: f6598 [PMID: 24222481 DOI: 10.1136/bmj.f6598]

3 **Haub C**. World population aging: clocks illustrate growth in population under age5 and over age 65. Population Bulletin. Available from: URL: http: //www.prb.org/Articles/2011/agingpopulationclocks.aspx.

4 **Qiu C**, Xu W, Fratiglioni L. Vascular and psychosocial factors in Alzheimer's disease: epidemiological evidence toward intervention. *J Alzheimers Dis* 2010; **20**: 689-697 [PMID: 20182015]

5 **Dubois B**, Feldman HH, Jacova C, Dekosky ST, Barberger-Gateau P, Cummings J, Delacourte A, Galasko D, Gauthier S, Jicha G, Meguro K, O'brien J, Pasquier F, Robert P, Rossor M, Salloway S, Stern Y, Visser PJ, Scheltens P. Research criteria for the diagnosis of Alzheimer's disease: revising the NINCDS-ADRDA criteria. *Lancet Neurol* 2007; **6**: 734-746 [PMID: 17616482 DOI: 10.1016/S1474-4422(07)70178-3]

6 **Hort J**, O'Brien JT, Gainotti G, Pirttila T, Popescu BO, Rektorova I, Sorbi S, Scheltens P. EFNS guidelines for the diagnosis and management of Alzheimer's disease. *Eur J Neurol* 2010; **17**: 1236-1248 [PMID: 20831773 DOI: 10.1111/j.1468-1331.2010.03040.x]

7 **Jack CR**, Albert MS, Knopman DS, McKhann GM, Sperling RA, Carrillo MC, Thies B, Phelps CH. Introduction to the recommendations from the National Institute on Aging-Alzheimer's Association workgroups on diagnostic guidelines for Alzheimer's disease. *Alzheimers Dement* 2011; **7**: 257-262 [PMID: 21514247 DOI: 10.1016/j.jalz.2011.03.004]

8 **NCC for Mental Health.** Dementia: The NICE-SCIE Guideline on supporting people with dementia and their carers in health and social care (National Clinical Practice Guideline). British Psychological RCPsych publications, 2007

9 **Sperling R**, Mormino E, Johnson K. The evolution of preclinical Alzheimer's disease: implications for prevention trials. *Neuron* 2014; **84**: 608-622 [PMID: 25442939 DOI: 10.1016/j.neuron.2014.10.038]

10 **Bermingham SL**. The appropriate use of neuroimaging in the diagnostic work-up of dementia: an economic literature review and cost-effectiveness analysis. *Ont Health Technol Assess Ser* 2014; **14**: 1-67 [PMID: 24592297]

11 **Toga AW**. The clinical value of large neuroimaging data sets in Alzheimer's disease. *Neuroimaging Clin N Am* 2012; **22**: 107-118, ix [PMID: 22284737 DOI: 10.1016/j.nic.2011.11.008]

12 **Gauthier S**, Reisberg B, Zaudig M, Petersen RC, Ritchie K, Broich K, Belleville S, Brodaty H, Bennett D, Chertkow H, Cummings JL, de Leon M, Feldman H, Ganguli M, Hampel H, Scheltens P, Tierney MC, Whitehouse P, Winblad B. Mild cognitive impairment. *Lancet* 2006; **367**: 1262-1270 [PMID: 16631882]

13 **Masters CL,** Selkoe DJ**.** Biochemistry of amyloid beta-protein and amyloidz deposits in AD. *Cold Spring Harb Perspect Med* 2012; **2**: a006262 [PMID: 22675658 DOI: 10.1101/cshperspect.a006262]

14 **Masters CL**, Simms G, Weinman NA, Multhaup G, McDonald BL, Beyreuther K. Amyloid plaque core protein in AD and Down syndrome. *Proc Natl Acad Sci USA* 1985; **82**: 4245-4259 [PMID: 3159021]

15 **Jack CR**, Knopman DS, Jagust WJ, Petersen RC, Weiner MW, Aisen PS, Shaw LM, Vemuri P, Wiste HJ, Weigand SD, Lesnick TG, Pankratz VS, Donohue MC, Trojanowski JQ. Tracking pathophysiological processes in Alzheimer's disease: an updated hypothetical model of dynamic biomarkers. *Lancet Neurol* 2013; **12**: 207-216 [PMID: 23332364 DOI: 10.1016/S1474-4422(12)70291-0]

16 **Eikelenboom P**, Stam FC. Immunoglobulins and complement factors in senile plaques. An immunoperoxidase study. *Acta Neuropathol* 1982; **57**: 239-242 [PMID: 6812382 DOI: 10.1007/BF00685397]

17 **Eikelenboom P**, Hack CE, Rozemuller JM, Stam FC. Complement activation in amyloid plaques in Alzheimer's dementia. *Virchows Arch B Cell Pathol Incl Mol Pathol* 1989; **56**: 259-262 [PMID: 2565620]

18 **Morris JC**, Roe CM, Grant EA, Head D, Storandt M, Goate AM, Fagan AM, Holtzman DM, Mintun MA. Pittsburgh compound B imaging and prediction of progression from cognitive normality to symptomatic Alzheimer disease. *Arch Neurol* 2009; **66**: 1469-1475 [PMID: 20008650 DOI: 10.1001/archneurol.2009.269]

19 **Jack CR**, Lowe VJ, Weigand SD, Wiste HJ, Senjem ML, Knopman DS, Shiung MM, Gunter JL, Boeve BF, Kemp BJ, Weiner M, Petersen RC. Serial PIB and MRI in normal, mild cognitive impairment and Alzheimer's disease: implications for sequence of pathological events in Alzheimer's disease. *Brain* 2009; **132**: 1355-1365 [PMID: 19339253 DOI: 10.1093/brain/awp062]

20 **Delacourte A**, David JP, Sergeant N, Buée L, Wattez A, Vermersch P, Ghozali F, Fallet-Bianco C, Pasquier F, Lebert F, Petit H, Di Menza C. The biochemical pathway of neurofibrillary degeneration in aging and Alzheimer's disease. *Neurology* 1999; **52**: 1158-1165 [PMID: 10214737 DOI: 10.1212/WNL.52.6.1158]

21 **Arriagada PV**, Growdon JH, Hedley-Whyte ET, Hyman BT. Neurofibrillary tangles but not senile plaques parallel duration and severity of Alzheimer's disease. *Neurology* 1992; **42**: 631-639 [PMID: 1549228 DOI: 10.1212/WNL.42.3.631]

22 **Bertram L**, Tanzi RE. Thirty years of Alzheimer's disease genetics: the implications of systematic meta-analyses. *Nat Rev Neurosci* 2008; **9**: 768-778 [PMID: 18802446 DOI: 10.1038/nrn2494]

23 **Chang YL**, Fennema-Notestine C, Holland D, McEvoy LK, Stricker NH, Salmon DP, Dale AM, Bondi MW. APOE interacts with age to modify rate of decline in cognitive and brain changes in Alzheimer's disease. *Alzheimers Dement* 2014; **10**: 336-348 [PMID: 23896613 DOI: 10.1016/j.jalz.2013.05.1763]

24 **Li YJ**, Hauser MA, Scott WK, Martin ER, Booze MW, Qin XJ, Walter JW, Nance MA, Hubble JP, Koller WC, Pahwa R, Stern MB, Hiner BC, Jankovic J, Goetz CG, Small GW, Mastaglia F, Haines JL, Pericak-Vance MA, Vance JM. Apolipoprotein E controls the risk and age at onset of Parkinson disease. *Neurology* 2004; **62**: 2005-2009 [PMID: 15184605 DOI: 10.1212/01.WNL.0000128089.53030.AC]

25 **McKhann GM**, Knopman DS, Chertkow H, Hyman BT, Jack CR, Kawas CH, Klunk WE, Koroshetz WJ, Manly JJ, Mayeux R, Mohs RC, Morris JC, Rossor MN, Scheltens P, Carrillo MC, Thies B, Weintraub S, Phelps CH. The diagnosis of dementia due to Alzheimer's disease: recommendations from the National Institute on Aging-Alzheimer's Association workgroups on diagnostic guidelines for Alzheimer's disease. *Alzheimers Dement* 2011; **7**: 263-269 [PMID: 21514250 DOI: 10.1016/j.jalz.2011.03.005]

26 **Sperling RA**, Aisen PS, Beckett LA, Bennett DA, Craft S, Fagan AM, Iwatsubo T, Jack CR, Kaye J, Montine TJ, Park DC, Reiman EM, Rowe CC, Siemers E, Stern Y, Yaffe K, Carrillo MC, Thies B, Morrison-Bogorad M, Wagster MV, Phelps CH. Toward defining the preclinical stages of Alzheimer's disease: recommendations from the National Institute on Aging-Alzheimer's Association workgroups on diagnostic guidelines for Alzheimer's disease. *Alzheimers Dement* 2011; **7**: 280-292 [PMID: 21514248 DOI: 10.1016/j.jalz.2011.03.003]

27 **Albert MS**, DeKosky ST, Dickson D, Dubois B, Feldman HH, Fox NC, Gamst A, Holtzman DM, Jagust WJ, Petersen RC, Snyder PJ, Carrillo MC, Thies B, Phelps CH. The diagnosis of mild cognitive impairment due to Alzheimer's disease: recommendations from the National Institute on Aging-Alzheimer's Association workgroups on diagnostic guidelines for Alzheimer's disease. *Alzheimers Dement* 2011; **7**: 270-279 [PMID: 21514249 DOI: 10.1016/j.jalz.2011.03.008]

28 **Braak H**, Braak E. Neuropathological stageing of Alzheimer-related changes. *Acta Neuropathol* 1991; **82**: 239-259 [PMID: 1759558 DOI: 10.1007/BF00308809]

29 **Harper L**, Barkhof F, Scheltens P, Schott JM, Fox NC. An algorithmic approach to structural imaging in dementia. *J Neurol Neurosurg Psychiatry* 2014; **85**: 692-698 [PMID: 24133287 DOI: 10.1136/jnnp-2013-306285]

30 **Ikram MA**, Vrooman HA, Vernooij MW, den Heijer T, Hofman A, Niessen WJ, van der Lugt A, Koudstaal PJ, Breteler MM. Brain tissue volumes in relation to cognitive function and risk of dementia. *Neurobiol Aging* 2010; **31**: 378-386 [PMID: 18501994 DOI: 10.1016/j.neurobiolaging.2008.04.008]

31 **Duara R**, Loewenstein DA, Potter E, Appel J, Greig MT, Urs R, Shen Q, Raj A, Small B, Barker W, Schofield E, Wu Y, Potter H. Medial temporal lobe atrophy on MRI scans and the diagnosis of Alzheimer disease. *Neurology* 2008; **71**: 1986-1992 [PMID: 19064880 DOI: 10.1212/01.wnl.0000336925.79704.9f]

32 **Frisoni GB**, Fox NC, Jack CR, Scheltens P, Thompson PM. The clinical use of structural MRI in Alzheimer disease. *Nat Rev Neurol* 2010; **6**: 67-77 [PMID: 20139996 DOI: 10.1038/nrneurol.2009.215]

33 **Jack CR Jr,** Bernstein MA, Borowski BJ, Gunter JL, Fox NC, Thompson PM, Schuff N, Krueger G, Killiany RJ, Decarli CS, Dale AM, Carmichael OW, Tosun D, Weiner MW; Alzheimer's Disease Neuroimaging Initiative. Update on the magnetic resonance imaging core of the Alzheimer's disease neuroimaging initiative. *Alzheimers Dement* 2010; **6**: 212-220 [PMID: 20451869 DOI: 10.1016/j.jalz.2010.03.004]

34 **Gao F**, Barker PB. Various MRS application tools for Alzheimer disease and mild cognitive impairment. *AJNR Am J Neuroradiol* 2014; **35**: S4-11 [PMID: 24742809]

35 **Alsop DC**, Dai W, Grossman M, Detre JA. Arterial spin labeling blood flow MRI: its role in the early characterization of Alzheimer's disease. *J Alzheimers Dis* 2010; **20**: 871-880 [PMID: 20413865]

36 **Wang Y**, Saykin AJ, Pfeuffer J, Lin C, Mosier KM, Shen L, Kim S, Hutchins GD. Regional reproducibility of pulsed arterial spin labeling perfusion imaging at 3T. *Neuroimage* 2011; **54**: 1188-1195 [PMID: 20800097 DOI: 10.1016/j.neuroimage.2010.08.043]

37 **Ogawa S**, Tank DW, Menon R, Ellermann JM, Kim SG, Merkle H, Ugurbil K. Intrinsic signal changes accompanying sensory stimulation: functional brain mapping with magnetic resonance imaging. *Proc Natl Acad Sci USA* 1992; **89**: 5951-5955 [PMID: 1631079 DOI: 10.1073/pnas.89.13.5951]

38 **Hafkemeijer A**, van der Grond J, Rombouts SA. Imaging the default mode network in aging and dementia. *Biochim Biophys Acta* 2012; **1822**: 431-441 [PMID: 21807094 DOI: 10.1016/j.bbadis.2011.07.008]

39 **Shivamurthy VK**, Tahari AK, Marcus C, Subramaniam RM. Brain FDG PET and the diagnosis of dementia. *AJR Am J Roentgenol* 2015; **204**: W76-W85 [PMID: 25539279 DOI: 10.2214/AJR.13.12363]

40 **Sanabria-Diaz G**, Martínez-Montes E, Melie-Garcia L. Glucose metabolism during resting state reveals abnormal brain networks organization in the Alzheimer's disease and mild cognitive impairment. *PLoS One* 2013; **8**: e68860 [PMID: 23894356 DOI: 10.1371/journal.pone.0068860]

41 **Del Sole A**, Clerici F, Chiti A, Lecchi M, Mariani C, Maggiore L, Mosconi L, Lucignani G. Individual cerebral metabolic deficits in Alzheimer's disease and amnestic mild cognitive impairment: an FDG PET study. *Eur J Nucl Med Mol Imaging* 2008; **35**: 1357-1366 [PMID: 18418593 DOI: 10.1007/s00259-008-0773-6]

42 **Clark CM**, Schneider JA, Bedell BJ, Beach TG, Bilker WB, Mintun MA, Pontecorvo MJ, Hefti F, Carpenter AP, Flitter ML, Krautkramer MJ, Kung HF, Coleman RE, Doraiswamy PM, Fleisher AS, Sabbagh MN, Sadowsky CH, Reiman EP, Zehntner SP, Skovronsky DM. Use of florbetapir-PET for imaging beta-amyloid pathology. *JAMA* 2011; **305**: 275-283 [PMID: 21245183 DOI: 10.1001/jama.2010.2008]

43 **Jack CR**, Lowe VJ, Senjem ML, Weigand SD, Kemp BJ, Shiung MM, Knopman DS, Boeve BF, Klunk WE, Mathis CA,

Petersen RC. 11C PiB and structural MRI provide complementary information in imaging of Alzheimer's disease and amnestic mild cognitive impairment. *Brain* 2008; **131**: 665-680 [PMID: 18263627 DOI: 10.1093/brain/awm336]

44 **Klunk WE**, Engler H, Nordberg A, Wang Y, Blomqvist G, Holt DP, Bergström M, Savitcheva I, Huang GF, Estrada S, Ausén B, Debnath ML, Barletta J, Price JC, Sandell J, Lopresti BJ, Wall A, Koivisto P, Antoni G, Mathis CA, Långström B. Imaging brain amyloid in Alzheimer's disease with Pittsburgh Compound-B. *Ann Neurol* 2004; **55**: 306-319 [PMID: 14991808 DOI: 10.1002/ana.20009]

45 **Dubois B**, Feldman HH, Jacova C, Hampel H, Molinuevo JL, Blennow K, DeKosky ST, Gauthier S, Selkoe D, Bateman R, Cappa S, Crutch S, Engelborghs S, Frisoni GB, Fox NC, Galasko D, Habert MO, Jicha GA, Nordberg A, Pasquier F, Rabinovici G, Robert P, Rowe C, Salloway S, Sarazin M, Epelbaum S, de Souza LC, Vellas B, Visser PJ, Schneider L, Stern Y, Scheltens P, Cummings JL. Advancing research diagnostic criteria for Alzheimer's disease: the IWG-2 criteria. *Lancet Neurol* 2014; **13**: 614-629 [PMID: 24849862 DOI: 10.1016/S1474-4422(14)70090-0]

46 **Zwan MD**, Okamura N, Fodero-Tavoletti MT, Furumoto S, Masters CL, Rowe CC, Villemagne VL. Voyage au bout de la nuit: Aβ and tau imaging in dementias. *Q J Nucl Med Mol Imaging* 2014; **58**: 398-412 [PMID: 25358680]

47 **Ossenkoppele R**, Jansen WJ, Rabinovici GD, Knol DL, van der Flier WM, van Berckel BN, Scheltens P, Visser PJ, Verfaillie SC, Zwan MD, Adriaanse SM, Lammertsma AA, Barkhof F, Jagust WJ, Miller BL, Rosen HJ, Landau SM, Villemagne VL, Rowe CC, Lee DY, Na DL, Seo SW, Sarazin M, Roe CM, Sabri O, Barthel H, Koglin N, Hodges J, Leyton CE, Vandenberghe R, van Laere K, Drzezga A, Forster S, Grimmer T, Sánchez-Juan P, Carril JM, Mok V, Camus V, Klunk WE, Cohen AD, Meyer PT, Hellwig S, Newberg A, Frederiksen KS, Fleisher AS, Mintun MA, Wolk DA, Nordberg A, Rinne JO, Chételat G, Lleo A, Blesa R, Fortea J, Madsen K, Rodrigue KM, Brooks DJ. Prevalence of amyloid PET positivity in dementia syndromes: a meta-analysis. *JAMA* 2015; **313**: 1939-1949 [PMID: 25988463 DOI: 10.1001/jama.2015.4669]

48 **Kadir A**, Almkvist O, Forsberg A, Wall A, Engler H, Långström B, Nordberg A. Dynamic changes in PET amyloid and FDG imaging at different stages of Alzheimer's disease. *Neurobiol Aging* 2012; **33**: 198.e1-198.14 [PMID: 20688420 DOI: 10.1016/j.neurobiolaging.2010.06.015]

49 **Gordon E**, Rohrer JD, Kim LG, Omar R, Rossor MN, Fox NC, Warren JD. Measuring disease progression in frontotemporal lobar degeneration: a clinical and MRI study. *Neurology* 2010; **74**: 666-673 [PMID: 20177120 DOI: 10.1212/WNL.0b013e3181d1a879]

50 **Steinacker P**, Hendrich C, Sperfeld AD, Jesse S, von Arnim CA, Lehnert S, Pabst A, Uttner I, Tumani H, Lee VM, Trojanowski JQ, Kretzschmar HA, Ludolph A, Neumann M, Otto M. TDP-43 in cerebrospinal fluid of patients with frontotemporal lobar degeneration and amyotrophic lateral sclerosis. *Arch Neurol* 2008; **65**: 1481-1487 [PMID: 19001167 DOI: 10.1001/archneur.65.11.1481]

51 **Kasai T**, Tokuda T, Ishigami N, Sasayama H, Foulds P, Mitchell DJ, Mann DM, Allsop D, Nakagawa M. Increased TDP-43 protein in cerebrospinal fluid of patients with amyotrophic lateral sclerosis. *Acta Neuropathol* 2009; **117**: 55-62 [PMID: 18989684 DOI: 10.1007/s00401-008-0456-1]

52 **Akiyama H**, Barger S, Barnum S, Bradt B, Bauer J, Cole GM, Cooper NR, Eikelenboom P, Emmerling M, Fiebich BL, Finch CE, Frautschy S, Griffin WS, Hampel H, Hull M, Landreth G, Lue L, Mrak R, Mackenzie IR, McGeer PL, O'Banion MK, Pachter J, Pasinetti G, Plata-Salaman C, Rogers J, Rydel R, Shen Y, Streit W, Strohmeyer R, Tooyoma I, Van Muiswinkel FL, Veerhuis R, Walker D, Webster S, Wegrzyniak B, Wenk G, Wyss-Coray T. Inflammation and Alzheimer's disease. *Neurobiol Aging* 2000; **21**: 383-421 [PMID: 10858586 DOI: 10.1016/S0197-4580(00)00124-X]

53 **Ahmed RM**, Paterson RW, Warren JD, Zetterberg H, O'Brien JT, Fox NC, Halliday GM, Schott JM. Biomarkers in dementia: clinical utility and new directions. *J Neurol Neurosurg Psychiatry* 2014; **85**: 1426-1434 [PMID: 25261571 DOI: 10.1136/jnnp-2014-307662]

54 **Royal College of Radiologists**. Evidence based indications for the use of PET-CT in the UK 2013. Available from: URL: https://www.rcr.ac.uk/sites/default/files/publication/2013_PETCT_RCP_RCR.pdf

55 **Seppälä TT**, Nerg O, Koivisto AM, Rummukainen J, Puli L, Zetterberg H, Pyykkö OT, Helisalmi S, Alafuzoff I, Hiltunen M, Jääskeläinen JE, Rinne J, Soininen H, Leinonen V, Herukka SK. CSF biomarkers for Alzheimer disease correlate with cortical brain biopsy findings. *Neurology* 2012; **78**: 1568-1575 [PMID: 22517093 DOI: 10.1212/WNL.0b013e3182563bd0]

56 **Moghekar A**, Li S, Lu Y, Li M, Wang MC, Albert M, O'Brien R. CSF biomarker changes precede symptom onset of mild cognitive impairment. *Neurology* 2013; **81**: 1753-1758 [PMID: 24132375 DOI: 10.1212/01.wnl.0000435558.98447.17]

57 **Rinne JO**, Kaasinen V, Järvenpää T, Någren K, Roivainen A, Yu M, Oikonen V, Kurki T. Brain acetylcholinesterase activity in mild cognitive impairment and early Alzheimer's disease. *J Neurol Neurosurg Psychiatry* 2003; **74**: 113-115 [PMID: 12486280 DOI: 10.1136/jnnp.74.1.113]

58 **Herholz K**, Weisenbach S, Kalbe E, Diederich NJ, Heiss WD. Cerebral acetylcholine esterase activity in mild cognitive impairment. *Neuroreport* 2005; **16**: 1431-1434 [PMID: 16110265 DOI: 10.1097/01.wnr.0000177007.21732.7b]

59 **Sabri O**, Kendziorra K, Wolf H, Gertz HJ, Brust P. Acetylcholine receptors in dementia and mild cognitive impairment. *Eur J Nucl Med Mol Imaging* 2008; **35** Suppl 1: S30-S45 [PMID: 18228017 DOI: 10.1007/s00259-007-0701-1]

60 **Jack CR**, Knopman DS, Jagust WJ, Shaw LM, Aisen PS, Weiner MW, Petersen RC, Trojanowski JQ. Hypothetical model of dynamic biomarkers of the Alzheimer's pathological cascade. *Lancet Neurol* 2010; **9**: 119-128 [PMID: 20083042 DOI: 10.1016/S1474-4422(09)70299-6]

61 **Bowler JV**. Modern concept of vascular cognitive impairment. *Br Med Bull* 2007; **83**: 291-305 [PMID: 17675645 DOI: 10.1093/bmb/ldm021]

62 **Kearney-Schwartz A**, Rossignol P, Bracard S, Felblinger J, Fay R, Boivin JM, Lecompte T, Lacolley P, Benetos A, Zannad F. Vascular structure and function is correlated to cognitive performance and white matter hyperintensities in older hypertensive patients with subjective memory complaints. *Stroke* 2009; **40**: 1229-1236 [PMID: 19246701 DOI: 10.1161/STROKEAHA.108.532853]

63 **Raz N**, Rodrigue KM, Kennedy KM, Acker JD. Vascular health and longitudinal changes in brain and cognition in middle-aged and older adults. *Neuropsychology* 2007; **21**: 149-157 [PMID: 17402815 DOI: 10.1037/0894-4105.21.2.149]

64 **Fischer P**, Krampla W, Mostafaie N, Zehetmayer S, Rainer M, Jungwirth S, Huber K, Bauer K, Hruby W, Riederer P, Tragl KH. VITA study: white matter hyperintensities of vascular and degenerative origin in the elderly. *J Neural Transm Suppl* 2007; **(72):** 181-188 [PMID: 17982893 DOI: 10.1007/978-3-211-73574-9_23]

65 **Jagust WJ**, Zheng L, Harvey DJ, Mack WJ, Vinters HV, Weiner MW, Ellis WG, Zarow C, Mungas D, Reed BR, Kramer JH, Schuff N, DeCarli C, Chui HC. Neuropathological basis of magnetic resonance images in aging and dementia. *Ann Neurol* 2008; **63**: 72-80 [PMID: 18157909 DOI: 10.1002/ana.21296]

66 **Doubal FN**, MacLullich AM, Ferguson KJ, Dennis MS, Wardlaw JM. Enlarged perivascular spaces on MRI are a feature of cerebral small vessel disease. *Stroke* 2010; **41**: 450-454 [PMID: 20056930 DOI: 10.1161/STROKEAHA.109.564914]

67 **Vernooij MW**, de Groot M, van der Lugt A, Ikram MA, Krestin GP, Hofman A, Niessen WJ, Breteler MM. White matter atrophy and lesion formation explain the loss of structural integrity of white matter in aging. *Neuroimage* 2008; **43**: 470-477 [PMID: 18755279 DOI: 10.1016/j.neuroimage.2008.07.052]

68 **Murray AD**, Staff RT, Shenkin SD, Deary IJ, Starr JM, Whalley LJ. Brain white matter hyperintensities: relative importance of vascular

risk factors in nondemented elderly people. *Radiology* 2005; **237**: 251-257 [PMID: 16126931 DOI: 10.1148/radiol.2371041496]

69 **Hunt AL**, Orrison WW, Yeo RA, Haaland KY, Rhyne RL, Garry PJ, Rosenberg GA. Clinical significance of MRI white matter lesions in the elderly. *Neurology* 1989; **39**: 1470-1474 [PMID: 2812324 DOI: 10.1212/WNL.39.11.1470]

70 **Inzitari D**, Pracucci G, Poggesi A, Carlucci G, Barkhof F, Chabriat H, Erkinjuntti T, Fazekas F, Ferro JM, Hennerici M, Langhorne P, O'Brien J, Scheltens P, Visser MC, Wahlund LO, Waldemar G, Wallin A, Pantoni L. Changes in white matter as determinant of global functional decline in older independent outpatients: three year follow-up of LADIS (leukoaraiosis and disability) study cohort. *BMJ* 2009; **339**: b2477 [PMID: 19581317 DOI: 10.1136/bmj.b2477]

71 **Jokinen H**, Kalska H, Ylikoski R, Madureira S, Verdelho A, van der Flier WM, Scheltens P, Barkhof F, Visser MC, Fazekas F, Schmidt R, O'Brien J, Waldemar G, Wallin A, Chabriat H, Pantoni L, Inzitari D, Erkinjuntti T. Longitudinal cognitive decline in subcortical ischemic vascular disease--the LADIS Study. *Cerebrovasc Dis* 2009; **27**: 384-391 [PMID: 19276621 DOI: 10.1159/000207442]

72 **Rosenberg GA**, Bjerke M, Wallin A. Multimodal markers of inflammation in the subcortical ischemic vascular disease type of vascular cognitive impairment. *Stroke* 2014; **45**: 1531-1538 [PMID: 24692476 DOI: 10.1161/STROKEAHA.113.004534]

73 **Fazekas F**, Chawluk JB, Alavi A, Hurtig HI, Zimmerman RA. MR signal abnormalities at 1.5 T in Alzheimer's dementia and normal aging. *AJR Am J Roentgenol* 1987; **149**: 351-356 [PMID: 3496763 DOI: 10.2214/ajr.149.2.351]

74 **Scheltens P**, Barkhof F, Leys D, Pruvo JP, Nauta JJP, Vermersch P, Steinling M, Valk J. A semiquantitative rating scale for the assessment of signal hyperintensities on magnetic resonance imaging. *J Neurol Sci* 1993; **114**: 7-12 [DOI: 10.1016/0022-510X(93)90041-V]

75 **de Boer R**, Vrooman HA, van der Lijn F, Vernooij MW, Ikram MA, van der Lugt A, Breteler MM, Niessen WJ. White matter lesion extension to automatic brain tissue segmentation on MRI. *Neuroimage* 2009; **45**: 1151-1161 [PMID: 19344687 DOI: 10.1016/j.neuroimage.2009.01.011]

76 **Wallin A**, Blennow K, Fredman P, Gottfries CG, Karlsson I, Svennerholm L. Blood brain barrier function in vascular dementia. *Acta Neurol Scand* 1990; **81**: 318-322 [PMID: 2360399 DOI: 10.1111/j.1600-0404.1990.tb01562.x]

77 **Hachinski V**, Iadecola C, Petersen RC, Breteler MM, Nyenhuis DL, Black SE, Powers WJ, DeCarli C, Merino JG, Kalaria RN, Vinters HV, Holtzman DM, Rosenberg GA, Wallin A, Dichgans M, Marler JR, Leblanc GG. National Institute of Neurological Disorders and Stroke-Canadian Stroke Network vascular cognitive impairment harmonization standards. *Stroke* 2006; **37**: 2220-2241 [PMID: 16917086 DOI: 10.1161/01.STR.0000237236.88823.47]

78 **Roman GC,** Erkinjuntti T, Wallin A, Pantoni L, Chui HC. Subcortical ischaemic vascular dementia. *Lancet Neurol* 2002; **1**: 426-436 [DOI: 10.1016/S1474-4422(02)00190-4]

79 **McKeith IG**, Dickson DW, Lowe J, Emre M, O'Brien JT, Feldman H, Cummings J, Duda JE, Lippa C, Perry EK, Aarsland D, Arai H, Ballard CG, Boeve B, Burn DJ, Costa D, Del Ser T, Dubois B, Galasko D, Gauthier S, Goetz CG, Gomez-Tortosa E, Halliday G, Hansen LA, Hardy J, Iwatsubo T, Kalaria RN, Kaufer D, Kenny RA, Korczyn A, Kosaka K, Lee VM, Lees A, Litvan I, Londos E, Lopez OL, Minoshima S, Mizuno Y, Molina JA, Mukaetova-Ladinska EB, Pasquier F, Perry RH, Schulz JB, Trojanowski JQ, Yamada M. Diagnosis and management of dementia with Lewy bodies: third report of the DLB Consortium. *Neurology* 2005; **65**: 1863-1872 [PMID: 16237129 DOI: 10.1212/01.wnl.0000187889.17253.b1]

80 **Bekris LM**, Mata IF, Zabetian CP. The genetics of Parkinson disease. *J Geriatr Psychiatry Neurol* 2010; **23**: 228-242 [PMID: 20938043 DOI: 10.1177/0891988710383572]

81 **Leverenz JB**, Quinn JF, Zabetian C, Zhang J, Montine KS, Montine TJ. Cognitive impairment and dementia in patients with Parkinson disease. *Curr Top Med Chem* 2009; **9**: 903-912 [PMID: 19754405]

82 **Burton EJ**, Karas G, Paling SM, Barber R, Williams ED, Ballard CG, McKeith IG, Scheltens P, Barkhof F, O'Brien JT. Patterns of cerebral atrophy in dementia with Lewy bodies using voxel-based morphometry. *Neuroimage* 2002; **17**: 618-630 [PMID: 12377138 DOI: 10.1006/nimg.2002.1197]

83 **Burton EJ**, McKeith IG, Burn DJ, Williams ED, O'Brien JT. Cerebral atrophy in Parkinson's disease with and without dementia: a comparison with Alzheimer's disease, dementia with Lewy bodies and controls. *Brain* 2004; **127**: 791-800 [PMID: 14749292 DOI: 10.1093/brain/awh088]

84 **Whitwell JL**, Weigand SD, Shiung MM, Boeve BF, Ferman TJ, Smith GE, Knopman DS, Petersen RC, Benarroch EE, Josephs KA, Jack CR. Focal atrophy in dementia with Lewy bodies on MRI: a distinct pattern from Alzheimer's disease. *Brain* 2007; **130**: 708-719 [PMID: 17267521 DOI: 10.1093/brain/awl388]

85 **Firbank MJ**, Blamire AM, Teodorczuk A, Teper E, Burton EJ, Mitra D, O'Brien JT. High resolution imaging of the medial temporal lobe in Alzheimer's disease and dementia with Lewy bodies. *J Alzheimers Dis* 2010; **21**: 1129-1140 [PMID: 21504120]

86 **Kantarci K**, Lowe VJ, Boeve BF, Weigand SD, Senjem ML, Przybelski SA, Dickson DW, Parisi JE, Knopman DS, Smith GE, Ferman TJ, Petersen RC, Jack CR. Multimodality imaging characteristics of dementia with Lewy bodies. *Neurobiol Aging* 2012; **33**: 2091-2105 [PMID: 22018896 DOI: 10.1016/j.neurobiolaging.2011.09.024]

87 **Rowe CC**, Ng S, Ackermann U, Gong SJ, Pike K, Savage G, Cowie TF, Dickinson KL, Maruff P, Darby D, Smith C, Woodward M, Merory J, Tochon-Danguy H, O'Keefe G, Klunk WE, Mathis CA, Price JC, Masters CL, Villemagne VL. Imaging beta-amyloid burden in aging and dementia. *Neurology* 2007; **68**: 1718-1725 [PMID: 17502554 DOI: 10.1212/01.wnl.0000261919.22630.ea]

88 **Ishii K**, Imamura T, Sasaki M, Yamaji S, Sakamoto S, Kitagaki H, Hashimoto M, Hirono N, Shimomura T, Mori E. Regional cerebral glucose metabolism in dementia with Lewy bodies and Alzheimer's disease. *Neurology* 1998; **51**: 125-130 [PMID: 9674790 DOI: 10.1212/WNL.51.1.125]

89 **Teune LK**, Bartels AL, de Jong BM, Willemsen AT, Eshuis SA, de Vries JJ, van Oostrom JC, Leenders KL. Typical cerebral metabolic patterns in neurodegenerative brain diseases. *Mov Disord* 2010; **25**: 2395-2404 [PMID: 20669302 DOI: 10.1002/mds.23291]

90 **Ishii K**, Soma T, Kono AK, Sofue K, Miyamoto N, Yoshikawa T, Mori E, Murase K. Comparison of regional brain volume and glucose metabolism between patients with mild dementia with lewy bodies and those with mild Alzheimer's disease. *J Nucl Med* 2007; **48**: 704-711 [PMID: 17475957 DOI: 10.2967/jnumed.106.035691]

91 **Booij J**, Speelman JD, Horstink MWIM, Wolters EC. The clinical benefit of imaging striatal dopamine transporters with FP-CIT SPECT in differentiating patients with presynaptic parkinsonism from those with other forms of parkinsonism. *Eur J Nucl Med* 2001; **28**: 266-272 [DOI: 10.1007/s002590000460]

92 **Staff RT**, Ahearn TS, Wilson K, Counsell CE, Taylor K, Caslake R, Davidson JE, Gemmell HG, Murray AD. Shape analysis of 123I-N-omega-fluoropropyl-2-beta-carbomethoxy-3beta-(4-iodophenyl) nortropane single-photon emission computed tomography images in the assessment of patients with parkinsonian syndromes. *Nucl Med Commun* 2009; **30**: 194-201 [PMID: 19262280 DOI: 10.1097/MNM.0b013e328314b863]

93 **Tatsch K**, Poepperl G. Nigrostriatal dopamine terminal imaging with dopamine transporter SPECT: an update. *J Nucl Med* 2013; **54**: 1331-1338 [PMID: 23864718 DOI: 10.2967/jnumed.112.105379]

94 **O'Brien JT**. Role of imaging techniques in the diagnosis of dementia. *Br J Radiol* 2007; **80** Spec No 2: S71-S77 [PMID: 18445747 DOI: 10.1259/bjr/33117326]

95 **Shimada H**, Hirano S, Shinotoh H, Aotsuka A, Sato K, Tanaka N, Ota T, Asahina M, Fukushi K, Kuwabara S, Hattori T, Suhara T, Irie T. Mapping of brain acetylcholinesterase alterations in Lewy body disease by PET. *Neurology* 2009; **73**: 273-278 [PMID: 19474411 DOI: 10.1212/WNL.0b013e3181ab2b58]

96 **Yoshita M**, Taki J, Yokoyama K, Noguchi-Shinohara M, Matsumoto Y, Nakajima K, Yamada M. Value of 123I-MIBG radioactivity in the differential diagnosis of DLB from AD. *Neurology* 2006; **66**: 1850-1854 [PMID: 16801649 DOI: 10.1212/01.wnl.0000219640.59984.a7]

97 **Ratnavalli E**, Brayne C, Dawson K, Hodges JR. The prevalence of frontotemporal dementia. *Neurology* 2002; **58**: 1615-1621 [PMID: 12058088 DOI: 10.1212/WNL.58.11.1615]

98 **Neary D**, Snowden JS, Gustafson L, Passant U, Stuss D, Black S, Freedman M, Kertesz A, Robert PH, Albert M, Boone K, Miller BL, Cummings J, Benson DF. Frontotemporal lobar degeneration: a consensus on clinical diagnostic criteria. *Neurology* 1998; **51**: 1546-1554 [PMID: 9855500 DOI: 10.1212/WNL.51.6.1546]

99 **Gorno-Tempini ML**, Hillis AE, Weintraub S, Kertesz A, Mendez M, Cappa SF, Ogar JM, Rohrer JD, Black S, Boeve BF, Manes F, Dronkers NF, Vandenberghe R, Rascovsky K, Patterson K, Miller BL, Knopman DS, Hodges JR, Mesulam MM, Grossman M. Classification of primary progressive aphasia and its variants. *Neurology* 2011; **76**: 1006-1014 [PMID: 21325651 DOI: 10.1212/WNL.0b013e31821103e6]

100 **Hu WT**, Seelaar H, Josephs KA, Knopman DS, Boeve BF, Sorenson EJ, McCluskey L, Elman L, Schelhaas HJ, Parisi JE, Kuesters B, Lee VM, Trojanowski JQ, Petersen RC, van Swieten JC, Grossman M. Survival profiles of patients with frontotemporal dementia and motor neuron disease. *Arch Neurol* 2009; **66**: 1359-1364 [PMID: 19901167 DOI: 10.1001/archneurol.2009.253]

101 **Rohrer JD**. Structural brain imaging in frontotemporal dementia. *Biochim Biophys Acta* 2012; **1822**: 325-332 [PMID: 21839829]

102 **Rosen HJ**, Gorno-Tempini ML, Goldman WP, Perry RJ, Schuff N, Weiner M, Feiwell R, Kramer JH, Miller BL. Patterns of brain atrophy in frontotemporal dementia and semantic dementia. *Neurology* 2002; **58**: 198-208 [PMID: 11805245 DOI: 10.1212/WNL.58.2.198]

103 **Jason DW**, Jonathan DR. Frontotemporal dementia. *BMJ* 2013; **6**: 347

104 **Risacher SL**, Saykin AJ. Neuroimaging biomarkers of neurodegenerative diseases and dementia. *Semin Neurol* 2013; **33**: 386-416 [PMID: 24234359 DOI: 10.1055/s-0033-1359312]

105 **Pievani M**, de Haan W, Wu T, Seeley WW, Frisoni GB. Functional network disruption in the degenerative dementias. *Lancet Neurol* 2011; **10**: 829-843 [PMID: 21778116 DOI: 10.1016/S1474-4422(11)70158-2]

106 **Zhou J,** Greicius MD, Gennatas ED, Growdon ME, Jang JY, Rabinovici GD, Kramer JH, Weiner M, Miller BL, Seeley WW. Divergent network connectivity changes in behavioural variant frontotemporal dementia and Alzheimer's disease. *Brain* 2010; **133** (Pt 5): 1352-1367 [PMID: 20410145 DOI: 10.1093/brain/awq075]

107 **Rohrer JD**, Schott JM. Primary progressive aphasia: defining genetic and pathological subtypes. *Curr Alzheimer Res* 2011; **8**: 266-272 [PMID: 21222598 DOI: 10.2174/156720511795563728]

108 **Rossor MN**, Fox NC, Mummery CJ, Schott JM, Warren JD. The diagnosis of young-onset dementia. *Lancet Neurol* 2010; **9**: 793-806 [PMID: 20650401 DOI: 10.1016/S1474-4422(10)70159-9]

109 **Flanagan EP**, McKeon A, Lennon VA, Boeve BF, Trenerry MR, Tan KM, Drubach DA, Josephs KA, Britton JW, Mandrekar JN, Lowe V, Parisi JE, Pittock SJ. Autoimmune dementia: clinical course and predictors of immunotherapy response. *Mayo Clin Proc* 2010; **85**: 881-897 [PMID: 20884824 DOI: 10.4065/mcp.2010.0326]

110 **Titulaer MJ**, Soffietti R, Dalmau J, Gilhus NE, Giometto B, Graus F, Grisold W, Honnorat J, Sillevis Smitt PA, Tanasescu R, Vedeler CA, Voltz R, Verschuuren JJ. Screening for tumours in paraneoplastic syndromes: report of an EFNS task force. *Eur J Neurol* 2011; **18**: 19-e3 [PMID: 20880069]

111 **Wu HM**, Lu CS, Huang CC, Lyu RK, Chen RS, Wu YR, Chen YC, Lai SC, Hung J, Tsai YT, Toh CH, Kuo HC. Asymmetric involvement in sporadic creutzfeldt-jakob disease: clinical, brain imaging, and electroencephalographic studies. *Eur Neurol* 2010; **64**: 74-79 [PMID: 20606451 DOI: 10.1159/000315148]

112 **Chang L**, Ernst T, Tornatore C, Aronow H, Melchor R, Walot I, Singer E, Cornford M. Metabolite abnormalities in progressive multifocal leukoencephalopathy by proton magnetic resonance spectroscopy. *Neurology* 1997; **48**: 836-845 [PMID: 9109865 DOI: 10.1212/WNL.48.4.836]

113 **Mark AS**, Atlas SW. Progressive multifocal leukoencephalopathy in patients with AIDS: appearance on MR images. *Radiology* 1989; **173**: 517-520 [PMID: 2798883 DOI: 10.1148/radiology.173.2.2798883]

114 **Ragin AB**, Storey P, Cohen BA, Epstein LG, Edelman RR. Whole brain diffusion tensor imaging in HIV-associated cognitive impairment. *AJNR Am J Neuroradiol* 2004; **25**: 195-200 [PMID: 14970017]

115 **Tate DF**, Conley J, Paul RH, Coop K, Zhang S, Zhou W, Laidlaw DH, Taylor LE, Flanigan T, Navia B, Cohen R, Tashima K. Quantitative diffusion tensor imaging tractography metrics are associated with cognitive performance among HIV-infected patients. *Brain Imaging Behav* 2010; **4**: 68-79 [PMID: 20503115 DOI: 10.1007/s11682-009-9086-z]

116 **Leite SC**, Corrêa DG, Doring TM, Kubo TT, Netto TM, Ferracini R, Ventura N, Bahia PR, Gasparetto EL. Diffusion tensor MRI evaluation of the corona radiata, cingulate gyri, and corpus callosum in HIV patients. *J Magn Reson Imaging* 2013; **38**: 1488-1493 [PMID: 23559497 DOI: 10.1002/jmri.24129]

P- Reviewer: Altamura C **S- Editor**: Qi Y **L- Editor**: A
E- Editor: Lu YJ

World Journal of Radiology

Submit a Manuscript: http://www.wjgnet.com/esps/
Help Desk: http://www.wjgnet.com/esps/helpdesk.aspx
DOI: 10.4329/wjr.v8.i3.255

World J Radiol 2016 March 28; 8(3): 255-267
ISSN 1949-8470 (online)

REVIEW

Some computer graphical user interfaces in radiation therapy

James C L Chow

James C L Chow, Radiation Medicine Program, Princess Margaret Cancer Center, University Health Network, Department of Radiation Oncology, University of Toronto, Toronto, ON M5G 2M9, Canada

Author contributions: Chow JCL did the data collection and literature review; he also wrote the article.

Conflict-of-interest statement: Author declares no conflict of interests for this article.

Correspondence to: James C L Chow, PhD, Radiation Medicine Program, Princess Margaret Cancer Center, University Health Network, Department of Radiation Oncology, University of Toronto, 610 University Avenue, Toronto, ON M5G 2M9, Canada. james.chow@rmp.uhn.on.ca
Telephone: +1-416-9464501
Fax: +1-416-9466566

Received: September 2, 2015
Peer-review started: September 8, 2015
First decision: November 3, 2015
Revised: December 17, 2015
Accepted: January 5, 2016
Article in press: January 7, 2016
Published online: March 28, 2016

Abstract

In this review, five graphical user interfaces (GUIs) used in radiation therapy practices and researches are introduced. They are: (1) the treatment time calculator, superficial x-ray treatment time calculator (SUPCALC) used in the superficial X-ray radiation therapy; (2) the monitor unit calculator, electron monitor unit calculator (EMUC) used in the electron radiation therapy; (3) the multileaf collimator machine file creator, sliding window intensity modulated radiotherapy (SWIMRT) used in generating fluence map for research and quality assurance in intensity modulated radiation therapy; (4) the treatment planning system, DOSCTP used in the calculation of 3D dose distribution using Monte Carlo simulation; and (5) the monitor unit calculator, photon beam monitor unit calculator (PMUC) used in photon beam radiation therapy. One common issue of these GUIs is that all user-friendly interfaces are linked to complex formulas and algorithms based on various theories, which do not have to be understood and noted by the user. In that case, user only needs to input the required information with help from graphical elements in order to produce desired results. SUPCALC is a superficial radiation treatment time calculator using the GUI technique to provide a convenient way for radiation therapist to calculate the treatment time, and keep a record for the skin cancer patient. EMUC is an electron monitor unit calculator for electron radiation therapy. Instead of doing hand calculation according to pre-determined dosimetric tables, clinical user needs only to input the required drawing of electron field in computer graphical file format, prescription dose, and beam parameters to EMUC to calculate the required monitor unit for the electron beam treatment. EMUC is based on a semi-experimental theory of sector-integration algorithm. SWIMRT is a multileaf collimator machine file creator to generate a fluence map produced by a medical linear accelerator. This machine file controls the multileaf collimator to deliver intensity modulated beams for a specific fluence map used in quality assurance or research. DOSCTP is a treatment planning system using the computed tomography images. Radiation beams (photon or electron) with different energies and field sizes produced by a linear accelerator can be placed in different positions to irradiate the tumour in the patient. DOSCTP is linked to a Monte Carlo simulation engine using the EGSnrc-based code, so that 3D dose distribution can

be determined accurately for radiation therapy. Moreover, DOSCTP can be used for treatment planning of patient or small animal. PMUC is a GUI for calculation of the monitor unit based on the prescription dose of patient in photon beam radiation therapy. The calculation is based on dose corrections in changes of photon beam energy, treatment depth, field size, jaw position, beam axis, treatment distance and beam modifiers. All GUIs mentioned in this review were written either by the Microsoft Visual Basic. net or a MATLAB GUI development tool called GUIDE. In addition, all GUIs were verified and tested using measurements to ensure their accuracies were up to clinical acceptable levels for implementations.

Key words: Graphical user interface; Cancer treatment; Treatment planning; Radiotherapy; Monitor unit calculation

Core tip: Computer graphical user interface (GUI) allows people to interact and control a device or job process without detailed knowledge of computer programming and related theory. Using the graphical windows, icons, buttons and visual indictor provided by the GUI, instead of giving computer commands in text that required specific training and understanding of the computer language, users can interact with the device or process through direct manipulation of graphical elements. This avoids a lot of unnecessary human errors and man-hours to fulfill a computer task, and makes calculations complete more systematic and well organized.

Chow JCL. Some computer graphical user interfaces in radiation therapy. *World J Radiol* 2016; 8(3): 255-267 Available from: URL: http://www.wjgnet.com/1949-8470/full/v8/i3/255.htm DOI: http://dx.doi.org/10.4329/wjr.v8.i3.255

INTRODUCTION

In radiation therapy, some treatment and pre-treatment procedures such as calculation of treatment time or monitor unit (MU) for the kV or MV radiation machine, quality assurance test for radiation therapy, treatment planning with accurate dose calculation, and dosimetric correction due to patients' internal organ motion and deformation, require complex theories and algorithms. Although nowadays the advance of computer technology allows the above tasks to be completed in a reasonable time, the clinical user needs to know computer programming and medical physics theory to interact with the computer. A computer graphical user interface (GUI) therefore helps radiation oncology staff such as radiation therapists, planners, oncologists and physicists to calculate and determine the required parameter values in radiation therapy without involving complex theory and algorithm.

Computer GUI contains graphical elements such as windows, scrolling bars, indicators and icons to assist the user to interact and control a device or process. Through direct manipulation of graphical elements, users do not need specific computer language on complex medical physics theory to complete a task in radiation therapy. This minimizes human error and man-hours in the treatment procedure and preparation. In this review, five GUIs developed mainly by the author's group and used in radiation therapy are introduced: (1) The treatment time calculator, superficial X-ray treatment time calculator (SUPCALC) used to determine the treatment time based on the prescription dose for the superficial X-ray machine[1]; (2) The electron MU calculator, electron monitor unit calculator (EMUC), used to calculate the required MU for an electron radiation therapy using a medical linear accelerator (linac)[2]; (3) The sliding window intensity modulated radiotherapy (SWIMRT), a GUI to generate the mulitleaf collimator (MLC) machine file for a specific fluence map in intensity modulated radiation therapy (IMRT)[3]; (4) The treatment planning GUI, DOSCTP, equipped with a Monte Carlo simulation engine running the EGSnrc-based code[4]; and (5) The photon beam MU calculator, PMUC, used to calculate the MU from the prescription dose for photon beam radiation therapy. All GUIs were written either by the Microsoft Visual Basic.net or a MATLAB GUI development tool called GUIDE. All GUIs were tested by measurements, can be clinically implemented in a cancer center or hospital, and have been distributed to the public.

SUPCALC is a GUI of treatment time calculator providing a convenient platform for the radiation staff in superficial radiation therapy. This GUI has the following features: (1) A flexible, password-protected database; (2) An irregular cutout calculator to calculate the peak scattering factor (PSF) of an irregular field; (3) Simplified import of the irregular field image to the calculator; and (4) Patient treatment record printing as an electronic file or hardcopy. SUPCALC was adapted to the Gulmay D3150 superficial X-ray unit in this review. Dosimetric information such as PSF table was needed for each treatment energy. They were measured and input in to the database. The predicted and measured dose in the commissioning should be smaller than ± 2%. The GUI and "HELP" menu made it easy for the user to calculate the treatment time compared to using forms and tables. It also reduced training time and human error. Physicist can setup, input and delete treatment beam in the database, which is password protected. For the irregular lead cutout, an irregular field calculator routine is associated with the software to determine the PSF using sector-integration algorithm. The user only needs to prepare a JPEG file of the irregular field printout using a scanner and import such graphic file to the GUI to determine the PSF. The aim of the SUPCALC is to provide a convenient way for the user to calculate the treatment time and keep a record.

In electron radiotherapy, a GUI for MU calculation is preferred as a treatment plan quality assurance tool or clinical mark-up MU calculator, though MU can be calculated by most treatment planning systems (TPSs)

based on various methods such as pencil-beam model[5], lateral build-up ratio[6], two-source model[7], and sector-integration[8].

EMUC is a GUI of electron MU calculator based on a new sector-integration algorithm to determine the relative output factor (ROF) of a treatment field. EMUC has four features: (1) Experimental data of ROF was mathematically fitted using the polynomial or exponential method so that ROF can be predicted more accurately; (2) A new sector-integration algorithm was introduced for measuring the irregular treatment field; (3) Optical scanner was used instead of the traditional film digitizer in the cutout image acquisition; and (4) Electronic file of the patient information, calculation parameters and results was produced as a record.

In photon radiotherapy, IMRT technique was employed to treat different cancer sites such as the head-and-neck[9], breast[10,11] and prostate[12,13]. IMRT involved a group of beam segments generated by a leaf sequencing method in the inverse treatment planning. The sliding window method[14-16] allows the MLC leaves to move when the beam is on. On the other hand, the step-and-shoot method[17-19] delivers the dose using individual beam segments with no leaf movement when the beam is on. In radiation dose delivery using the sliding window method, a group of beam segments with calculated dose-fraction order was transferred from the TPS to the linac console as a machine file, including information of the MLC positions in each beam fraction. SWIMRT is a computer GUI designed to study the MLC mechanical and dosimetric properties based on the sliding window technique. SWIMRT interacts with the machine file of the MLC and has the following features: (1) A convenient interface for the import of the fluence map; (2) An accurate MLC mechanical and dosimetric calibration; (3) Computer code (MATLAB) is easy to edit and update; (4) Simple image processing functions such as field trimming, region of interest cropping and selecting; and (5) Linked to a comprehensive database. In SWIMRT, the machine file can be generated only by importing a fluence map with a graphical file format. Film dosimetry was used to verify SWIMRT for both clinical and non-clinical fluence maps, and the GUI can be used to study the leaf sequencing algorithm and MLC dosimetry.

One goal in external beam treatment planning is to provide highly conformal dose coverage at the cancer target while sparing the surrounding critical tissues. In dose calculation of a treatment plan, Monte Carlo method is well known as a benchmark to predict accurate dose distribution in inhomogeneous media such as bone and lung[20-24]. The Monte Carlo dose calculation requires a patient's CT image set (DICOM, RTOG or Pinnacle^3 format) which can be converted to a 3D inhomogeneous phantom using the CTCREATE routine[25] in the EGSnrc-based Monte Carlo code.

DOSCTP is a simple treatment planning GUI using the EGSnrc Monte Carlo code as a dose calculation engine, and has the following features: (1) A comprehensive interface to convert the CT image set to a 3D DOSXYZnrc phantom; (2) Contouring the regional of interest in the transverse, sagittal and coronal display; (3) Database for the custom beam phase space files based on the BEAMnrc[26,27]; (4) Linked to the DOSXYZnrc code for simulation; and (5) Display of the contour and calculated dose for plan evaluation.

In the clinical radiation treatment process, the prescribed dose at the tumour target volume is delivered in terms of a certain number of MU by the linac. Such MU is measured by an internal ionization chamber inside the head of the gantry of the accelerator. Absolute dose calibration sets up a well-defined dose rate (cGy/MU) at a well-defined location inside a water phantom. The number of MU delivered to the target volume is therefore calculated by a simple equation, MU = Prescribed dose/dose rate. However, this equation is only true when the dose is prescribed in a water tank in exactly the same beam setup geometry used for the absolute dose calibration. This is obviously not right in a typical clinical treatment situation because: (1) The target volume may be at different treatment depth in the patient; (2) The field size may not be the one used in absolute calibration and may be irregular; (3) Block or MLC may be used during the treatment; (4) The dose may be prescribed off from the central beam axis; (5) Physical and/or dynamic wedge may be used during the treatment; (6) Compensator and different types of tray may be inserted between the gantry head and the patient; and (7) The source to the target distance may be changed from 100 cm, which is the typical source-to-axis distance (SAD) in radiation therapy. In view of the above variations during the treatment set up, the above equation should be modified to calculate the correct MU for the prescription dose. This modification/correction can be done by applying different correction factors and dose ratios in the equation. The MU can therefore be calculated by using a more detailed formula. PMUC is a GUI of MU calculator for clinical radiation treatment using MV photon beams.

ALGORITHMS

In this review, all GUIs were written either by the Microsoft Visual Basic.net or a MATLAB GUI development tool called GUIDE. In addition, all GUIs were verified and tested by dosimetric measurements to ensure their accuracies were up to the clinical acceptable levels for implementations.

SUPCALC

The superficial X-ray treatment time calculator is based on the following equation:

$$DR^{c}_{muscle} = [M/(t-a)] \times N_x \times P_{ion} \times FTP \times PSF \times f_{muscle} \times ISL \times OF \quad (1)$$

Where DR^{c}_{muscle} = Absolute calibrated dose rate of muscle at source-to-surface distance (SSD) = 15 cm, M = electrometer reading, t = treatment time, a = shutter error, N_x = NRC calibration constant, P_{ion} = coefficient corrects for ionization recombination losses, FTP = (760/P) × [(273 + T)/295], PSF = Peak scattering factor,

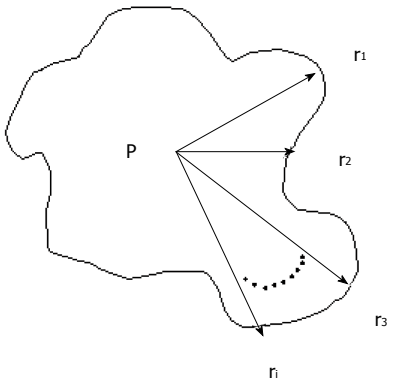

Figure 1 Sector-integration of irregular field.

f_{muscle} = f factor for muscle, ISL = inverse square law, and OF = output factor measured in air. From Eq. 1, we can write:

Dose in muscle = $M \times N_x \times P_{ion} \times FTP \times f_{muscle} \times ISL \times OF$ (2)

To calculate the treatment time, it is noted that when the cone size is changed, both the PSF and OF are changed. When the SSD is changed, ISL should be applied to modify the DR^c_{muscle}. Since the OF depends on cone size and PSF depends on lead cutouts, the treatment dose rate, DR^t_{muscle} can be written as:

$DR^t_{muscle} = DR^c_{muscle} \times [PSF(CS)/PSF(5)] \times OF \times [SSD^2/(SSD + airgap)^2]$ (3)

For example, using Eq. 3, if the cone size (diameter) = 5 cm, then OF = 1 and PSF(5)/PSF(5) =1 (because 5 cm cone is used for the absolute calibration). If the distance between the cone and patient = 0 cm, with our calibration SSD = 15 cm and air gap = 0 cm, Eq. 3 becomes: $DR^t_{muscle} = DR^c_{muscle}$. In superficial X-ray treatment, irregular cutout field is commonly used to conform to the surface lesion. When the cutout field is irregular, the PSF would be difficult to determine as the field has a variation of radii starting from the center of the field (point P) as shown in Figure 1. Clarkson Integral is therefore employed to solve this problem. According to the Integral, the PSF is calculated using the following equation:

$$PSF(r) = \frac{1}{n}\sum_{i=1}^{n} PSF(r_i) \quad (4)$$

Where n is the angle between two radii, r_i and r_{i-1}, r_i is the radius from the point P in the cutout field as shown in Figure 1. Basically, n is selected to be 36 and therefore the angle between two radii is 10° in the calculator. Eq. 4 calculated PSF(r) for a particular energy and such value would be input to Eq. 3 for the treatment time calculation.

EMUC

EMUC predicts the electron MU using the effective SSD technique[28-30]:

$MU = (Dose/fraction)/\{D_0 \times C \times (IDL/100) \times ROF \times [(SSD_{eff} + d_0)/(SSD_{eff} + d_0 + g)]^2\}$ (5)

In Eq. 5, D_o is the dose calibrated as 1 cGy/MU at the SSD = 100 cm and depth of reference (d_{ref}) using the AAPM TG-51 protocol[31]. C is the correction factor between the d_{ref} (used in planning) and depth of maximum dose (d_m). IDL is the isodose line in the treatment plan. d_0 is the depth of treatment and SSD_{eff} is the effective SSD. g is the air gap between the regular and treatment SSD. It should be noted that ROF varies with the applicator size, shape of cutout and beam energy. In Eq. 5, IDL = 1 when the treatment SSD = 100 cm. It is because g = 0 in such geometry.

A sector-integration formula was used to calculate the ROF as a function of treatment field:

$$ROF = \frac{1}{n}\sum_{i=1}^{n} ROF_i \quad (6)$$

In Eq. 6, the angular segment number (n) divides the treatment field into 360°/n segments. The ROF of circular field, with radius equal to the distance between the edge of each angular segment and the central beam axis, is equal to ROF_i. A predetermined ROF database as a function of field sizes, beam energies and applicator sizes was set up according to Eq. 6. In this review, the database contains electron beam energies of 4, 6, 9, 12 and 16 MeV, and applicator sizes of 5 cm × 5 cm, 10 cm × 10 cm, 15 cm × 15 cm, 20 cm × 20 cm and 25 cm × 25 cm. When the treatment field is a square or rectangle, sector-integration is not needed. The ROF is therefore calculated using the following expression[32]:

$$ROF(X, Y) = \sqrt{ROF(X, X) \times ROF(Y, Y)} \quad (7)$$

Where ROF(X,X) and ROF(Y,Y) are ROFs of square cutouts, and ROF(X,Y) is the ROF of a rectangular cutout (side lengths = X and Y).

SWIMRT

SWIMRT uses a leaf sequencing algorithm[25,33,34] to convert a matrix of dose values into exposure times based on dose rate. The conversion function is written as:

Exposure time = Dose/Doserate (8)

Eq. 8 can be modified to Eq. 9 by considering corrections to the dose map such as MLC leaf leakages.

Exposure time = [Dose-f(Dose)]/Doserate (9)

In Eq. 9, the dose correction is expressed as f(Dose). For a leaf pair profile, the first leaf movement results in an exposure until the second leaf reaches the same position. Therefore, both the sampled arrays of the first and second leaf exposure should be determined by the algorithm. One simple way to start the calculation is to assign the first leaf array the desired exposure times and the second leaf array zero times. However, this leads to the second leaf requiring infinite velocity to catch up with the first leaf. To solve this problem, the portion of arrays is allowed to be interchanged between the two leaves as shown in Figure 2[3]. Figure 2A gives an example of a leaf pair profile with Figure 2B showing

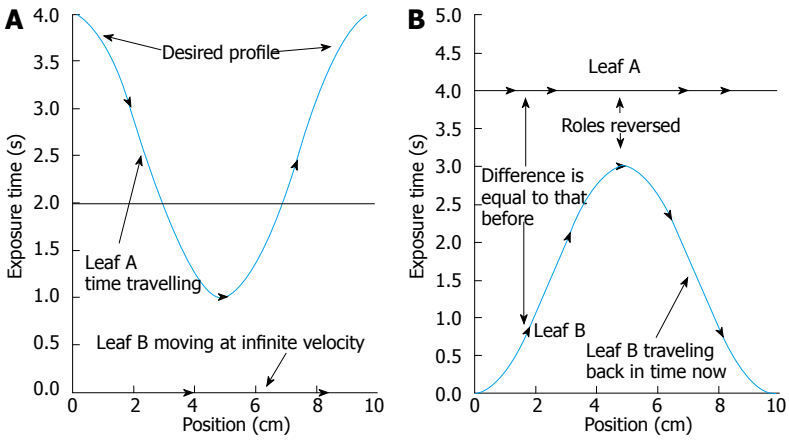

Figure 2 The portion of arrays is allowed to be interchanged between the two leaves as shown. A: An example of a leaf pair exposure-time profile; B: The first half of the profile is made realizable by reversing the roles of leaf A and leaf B.

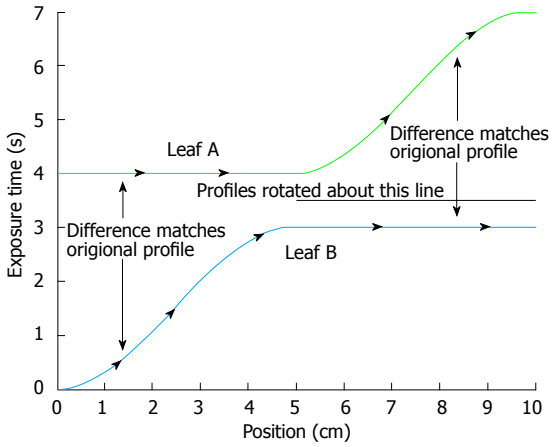

Figure 3 The roles of leaf A and leaf B are reversed again after the mid position.

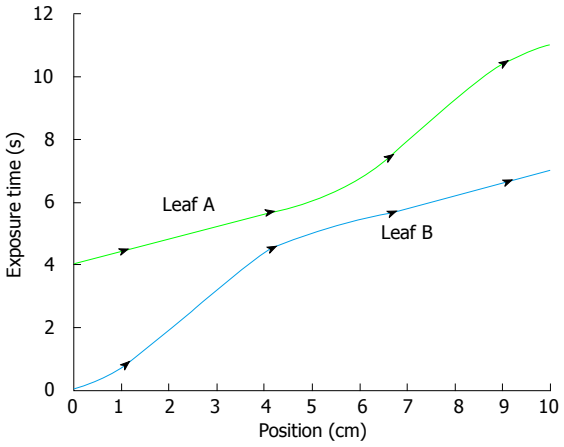

Figure 4 Profiles for both leaves are skewed to eliminate large velocities.

the reversed roles of leaf A and leaf B. It is seen in Figure 2 that there is still the same problem with leaf A, and vice versa. Therefore, the roles of leaves can be reversed again from the mid-position as shown in Figure 3[3].

The issue of infinite velocity can be solved by skewing the profiles as per the maximum velocity of leaves. A linear function is added:

$$f(d) = (1/\text{Maximum Velocity})\, d \quad (10)$$

Where d is the leaf position. Figure 4 shows the profile using the maximum leaf velocity of 2.5 cm/s with both MLC leaves skewed to remove large velocities. Eq. 10 was used through each leaf pair profile[3].

The machine file is generated by changing the arrays from spatial to time samples. Since it is unlikely that the time samples will occur at extract times inside the matrix, averaging time is used here. For example, the leaf in the array moves from positions 3 mm to 4 mm with times 1.95 s and 2.15 s, respectively. The leaf position of 2 s (*i.e.*, 2.15 s - 1.95 s) can be calculated as:

$$d = \text{startDist} + (\text{endDist} - \text{startDist}) \times [(\text{value} - \text{startTime})/(\text{endTime} - \text{startTime})] = 3 + (4 - 3) \times [(2 - 1.95)/(2.15 - 1.95)] \quad (11)$$

In Eq. 11, startTime (before) and endTime (after) are times found from the array elements. Similarly, startDist (before) and endDist (after) are the corresponding distances. The function searches the zero dose in the profile at the beginning and/or in the end. When the leaf pair satisfy this criteria, the leaves are set to stop. Once all details of leaf pair profiles are determined, the MLC machine file was generated by SWIMRT.

DOSCTP

The flow chart of DOSCTP is shown in Figure 5[4]. The GUI includes four components including the "Treatment Planning", "Monte Carlo Simulation with DOSXYZnrc", "Dose Visualization" and "Export". First, the user imports a CT image set with DICOM format using the "Treatment Planning" block. A plan is then created with definition of isocenter position, contouring and beam placement. The user can edit the converted 3D inhomogeneous phantom and go to the "Monte Carlo Simulation with DOSXYZnrc" block. A set of DOSXYZnrc simulation parameters is needed to input for Monte Carlo simulation. When the Monte Carlo set up is done, DOSCTP automatically generates input file(s) for each beam in simulations. Result of Monte Carlo simulation can then be viewed using the "Dose Visualization" block which displays the isodose lines with the CT image set. The user can also carry out dose normalization at different positions. In the "Export" block, all plan information can be exported to an

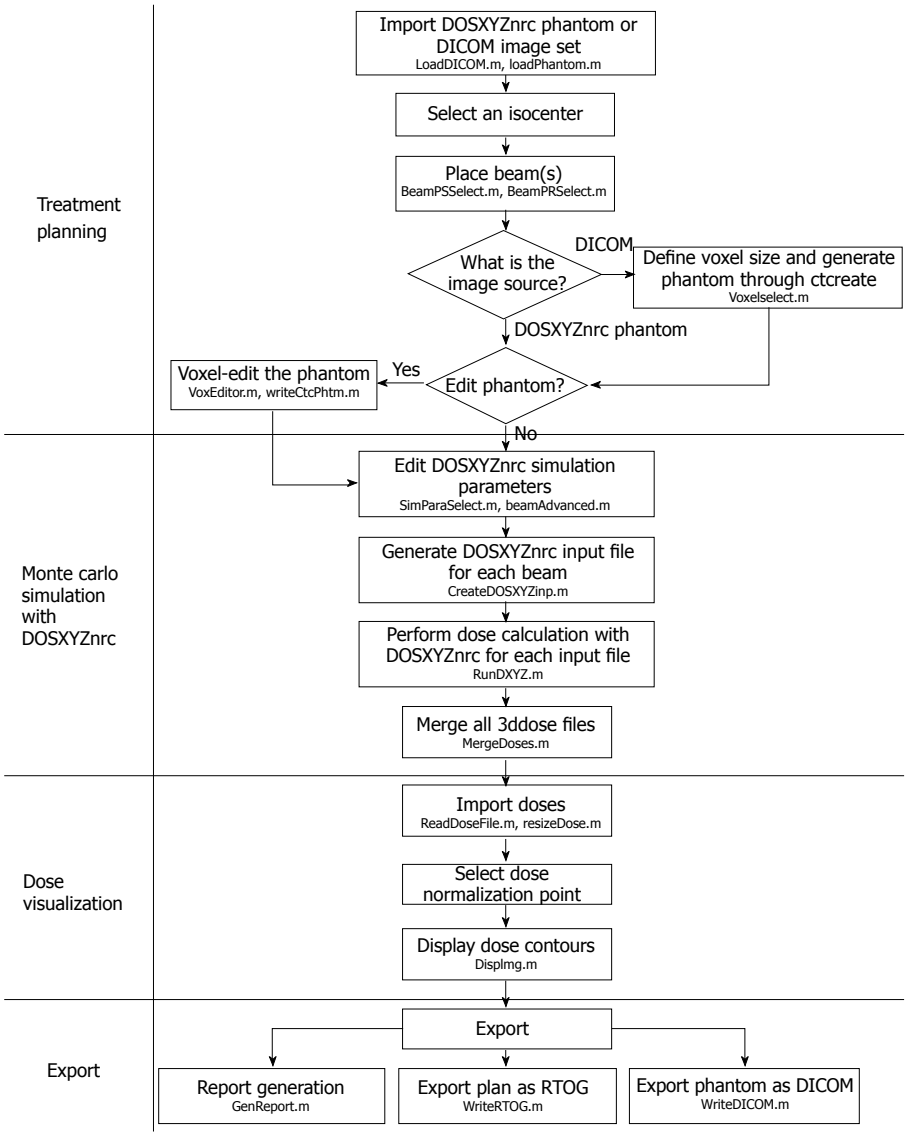

Figure 5 Block diagram showing the flowchart with main components of DOSCTP.

electronic file in DICOM format for commercial TPSs.

PMUC

In PMUC, if the prescription depth is different from that in the absolute calibration condition, a depth correction is carried out from the absolute dose calibration point. Typically, the absolute calibrated dose rate (D_{cal}) = 1 cGy/MU and it is set at the beam geometry mentioned above. To obtain the dose rate at another water depth from 5 cm with the same field size (FS), Tissue Maximum Ratio (TMR) is employed in the conversion. The new dose rate (D_{pt1}) in a depth of d cm from the water surface can be calculated as:

$$D_{pt1} = D_{cal} \times [TMR(10 \times 10, d\ cm)/TMR(10 \times 10, 5\ cm)] \quad (12)$$

This is the dose rate by changing the depth only, while keeping the FS the same as in the absolute dose calibration (10 cm × 10 cm). If the FS of the beam is also changed either by applying block or MLC, PSF is used to fulfill such correction. Eq. 12 is therefore modified as:

$$D_{pt1} = D_{cal} \times [TMR(10 \times 10, d\ cm)/TMR(10 \times 10, 5\ cm)] \times [PSF(FS)/PSF(10 \times 10)] \quad (13)$$

In Eq. 13, the new FS is rescaled using the PSF ratio, where 10 cm × 10 cm is the FS used in the absolute dose calibration. A term Phantom Scattering (PS) Factor based on Eq. 13 is defined as:

$$PS = [TMR(10 \times 10, d\ cm)/TMR(10 \times 10, 5\ cm)] \times [PSF(FS)/PSF(10 \times 10)] \quad (14)$$

So that,

$$D_{pt1} = D_{cal} \times PS \quad (15)$$

On the other hand, changing the jaw position varies the dose at the central axis with the same water depth. This change is mainly contributed by the beam scattered from the jaws. Therefore, such change (whether the jaw position is symmetric or asymmetric) has to be noted and measured in advances, so that correction can be made when the jaw setting is no longer FS = 10 cm × 10 cm. The Collimator Scattering (CS) Factor is hence defined as:

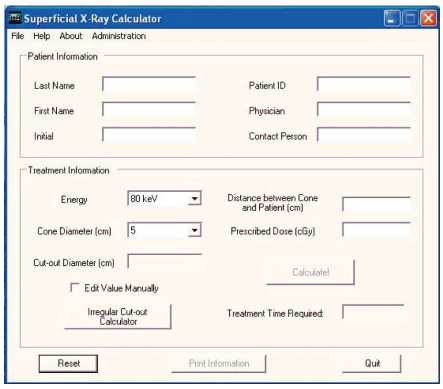

Figure 6 Front end window of superficial x-ray treatment time calculator.

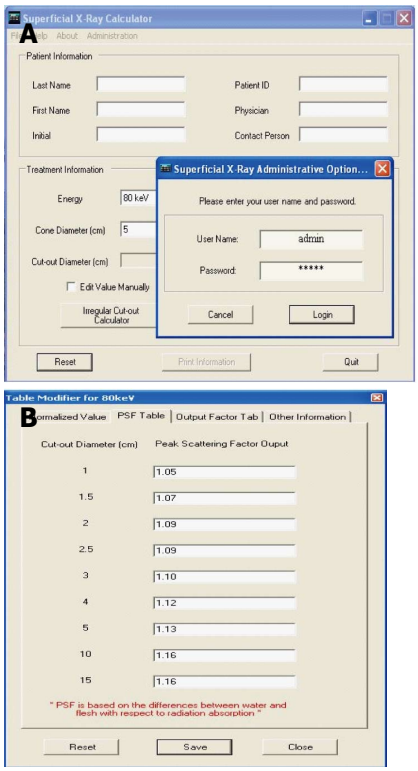

Figure 7 Password protected database (A) and comprehensive database (B).

$$CS = [D_{air}(X,Y; d_m)]/[D_{air}(10 \times 10; d_m)] \quad (16)$$

X and Y are the X and Y jaw position, and d_m is the depth of the maximum dose of particular photon beam energy (*e.g.*, 6/15 MV). D_{air} is the dose measured in air. Eq. 16 can be combined to Eq. 15 so that:

$$D_{pt2} = D_{cal} \times PS \times CS \quad (17)$$

D_{pt2} is the dose rate after corrections of the treatment depth, field size and jaw position.

In some radiation treatments, due to the application of the asymmetric jaw and half beam block, the dose is prescribed away from the central beam axis. This is because the absolute dose calibration is done at the central axis with symmetry of the beam profile; a correction is needed for the off-axis dose point by considering various flatness and symmetry along the horizontal beam profile. An Off-Axis Ratio (OAR) is therefore defined as:

OAR (x, d) = (Dose at the Central Axis in depth d)/(Dose away from the Central Axis at a distance x in the same depth d) (18)

This ratio should be multiplied in the right hand side of Eq. 17 in order to obtain the corrected MU.

In some radiation treatments, it is usual to put beam modifiers such as compensator, wedge (physical or dynamic) and tray between the beam source and the patient surface to achieve an appreciate dose distribution in the target volume. However, the treatment beam is unavoidably attenuated by the presence of modifier, resulting in more MU should be given in the irradiation. The attenuation factors of wedge (wedge factor, WF), compensator (compensator factor, CF) and tray (tray factor, TF) have to be multiplied to the right hand side of Eq. 17. When the source to treatment point distance (SPD) is different from 1 m, the beam reaching the target volume is stronger or weaker due to the distance decreasing or increasing from the absolute dose calibration setting, respectively. The change of dose can be corrected by applying the inverse square law (ISL = $1/SPD^2$), and this factor should be put in the right hand side of Eq. 17.

To sum up, the final equation in MU calculation is:

$$MU = (\text{Prescribed Dose})/(D_{cal} \times CS \times PS \times OAR \times WF \times TF \times CF \times ISL) \quad (19)$$

This equation is used in PMUC.

In addition, PMUC uses an improved interpolation algorism for obtaining the PS value among the points in the database. In PMUC, bi-linear interpolation algorism was selected to deal with interpolation values within the database, while Spine interpolation algorism was selected to deal with values outside or on the edge of the database. It is found that by using these combinations, the interpolated PS value was more accurate than that being done by other algorithms like inverse-square interpolation.

APPLICATIONS

SUPCALC

SUPCALC provides a front-end window interface, and a detailed "help" menu to provide the basic operational instruction as shown in Figure 6. Users can input the patient information in the upper part of the window, and treatment beam parameters in the bottom. The beam parameters include kV X-ray energy, treatment cone diameter, distance between the cone to the patient surface, prescribed dose and cutout (treatment field) diameter. A flexible, password-protected database of the calculator to add or delete beam energy for the machine is shown in Figure 7. Figure 7A shows the database is password protected so that only the authorized person such as a medical physicist can change the content. Figure 7B shows the PSFs for different cutout diameter. These factors were determined by dosimetric

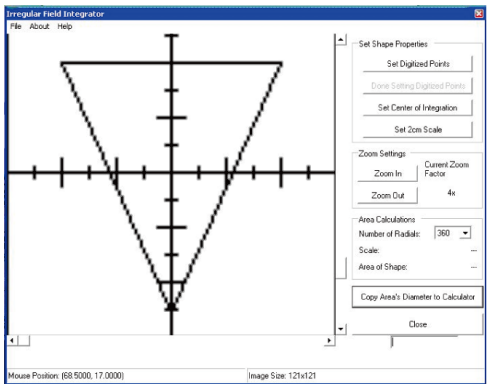

Figure 8 Irregular field calculator.

Superficial x-ray machine treatment report

Patient name: Joe, John A Patient ID: 1234567

Name and Address of Hospital:
Grand River Hospital
P.O. Box 9056
835 King St. West
Kitchener, ON N2G 1G3

Physician: Dr Smith

Contact person: Mary Joe

Total time required = 1.8 min

Treatment details:

Treatment dose (cGy)	Treatment energy (kVp)	Cutout radius (cm)	Distance to patient (cm)	Cone radius (cm)
300 cGy	100kV	2.5 cm	5 cm	2.5 cm

Comments:
This is a trial.

Signature:

Report created on: 16/01/2006 9:58:27 PM

Figure 9 Record printout (hardcopy or electronic).

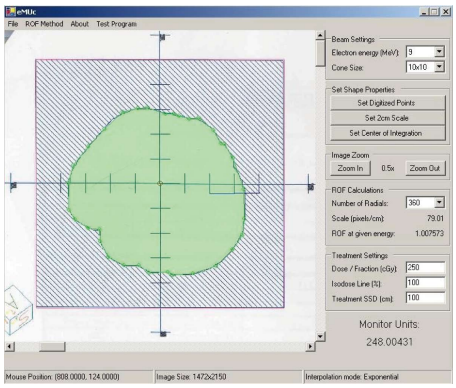

Figure 10 The front-end window of electron monitor unit calculator showing the imported irregular electron field image in the left hand side and the patient treatment parameters in the right hand side.

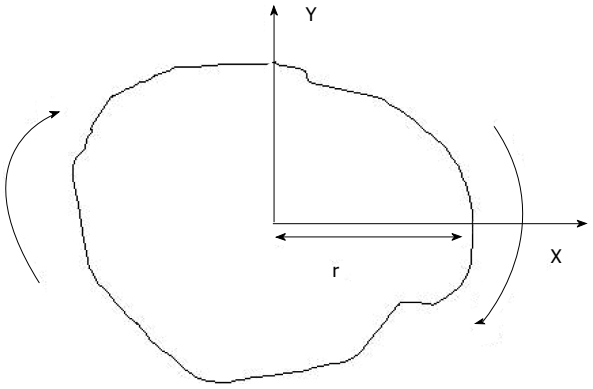

Figure 11 Schematic diagram showing the algorithm to acquire the radius in each divided angular segment in the irregular field. Instead of rotating the vectors from the central axis towards the field edge, the whole field is rotated cutting through the positive X-axis.

measurements. An irregular cutout calculator to predict the PSF of an irregular field is shown in Figure 8. It should be noted that the import of the irregular cutout field image is simplified by using only a commercial optical scanner. Finally, patient treatment record printing and transferred to a database are possible as shown in Figure 9.

EMUC

The front-end window of EMUC (Figure 10) provides an user-friendly interface to input the related treatment parameters such as electron beam energy, IDL, SSD, applicator size and prescribed dose for MU calculation[2].

A novel sector-integration algorithm was used in EMUC. This algorithm rotates the irregular field with the positive x-axis as a static vector instead of rotating a vector from the central field axis to the field edge[35]. The radius of each angular segment (r_i) is therefore measured with the whole field rotated 360°. Moreover, taking advantage of the fast computing speed, the number of angular segments can be increased to 360 compared to 36 or less used in previous works[35-37]. This can help to increase the accuracy when calculating electron MU for a highly irregular field. A Microsoft Access database was used to store the integration parameters. The database included parameters in Eq. 5 such as C, d_m, d_{ref} and SSD_{eff}. The database also stored the ROFs *vs* radii of circular fields and the ROFs for different square and rectangular sizes in Figure 11[2].

SWIMRT

The fluence map or picture can be imported or created using SWIMRT as shown in Figure 12[3]. To create a fluence map, a gird of specified "X size" and "Y size" can be generated using the "Create New Grid" button. Figure 13 shows the "SWIMRTgridder" editor to modify and change every beam intensity element in the grid[3]. The fluence map can also be rotated using the "Rotate Image" button at the lower left hand corner in Figure 12.

DOSCTP

The CT images are displayed in the viewing windows of DOSCTP as shown in Figure 14[4]. The beam configuration is managed by a panel on the top left of the GUI. The user can call the phase space beams (P.S. Beam) pre-

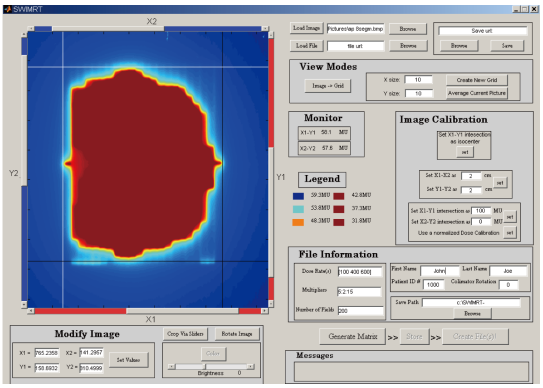

Figure 12 Front-end window of sliding window intensity modulated radiotherapy.

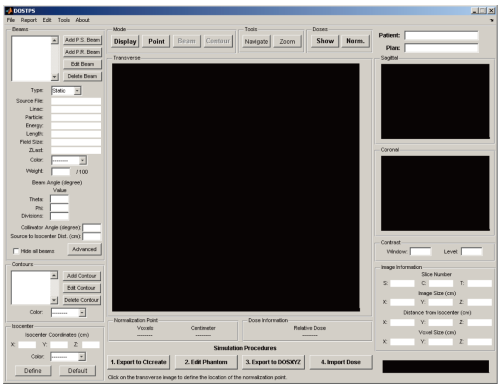

Figure 14 The front-end window of DOSCTP.

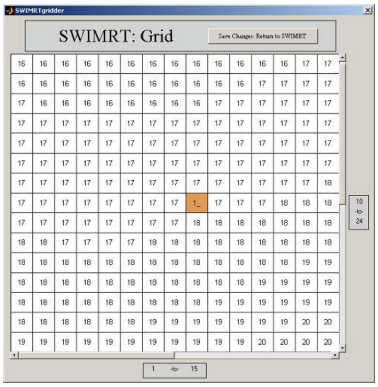

Figure 13 The editable image grid under the subroutine "SWIMRTgridder".

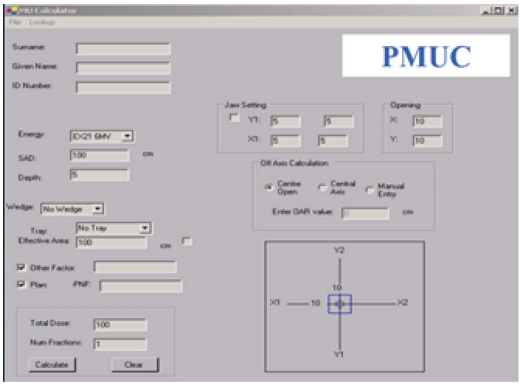

Figure 15 The front-end window of photon beam monitor unit calculator.

generated using the BEAMnrc code from the library or monoenergetic parallel beams (P.R. beam) which does not require pre-calculations. The contour panel is located in the middle left of the GUI to add and edit contour for the region of interest. The isocenter is defined by the isocenter panel at the bottom left of the GUI, and a tool panel is used to navigate the CT images. The "1. Export to Ctcreate", "2. Edit Phantom", "3. Export to DOSXYZ" and "4. Import Dose" are four buttons near the bottom of the GUI. These buttons control the dose calculation using the DOSXYZnrc when activated in numbered sequence.

PMUC

The front-end window of PMUC is shown in Figure 15. The user (therapist, dosimetrist and physicist) just needs to input all beam treatment setup and correction factor options such as beam energy, field size, treatment depth, OAR, selection of wedge (physical or dynamic) and so on. When the "Calculate" button is pressed, the MU calculation starts, and the result with those input parameters are shown.

This MU calculator can build up a full treatment patient MU calculation record and store it to a database. Each patient to be treated has his/her own file of information according to his/her name and patient ID number. The MU calculated from each beam setting was kept within that patient file created by the user. Furthermore, the calculated MU with the input parameters can be printed out both electronically and from a printer. The electronic printout is a graphic file being kept in the Varis Document of the patient database for reference and quality assurance. The hardcopy of the MU record was used as a back-up only.

VALIDATIONS AND IMPLEMENTATIONS

SUPCALC

A superficial X-ray unit (D3150, Gulmay Medical Ltd.), which can produce X-rays from 100 to 150 kVp over a range of mA (0-30 mA), was taken as an example here to demonstrate the implementation (Figures 6-9). However, due to the convenience of the comprehensive database, other superficial units can be adapted to the SUPCALC. Radiation oncologist and physicist can decide which energies should be commissioned and used. The dosimetric information of particular beam energy is easy to store, modify and delete in the database. Physicist only needs to input the specified dosimetric tables such as PSF and OF to the database, and verification can then be done in the commissioning. The predicted and measured dose should be smaller than ± 2%. Since GUI was used and the software had a "help" menu, radiation therapist and dosimetrist would find it easy to use. The training time is therefore greatly reduced.

Table 1 A comparison of predicted doses based on the calculated electron monitor unit by electron monitor unit calculator and measured doses for irregular fields at different electron beam energies, applicators, interpolation methods and source-to-surface distances

Energy (MeV)	Applicator (cm × cm)	SSD (cm)	Measured dose (cGy)	Predicted dose (Poly) (cGy)	Percentage difference (%)	Predicted dose (Exp) (cGy)	Percentage difference (%)
4	10 × 10	100	100.5	101.5	1.04	102.3	1.83
4	15 × 15	100	102.0	103.8	1.79	103.8	1.79
6	10 × 10	100	100.3	101.5	1.16	101.5	1.16
6	15 × 15	100	100.7	101.8	1.08	101.5	0.78
6	15 × 15	105	90.5	91.5	1.12	91.2	0.78
6	15 × 15	110	81.4	82.7	1.58	82.4	1.22
9	10 × 10	100	100.2	101	0.79	100.8	0.59
9	10 × 10	105	89.5	90.8	1.44	90.6	1.22
9	15 × 15	100	100.2	101	0.92	100.5	0.32
9	15 × 15	105	89.8	90.9	1.18	90.3	0.51
9	15 × 15	110	80.8	81.7	1.01	81.7	1.01
12	10 × 10	100	98.7	98.6	-0.11	98.8	0.06
12	10 × 10	105	88.0	88.7	0.85	88.9	1.03
12	10 × 10	110	79.2	80.3	1.29	80.4	1.46
12	15 × 15	100	100.1	100.7	0.56	99.8	-0.29
12	15 × 15	105	89.8	90.6	0.86	89.8	-0.03
16	10 × 10	100	97.6	98.4	0.78	98.6	0.99
16	10 × 10	105	87.3	88.6	1.50	88.8	1.7
16	10 × 10	110	79.1	80.2	1.35	80.3	1.55
16	15 × 15	100	99.7	100.7	0.96	99.9	0.11
16	15 × 15	105	89.5	90.7	1.32	89.9	0.42
16	15 × 15	110	80.8	81.4	0.69	81.35	0.69

SSD: Source-to-surface distance.

EMUC

EMUC is verified by comparison between predicted and measured doses for different beam energies, applicators, interpolation methods and SSDs (Table 1)[2]. In the GUI verification, 100 MU were used for an irregular field with dose at d_m. Farmer-type ionization chamber was used in experimental dosimetry while very small fields were measured using radiographic film. From Table 1, percentage deviations between the predicted and measured doses are within ± 2%, which are acceptable.

SWIMRT

SWIMRT was verified using a clinical fluence map from a prostate patient. The treatment plan was generated using a five-beam IMRT technique. The 6 MV photon beams were used in the treatment. Fluence map of an anterior-posterior beam segment is shown in Figure 16A[3]. The fluence map was exposed on a radiographic film with related machine file generated by SWIMRT. Beam profiles of broken lines in Figure 16 were measured as shown in Figure 16B-E. It can be seen in Figure 16B-E that profiles generated by the step-and-shoot and sliding window algorithm agree well with each other. The small deviation of less than 5% may be due to the uncertainty of the MLC mechanical instability or film dosimetry.

DOSCTP

A comparison of dose distributions from different plans performed by DOSCTP and Pinnacle^3 was carried out. The goal is to demonstrate the ability of DOSCTP to produce the same plan as Pinnacle^3, and also act as a platform for comparing dose calculation algorithms from external TPSs against Monte Carlo simulation. Figure 17A and B display plans produced by DOSCTP and Pinnacle^3, respectively[4]. All dose calculations have been performed with the Collapsed Cone Convolution algorithm in Pinnacle^3[38]. For Monte Carlo simulations, 2 billion histories were used for each plan.

The phantom used in the plan is an inhomogeneous solid phantom with a 0.5 g/cm^3 lung slab of 10 cm thickness located between 5 and 15 cm blocks of water. The isocenter is located at a depth of 12.25 cm in the center of the phantom. Three 6 MV photon beams were used in the plan. They were modeled according to the Varian 21 EX linac in the BEAMnrc. In Pinnacle^3, this was a commissioned built-in source. Beam 1, at zero gantry angle as shown in Figure 17, had a field size of 10 cm × 10 cm, and was assigned a weight of 50%. Beams 2 and 3, with gantry angles of 330° and 30° as shown in Figure 17, respectively, had a field size of 4 cm × 4 cm, each assigned a weight of 25%. This plan demonstrates the ability of DOSCTP to perform multi-beam planning using the DOSXYZnrc code. It can be seen from the figures that DOSCTP is able to produce a plan with similar beam setup and geometry compared to Pinnacle^3. Although the dose distributions are not identical due to the different dose calculation algorithms, the dosimetric comparison shows that DOSCTP can perform well for simple treatment planning.

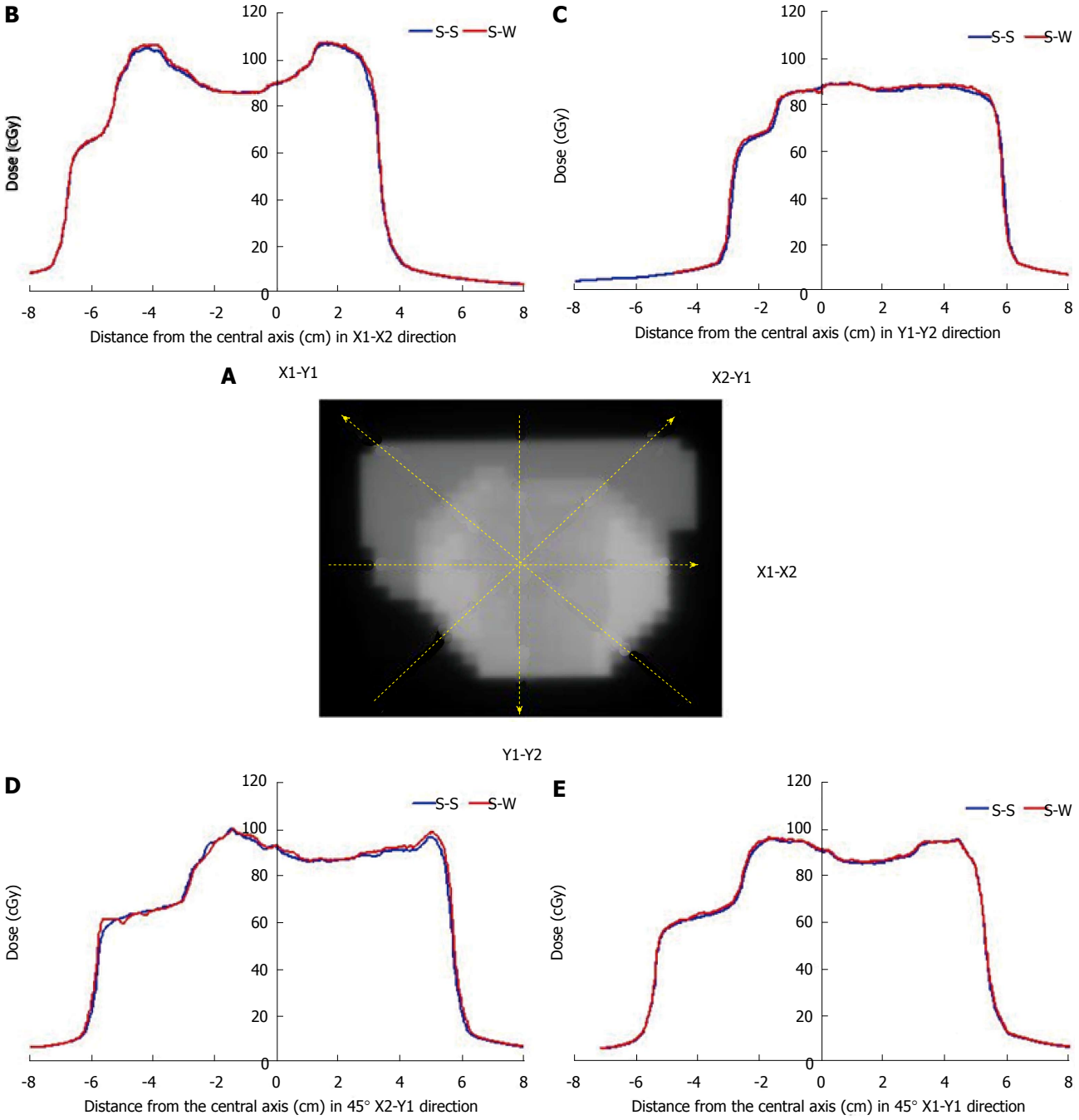

Figure 16 Fluence map of an anterior-posterior beam segment. A: Fluence map for an anterior-posterior segmental beam for the prostate IMRT; B-E: The broken lines represent the beam profiles measured at the X1-X2 (B), Y1-Y2 (C), 45° X2-Y1 (D) and 45° X1-Y1 (E) direction. The blue curve is the profile using the step-and-shoot algorithm (S-S), while the red curve is the profile using the sliding window (S-W) algorithm from Pinnacle[3] and SWIMRT respectively.

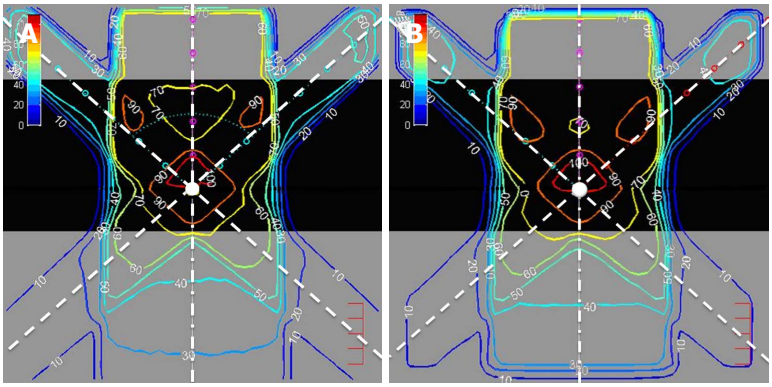

Figure 17 Two dimensional dose distributions of an inhomogeneous solid phantom with lung slab of 0.5 g/cm^3 irradiated by three 6 MV photon beams calculated using DOSCTP (A) and Pinnacle^3 (B).

PMUC

The PMUC was tested with the TTC2000 used in the London Regional Cancer Program (LRCP), London, Canada. The reason is that though the two in-house calculators use different interpolation methods to calculate the MU, they use the same concept in the MU calculation. However, only 6 MV photon beam could be verified because LRCP does not have the 15 MV photon beam information. In this energy, Pinnacle^3 MU calculator with a disabled inhomogeneous correction function was used in the verification.

In the first phase of the test, the same dose ratio and correction factor database of TTC2000 was used by PMUC. In this situation, both of them should give very close calculated MU values because the only difference between the two calculators is the interpolation method. After passing this test, measured PS and CS tables for the 6 MV photon beams were compared to those of TTC2000. The reason is that the structure of the Varian 21C/D linac used in LRCP for TTC2000 is very similar to the Varian 21 EX linac for PMUC. Under the same 6 MV photon beam energy, the PS and CS tables of TTC2000 were very close to PMUC within ± 1%.

CONCLUSION

SUPCALC provides a convenient way for the user to calculate the treatment time and keep record. The database is password protected and it is easy to add or delete treatment beams with the commissioning data. Commissioning of SUPCALC is needed to ensure that the difference between the predicted and prescribed dose is less than ± 2%. It is concluded that SUPCALC can reduce the man-hours and increase the efficiency in the superficial X-ray treatment.

EMUC is developed using a novel sector-integration algorithm for determining the radius of each angular segment in an irregular treatment field. The GUI also used exponential curve fitting method for more accurate data interpolation. Verification results showed that the deviation between the predicted and measured MU is within ± 2%. It is therefore concluded that electron MU calculation can be carried out accurately and effectively using EMUC in electron radiotherapy.

SWIMRT is developed based on the sliding window algorithm. A machine file controlling the MLC console in the linac can be generated by SWIMRT with an import of a fluence map. Sources of the fluence map can be from the TPS or the user. SWIMRT provides a fluence map editor so that the user can edit the imported beam intensity matrix pixel by pixel. The GUI was verified by comparing the fluence maps generated by the TPS using the film dosimetry.

DOSCTP is developed for radiation treatment planning. It is an implementation of Monte Carlo TPS that utilizes the EGSnrc and DOSXYZnrc code to simulate photon and electron transport in a Cartesian volume. Both CT DICOM image datasets and user-created phantoms are supported. DOSCTP provides a GUI to manage the CT image set for the DOSXYZnrc and CTCREATE with a number of features. The GUI can perform Monte Carlo dose calculation for multiple-beam plan. Moreover, the converted 3D Monte Carlo phantom can be edited before simulation. The edited CT image set is compatible to commercial TPSs or CERR[39].

PMUC uses some novel techniques such as a more advanced data interpolation algorism, patient registration system and physical wedge orientation interlock. The dose ratio and correction factor required for the calculation were measured. The accuracy of the calculator was verified, and it gave the calculated MU within ± 1% error range compared to the measurement. It should be noted that as the database of the calculator is based on water tank measurement, PMUC should not be used to calculate MU in inhomogeneous system. However, it is designed for emergency radiation treatment and rough routine MU quality assurance test for the treatment planning.

ACKNOWLEDGMENTS

The author would like to thank Sam Leung, Dr. Grigor Grigorov, Christopher MacGregor, Nuri Yazdani, Michael Leung, Walter Bawa and Jeannie Fung for assisting in these studies. Special thanks to Dr. Rob Barnett and Dr. Ernest Osei of Grand River Hospital, and Dr. David Jaffray of Princess Margaret Cancer Center to support these GUI projects.

REFERENCES

1 **Chow JCL**, Leung S. A graphical user interface for a superficial x-ray treatment time calculator. *Med Phys* 2006; **33**: 2054 [DOI: 10.1118/1.2240922]

2 **Chow JC**, Grigorov GN, MacGregor C. A graphical user interface for an electron monitor unit calculator using a sector-integration algorithm and exponential curve-fitting method. *J Appl Clin Med Phys* 2006; **7**: 52-64 [PMID: 16518317 DOI: 10.1120/jacmp.2027.25371]

3 **Chow JC**, Grigorov GN, Yazdani N. SWIMRT: a graphical user interface using sliding window algorithm to construct a fluence map machine file. *J Appl Clin Med Phys* 2006; **7**: 69-85 [PMID: 17533330 DOI: 10.1120/jacmp.v7i2.2231]

4 **Chow JC**, Leung MK. Treatment planning for a small animal using Monte Carlo simulation. *Med Phys* 2007; **34**: 4810-4817 [PMID: 18196809 DOI: 10.1118/1.2805254]

5 **Ebert MA**, Hoban PW. A model for electron-beam applicator scatter. *Med Phys* 1995; **22**: 1419-1429 [PMID: 8531867 DOI: 10.1118/1.597415]

6 **Khan FM**, Higgins PD, Gerbi BJ, Deibel FC, Sethi A, Mihailidis DN. Calculation of depth dose and dose per monitor unit for irregularly shaped electron fields. *Phys Med Biol* 1998; **43**: 2741-2754 [PMID: 9814514 DOI: 10.1088/0031-9155/43/10/005]

7 **Chen JZ**, VanDyk J, Lewis C, Battista JJ. A two-source model for electron beams: calculation of relative output factors. *Med Phys* 2001; **28**: 1735-1745 [PMID: 11548944 DOI: 10.1118/1.1386423]

8 **Bruinvis IAD**, Mathol WAF. Calculation of electron beam depth-dose curves and output factors for arbitrary field shapes. *Radiother Oncol* 1998; **11**: 395-404 [DOI: 10.1016/0167-8140(88)90211-3]

9 **Garden AS**, Morrison WH, Rosenthal DI, Chao KS, Ang KK. Target

coverage for head and neck cancers treated with IMRT: review of clinical experiences. *Semin Radiat Oncol* 2004; **14**: 103-109 [PMID: 15095256 DOI: 10.1053/j.semradonc.2003.12.004]

10 **Li JS**, Freedman GM, Price R, Wang L, Anderson P, Chen L, Xiong W, Yang J, Pollack A, Ma CM. Clinical implementation of intensity-modulated tangential beam irradiation for breast cancer. *Med Phys* 2004; **31**: 1023-1031 [PMID: 15191288 DOI: 10.1118/1.1690195]

11 **Meier R**, Hatton J, Mehta V. Forward-planning breast IMRT: early clinical experience. *Int J Radiat Oncol Biol Phys* 2003; **57**: S369 [DOI: 10.1016/S0360-3016(03)01279-3]

12 **Boehmer D**, Bohsung J, Eichwurzel I, Moys A, Budach V. Clinical and physical quality assurance for intensity modulated radiotherapy of prostate cancer. *Radiother Oncol* 2004; **71**: 319-325 [PMID: 15172148 DOI: 10.1016/j.radonc.2004.02.016]

13 **Jani AB**, Roeske JC, Rash C. Intensity-modulated radiation therapy for prostate cancer. *Clin Prostate Cancer* 2003; **2**: 98-105 [PMID: 15040870 DOI: 10.3816/CGC.2003.n.016]

14 **Ma CM**, Mok E, Kapur A, Pawlicki T, Findley D, Brain S, Forster K, Boyer AL. Clinical implementation of a Monte Carlo treatment planning system. *Med Phys* 1999; **26**: 2133-2143 [PMID: 10535630 DOI: 10.1118/1.598729]

15 **Convery DJ**, Rosenbloom L. The generation of intensity-modulated fields for conformal radiotherapy by dynamic collimation. *Phys Med Biol* 1991; **37**: 1359-1374 [DOI: 10.1088/0031-9155/37/6/012]

16 **Chui CS**, LoSasso T, Spirou S. Dose calculation for photon beams with intensity modulation generated by dynamic jaw or multileaf collimations. *Med Phys* 1994; **21**: 1237-1244 [DOI: 10.1118/1.597206]

17 **Chang SX**, Cullip TJ, Deschesne KM. Intensity modulation delivery techniques: "step & amp; shoot" MLC auto-sequence versus the use of a modulator. *Med Phys* 2000; **27**: 948-959 [PMID: 10841397 DOI: 10.1118/1.598989]

18 **Xia P**, Verhey LJ. Multileaf collimator leaf sequencing algorithm for intensity modulated beams with multiple static segments. *Med Phys* 1998; **25**: 1424-1434 [DOI: 10.1118/1.598315]

19 **Galvin JM**, Chen XG, Smith RM. Combining multileaf fields to modulate fluence distributions. *Int J Radiat Oncol Biol Phys* 1993; **27**: 697-705 [PMID: 8226167 DOI: 10.1016/0360-3016(93)90399-G]

20 **Nelson WR**, Hirayama H, Rogers DWO. The EGS4 code system 1985 Standford Linear Accelerator Center, Internal Report SLAC 265. CA: Stanford Linear Accelerator Center,1985

21 **Briesmeister JF**. MCNP - A general Monte Carlo N-particle transport code 1993, Version 4A, Los Alamos National Laboratory Report, LA-12625. NM: Los Alamos National Laboratory, 1993

22 **Ma CM**, Reckwerdt P, Holmes M, Rogers DWO, Geiser B. DOSXYZ User Manual 1995, National Research Council of Canada Report No. PIRS-0509B. NRC, Ottawa: ICRU, 1995

23 **Cox LJ**, Schach von Wittenau AE, Bergstrom PM Jr, Mohan R, Libby B, Wu Q, Lovelock DMJ. Photon beam description in REREGRINE for Monte Carlo dose calculations 1997 Lawrence Livermore National Laboratory Internal Report UCRL-JC-126731. USA: Lawrence Livermore National Laboratory, 1995

24 **Ma L**, Boyer AL, Ma CM, Xing L. Synchronizing dynamic multileaf collimators for producing two-dimensional intensity-modulated fields with minimum beam delivery time. *Int J Radiat Oncol Biol Phys* 1999; **44**: 1147-1154 [PMID: 10421549 DOI: 10.1016/S0360-3016(99)00121-2]

25 **Ma L**, Boyer AL, Xing L, Ma CM. An optimized leaf-setting algorithm for beam intensity modulation using dynamic multileaf collimators. *Phys Med Biol* 1998; **43**: 1629-1643 [PMID: 9651030 DOI: 10.1088/0031-9155/43/6/019]

26 **Rogers DWO**, Faddegon BA, Ding GX, Ma CM, Wei J, Mackie TR. BEAM: A Monte Carlo code to simulate radiotherapy treatment units. *Med Phys* 1995: **22**; 503-524 [DOI: 10.1118/1.597552]

27 **Rogers DWO**, Ma CM, Ding GX, Walters B, Sheikh-Bagheri D, Zhang GG. BEAMnrc users manual 2001 NRC Report PIRS 509b (revF). USA: NRC, 2001

28 **Sharma SC**, Johnson MW. Electron beam effective source surface distances for a high energy linear accelerator. *Med Dosim* 1991; **16**: 65-70 [PMID: 1907830]

29 **Roback DM**, Khan FM, Gibbons JP, Sethi A. Effective SSD for electron beams as a function of energy and beam collimation. *Med Phys* 1995; **22**: 2093-2095 [PMID: 8746715 DOI: 10.1118/1.597651]

30 **Cygler J**, Li XA, Ding GX, Lawrence E. Practical approach to electron beam dosimetry at extended SSD. *Phys Med Biol* 1997; **42**: 1505-1514 [PMID: 9279902 DOI: 10.1088/0031-9155/42/8/003]

31 **Almond PR**, Biggs PJ, Coursey BM, Hanson WF, Huq MS, Nath R, Rogers DW. AAPM's TG-51 protocol for clinical reference dosimetry of high-energy photon and electron beams. *Med Phys* 1999; **26**: 1847-1870 [PMID: 10505874 DOI: 10.1118/1.598691]

32 **Hogstrom KR**, Mills MD, Almond PR. Electron beam dose calculations. *Phys Med Biol* 1981; **26**: 445-459 [PMID: 6787621 DOI: 10.1088/0031-9155/26/3/008]

33 **Kamath S**, Sahni S, Palta J, Ranka S. Algorithms for optimal sequencing of dynamic multileaf collimators. *Phys Med Biol* 2004; **49**: 33-54 [PMID: 14971771 DOI: 10.1088/0031-9155/49/1/003]

34 **Dirkx ML**, Heijmen BJ, van Santvoort JP. Leaf trajectory calculation for dynamic multileaf collimation to realize optimized fluence profiles. *Phys Med Biol* 1998; **43**: 1171-1184 [PMID: 9623648 DOI: 10.1088/0031-9155/43/5/009]

35 **Jursinic PA**, Mueller R. A sector-integration method for calculating the output factors of irregularly shaped electron fields. *Med Phys* 1997; **24**: 1765-1769 [PMID: 9394283 DOI: 10.1118/1.597962]

36 **Jones D**, Andre P, Washington JT, Hafermann MD. A method for the assessment of the output of irregularly shaped electron fields. *Br J Radiol* 1990; **63**: 59-64 [PMID: 2106361 DOI: 10.1259/0007-1285-63-745-59]

37 **Khan FM**, Deibel FC, Gerbi BJ, Das IJ. Dosimetry of irregularly shaped electron fields. *Med Phys* 1987; **14**: 473

38 **Ahnesjö A**. Collapsed cone convolution of radiant energy for photon dose calculation in heterogeneous media. *Med Phys* 1989; **16**: 577-592 [PMID: 2770632 DOI: 10.1118/1.596360]

39 **Deasy JO**, Blanco AI, Clark VH. CERR: a computational environment for radiotherapy research. *Med Phys* 2003; **30**: 979-985 [PMID: 12773007 DOI: 10.1118/1.1568978]

P- Reviewer: Cerwenka HR, Chen F, Furka A **S- Editor**: Qiu S
L- Editor: A **E- Editor**: Lu YJ

World Journal of Radiology

Submit a Manuscript: http://www.wjgnet.com/esps/
Help Desk: http://www.wjgnet.com/esps/helpdesk.aspx
DOI: 10.4329/wjr.v8.i3.268

World J Radiol 2016 March 28; 8(3): 268-274
ISSN 1949-8470 (online)

Utility of positron emission tomography-magnetic resonance imaging in musculoskeletal imaging

Ammar A Chaudhry, Maryam Gul, Elaine Gould, Mathew Teng, Kevin Baker, Robert Matthews

Ammar A Chaudhry, Department of Radiology, Johns Hopkins Medicine, Baltimore, MD 21287, United States

Maryam Gul, Department of Rheumatology, National Institute of Arthritis and Musculoskeletal and Skin Diseases, National Institute of Health, Bethesda, MD 20892, United States

Elaine Gould, Mathew Teng, Kevin Baker, Robert Matthews, Department of Radiology, Stony Brook University Hospital, Stony Brook, NY 11794, United States

Author contributions: Chaudhry AA performed majority of the writing; Gul M edited the initial manuscript prior to submission, prepared figures/captions and did literature review for the manuscript; Teng M and Baker K provided input in writing the paper; Gould E (MSK expert) and Matthews R (nuclear medicine expert) had provided the cases and designed the outline and coordinated writing of the paper.

Conflict-of-interest statement: There is no potential conflict of interest. None of the authors in this manuscript received any financial support before or during the production of this manuscript.

Correspondence to: Ammar A Chaudhry, MD, Department of Radiology, Johns Hopkins Medicine, 601 North Wolfe Street, Phipps B-100, Baltimore, MD 21287, United States. achaud23@jhmi.edu
Telephone: +1-646-3881995
Fax: +1-410-6141213

Received: September 15, 2015
Peer-review started: September 17, 2015
First decision: October 30, 2015
Revised: November 16, 2015
Accepted: January 8, 2016

Article in press: January 11, 2016
Published online: March 28, 2016

Abstract

Differentiation between neoplastic and nonneoplastic conditions magnetic resonance imaging (MRI) has established itself as one of the key clinical tools in evaluation of musculoskeletal pathology. However, MRI still has several key limitations which require supplemental information from additional modalities to complete evaluation of various disorders. This has led to the development hybrid positron emission tomography (PET)-MRI which is rapidly evolving to address key clinical questions by using the morphological strengths of MRI and functional information of PET imaging. In this article, we aim to review physical principles and techniques of PET-MRI and discuss clinical utility of functional information obtained from PET imaging and structural information obtained from MRI imaging for the evaluation of musculoskeletal pathology. More specifically, this review highlights the role of PET-MRI in musculoskeletal oncology including initial diagnosis and staging, treatment planning and post-treatment follow-up. Also we will review utility of PET-MRI in evaluating musculoskeletal infections (especially in the immunocompromised and diabetics) and inflammatory condition. Additionally, common pitfalls of PET-MRI will be addressed.

Key words: Magnetic resonance imaging; Osteosarcoma; Positron emission tomography-magnetic resonance imaging; Osteomyelitis; Positron emission tomography-computed tomography; Positron emission tomography; Multiple myeloma; Lymphoma

Core tip: Positron emission tomography-magnetic

resonance imaging is a rapidly emerging technique which provides detailed anatomic and functional imaging simultaneously and allows for differentiation of neoplastic from non-neoplastic conditions. This modality can prove to be both time and cost effective means of evaluating complex cases in patients with coexisting neoplastic, infectious and/or inflammatory conditions. Additional benefits include reducing radiation exposure in patient cohort who is likely to undergo multiple radiologic evaluation over their life time for follow-up.

Chaudhry AA, Gul M, Gould E, Teng M, Baker K, Matthews R. Utility of positron emission tomography-magnetic resonance imaging in musculoskeletal imaging. *World J Radiol* 2016; 8(3): 268-274 Available from: URL: http://www.wjgnet.com/1949-8470/full/v8/i3/268.htm DOI: http://dx.doi.org/10.4329/wjr.v8.i3.268

INTRODUCTION

For the last few decades, magnetic resonance imaging (MRI) has been the "gold standard" for certain aspects of musculoskeletal imaging due to its capability of noninvasively providing high-resolution, high-tissue contrast images of osseous, articular and soft tissue structures[1]. MRI can reliably diagnose structural abnormalities (*e.g.*, meniscal/ligament/tendon tears, occult fractures, myopathy/muscle atrophy, *etc.*)[2] and articular derangements (especially in osteoarthritis, rheumatoid arthritis)[1,2]. More recently, whole-body MRI has shown ability to potentially screen, diagnose and stage musculoskeletal neoplasms (such as multiple myeloma, skeletal and soft tissue sarcomas) and diffuse musculoskeletal processes (*e.g.*, muscular dystrophy, inflammatory myopathies, *etc.*)[1,3].

While MRI is widely considered the best imaging modality to evaluate bone marrow and soft tissue pathology (especially in delineating tissue extent of the lesion), it frequently fails to characterize cortical involvement and evaluate cortex-based lesions (*e.g.*, osteoid osteoma). In such cases, radiographs, computed tomography (CT) and positron emission tomography (PET) often remain preferred modalities[4-6].

Unlike MRI, PET provides biochemical and physiologic information which gives key diagnostic information uncovering pathology using various radiochemical agents. The most common PET imaging agent is ^{18}F-fluorodeoxyglucose (FDG), which is commonly used to assess for glucose metabolism and forms the basis of tumor imaging. FDG is a positron emitter with a half-life of approximately 110 min. FDG is a glucose analog, which is taken up by cells. Once inside the cell, the FDG is phosphorylated and effectively trapped within the cell. Highly metabolic tissues will uptake more glucose in order to sustain their metabolic activity. Most malignant tumors as well as inflammatory processes have a relatively high degree of metabolic activity amongst their cellular background. This forms the basis of PET-FDG imaging. Of note, particular organs a relatively high baseline glucose metabolism will inherently uptake more FDG relative to the remainder of the body. For example, the brain has a normal intense uptake of glucose and will concentrate a significant portion of the injected FDG. Similarly, FDG is concentrated in the urine, and as such, the kidneys, ureters, and bladder will appear hyperintense[1,2,4-9].

Over the last forty years, PET has played a critical role in evaluation of oncologic processes (tumor diagnosis and follow-up), cardiac perfusion imaging and brain perfusion imaging. PET can aid in initial staging and follow up of patients who receive surgery, radiation, or chemotherapy. However, PET has several shortcomings and limitations, with one of the most important being its low spatial resolution[6]. Fusion of PET-acquired images with CT images has allowed radiologists to alleviate some of this spatial resolution limitation. As important as PET-CT has been in evaluation of oncologic diseases, its utility for complete characterization of musculoskeletal disorders (including neoplasms) has not been as extensive, largely due to the comparatively lower soft tissue resolution of CT compared to MRI[1,2]. The advent of PET-MRI therefore provides a potential highly useful imaging modality for musculoskeletal imaging, as it couples the molecular and physiologic information acquired from PET with the unparalleled soft tissue resolution of MRI to provide a superior level of anatomic and functional patient information. Also, two major benefits of utilizing a combined PET-MRI unit include reduction of image acquisition time and misregistration artifacts. Additionally, using PET-MRI over PET-CT has the obvious benefit of substantial reduction of patient ionizing radiation exposure, especially in those who require multiple follow-up examinations[1]. PET-MRI exam radiation dose is approximately 4.6 mSv which is about 20% of an average PET-CT[7,8], a statistic that is particularly important for pediatric patients due to their increased radiation sensitivity[2,7,8].

In this review article, we aim to review clinical utility of PET-MRI in musculoskeletal imaging with emphasis on clinical value in oncologic, inflammatory and infectious processes.

Limitations of PET-MRI

Current MRI technique is limited in evaluation of small pulmonary nodules[4]. Additionally, there are inherent limitation of MRI-based modalities that can preclude imaging of patients with implanted medical devices such as some defibrillators and pacemakers.

PET-MRI AND ONCOLOGIC IMAGING

Staging of neoplasms is one of the key determinants in identifying patient treatment options and determining overall prognosis. TNM staging is the most commonly used system to evaluate extent of neoplastic burden in a patient and is based on tumor size (T), degree/number of lymph node involvement (N) and presence or absence of metastasis (M). Imaging evaluation allows to assess

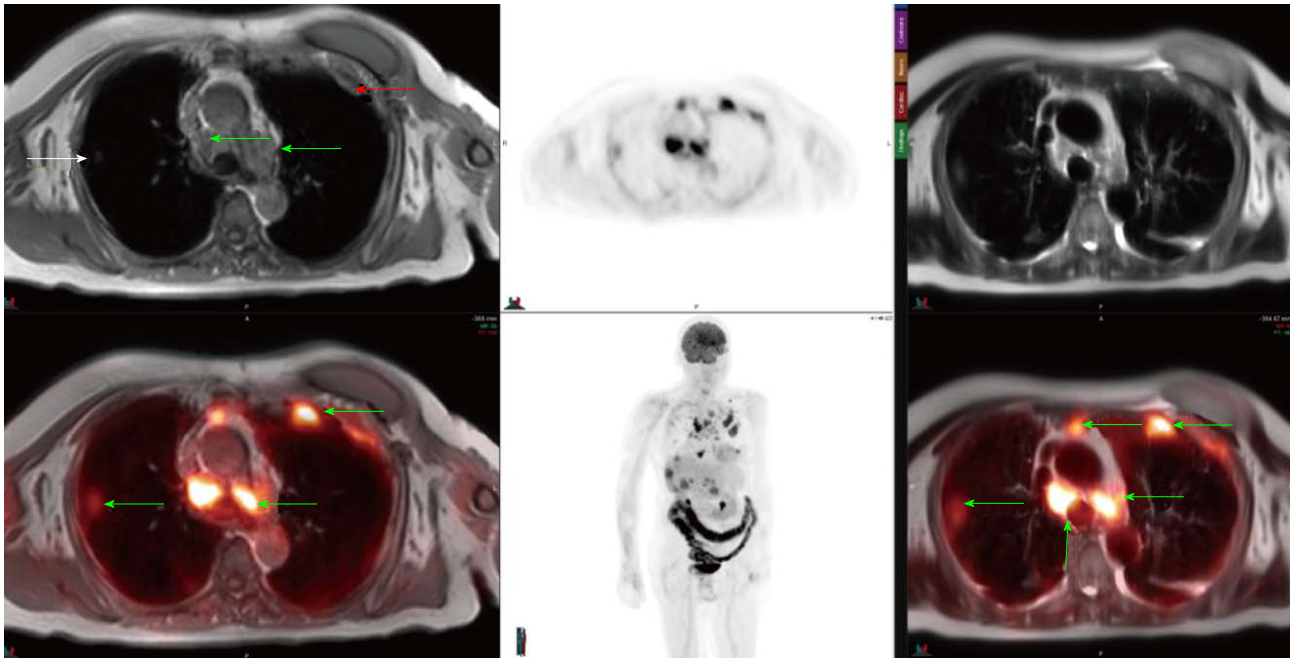

Figure 1 A 65-year-old patient with osteosarcoma underwent positron emission tomography-magnetic resonance imaging for annual follow-up. There were multiple nodular T1 isointense and T2 hyperintense foci (relative to skeletal muscle) noted which demonstrated FDG uptake, compatible with neoplastic activity. Biopsy were positive for metastatic osteosarcoma. FDG: 18F-fluorodeoxyglucose.

for all three of these factors (T, N, M) and therefore diagnostic precision and accuracy are key determinants in developing appropriate treatment plan for the patient. PET-MRI can provide high tissue contrast detail allowing for tumor detection with increased sensitivity (PET) and specificity (MRI)[10].

There are no randomized controlled studies performed using PET-MRI to define standardized uptake value (SUV) cut-off value for discern benign and malignant lesions. Data from prior PET and PET-CT has been used to use very low SUV value of less than 2 to 2.5 as the cut-off threshold value[11]. It should be noted, that though this cut-off value is helpful, it is by no means definitive and therefore, in cases with high index of suspicion where SUV values appear discordant with clinical findings, a tissue biopsy and/or interval follow-up may be warranted for a more definitive diagnosis.

Sarcomas

Approximately 2% of all cancer related deaths are due to sarcomas (soft tissue and osseous) which account for less than 1% of all cancers and carry overall five-year survival of 60%[6]. MRI is the initial modality of choice for evaluation of sarcomas and contrast-enhanced MRI can provide fairly accurate assessment of sarcomas. However, occasionally it is difficult to discriminate between infiltrative tumor *vs* edema on both initial and follow-up evaluations, and it is also sometimes challenging to discern post-surgical change from tumor recurrence. Our initial clinical experience with PET-MRI using the SUV obtained from PET in conjunction with soft tissue detail of MRI to help discern neoplastic from non-neoplastic tissue has yielded a fair amount of cases which would previously have been equivocal and prompted tissue biopsy to exclude tumor recurrence (Figures 1 and 2).

Whole-body PET-MRI allows for simultaneous loco-regional examination and whole-body evaluation for distant disease[1,2,4-6]. PET-MRI is especially helpful in overcoming PET-CT limitations of evaluation of disease in organs with high background PET activity such as the brain, liver, kidney and spinal canal[1,5,6].

The most common PET imaging agent is FDG, which is commonly used to assess for glucose metabolism and forms the basis of tumor imaging. FDG is a positron emitter with a half-life of approximately 110 min. FDG is a glucose analog, which is taken up by cells. Once inside the cell, the FDG is phosphorylated and effectively trapped within the cell. Highly metabolic tissues will uptake more glucose in order to sustain their metabolic activity. Most malignant tumors as well as inflammatory processes have a relatively high degree of metabolic activity amongst their cellular background. This forms the basis of PET-FDG imaging. Of note, particular organs a relatively high baseline glucose metabolism will inherently uptake more FDG relative to the remainder of the body. For example, the brain has a normal intense uptake of glucose and will concentrate a significant portion of the injected FDG. Similarly, FDG is concentrated in the urine, and as such, the kidneys, ureters, and bladder will appear hyperintense[1,2,5-8,12].

PET-FDG has proven itself to be the standard radiotracer for PET imaging, given its significant versatility for both pretreatment and follow-up clinical situations. Most other

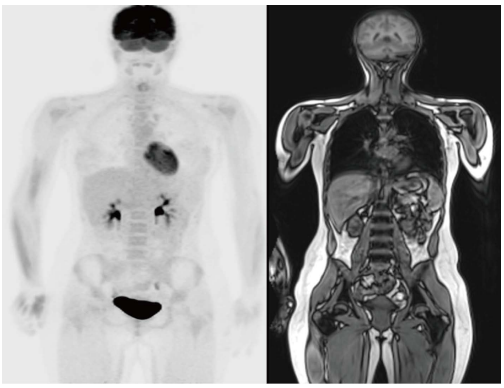

Figure 2 A 17-year-old male with history of Ewing sarcoma underwent follow up whole body positron emission tomography-magnetic resonance imaging which did not reveal any focal abnormal ^{18}F-fluorodeoxyglucose uptake nor was there any focal abnormal marrow signal within the imaged musculoskeletal system to suggest recurrence.

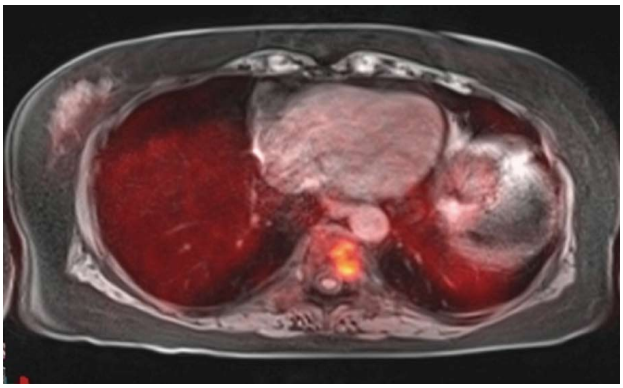

Figure 3 A 63-year-old female with renal failure and abnormal serum protein electrophoresis. Positron emission tomography-magnetic resonance imaging revealed focal abnormal heterogeneously T1 hypointense and T2 hyperintense lesion with corresponding increased FDG uptake. Lesion biopsy was positive for multiple myeloma. FDG: ^{18}F-fluorodeoxyglucose.

radiotracers in practice have been developed for non-MSK purposes, including myocardial perfusion imaging (for example, Rubidium-82, Nitrogen-13 ammonia)[4] or for brain perfusion imaging (for example, Oxygen-15 water)[9]. Several other radiotracers are still under investigation, including ^{11}C-choline, which has yielded encouraging results in providing more accurate lymph node involvement (N-staging) when used in conjunction with diffusion weighted imaging (DWI) or short-tau inversion recover (STIR) sequences. There are other investigational radiotracers are currently under study for tumor characterization, such as ^{18}F-fluoromisonidazole (FMISO), which is a marker for tumor hypoxia. Many of these emerging radiotracers are still under investigation[13].

The ability to calculate the change of PET agent uptake between initial and follow-up exams can provide information on treatment response, which is especially important in patients who receive adjuvant therapy where tumor size does not change and MRI alone would have otherwise failed to discern positive or negative treatment response[5]. It should be noted, however, that randomized controlled studies are required to assess for overall impact of PET-MRI based staging on overall survival.

MULTIPLE MYELOMA

As with sarcoma, precise staging on initial and follow-up treatment is critical to patient care. PET-CT can provide valuable information on focal lesional activity which correlates with disease activity[10,11,14]. However, unlike PET-CT, whole-body MRI is superior to more accurately characterize extent of bone marrow involvement in myeloma[15] especially in small lesions that are not well characterized on PET-CT[10,15-17]. Shortt *et al*[15] showed that combination of data acquired from PET and whole-body MRI can improved specificity and positive predictive value. Our initial anecdotal experience with PET-MRI suggests myeloma lesions to be T1-hypointense with variable degree of contrast enhancement and SUV uptake (Figure 3).

OSSEOUS METASTASIS

PET, PET-CT and MRI are all used in various clinical settings for evaluation of osseous metastasis, with each modality offering high sensitivity with variable degrees of specificity. The major shortcoming of PET and PET-CT are their higher number of false positives and lower positive predictive value due to suboptimal soft tissue resolution. Additionally, PET and PET-CT yield higher rates of false positives for lesions that are 5 mm or smaller[12]. MRI, especially with diffusion weighted imaging, provides precise pre-treatment evaluation, but this information following adjuvant treatment is less sensitive and specific. In such instances, PET-MRI can help provide the superior MRI tissue contrast detailing anatomic extent of disease while PET helps discern presence or absence of treatment response based on changes in neoplasm metabolic activity (Figures 4 and 5)[12].

LYMPHOMA

PET-CT has solidified itself as the imaging modality of choice for initial staging, monitoring of treatment response and follow-up of patients with lymphoma[12]. PET-CT can detect lymphoma with 90% sensitivity and 91% specificity, although overall positive predictive value is low especially for disease progression[12]. Increasing number of false positive PET-CT results has been noted in patients on rituximab[12]. MRI, to a certain extent, can provide information about changes in cellular content of lesions (*e.g.*, on DWI and MRI spectroscopy), and the combination of MRI information with PET has shown promising results in initial studies[12,18]. Additionally, PET-MRI can be used in evaluating patients for post-treatment changes (*e.g.*, thymic hyperplasia, nodal necrosis, *etc.*) in addition to the standard changes in SUV values seen on PET and PET-CT[12,19].

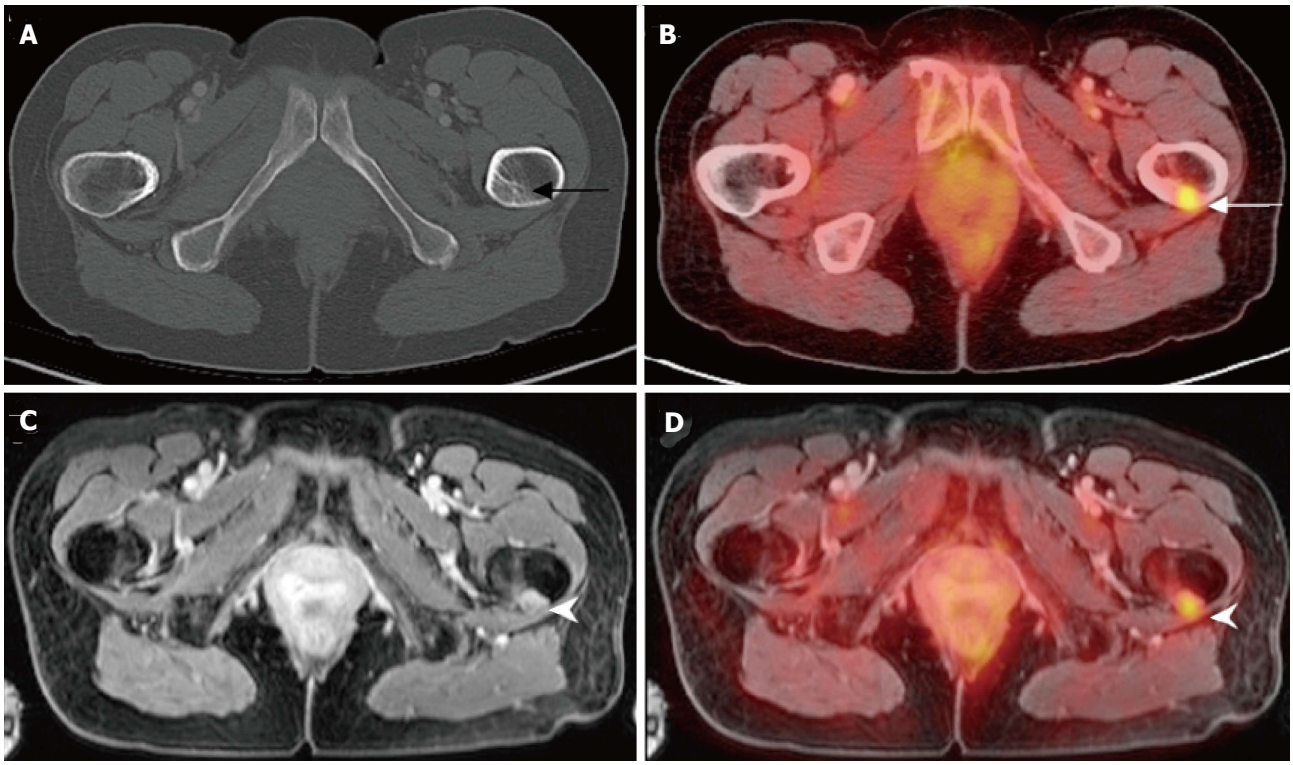

Figure 4 A 59-year-old female with history of breast cancer status post resection and chemoradiation presents with left hip pain. Noncontrast CT of the pelvis (A) was unremarkable. PET/CT revealed increased focus of FDG uptake within the proximal left femur. Contrast-enhanced pelvic MRI (C) and PET-MRI (D) acquired simultaneously demonstrates abnormal nodular soft tissue mass within the proximal left femoral cortex with increased radiotracer uptake compatible with metastasis in this patient with breast carcinoma. PET: Positron emission tomography; MRI: Magnetic resonance imaging; CT: Computed tomography; FDG: ^{18}F-fluorodeoxyglucose.

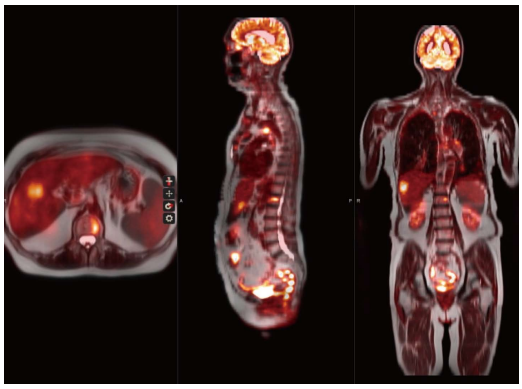

Figure 5 A 66-year-old female with history of breast cancer status post resection and chemoradiation presents with chest pain. Whole-body PET-MRI reveal multiple abnormal nodular soft tissue masses within the lungs, mediastinum, ribs, liver and lumbar spine with increased FDG uptake consistent with metastasis in this patient with breast carcinoma. PET: Positron emission tomography; MRI: Magnetic resonance imaging; FDG: ^{18}F-fluorodeoxyglucose.

POST-TREATMENT FOLLOW-UP

Clinical response to therapy (including chemotherapy, radiotherapy, surgery) as evaluated on imaging can provide prognostic information of disease-free survival especially in patients being evaluated for sarcomas[12]. At present, for most oncologic diseases, functional information derived from PET-based imaging units (PET and PET-CT) provides this information with the notion that change in radiotracer uptake is theorized to directly correlate with treatment response, so that decreased radiotracer uptake on PET is indicative of positive treatment response and conversely increased PET uptake is indicative of an insufficient or lack of a treatment response[12]. In the post-surgical setting, however, this is less true, as a reparative response can generate a variable degree of radiotracer uptake in the surgical bed with SUV of greater than 2.5. This is further complicated by distortion of normal anatomy in post-surgical cases where the lack of distinction between neoplasm and edema makes definitive diagnosis enigmatic. In such scenarios, multisequence MRI (including DWI, spectroscopy, *etc*.) along with PET information can improve specificity of findings[12].

Non-neoplastic conditions

PET and PET-CT studies have shown that radiotracer uptake can be seen in non-neoplastic conditions including infectious and inflammatory conditions. Generally speaking, SUV of less than 2.5 has been used as a rule-of-thumb to suggest non-neoplastic conditions. However, many infectious processes and inflammatory conditions can cause SUV values of greater than 2.5. Therefore, as always, correlation with clinical history is imperative for optimal interpretation of PET, PET-CT and PET-MRI. PET-CT has a limited role with conditions such as Charcot arthropathy or organ system disorders (*i.e.*, CNS, liver,

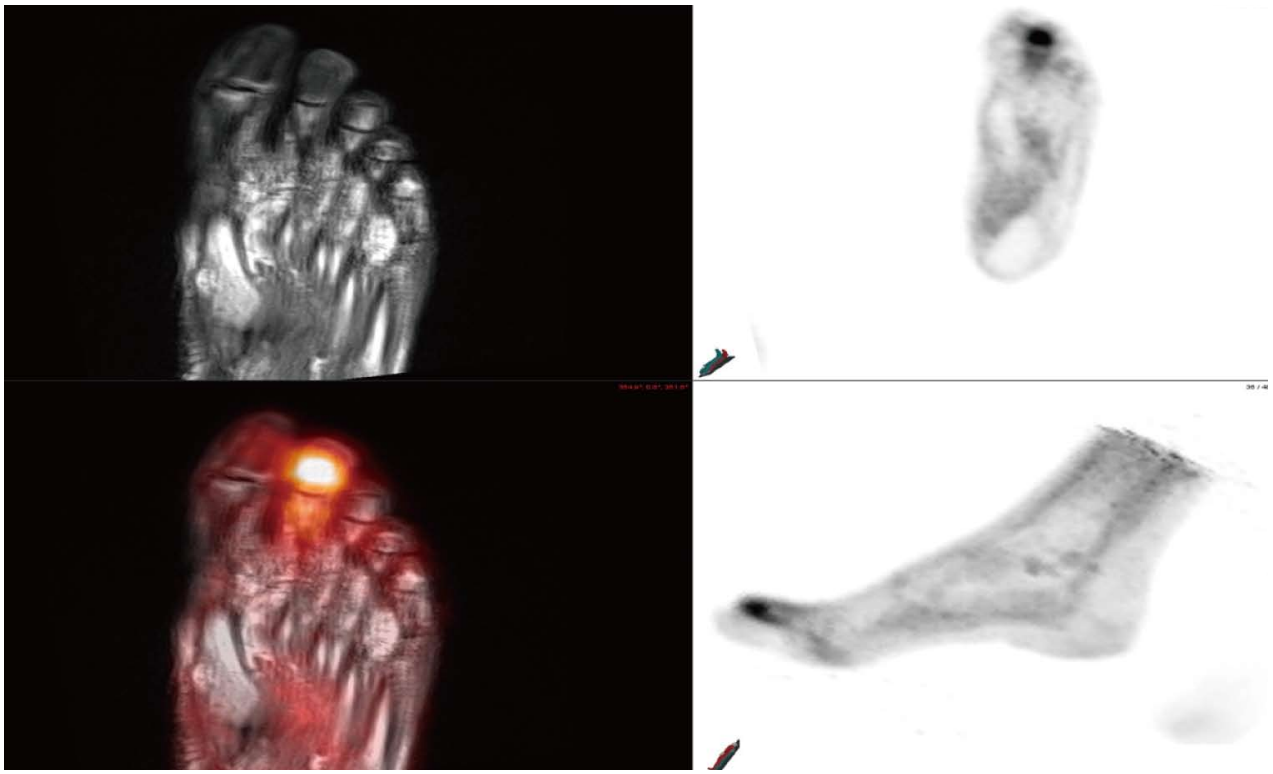

Figure 6 A 71-year-old male with poorly controlled diabetes and end-stage renal disease presents with worsening right foot pain. Bone scan revealed diffuse radiotracer uptake within the right foot without focal abnormality. MRI of the right foot demonstrate diffuse abnormal T1 and T2 signal within the right foot digits. Multiplanar PET-MRI images reveal focal FDG uptake within the distal right second digit with corresponding heterogeneous T1 hypointense, T2 hyperintense signal compatible with osteomyelitis. PET: Positron emission tomography; MRI: Magnetic resonance imaging; FDG: 18F-fluorodeoxyglucose.

spleen) where CT cannot provide the soft tissue contrast needed to fully characterize the clinical process[1,12], and our initial experience with PET-MRI has shown its advantage to PET-CT for the evaluation osteomyelitis in patients with Charcot arthropathy with better diagnostic yield (Figure 6).

PET-MRI imaging safety

Caution must be used when administering gadolinium-based contrast for MRI in patients. Nephrogenic system fibrosis (NSF) is a rare but serious disease of fibrosis of the skin and organs that may develop in patients with poor renal function and a low glomerular filtration rate (GFR). Additionally, care should also be taken for patients who require multiple follow-up contrast-enhanced MRI studies. A recent FDA report in July 2015 demonstrated potential gadolinium deposits in the brain. This is of uncertain clinical significance, however, referring clinicians should be aware of this fact. However, reducing the contrast need may be one the potential unseen benefits of PET-MRI; the inherent improved soft tissue resolution with the combined PET-tumor characterization may obviate the need for contrast in certain clinical situations[20].

CONCLUSION

Although data on PET-MRI utility is limited at present, emerging studies demonstrate positive application of this hybrid modality, especially in oncologic diagnosis and follow-up. PET-MRI provides detailed anatomic (MRI) and functional (PET) information which shows promise in improving sensitivity and specificity, which will facilitate a more accurate and reliable TNM-staging of various primary and secondary musculoskeletal neoplasms as these conditions require diagnostic modalities with high tissue contrast and resolution for accurate diagnosis. There also is the added benefit of substantially reduced patient radiation exposure. Larger studies are required to evaluate the overall impact on patient survival, which serves as the clinical benchmark for all diagnostic and therapeutic interventions. In addition to accuracy, cost-benefit analyses comparing PET-CT and PET-MRI are required, which should factor in both monetary and health-risk (*i.e.*, radiation exposure) cost.

REFERENCES

1 **Disselhorst JA**, Bezrukov I, Kolb A, Parl C, Pichler BJ. Principles of PET/MR Imaging. *J Nucl Med* 2014; **55**: 2S-10S [PMID: 24819419 DOI: 10.2967/jnumed.113.129098]

2 **Werner MK**, Schmidt H, Schwenzer NF. MR/PET: a new challenge in hybrid imaging. *AJR Am J Roentgenol* 2012; **199**: 272-277 [PMID: 22826387 DOI: 10.2214/AJR.12.8724]

3 **Chatal JF**, Rouzet F, Haddad F, Bourdeau C, Mathieu C, Le Guludec D. Story of Rubidium-82 and Advantages for Myocardial Perfusion PET Imaging. *Front Med* (Lausanne) 2015; **2**: 65 [PMID: 26442267 DOI: 10.3389/fmed.2015.00065]

4 **National Cancer Institute**. Cancer staging: TNM staging. Available from: URL: http://www.cancer.gov/about-cancer/diagnosis-staging/staging/staging-fact-sheet#q3
5 **Partovi S**, Kohan AA, Zipp L, Faulhaber P, Kosmas C, Ros PR, Robbin MR. Hybrid PET/MR imaging in two sarcoma patients - clinical benefits and implications for future trials. *Int J Clin Exp Med* 2014; **7**: 640-648 [PMID: 24753758]
6 **Fahey FH**, Treves ST, Adelstein SJ. Minimizing and communicating radiation risk in pediatric nuclear medicine. *J Nucl Med Technol* 2012; **40**: 13-24 [PMID: 22393223 DOI: 10.2967/jnumed.109.069609]
7 **Hirsch FW**, Sattler B, Sorge I, Kurch L, Viehweger A, Ritter L, Werner P, Jochimsen T, Barthel H, Bierbach U, Till H, Sabri O, Kluge R. PET/MR in children. Initial clinical experience in paediatric oncology using an integrated PET/MR scanner. *Pediatr Radiol* 2013; **43**: 860-875 [PMID: 23306377]
8 **Chawla SC**, Federman N, Zhang D, Nagata K, Nuthakki S, McNitt-Gray M, Boechat MI. Estimated cumulative radiation dose from PET/CT in children with malignancies: a 5-year retrospective review. *Pediatr Radiol* 2010; **40**: 681-686 [PMID: 19967534]
9 **Watabe T**, Shimosegawa E, Kato H, Isohashi K, Ishibashi M, Tatsumi M, Kitagawa K, Fujinaka T, Yoshimine T, Hatazawa J. Paradoxical reduction of cerebral blood flow after acetazolamide loading: a hemodynamic and metabolic study with (15)O PET. *Neurosci Bull* 2014; **30**: 845-856 [PMID: 25096497]
10 **Breyer RJ**, Mulligan ME, Smith SE, Line BR, Badros AZ. Comparison of imaging with FDG PET/CT with other imaging modalities in myeloma. *Skeletal Radiol* 2006; **35**: 632-640 [PMID: 16758246]
11 **Durie BG**, Waxman AD, D'Agnolo A, Williams CM. Whole-body (18)F-FDG PET identifies high-risk myeloma. *J Nucl Med* 2002; **43**: 1457-1463 [PMID: 12411548]
12 **Lee IS**, Jin YH, Hong SH, Yang SO. Musculoskeletal applications of PET/MR. *Semin Musculoskelet Radiol* 2014; **18**: 203-216 [PMID: 24715451]
13 **Jennings M**, Marcu LG, Bezak E. PET-specific parameters and radiotracers in theoretical tumour modelling. *Comput Math Methods Med* 2015; **2015**: 415923 [PMID: 25788973 DOI: 10.1155/2015/415923]
14 **Schirrmeister H**, Bommer M, Buck AK, Müller S, Messer P, Bunjes D, Döhner H, Bergmann L, Reske SN. Initial results in the assessment of multiple myeloma using 18F-FDG PET. *Eur J Nucl Med Mol Imaging* 2002; **29**: 361-366 [PMID: 12002711]
15 **Shortt CP**, Gleeson TG, Breen KA, McHugh J, O'Connell MJ, O'Gorman PJ, Eustace SJ. Whole-Body MRI versus PET in assessment of multiple myeloma disease activity. *AJR Am J Roentgenol* 2009; **192**: 980-986 [PMID: 19304704]
16 **Bredella MA**, Steinbach L, Caputo G, Segall G, Hawkins R. Value of FDG PET in the assessment of patients with multiple myeloma. *AJR Am J Roentgenol* 2005; **184**: 1199-1204 [PMID: 15788594]
17 **Lecouvet FE**, Dechambre S, Malghem J, Ferrant A, Vande Berg BC, Maldague B. Bone marrow transplantation in patients with multiple myeloma: prognostic significance of MR imaging. *AJR Am J Roentgenol* 2001; **176**: 91-96 [PMID: 11133544]
18 **Lin C**, Itti E, Luciani A, Zegai B, Lin SJ, Kuhnowski F, Pigneur F, Gaillard I, Paone G, Meignan M, Haioun C, Rahmouni A. Whole-body diffusion-weighted imaging with apparent diffusion coefficient mapping for treatment response assessment in patients with diffuse large B-cell lymphoma: pilot study. *Invest Radiol* 2011; **46**: 341-349 [PMID: 21263330]
19 **Inaoka T**, Takahashi K, Mineta M, Yamada T, Shuke N, Okizaki A, Nagasawa K, Sugimori H, Aburano T. Thymic hyperplasia and thymus gland tumors: differentiation with chemical shift MR imaging. *Radiology* 2007; **243**: 869-876 [PMID: 17463136]
20 **FDA Drug Safety Communication**. FDA evaluating the risk of brain deposits with repeated use of gadolinium-based contrast agents for magnetic resonance imaging (MRI). Available from: URL: http://www.fda.gov/Drugs/DrugSafety/ucm455386.htm

P- Reviewer: Morbelli SD, Schoenhagen P **S- Editor**: Ji FF
L- Editor: A **E- Editor**: Lu YJ

World Journal of Radiology

Submit a Manuscript: http://www.wjgnet.com/esps/
Help Desk: http://www.wjgnet.com/esps/helpdesk.aspx
DOI: 10.4329/wjr.v8.i3.275

World J Radiol 2016 March 28; 8(3): 275-280
ISSN 1949-8470 (online)

MINIREVIEWS

Endovascular treatment of aortoiliac aneurysms: From intentional occlusion of the internal iliac artery to branch iliac stent graft

Stevo Duvnjak

Stevo Duvnjak, Department of Radiology, Division of Interventional Radiology, Odense University Hospital, C 5000 Odense, Denmark

Author contributions: Duvnjak S designed and wrote the entire manuscript.

Conflict-of-interest statement: There are no potential conflicts of interest.

Correspondence to: Stevo Duvnjak, MD, EBIR, Department of Radiology, Division of Interventional Radiology, Odense University Hospital, Sdr. Boulevard 29, C 5000 Odense, Denmark. duvnjak.stevo@gmail.com
Telephone: +45-513-08867

Received: August 8, 2015
Peer-review started: August 11, 2015
First decision: October 16, 2015
Revised: October 23, 2015
Accepted: December 29, 2015
Article in press: January 4, 2016
Published online: March 28, 2016

Abstract

Approximately 20%-40% of patients with abdominal aortic aneurysms can have unilateral or bilateral iliac artery aneurysms and/or ectasia. This influences and compromises the distal sealing zone during endovascular aneurysm repair. There are a few endovascular techniques that are used to treat these types of aneurysms, including intentional occlusion/over-stenting of the internal iliac artery on one or both sides, the "bell-bottom" technique, and the more recent method of using an iliac branch stent graft. In some cases, other options include the "snorkel and sandwich" technique and hybrid interventions. Pelvic ischemia, represented as buttock claudication, has been reported in 16%-55% of cases; this is followed by impotence, which has been described in 10%-17% of cases following internal iliac artery occlusion. The bell-bottom technique can be used for a common iliac artery up to 24 mm in diameter given that the largest diameter of the stent graft is 28 mm. There is a paucity of data and evidence regarding the "snorkel and sandwich" technique, which can be used in a few clinical scenarios. The hybrid intervention is comprised of a surgical operation, and is not purely endovascular. The newest branch stent graft technology enables preservation of the anterograde flow of important side branches. Technical success with the newest technique ranges from 85%-96.3%, and in some small series, technical success is 100%. Buttock claudication was reported in up to 4% of patients treated with a branch stent graft at 5-year follow-up. Mid- and short-term follow-up results showed branch patency of up to 88% during the 5-6-year period. Furthermore, branch graft occlusion is a potential complication, and it has been described to occur in 1.2%-11% of cases. Iliac branch stent graft placement represents a further development in endovascular medicine, and it has a high technical success rate without serious complications.

Key words: Aortoiliac artery aneurysm; Branch iliac stent graft; Stent graft; Endovascular aneurysm repair; Angiography

Core tip: There are a few endovascular techniques that have been used to treat aortoiliac artery aneurysms in cases where the distal landing zone is challenging;

these include intentional occlusion/over-stenting of the internal iliac artery on one or both sides to create a distal landing zone in the external iliac artery, the "bell-bottom" technique, the "snorkel and sandwich" technique, and the more recent treatment of using an iliac branch stent graft. This review describes the pros and cons of these different endovascular techniques, while paying particular attention to the latest developments in branch stent graft technology.

Duvnjak S. Endovascular treatment of aortoiliac aneurysms: From intentional occlusion of the internal iliac artery to branch iliac stent graft. *World J Radiol* 2016; 8(3): 275-280 Available from: URL: http://www.wjgnet.com/1949-8470/full/v8/i3/275.htm DOI: http://dx.doi.org/10.4329/wjr.v8.i3.275

INTRODUCTION

Approximately 20%-40% of patients with abdominal aortic aneurysms (AAA) can have unilateral or bilateral iliac artery aneurysms and/or ectasia[1,2]. This influences and compromises the distal sealing zone during endovascular aneurysm repair (EVAR). There are a few endovascular techniques that can be used to treat these types of aneurysms, such as intentional occlusion/over-stenting of the internal iliac artery on one or both sides to create a distal landing zone in the external iliac artery, as well as the "bell-bottom" technique. There is a paucity of data and evidence for the "snorkel and sandwich" technique, which can be useful in a few clinical scenarios[3]. The most recent endovascular technique features treatment with an iliac branch stent graft. This review discusses the currently available endovascular techniques, and it outlines the pros and cons of each method, while paying particular attention to the branch iliac stent graft.

Occlusion of the internal iliac artery

The occlusion of one or both internal iliac arteries, usually with coils and/or an Amplatz plug to create an optimal distal landing zone during EVAR, represents the longest established technique. While there is good long-term follow-up evidence regarding endoleak and the technique's high technical success[4], this procedure can have significant negative effects on a patient's quality of life. The major problem associated with unilateral and/or bilateral internal iliac artery occlusion is buttock claudication, which can disappear with time, but is unpredictable[5]. The available literature describes buttock claudication in 16%-55% of cases, followed by impotence in 10%-17% of cases after embolization of the internal iliac arteries[6,7]. Additionally, rare serious complications, such as spinal and bowel ischemia, may occur in up to 1%-3% of bilateral internal iliac artery occlusion cases, and gluteus necrosis may also occur[8]. There is no general consensus regarding the use of either sequential or staged embolization of both internal iliac arteries, but in a majority of centres where both internal iliac arteries should be embolized, the staged strategy is most common[9]. Proximal embolization of the internal iliac artery is strongly advised to allow for collateral circulation[10]. Generally, the intention should be to maintain the patency of at least one internal iliac artery, and factors such as the patient's age, activity level, cardiac status, and possible future thoracic abdominal aortic interventions should be analysed throughout the treatment decision-making process.

"Bell-bottom" technique

The other endovascular technique used to treat a "hostile" distal landing zone is the bell-bottom technique. This technique is relatively simple (Figure 1) but it can be used in an iliac artery of up to 24 mm in diameter given that the largest diameter of the stent graft is 28 mm. Attention should be paid to the quality of the distal landing zone, as well as the assessment of calcification, thrombus, and the length of the distal landing zone. During long-term follow-up, the "bell-bottom" technique has shown increased frequency of the need for a secondary intervention, mainly due to the progression of artery dilatation, and also based on migration of the stent graft[11].

"Snorkel/chimney and sandwich/parallel" technique

The use of a parallel stent graft to maintain an open internal iliac artery was first described by Lobato. He suggests that creating an overlap between the internal iliac artery stent and external iliac artery stent of at least 5 cm can minimize possible endoleak within the gutters of both stent grafts[12]. This technique offers the potential to treat more patients when compared with other endovascular techniques. Lobato described achieving a good result with this technique; however, there is sparse literature available on this method. Transbrachial and/or axillary (unilateral or bilateral) access are necessary for placement of the stent graft. The other problems associated with the sandwich parallel stent graft include the fact that the two grafts can compress each other, increasing the risk for thrombosis, further manipulation in the aortic arch during placement of the stent graft, increasing the risk for cerebral embolization; and the stent graft is generally longer when compared with branch stent graft technology.

The snorkel or chimney technique has been primarily used to treat pararenal AAA and thoracoabdominal aneurysms in acute settings with promising initial results[13,14]. This procedure can also be used as a bailout intervention following unintentional covering of important side branch, or in the treatment of, endoleak type 1 after EVAR in selected cases[15]. The first published report of the snorkel technique was described by Greenberg *et al*[16] in 2003. There are various articles that describe high technical success, good mid-term follow-up, and patency of the snorkel/chimney stent graft in the treatment of thoracoabdominal aneurysms in selected patients[17]. However, problems associated with endoleak and missing

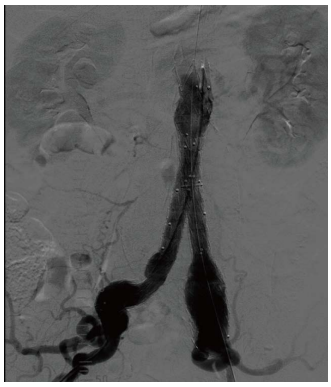

Figure 1 A 73-year-old patient with abdominal aortic aneurysm and bilateral common iliac artery aneurysm treated with flared limb ("Bell-Bottom" technique).

Figure 2 Zenith branch iliac stent grafts. Straight-side iliac branch device.

long-term follow-up are still limiting factors. Furthermore, the periscope technique was developed as a modification of the snorkel technique; for this procedure, the stent graft is placed transfemorally, is distally orientated, and is used to facilitate retrograde flow through the artery. It is important to note that the majority of patients treated with the snorkel and/or periscope technique are thoracoabdominal aneurysm cases, not aortoiliac aneurysm cases, with internal iliac artery preservation.

Finally, the iliac artery's tortuosity and problems associated with placement and force on the placed stent graft are the main constraints of this technique in the treatment of aortoiliac aneurysms. There are some other innovative treatment options, such as the crossover chimney technique, that can preserve the internal iliac artery as well[18].

HYBRID INTERVENTION

Internal iliac artery bypass or transposition, combined with either aortouniiliac or bifurcated stent graft placement, is one option that can be used to maintain pelvic circulation with good patency[19]. However, providing a more detailed description and analysis of this technique is beyond the scope of this work.

BRANCH ILIAC STENT GRAFT

The newest branch stent graft technology expands upon the endovascular treatment of aortoiliac aneurysms, while maintaining and preserving the anterograde flow of important side branches. There are a few devices currently on the market (Zenith Cook, Bloomington, IN, United States; JOTEC E-iliac stent graft, JOTEC GmbH, Hechingen, Germany; and Gore Excluder iliac branch stent graft, GORE and Associates, Newark, DE, United States). The majority of the available literature features the Cook Zenith iliac branch device (IBD). There are three different IBD devices: The straight-side IBD (S-IBD) (Figure 2), the helical-side IBD (H-IBD), and the bifurcated-bifurcated IBD (BB-IBD). The difference between the S-IBD and H-IBD lies in the overlapping zone; in the first option, a balloon-expandable stent graft is used, and in H-IBD, a self-expandable stent is used given its longer overlapping zone. Furthermore, H-IBD performs better in cases of a tortuous internal iliac artery. Both stent grafts feature a 20 French (Fr) delivery system with a preloaded catheter. The preloaded catheter allows for guide wire placement, which is snared from the contralateral side and/or *via* brachial access, and it provides a path through which to place the bridge stent graft. The S-IBD, which is the device that is most frequently reported in the literature, is a second-generation, modular, two-branch vessel device that consists of a main iliac limb and features an additional reinforced stump for the internal iliac artery side branch. The proximal segment of the IBD has a diameter of 12 mm, and the distal segment can be 10 mm or 12 mm in diameter. The common iliac segment can be 45 mm or 61 mm in length, while the external iliac artery segment is either 41 mm or 58 mm in length. Briefly bilateral femoral artery exposure or percutaneous access is used during the intervention. The S-IBD is orientated and partially deployed above the internal iliac artery with the help of four markers. The 12 Fr sheath is placed in the contralateral femoral artery after the long guide wire is snared. Once the S-IBD is in the desired position, the side arm is exposed, and the sheath is withdrawn. The 12 Fr sheath advances from the contralateral side over the aortic bifurcation into the side branch. The 5 Fr sheath and/or diagnostic catheter are placed following puncture of the valve of the 12 Fr sheath, and selective catheterisation of the internal iliac artery is performed. Once selective catheterisation of the internal iliac artery guide wire is complete, the wire is usually exchanged for a stiffer stainless steel guide wire; when this is achieved, the stent graft is deployed in a standard manner. The main bifurcated stent graft is usually placed *via* the opposite site to the S-IBD. The most recent development in this treatment modality is the BB-IBD device, which represents a combination of H-IBD and the bifurcated distal component of a fenestrated device[20].

Indications and anatomical constraints for using the iliac branch stent graft

Generally, the indication for AAA treatment is a large

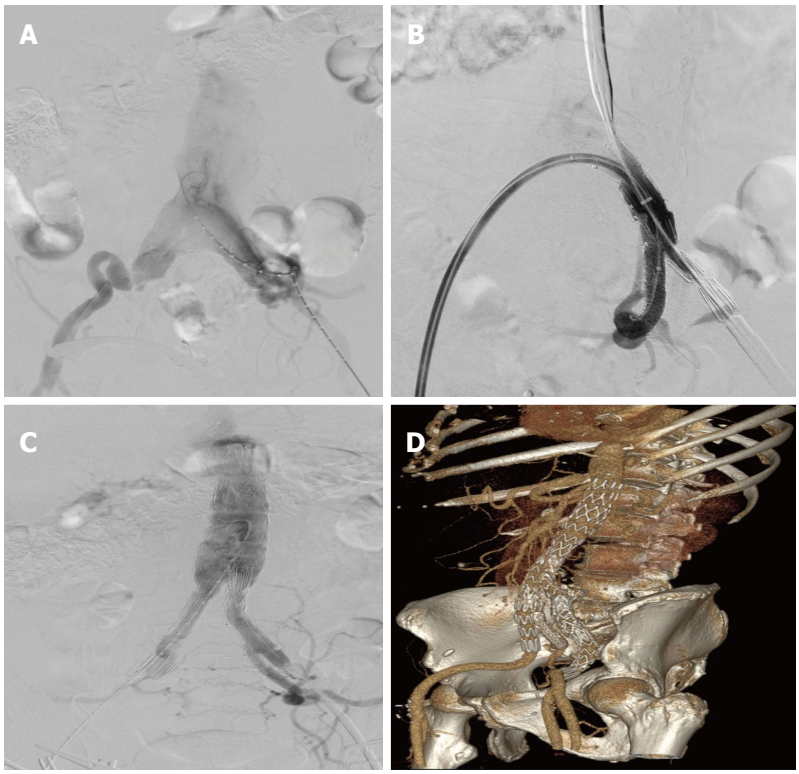

Figure 3 A 68-year-old male with an abdominal aortic aneurysm and an iliac artery aneurysm. A: Preoperative angiography; B: Control angiography after the placement of an Advanta stent graft in the left internal iliac artery without endoleak; C: Control angiography after the deployment of IBD and a bifurcated stent graft; D: Computed tomography angiography and three dimensional reconstruction at 3 mo. IBD: Iliac branch device.

aneurysm (> 5.5 cm in men and > 5 cm in women), and an aneurysm of the iliac artery > 3-3.5 cm (Figure 3).

To ensure that the intervention is successful, proper patient selection is very important. However, no standardised morphological criteria have been established for the use of IBD, although the following anatomical criteria must be present: (1) A length from the aortic bifurcation to the iliac bifurcation of > 50 mm (for S-IBD and H-IBD); (2) An inner iliac bifurcation diameter of at least 16 mm; (3) An internal iliac artery featuring a landing zone of at least 10 mm in the healthy segment; (4) An internal iliac artery diameter of 5-11 mm; (5) An assessment of the aortic bifurcation, iliac artery tortuosity, and stenosis, as well as calcification and thrombus in the iliac artery; and (6) A sufficient external iliac artery with a landing zone > 2 cm.

Some of the potential problems associated with these methods can be overcome with transbrachial access during deployment of the stent grafts in the internal iliac arteries.

Precise placement of a bridge stent graft is another technical issue. There are several peripheral stent grafts, such as the Advanta stent graft (Atrium Medical, Hudson, NH, United States), Fluency and Life stent grafts (Bard Peripheral Vascular Inc., Murray Hill, NJ, United States), Viabahn stent graft (Karlsruhe, Germany), and Be stent graft (Bentley InnoMed GmbH, Hechingen, Germany).

In the event that an internal iliac artery aneurysm presents itself, a stent graft may eventually be placed in one of the two side branches of the internal iliac artery; however, there could be an increased risk of endoleak[21].

Technical success and complications

Technical success is defined as the uneventful placement of a stent graft with accompanying branch patency, and without type 1 or type 3 endoleak by the end of the intervention. As with other new techniques, a learning curve and the mastering of patient selection improve the results and technical success of this procedure, which ranges from 85%-96.3%[22-24]. In some small series, technical success is 100%[25]. The placement of a branched device is achieved through an intervention, and it is not associated with major complications; however, complications can occur - one such example includes rupture of the external iliac artery during manipulation (Figure 4). Until now, there have been no reports on the mortality rates associated with branch device implantation. Endoleak type 1 is rare and can occur in about 0.5% of patients, while endoleak type 3 occurs in 1%[26]; transbrachial access and placement of an additional stent graft usually solves this problem (Figure 5). Moreover, buttock claudication was reported in up to 4% of patients with ZBIS at 5-year follow-up[27]. Verzini *et al*[28] compared IBD and occlusion of the internal iliac artery, where the rate of buttock claudication in the IBD group was 4%, as compared with 22% in the iliac artery embolization group. The same research group reported endoleak type 2 in 4% of patients in the IBD group and in 19% of patients in the embolization group[29].

Follow-up and secondary interventions

Encouraging mid- and short-term follow-up results featuring branch patency of up to 88% in a 5-6-year period were reported[27,29]. An absence of long-term results still limits the wide use of a branch stent graft, and the costs of the device play a role as well. Branch graft occlusion is a potential complication of this procedure, and it has reportedly occurred in 1.2%-11% of cases[23,27,30];

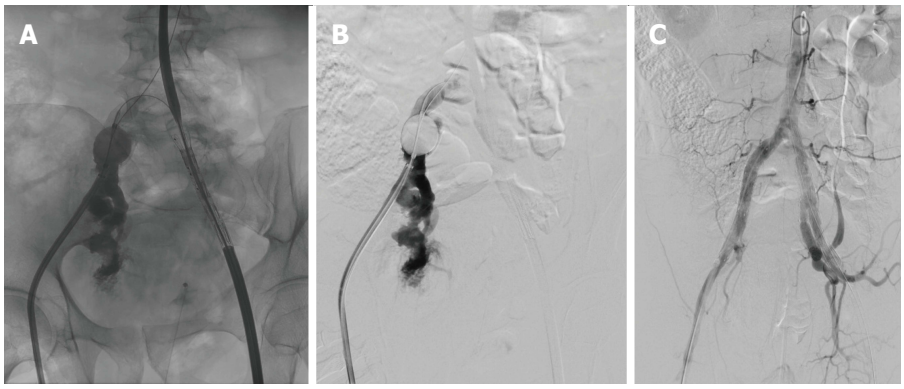

Figure 4 Rupture of the right external iliac artery during manipulation. A, B: Partially deployed IBD on the left side. An occlusive balloon placed in the right common iliac artery. Angiography revealed the rupture site at the proximal part of the external iliac artery; C: Control angiography following placement of the two fluency stent grafts on the right side, and completion of the procedure with the placement of an IBD device on the left side. IBD: Iliac branch device.

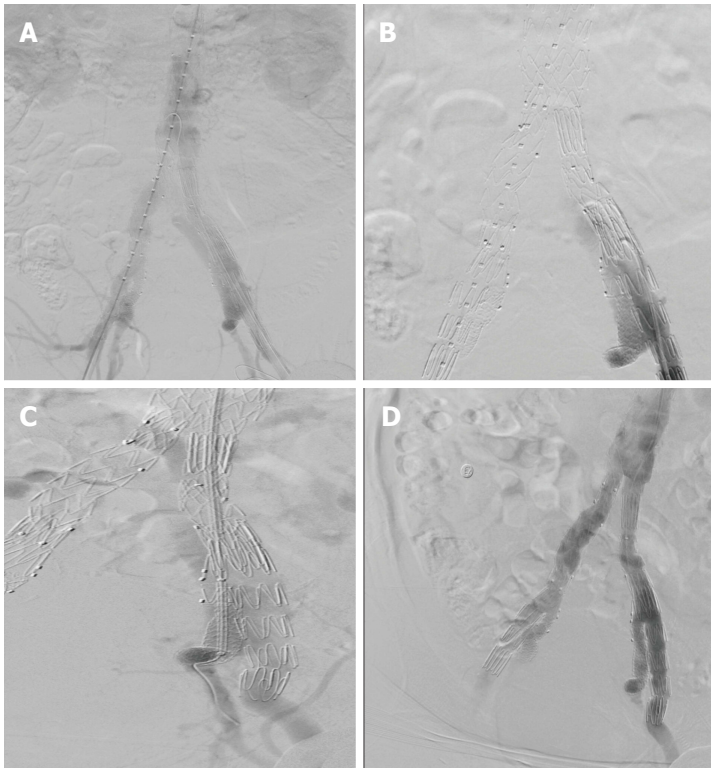

Figure 5 Bilaterally placed branch stent graft. A, B: Control angiography with endoleak type 3 on the left side; C: Transbrachial access and placement of an additional stent graft; D: Final control angiography featuring a good result and without endoleak.

moreover, graft limb occlusion in the external iliac artery has also been reported. Branch graft occlusion is usually asymptomatic, while external iliac limb occlusion can be treated with crossover bypass and/or thrombectomy, or with the use of thrombolytic treatment.

CONCLUSION

Iliac branch stent graft placement represents a further development in endovascular medicine, and it has been associated with a high technical success rate without serious complications in the hands of an experienced professional. Very good results were obtained during short- and mid-term follow-up. Occlusion of the internal iliac artery is a rare cause of serious complications, but it can heavily impact quality of life, especially in asymptomatic patients where incidentally discovered AAA and iliac artery aneurysms require treatment. Although the costs of the stent graft can impact treatment decisions, an iliac branch stent graft should be used in selected patients as a means of maintaining patency of at least one internal iliac artery or, in some cases, bilaterally, especially in younger patients.

ACKNOWLEDGMENTS

English-language editing of this manuscript was provided by Journal Prep.

REFERENCES

1 **Armon MP**, Wenham PW, Whitaker SC, Gregson RH, Hopkinson

BR. Common iliac artery aneurysms in patients with abdominal aortic aneurysms. *Eur J Vasc Endovasc Surg* 1998; **15**: 255-257 [PMID: 9587341 DOI: 10.1016/j.ejvs.2015.05.021]
2 **Hobo R**, Sybrandy JE, Harris PL, Buth J. Endovascular repair of abdominal aortic aneurysms with concomitant common iliac artery aneurysm: outcome analysis of the EUROSTAR Experience. *J Endovasc Ther* 2008; **15**: 12-22 [PMID: 18254666 DOI: 10.1583/07-2217.1]
3 **Fatima J**, Correa MP, Mendes BC, Oderich GS. Pelvic revascularization during endovascular aortic aneurysm repair. *Perspect Vasc Surg Endovasc Ther* 2012; **24**: 55-62 [PMID: 23196714 DOI: 10.1177/1531003512468036]
4 **Schoder M**, Zaunbauer L, Hölzenbein T, Fleischmann D, Cejna M, Kretschmer G, Thurnher S, Lammer J. Internal iliac artery embolization before endovascular repair of abdominal aortic aneurysms: frequency, efficacy, and clinical results. *AJR Am J Roentgenol* 2001; **177**: 599-605 [PMID: 11517053 DOI: 10.2214/ajr.177.3.1770599]
5 **Bratby MJ**, Munneke GM, Belli AM, Loosemore TM, Loftus I, Thompson MM, Morgan RA. How safe is bilateral internal iliac artery embolization prior to EVAR? *Cardiovasc Intervent Radiol* 2008; **31**: 246-253 [PMID: 17957407 DOI: 10.007/s00270-007-9203-6]
6 **Rayt HS**, Bown MJ, Lambert KV, Fishwick NG, McCarthy MJ, London NJ, Sayers RD. Buttock claudication and erectile dysfunction after internal iliac artery embolization in patients prior to endovascular aortic aneurysm repair. *Cardiovasc Intervent Radiol* 2008; **31**: 728-734 [PMID: 18338212 DOI: 10.1007/s00270-008-9319-3]
7 **Lin PH**, Bush RL, Chaikof EL, Chen C, Conklin B, Terramani TT, Brinkman WT, Lumsden AB. A prospective evaluation of hypogastric artery embolization in endovascular aortoiliac aneurysm repair. *J Vasc Surg* 2002; **36**: 500-506 [PMID: 12218973 DOI: 10.1067/mva.2002.127350]
8 **Brewster DC**, Franklin DP, Cambria RP, Darling RC, Moncure AC, Lamuraglia GM, Stone WM, Abbott WM. Intestinal ischemia complicating abdominal aortic surgery. *Surgery* 1991; **109**: 447-454 [PMID: 1844392]
9 **Chun JY**, Mailli L, Abbasi MA, Belli AM, Gonsalves M, Munneke G, Ratnam L, Loftus IM, Morgan R. Embolization of the internal iliac artery before EVAR: is it effective? Is it safe? Which technique should be used? *Cardiovasc Intervent Radiol* 2014; **37**: 329-336 [PMID: 23771327 DOI: 10.1007/s00270-013-0659-2]
10 **Kritpracha B**, Pigott JP, Price CI, Russell TE, Corbey MJ, Beebe HG. Distal internal iliac artery embolization: a procedure to avoid. *J Vasc Surg* 2003; **37**: 943-948 [PMID: 12756337]
11 **McDonnell CO**, Semmens JB, Allen YB, Jansen SJ, Brooks DM, Lawrence-Brown MM. Large iliac arteries: a high-risk group for endovascular aortic aneurysm repair. *J Endovasc Ther* 2007; **14**: 625-629 [PMID: 17924726]
12 **Lobato AC**. Sandwich technique for aortoiliac aneurysms extending to the internal iliac artery or isolated common/internal iliac artery aneurysms: a new endovascular approach to preserve pelvic circulation. *J Endovasc Ther* 2011; **18**: 106-111 [PMID: 21314358 DOI: 10.1583/10-3320.1]
13 **Dorsey C**, Chandra V, Lee JT. The "terrace technique"--totally endovascular repair of a type IV thoracoabdominal aortic aneurysm. *Ann Vasc Surg* 2014; **28**: 1563.e11-1563.e16 [PMID: 24704581 DOI: 10.1016/j.avsg.2014.03.010]
14 **Wilson A**, Zhou S, Bachoo P, Tambyraja AL. Systematic review of chimney and periscope grafts for endovascular aneurysm repair. *Br J Surg* 2013; **100**: 1557-1564 [PMID: 24264776 DOI: 10.1002/bjs.9274]
15 **Donas KP**, Telve D, Torsello G, Pitoulias G, Schwindt A, Austermann M. Use of parallel grafts to save failed prior endovascular aortic aneurysm repair and type Ia endoleaks. *J Vasc Surg* 2015; **62**: 578-584 [PMID: 26087878 DOI: 10.1016/j.jvs.2015.04.395]
16 **Greenberg RK**, Clair D, Srivastava S, Bhandari G, Turc A, Hampton J, Popa M, Green R, Ouriel K. Should patients with challenging anatomy be offered endovascular aneurysm repair? *J Vasc Surg* 2003; **38**: 990-996 [PMID: 14603205]
17 **Lindblad B**, Bin Jabr A, Holst J, Malina M. Chimney Grafts in Aortic Stent Grafting: Hazardous or Useful Technique? Systematic Review of Current Data. *Eur J Vasc Endovasc Surg* 2015; Epub ahead of print [PMID: 26371416]
18 **Wu IH**, Chou HW, Chang CH, Lin CF, Chi NH, Wang SS. Crossover chimney technique to preserve the internal iliac artery during endovascular repair of iliac or aortoiliac aneurysms: midterm results. *J Endovasc Ther* 2015; **22**: 388-395 [PMID: 25878024 DOI: 10.1177/1526602815581596]
19 **Parodi JC**, Ferreira M. Relocation of the iliac artery bifurcation to facilitate endoluminal treatment of abdominal aortic aneurysms. *J Endovasc Surg* 1999; **6**: 342-347 [PMID: 10893136]
20 **Wong S**, Greenberg RK, Brown CR, Mastracci TM, Bena J, Eagleton MJ. Endovascular repair of aortoiliac aneurysmal disease with the helical iliac bifurcation device and the bifurcated-bifurcated iliac bifurcation device. *J Vasc Surg* 2013; **58**: 861-869 [PMID: 23790453 DOI: 10.1016/j.jvs.2013.02.033]
21 **Noel-Lamy M**, Jaskolka J, Lindsay TF, Oreopoulos GD, Tan KT. Internal Iliac Aneurysm Repair Outcomes Using a Modification of the Iliac Branch Graft. *Eur J Vasc Endovasc Surg* 2015; **50**: 474-479 [PMID: 26188719]
22 **Tielliu IF**, Bos WT, Zeebregts CJ, Prins TR, Van Den Dungen JJ, Verhoeven EL. The role of branched endografts in preserving internal iliac arteries. *J Cardiovasc Surg* (Torino) 2009; **50**: 213-218 [PMID: 19329918]
23 **Karthikesalingam A**, Parmar J, Cousins C, Hayes PD, Varty K, Boyle JR. Midterm results from internal iliac artery branched endovascular stent grafts. *Vasc Endovascular Surg* 2010; **44**: 179-183 [PMID: 20034945 DOI: 10.1177/1538574409352692]
24 **Dias NV**, Resch TA, Sonesson B, Ivancev K, Malina M. EVAR of aortoiliac aneurysms with branched stent-grafts. *Eur J Vasc Endovasc Surg* 2008; **35**: 677-684 [PMID: 18378472 DOI: 10.1016/j.ejvs.2007.10.022]
25 **Pua U**, Tan K, Rubin BB, Sniderman KW, Rajan DK, Oreopoulos GD, Lindsey TF. Iliac branch graft in the treatment of complex aortoiliac aneurysms: early results from a North American institution. *J Vasc Interv Radiol* 2011; **22**: 542-549 [PMID: 21463759 DOI: 10.1016/j.jvir.2011.01.429]
26 **Karthikesalingam A**, Hinchliffe RJ, Holt PJ, Boyle JR, Loftus IM, Thompson MM. Endovascular aneurysm repair with preservation of the internal iliac artery using the iliac branch graft device. *Eur J Vasc Endovasc Surg* 2010; **39**: 285-294 [PMID: 19962329 DOI: 10.1016/j.ejvs.2009.11.018]
27 **Parlani G**, Verzini F, De Rango P, Brambilla D, Coscarella C, Ferrer C, Cao P. Long-term results of iliac aneurysm repair with iliac branched endograft: a 5-year experience on 100 consecutive cases. *Eur J Vasc Endovasc Surg* 2012; **43**: 287-292 [PMID: 22240335 DOI: 10.1016/j.ejvs.2011.12.011]
28 **Verzini F**, Parlani G, Romano L, De Rango P, Panuccio G, Cao P. Endovascular treatment of iliac aneurysm: Concurrent comparison of side branch endograft versus hypogastric exclusion. *J Vasc Surg* 2009; **49**: 1154-1161 [PMID: 19394544 DOI: 10.1016/j.jvs.2008.11.100]
29 **Ziegler P**, Avgerinos ED, Umscheid T, Perdikides T, Erz K, Stelter WJ. Branched iliac bifurcation: 6 years experience with endovascular preservation of internal iliac artery flow. *J Vasc Surg* 2007; **46**: 204-210 [PMID: 17600664]
30 **Pratesi G**, Fargion A, Pulli R, Barbante M, Dorigo W, Ippoliti A, Pratesi C. Endovascular treatment of aorto-iliac aneurysms: four-year results of iliac branch endograft. *Eur J Vasc Endovasc Surg* 2013; **45**: 607-609 [PMID: 23540808 DOI: 10.1016/j.ejvs.2013.02.017]

P- Reviewer: Casciaro S, Cerwenka HR, Chow J, Razek AAKA
S- Editor: Qiu S **L- Editor**: A **E- Editor**: Lu YJ

World Journal of Radiology

Submit a Manuscript: http://www.wjgnet.com/esps/
Help Desk: http://www.wjgnet.com/esps/helpdesk.aspx
DOI: 10.4329/wjr.v8.i3.281

World J Radiol 2016 March 28; 8(3): 281-287
ISSN 1949-8470 (online)

MINIREVIEWS

Grey-scale sonography and sonoelastography for diagnosing carpal tunnel syndrome

Hideaki Miyamoto, Yutaka Morizaki, Takahiro Kashiyama, Sakae Tanaka

Hideaki Miyamoto, Yutaka Morizaki, Takahiro Kashiyama, Sakae Tanaka, Department of Orthopaedic Surgery, Graduate School of Medicine, the University of Tokyo, Tokyo 113-8655, Japan

Author contributions: All authors contributed equally to this work; wrote and reviewed the paper.

Conflict-of-interest statement: There is no conflict of interest associated with any of the senior author or other coauthors contributed their efforts in this manuscript.

Correspondence to: Hideaki Miyamoto, MD, Department of Orthopaedic Surgery, Graduate School of Medicine, the University of Tokyo, 7 Chome-3-1 Hongo, Bunkyo, Tokyo 113-8655, Japan. s70842000@yahoo.co.jp
Telephone: +81-3-38155411
Fax: +81-3-38184082

Received: August 27, 2015
Peer-review started: August 31, 2015
First decision: November 24, 2015
Revised: December 6, 2015
Accepted: January 5, 2016
Article in press: January 7, 2016
Published online: March 28, 2016

Abstract

Carpal tunnel syndrome (CTS) is a common peripheral entrapment neuropathy of the median nerve at wrist level, and is thought to be caused by compression of the median nerve in the carpal tunnel. There is no standard quantitative reference for the diagnosis of CTS. Grey-scale sonography and sonoelastography (SEL) have been used as diagnostic tools. The most commonly agreed findings in grey-scale sonography for the diagnosis of CTS is enlargement of the median nerve cross-sectional area (CSA). Several authors have assessed additional parameters. "Delta CSA" is the difference between the proximal median nerve CSA at the pronator quadratus and the maximal CSA within the carpal tunnel. The "CSA ratio" is the ratio of CSA in the carpal tunnel to the CSA at the mid forearm. These additional parameters showed better diagnostic accuracy than CSA measurement alone. Recently, a number of studies have investigated the elasticity of the median nerve using SEL, and have shown that this also has diagnostic value, as it was significantly stiffer in CTS patients compared to healthy volunteers. In this review, we summarize the usefulness of grey-scale sonography and SEL in diagnosing CTS.

Key words: Carpal tunnel syndrome; Cross-sectional area; Gray-scale sonography; Diagnosis; Median nerve; Sonoelastography; Elasticity

Core tip: The diagnostic value of grey-scale sonography and sonoelastography in carpal tunnel syndrome (CTS) is reviewed. Sonography can potentially allow a noninvasive screening, and could therefore be a preferable first-line approach to detect pathological changes of the intracarpal tunnel contents. This review summarizes the current knowledge of sonographic findings as a diagnostic tool in CTS.

Miyamoto H, Morizaki Y, Kashiyama T, Tanaka S. Grey-scale sonography and sonoelastography for diagnosing carpal tunnel syndrome. *World J Radiol* 2016; 8(3): 281-287 Available from: URL: http://www.wjgnet.com/1949-8470/full/v8/i3/281.htm DOI:

http://dx.doi.org/10.4329/wjr.v8.i3.281

INTRODUCTION

Carpal tunnel syndrome (CTS) is a common compression neuropathy of the median nerve at wrist level, with an estimated prevalence of 50 cases per 1000 population per year[1]. The main symptoms of CTS include numbness and tingling in the area of the median nerve distribution and weakness in the opposition of the thumb.

The median nerve in the carpal tunnel lies between the transverse carpal ligament superiorly and the flexor tendons and carpal bones inferiorly[2]. CTS is thought to be caused by compression of the median nerve within its surrounding structures, including the transverse carpal ligament, finger flexor tendons, and tenosynovial tissue[3,4]. Therefore, it is important to investigate morphological changes in the intracarpal tunnel contents in order to understand the pathophysiology of CTS.

Sonography can provide information on anatomical abnormalities of the median nerve and intracarpal tunnel contents, which are causative factors in CTS. Sonoelastography (SEL) is a modality for quantitatively measuring the elasticity of soft tissue through conventional grey-scale sonography with estimated Young's modulus or semi-quantitative values as strain ratios, and promising preliminary results have been obtained for SEL in the diagnosis of liver, breast, pancreas, prostate, and thyroid masses using the appropriate cut-off values[5-9]. Recently, several studies have investigated the elasticity of the intracarpal tunnel contents to clarify the pathophysiology of CTS using SEL[10-15].

In this review, we summarize the usefulness of grey-scale sonography and sonoelastography in diagnosing CTS.

GREY-SCALE SONOGRAPHY

The most commonly agreed findings in grey-scale sonography for the diagnosis of CTS is the enlargement of the median nerve cross-sectional area (CSA). Nerve enlargement is thought to result from large myelinated fibers at the periphery of the fascicles, interfascicular epineurial fibrosis, and/or perineural thickening under chronic nerve compression[16]. Table 1 gives the diagnostic accuracy of using the CSA from previous studies and includes the CSA cut-off values used and the location where the CSA was measured. The reported CSA cut-off values in the carpal tunnel measured by sonography ranged from 8.5 to 12 mm^2. The majority of studies measured the CSA at the tunnel inlet, which is described as being level with the pisiform bone in some studies. The findings of these studies revealed a wide variation in sensitivity (62%-99%) and specificity (57%-100%). In a meta-analysis, the single CSA test for CTS was reported to have 87.3% sensitivity and 83.3% specificity, with an area under the receiver operating characteristic curve of 0.93[17]. However, a limitation of this analysis was that measurements were obtained in different proportions of patients at different points along the carpal tunnel.

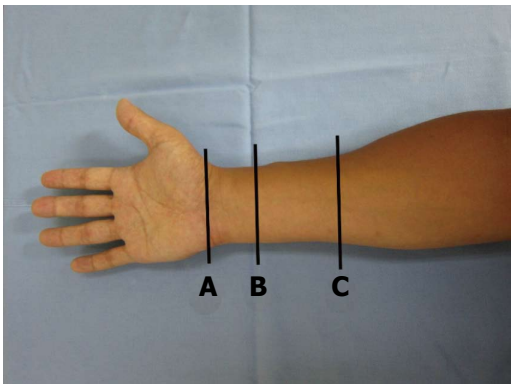

Figure 1 Demonstration of probe location at the forearm. The cross sectional area of the median nerve was measured (A) level with the pisiform bone (B) level with the proximal third of the pronator quadratus and (C) level with a point 12 cm proximal to the pisiform bone.

In order to overcome the limitations arising from individual anatomical differences when using the CSA to diagnose CTS, Klauser *et al*[18] assessed "delta CSA", which is the difference between the proximal median nerve CSA at the level of the pronator quadratus and the maximal CSA within the carpal tunnel, resulting in a threshold of 2 mm^2. However, there are few studies using "delta CSA" for diagnosing CTS[18-20], and further research is needed to validate this diagnostic parameter. Other studies reported the diagnostic accuracy of a ratio between a CSA in the carpal tunnel and a proximal CSA at the mid forearm (the "CSA ratio")[19,21-25]. These two parameters allowed a more accurate detection of CTS than CSA alone. Tables 2 and 3 summarize the previously reported diagnostic accuracies of these two parameters. Probe locations at the forearm in major studies are shown in Figure 1, and representative grey-scale sonographic images of a CTS patient are shown in Figure 2.

Other characteristic parameters of CTS have been reported, including the thickness of the transverse carpal ligament, palmar bowing of the flexor retinaculum, flattening of the median nerve, and decreased longitudinal excursion on dynamic assessment, all of which can aid in the sonographic diagnosis of CTS[26-28]. In addition, it is recognized that hypervascularity and hypoechogenicity of the median nerve are present in CTS with a larger CSA, and investigation of the vascularity of the median nerve using Doppler sonography has been used as an adjunct to the diagnosis of CTS[29,30]. Despite these characteristic findings, few validated quantitative scoring systems have been created for assessing hypervascularity and hypoechogenicity of the median nerve as a reference standard for CTS diagnosis[31].

SONOELASTOGRAPHY

There are two major stress applications in SEL;

Table 1 Summary of previous studies reporting the diagnostic value of the median nerve cross-sectional area in carpal tunnel syndrome

Ref.	CSA cut-off (mm^2)	CTS wrists	Control wrists	Location	Sensitivity (%)	Specificity (%)	AUC
Duncan *et al*[47]	9	102	68	Pisiform	82	97	NA
Lee *et al*[48]	15	100	56	Scaphoid tuberosity and the pisiform	88	96	NA
Sarría *et al*[26]	11	64	42	Hook of hamate	75	57	NA
Swen *et al*[49]	10	63	20	Pisiform	70	63	NA
Nakamichi and Tachibana[50]	12	414	408	Mean location of the proximal, mid and distal tunnel	67	97	NA
Wong *et al*[51]	9.8	35	35	Tunnel inlet	89	83	0.91
Kele *et al*[52]	11	110	55	Tunnel inlet	74	98	NA
Altinok *et al*[53]	9	40	40	Pisiform	65	93	NA
El Miedany *et al*[54]	10	96	156	Tunnel inlet	98	100	NA
Keleş *et al*[55]	9.3	35	40	Middle carpal tunnel	80	76	0.833
Ziswiler *et al*[56]	10	78	23	The largest CSA	82	87	0.89
Mallouhi *et al*[57]	11	172	None	Maximal CSA in the carpal tunnel	91	47	NA
Wiesler *et al*[58]	11	44	86	The distal wrist crease	91	84	NA
Naranjo *et al*[59]	9.7	80	25	Tunnel inlet	86	48	0.78
Kaymak *et al*[60]	12	34	38	Pisiform	88	66	0.84
Kwon *et al*[61]	10.7	41	41	Tunnel inlet	66	63	0.75
Pinilla *et al*[62]	6.5	40	30	Tunnel inlet	89.5	93	NA
Sernik *et al*[28]	10	40	63	Pisiform	85	92.1	NA
Visser *et al*[63]	10	265	137	Tunnel inlet	78	91	0.90
Ashraf *et al*[64]	9.3	70	80	Middle carpal tunnel	80	77.5	0.796
Klauser *et al*[18]	12	100	93	Maximal CSA in the carpal tunnel	94	95	0.9896
Pastare *et al*[65]	9	97	None	Tunnel inlet	62	100	0.842
Mohammadi *et al*[66]	8.5	132	32	Tunnel inlet	97	98	NA
Ghasemi-Esfe *et al*[29]	10.5	85	49	Pisiform	69	94	NA
Roll *et al*[19]	10.3	83	83	Pisiform	80.4	90.6	0.899
Kang *et al*[23]	9.5	110	38	Distal wrist crease	96	92	0.988
Ulaşli *et al*[67]	10.5	95	48	Maximal CSA in the carpal tunnel	91	81	0.934
Fowler *et al*[42]	10	55	30	Pisiform	89	90	NA
Kantarci *et al*[35]	9.5	60	36	Tunnel inlet	60	91.7	0.844
Miyamoto *et al*[37]	11	43	44	Pisiform	82	75	0.85
Ooi *et al*[68]	9.8	95	30	Pisiform	92	90	0.95

CSA: Cross-sectional area; CTS: Carpal tunnel syndrome; AUC: Area under curve; NA: Not available.

Table 2 Summary of studies reporting the diagnostic value of the delta cross-sectional area of the median nerve for carpal tunnel syndrome

Ref.	delta CSA cut-off (mm^2)	CTS wrists	Control wrists	Location	Sensitivity (%)	Specificity (%)	AUC
Klauser *et al*[18]	2	100	93	Maximal CSA in the carpal tunnel/proximal third of the pronator quadratus	99	100	0.9988
Roll *et al*[19]	4.16	83	83	Pisiform/6 cm proximal to the distal wrist crease	82.4	87.5	0.886
Tajika *et al*[20]	2	50	81	Pisiform/distal radioulnar joint	100	99	0.996

CSA: Cross-sectional area; CTS: Carpal tunnel syndrome; AUC: Area under curve.

compression elastography and shear-wave elastography. Compression elastography, also described as static strain elastography, is based on the principle that the compression of tissue produces strain. Displacement is calculated in real time by repeated manual compression to the tissue using a hand-held sonographic transducer. The displacement is then converted to a color-coded strain distribution map, which is often superimposed over the conventional B-mode image or displayed next to it. Most compression elastography systems provide both a visual representation of pressure and a quantitative measurement in the form of the strain ratio, which is an index of the relative elasticity between an objective region of interest (ROI) and a reference ROI. Compression elastography can draw the calculation area as a relatively free shape (*e.g.,* elliptical or bowing). The strain is lower in firmer tissues. However, compression elastographic assessment is subject to a number of technical difficulties. The compression force for measurements of tissue strain can be regulated by freehand, and the probe should always be held perpendicular to the objectives so that the appropriate strain is adjusted with reference to the feedback indicator. This is necessary because the nonlinear compression force can result in the elasticity of the objectives being measured incorrectly. To minimize intra- and inter-observer variation and to avoid transient temporal fluctuations, Yoshii *et al*[32,33] developed a cyclic compression apparatus with automatic vibratory

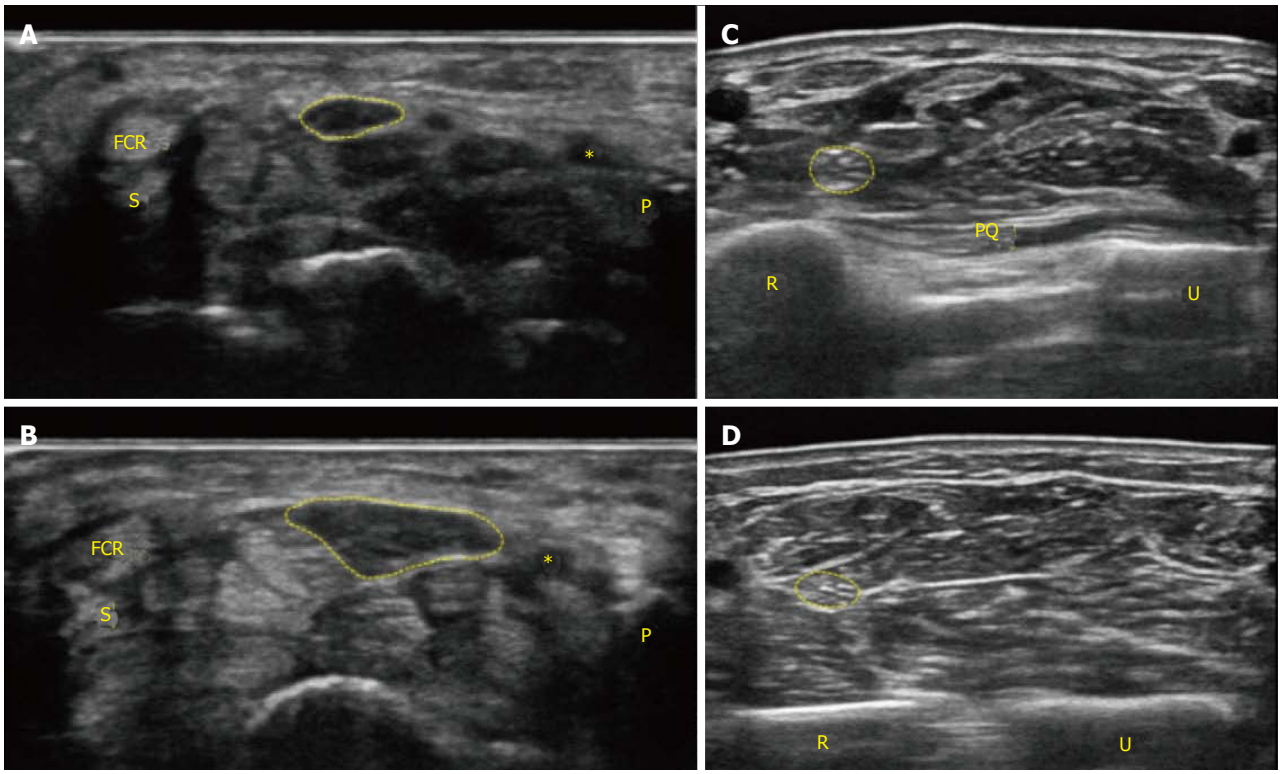

Figure 2 Transverse images in a 79-year-old female with carpal tunnel syndrome. A: A conventional grey scale sonographic image shows the cross-sectional area of the median nerve (CSA) corresponding to the circle in the normal side with an area of 8 mm^2 at the level of the pisiform bone; B: CSA in the carpal tunnel syndrome (CTS) side shows 21 mm^2 at pisiform bone level; C: CSA in the CTS side shows 7 mm^2 at the proximal third of the pronator quadratus level; D: CSA in the CTS side shows 6 mm^2 at a point 12 cm proximal to the pisiform bone. In this case, the calculated "delta CSA" and "CSA ratio" were 14 mm^2 and 3.5, respectively. *: Ulnar artery. FCR: Flexor carpi radialis; P: Pisiform bone; S: Scaphoid bone; PQ: Pronator quadratus muscle; R: Radius; U: Ulnar.

Table 3 Summary of studies reporting the diagnostic value of the cross-sectional area ratio of the median nerve for carpal tunnel syndrome

Ref.	CSA ratio cut-off	CTS wrists	Control wrists	Location	Sensitivity (%)	Specificity (%)	AUC
Hobson-Webb *et al*[21]	1.4	44	18	Distal wrist crease/12 cm proximal in the forearm	100	NA	NA
Visser *et al*[22]	2	265	137	Tunnel inlet/forearm	69	90	0.83
Roll *et al*[19]	1.70	83	83	Pisiform/6 cm proximal to the distal wrist crease	80.4	81.2	0.842
Kang *et al*[23]	1.34	110	38	Distal wrist crease/12 cm proximal in the forearm	99.9	100	0.988
Mhoon *et al*[24]	1.4	192	50	Distal wrist crease/12 cm proximal in the forearm	97	28	0.789
Fu *et al*[25]	1.3	46	44	Tunnel inlet/outlet	91	93	0.98

CSA: Cross-sectional area; CTS: Carpal tunnel syndrome; AUC: Area under curve; NA: Not available.

equipment.

Shear-wave elastography employs a directional force that leads to shear deformation propagating as a shear wave. Shear-wave elastography, also termed dynamic elastography, is based on the measurement of the propagation velocity distribution of a directional shear wave produced by an ultrasound pulse[34]. The velocity of the shear waves can be measured and used to evaluate tissue elasticity because the shear waves travel faster in harder materials: Young modulus (E) can be calculated as a function of shear velocity (Cs) and material density (ρ) using the equation $E = 3\rho Cs^2$[34]. This technique allows for quantitative measurements that can be expressed in kilopascals or in centimeters per second. A disadvantage of shear-wave elastographic evaluation is that only limited ROI shapes (*e.g.*, a 5 mm × 5 mm box or a 1 mm × 1 mm circle) are currently available for the quantitative measurement of elasticity.

The diagnostic significance of median nerve stiffness using SEL has also been investigated (Table 4). Kantarci *et al*[35] found that the median nerve at the carpal tunnel inlet was significantly stiffer in CTS patients than in healthy volunteers using shear-wave elastography. They evaluated the median nerve elasticity within a defined 2 mm diameter circle at the carpal tunnel inlet in the longitudinal image, and reported that a 40.4 kPa cut-off value on shear-wave elastography gave a high diagnostic accuracy. Two further studies evaluated the elasticity of the median nerve by compression elastography[36,37]. The median nerve in CTS patients

Table 4 Summary of studies reporting the diagnostic accuracy for carpal tunnel syndrome of the median nerve elasticity determined using sonoelastography

Ref.	Type of sonoelastography	CTS wrists	Control wrists	Location	Sensitivity (%)	Specificity (%)	AUC
Orman *et al*[36]	Compression	74	45	Pisiform-scaphoid	84	54	NA
Miyamoto *et al*[37]	Compression	43	44	Pisiform-scaphoid	82	68	0.78
Kantarci *et al*[35]	Shear wave	60	36	Tunnel inlet	93.3	88.9	0.956

CTS: Carpal tunnel syndrome; AUC: Area under curve; NA: Not available.

was significantly stiffer than that in healthy volunteers in both studies. These studies also evaluated the diagnostic value of median nerve elasticity. Orman *et al*[36] reported that an appropriate median nerve strain cut-off value could detect CTS with 84% sensitivity and 54% specificity, although this was not a significant improvement over conventional grey-scale sonography.

We reported different findings for CTS diagnosis using compression elastography. In our study, we used a reference medium with a constant elasticity for quantitative assessment. On the basis of a receiver operating characteristic analysis, a logistic combined model with both median nerve stiffness and the CSA was providing a sensitivity of 81% and a specificity of 91%, with an area under receiver operating characteristics curve of 0.91[37].

FUTURE PERSPECTIVE

The general approaches for diagnosing CTS are combinations of clinical provocation tests and nerve conduction studies (NCS)[1]. However, studies of Phalen's maneuver reported a wide range of values for sensitivity of 10% to 71% and specificity of 55% to 86%[38]. The sensitivity of Tinel's sign ranged from 9% to 89% and a specificity of 55% to 96%[38]. Whereas, Graham *et al*[39] developed original clinical diagnostic criteria for CTS by analyzing selected highly ranked predictors from clinical provocation tests and symptoms. They reported that what they call "CTS-6" (numbness in the median nerve distribution, nocturnal numbness, weakness/atrophy of the thenar musculature, Tinel's sign, Phalen's test, loss of 2-point discrimination) contributed to the diagnostic model of CTS. The correlation between the probability of CTS predicted by CTS-6 and a panel of expert clinicians was 0.71[39].

However, there is no quantitative gold standard of reference for CTS diagnosis. NCS has been widely used in the quantitative diagnosis of CTS. But, NCS tests have a reported sensitivity of 56% to 85%[40], and the false-negative rate for NCS testing has been reported to be between 16% and 34%[41]. By comparing sonography with NCS using CTS-6 as the reference standard, Fowler *et al*[42] showed that sonography could be used to confirm the diagnosis of CTS with better specificity and equal sensitivity as those of NCS. It could therefore be an alternative method to NCS in clinical practice to use sonography as a first-line approach for CTS screening because it is non-invasive, allows real-time access, and is cost-effective[43].

Previous studies have shown that sonography can be useful also to monitor therapeutic response following surgery[44,45] and corticosteroid injection[15,46]. Smidt *et al*[44] reported that CSA of the median nerve at least 6 mo after surgery decreased from 14 mm^2 to 11 mm^2 in a patient group with a good outcome, whereas CSA remained almost the same in a group with a poor outcome. Kim *et al*[45] found CSA decreased in the first 3 wk after surgery. These findings indicate that measurement of CSA may provide clinicians with a tool to estimate the response to CTS surgery.

Palpation-guided injection into the carpal tunnel is often performed in general clinical practice. The major risk of the palpation-guided injection is damaging the intracarpal intact structures including the median nerve, flexor tendons and vessels. Moreover, if the injected steroid is not adequately placed inside the carpal tunnel, patients cannot obtain therapeutic effectiveness. Therefore, in order to improve the accuracy of the injection, a sonography-guided technique should be useful. Comparing a sonography-guided group to a palpation-guided group, the improvement in symptom in the sonography-guided group at 12 wk after injection was higher than that in the palpation-guided group[46]. The average time to symptom relief was also shorter in the sonography-guided group[46]. We measured the stiffness of the intracarpal tunnel contents by using SEL. The stiffness of the intracarpal tunnel contents surrounding the median nerve in CTS patients was higher than that of healthy volunteers but decreased 6 wk after corticosteroid injection[15].

In addition to diagnostic tools, grey-scale sonography and SEL could be key skills for objectively assessing the response and predicting the prognosis following therapeutic intervention and operative treatment in CTS.

REFERENCES

1 **Keith MW**, Masear V, Chung KC, Maupin K, Andary M, Amadio PC, Watters WC, Goldberg MJ, Haralson RH, Turkelson CM, Wies JL, McGowan R. American Academy of Orthopaedic Surgeons Clinical Practice Guideline on diagnosis of carpal tunnel syndrome. *J Bone Joint Surg Am* 2009; **91**: 2478-2479 [PMID: 19797585 DOI: 10.2106/JBJS.I.00643]

2 **Ghasemi-Rad M**, Nosair E, Vegh A, Mohammadi A, Akkad A, Lesha E, Mohammadi MH, Sayed D, Davarian A, Maleki-Miyandoab T, Hasan A. A handy review of carpal tunnel syndrome: From anatomy to diagnosis and treatment. *World J Radiol* 2014; **6**: 284-300 [PMID: 24976931 DOI: 10.4329/wjr.v6.i6.284]

3 **Werner RA**, Andary M. Carpal tunnel syndrome: pathophysiology and clinical neurophysiology. *Clin Neurophysiol* 2002; **113**: 1373-1381

[PMID: 12169318 DOI: 10.1016/S1388-2457(02)00169-4]
4 **Ettema AM**, Amadio PC, Zhao C, Wold LE, An KN. A histological and immunohistochemical study of the subsynovial connective tissue in idiopathic carpal tunnel syndrome. *J Bone Joint Surg Am* 2004; **86-A**: 1458-1466 [PMID: 15252093]
5 **Onur MR**, Poyraz AK, Ucak EE, Bozgeyik Z, Özercan IH, Ogur E. Semiquantitative strain elastography of liver masses. *J Ultrasound Med* 2012; **31**: 1061-1067 [PMID: 22733855]
6 **Fischer T**, Peisker U, Fiedor S, Slowinski T, Wedemeyer P, Diekmann F, Grigoryev M, Thomas A. Significant differentiation of focal breast lesions: raw data-based calculation of strain ratio. *Ultraschall Med* 2012; **33**: 372-379 [PMID: 21614749 DOI: 10.1055/s-0031-1273222]
7 **Itokawa F**, Itoi T, Sofuni A, Kurihara T, Tsuchiya T, Ishii K, Tsuji S, Ikeuchi N, Umeda J, Tanaka R, Yokoyama N, Moriyasu F, Kasuya K, Nagao T, Kamisawa T, Tsuchida A. EUS elastography combined with the strain ratio of tissue elasticity for diagnosis of solid pancreatic masses. *J Gastroenterol* 2011; **46**: 843-853 [PMID: 21505859 DOI: 10.1007/s00535-011-0399-5]
8 **Zhang Y**, Tang J, Li YM, Fei X, Lv FQ, He EH, Li QY, Shi HY. Differentiation of prostate cancer from benign lesions using strain index of transrectal real-time tissue elastography. *Eur J Radiol* 2012; **81**: 857-862 [PMID: 21392908 DOI: 10.1016/j.ejrad.2011.02.037]
9 **Ning CP**, Jiang SQ, Zhang T, Sun LT, Liu YJ, Tian JW. The value of strain ratio in differential diagnosis of thyroid solid nodules. *Eur J Radiol* 2012; **81**: 286-291 [PMID: 21237598 DOI: 10.1016/j.ejrad.2010.12.010]
10 **Shen ZL**, Vince DG, Li ZM. In vivo study of transverse carpal ligament stiffness using acoustic radiation force impulse (ARFI) imaging. *PLoS One* 2013; **8**: e68569 [PMID: 23861919 DOI: 10.1371/journal.pone.0068569]
11 **Liao YY**, Lee WN, Lee MR, Chen WS, Chiou HJ, Kuo TT, Yeh CK. Carpal tunnel syndrome: US strain imaging for diagnosis. *Radiology* 2015; **275**: 205-214 [PMID: 25599155 DOI: 10.1148/radiol.14140017]
12 **Ghajarzadeh M**, Dadgostar M, Sarraf P, Emami-Razavi SZ, Miri S, Malek M. Application of ultrasound elastography for determining carpal tunnel syndrome severity. *Jpn J Radiol* 2015; **33**: 273-278 [PMID: 25895157 DOI: 10.1007/s11604-015-0416-3]
13 **Klauser AS,** Miyamoto H, Martinoli C, Tagliafico AS, Szantkay J, Feuchtner G, Jaschke W. Sonoelastographic Findings of Carpal Tunnel Injection. *Ultraschall Med* 2015; **36**: 618-622 [PMID: 25734410 DOI: 10.1055/s-0034-1385836]
14 **Miyamoto H**, Miura T, Morizaki Y, Uehara K, Ohe T, Tanaka S. Comparative study on the stiffness of transverse carpal ligament between normal subjects and carpal tunnel syndrome patients. *Hand Surg* 2013; **18**: 209-214 [PMID: 24164125 DOI: 10.1142/S0218810413500251]
15 **Miyamoto H**, Siedentopf C, Kastlunger M, Martinoli C, Gabl M, Jaschke WR, Klauser AS. Intracarpal tunnel contents: evaluation of the effects of corticosteroid injection with sonoelastography. *Radiology* 2014; **270**: 809-815 [PMID: 24475831 DOI: 10.1148/radiol.13131083]
16 **Mackinnon SE**, Dellon AL, Hudson AR, Hunter DA. Chronic nerve compression--an experimental model in the rat. *Ann Plast Surg* 1984; **13**: 112-120 [PMID: 6476732 DOI: 10.1097/00000637-198408000-00004]
17 **Tai TW**, Wu CY, Su FC, Chern TC, Jou IM. Ultrasonography for diagnosing carpal tunnel syndrome: a meta-analysis of diagnostic test accuracy. *Ultrasound Med Biol* 2012; **38**: 1121-1128 [PMID: 22542258 DOI: 10.1016/j.ultrasmedbio.2012.02.026]
18 **Klauser AS**, Halpern EJ, De Zordo T, Feuchtner GM, Arora R, Gruber J, Martinoli C, Löscher WN. Carpal tunnel syndrome assessment with US: value of additional cross-sectional area measurements of the median nerve in patients versus healthy volunteers. *Radiology* 2009; **250**: 171-177 [PMID: 19037017 DOI: 10.1148/radiol.2501080397]
19 **Roll SC**, Evans KD, Li X, Freimer M, Sommerich CM. Screening for carpal tunnel syndrome using sonography. *J Ultrasound Med* 2011; **30**: 1657-1667 [PMID: 22124001]
20 **Tajika T**, Kobayashi T, Yamamoto A, Kaneko T, Takagishi K. Diagnostic utility of sonography and correlation between sonographic and clinical findings in patients with carpal tunnel syndrome. *J Ultrasound Med* 2013; **32**: 1987-1993 [PMID: 24154903 DOI: 10.7863/ultra.32.11.1987]
21 **Hobson-Webb LD**, Massey JM, Juel VC, Sanders DB. The ultrasonographic wrist-to-forearm median nerve area ratio in carpal tunnel syndrome. *Clin Neurophysiol* 2008; **119**: 1353-1357 [PMID: 18387336 DOI: 10.1016/j.clinph.2008.01.101]
22 **Visser LH**, Smidt MH, Lee ML. Diagnostic value of wrist median nerve cross sectional area versus wrist-to-forearm ratio in carpal tunnel syndrome. *Clin Neurophysiol* 2008; **119**: 2898-2899; author reply 2899 [PMID: 18926765 DOI: 10.1016/j.clinph.2008.08.022]
23 **Kang S**, Kwon HK, Kim KH, Yun HS. Ultrasonography of median nerve and electrophysiologic severity in carpal tunnel syndrome. *Ann Rehabil Med* 2012; **36**: 72-79 [PMID: 22506238 DOI: 10.5535/arm.2012.36.1.72]
24 **Mhoon JT**, Juel VC, Hobson-Webb LD. Median nerve ultrasound as a screening tool in carpal tunnel syndrome: correlation of cross-sectional area measures with electrodiagnostic abnormality. *Muscle Nerve* 2012; **46**: 871-878 [PMID: 23041984 DOI: 10.1002/mus.23426]
25 **Fu T**, Cao M, Liu F, Zhu J, Ye D, Feng X, Xu Y, Wang G, Bai Y. Carpal tunnel syndrome assessment with ultrasonography: value of inlet-to-outlet median nerve area ratio in patients versus healthy volunteers. *PLoS One* 2015; **10**: e0116777 [PMID: 25617835 DOI: 10.1371/journal.pone.0116777]
26 **Sarría L**, Cabada T, Cozcolluela R, Martínez-Berganza T, García S. Carpal tunnel syndrome: usefulness of sonography. *Eur Radiol* 2000; **10**: 1920-1925 [PMID: 11305571 DOI: 10.1007/s003300000502]
27 **Hough AD**, Moore AP, Jones MP. Reduced longitudinal excursion of the median nerve in carpal tunnel syndrome. *Arch Phys Med Rehabil* 2007; **88**: 569-576 [PMID: 17466724 DOI: 10.1016/j.apmr.2007.02.015]
28 **Sernik RA**, Abicalaf CA, Pimentel BF, Braga-Baiak A, Braga L, Cerri GG. Ultrasound features of carpal tunnel syndrome: a prospective case-control study. *Skeletal Radiol* 2008; **37**: 49-53 [PMID: 17989976 DOI: 10.1007/s00256-007-0372-9]
29 **Ghasemi-Esfe AR**, Khalilzadeh O, Mazloumi M, Vaziri-Bozorg SM, Niri SG, Kahnouji H, Rahmani M. Combination of high-resolution and color Doppler ultrasound in diagnosis of carpal tunnel syndrome. *Acta Radiol* 2011; **52**: 191-197 [PMID: 21498348 DOI: 10.1258/ar.2010.100299]
30 **Vanderschueren GA**, Meys VE, Beekman R. Doppler sonography for the diagnosis of carpal tunnel syndrome: a critical review. *Muscle Nerve* 2014; **50**: 159-163 [PMID: 24633597 DOI: 10.1002/mus.24241]
31 **Ghasemi-Esfe AR**, Khalilzadeh O, Vaziri-Bozorg SM, Jajroudi M, Shakiba M, Mazloumi M, Rahmani M. Color and power Doppler US for diagnosing carpal tunnel syndrome and determining its severity: a quantitative image processing method. *Radiology* 2011; **261**: 499-506 [PMID: 21900619 DOI: 10.1148/radiol.11110150]
32 **Yoshii Y,** Ishii T, Tanaka T, Tung WL, Sakai S. Detecting median nerve strain changes with cyclic compression apparatus: a comparison of carpal tunnel syndrome patients and healthy controls. *Ultrasound Med Biol* 2015; **41**: 669-674 [PMID: 25619788 DOI: 10.1016/j.ultrasmedbio.2014.09.020]
33 **Yoshii Y**, Ishii T, Etou F, Sakai S, Tanaka T, Ochiai N. Reliability of automatic vibratory equipment for ultrasonic strain measurement of the median nerve. *Ultrasound Med Biol* 2014; **40**: 2352-2357 [PMID: 25130452 DOI: 10.1016/j.ultrasmedbio.2014.04.005]
34 **Parker KJ**, Fu D, Graceswki SM, Yeung F, Levinson SF. Vibration sonoelastography and the detectability of lesions. *Ultrasound Med Biol* 1998; **24**: 1437-1447 [PMID: 10385965 DOI: 10.1016/S0301-5629(98)00123-9]
35 **Kantarci F**, Ustabasioglu FE, Delil S, Olgun DC, Korkmazer B, Dikici AS, Tutar O, Nalbantoglu M, Uzun N, Mihmanli I. Median nerve stiffness measurement by shear wave elastography: a potential sonographic method in the diagnosis of carpal tunnel syndrome. *Eur Radiol* 2014; **24**: 434-440 [PMID: 24220753 DOI: 10.1007/s00330-013-3023-7]

36 **Orman G**, Ozben S, Huseyinoglu N, Duymus M, Orman KG. Ultrasound elastographic evaluation in the diagnosis of carpal tunnel syndrome: initial findings. *Ultrasound Med Biol* 2013; **39**: 1184-1189 [PMID: 23643060 DOI: 10.1016/j.ultrasmedbio.2013.02.016]

37 **Miyamoto H**, Halpern EJ, Kastlunger M, Gabl M, Arora R, Bellmann-Weiler R, Feuchtner GM, Jaschke WR, Klauser AS. Carpal tunnel syndrome: diagnosis by means of median nerve elasticity--improved diagnostic accuracy of US with sonoelastography. *Radiology* 2014; **270**: 481-486 [PMID: 24471391 DOI: 10.1148/radiol.13122901]

38 **Kuhlman KA**, Hennessey WJ. Sensitivity and specificity of carpal tunnel syndrome signs. *Am J Phys Med Rehabil* 1997; **76**: 451-457 [PMID: 9431262 DOI: 10.1097/00002060-199711000-00004]

39 **Graham B**, Regehr G, Naglie G, Wright JG. Development and validation of diagnostic criteria for carpal tunnel syndrome. *J Hand Surg Am* 2006; **31**: 919-924 [PMID: 16886290 DOI: 10.1016/j.jhsa.2006.03.005]

40 **LeBlanc KE**, Cestia W. Carpal tunnel syndrome. *Am Fam Physician* 2011; **83**: 952-958 [PMID: 21524035]

41 **Witt JC**, Hentz JG, Stevens JC. Carpal tunnel syndrome with normal nerve conduction studies. *Muscle Nerve* 2004; **29**: 515-522 [PMID: 15052616]

42 **Fowler JR**, Munsch M, Tosti R, Hagberg WC, Imbriglia JE. Comparison of ultrasound and electrodiagnostic testing for diagnosis of carpal tunnel syndrome: study using a validated clinical tool as the reference standard. *J Bone Joint Surg Am* 2014; **96**: e148 [PMID: 25187592 DOI: 10.2106/JBJS.M.01250]

43 **Fowler JR**, Maltenfort MG, Ilyas AM. Ultrasound as a first-line test in the diagnosis of carpal tunnel syndrome: a cost-effectiveness analysis. *Clin Orthop Relat Res* 2013; **471**: 932-937 [PMID: 23129465 DOI: 10.1007/s11999-012-2662-3]

44 **Smidt MH**, Visser LH. Carpal tunnel syndrome: clinical and sonographic follow-up after surgery. *Muscle Nerve* 2008; **38**: 987-991 [PMID: 18537147 DOI: 10.1002/mus.20982]

45 **Kim JY**, Yoon JS, Kim SJ, Won SJ, Jeong JS. Carpal tunnel syndrome: Clinical, electrophysiological, and ultrasonographic ratio after surgery. *Muscle Nerve* 2012; **45**: 183-188 [PMID: 22246872 DOI: 10.1002/mus.22264]

46 **Ustün N**, Tok F, Yagz AE, Kizil N, Korkmaz I, Karazincir S, Okuyucu E, Turhanoglu AD. Ultrasound-guided vs. blind steroid injections in carpal tunnel syndrome: A single-blind randomized prospective study. *Am J Phys Med Rehabil* 2013; **92**: 999-1004 [PMID: 23811617 DOI: 10.1097/PHM.0b013e31829b4d72]

47 **Duncan I**, Sullivan P, Lomas F. Sonography in the diagnosis of carpal tunnel syndrome. *AJR Am J Roentgenol* 1999; **173**: 681-684 [PMID: 10470903]

48 **Lee D**, van Holsbeeck MT, Janevski PK, Ganos DL, Ditmars DM, Darian VB. Diagnosis of carpal tunnel syndrome. Ultrasound versus electromyography. *Radiol Clin North Am* 1999; **37**: 859-872, x [PMID: 10442084]

49 **Swen WA**, Jacobs JW, Bussemaker FE, de Waard JW, Bijlsma JW. Carpal tunnel sonography by the rheumatologist versus nerve conduction study by the neurologist. *J Rheumatol* 2001; **28**: 62-69 [PMID: 11196545]

50 **Nakamichi K**, Tachibana S. Ultrasonographic measurement of median nerve cross-sectional area in idiopathic carpal tunnel syndrome: Diagnostic accuracy. *Muscle Nerve* 2002; **26**: 798-803 [PMID: 12451604]

51 **Wong SM**, Griffith JF, Hui AC, Tang A, Wong KS. Discriminatory sonographic criteria for the diagnosis of carpal tunnel syndrome. *Arthritis Rheum* 2002; **46**: 1914-1921 [PMID: 12124876]

52 **Kele H**, Verheggen R, Bittermann HJ, Reimers CD. The potential value of ultrasonography in the evaluation of carpal tunnel syndrome. *Neurology* 2003; **61**: 389-391 [PMID: 12913205]

53 **Altinok T**, Baysal O, Karakas HM, Sigirci A, Alkan A, Kayhan A, Yologlu S. Ultrasonographic assessment of mild and moderate idiopathic carpal tunnel syndrome. *Clin Radiol* 2004; **59**: 916-925 [PMID: 15451352]

54 **El Miedany YM**, Aty SA, Ashour S. Ultrasonography versus nerve conduction study in patients with carpal tunnel syndrome: substantive or complementary tests? *Rheumatology* (Oxford) 2004; **43**: 887-895 [PMID: 15100417]

55 **Keleş I**, Karagülle Kendi AT, Aydin G, Zöğ SG, Orkun S. Diagnostic precision of ultrasonography in patients with carpal tunnel syndrome. *Am J Phys Med Rehabil* 2005; **84**: 443-450 [PMID: 15905658]

56 **Ziswiler HR**, Reichenbach S, Vögelin E, Bachmann LM, Villiger PM, Jüni P. Diagnostic value of sonography in patients with suspected carpal tunnel syndrome: a prospective study. *Arthritis Rheum* 2005; **52**: 304-311 [PMID: 15641050]

57 **Mallouhi A**, Pülzl P, Trieb T, Piza H, Bodner G. Predictors of carpal tunnel syndrome: accuracy of gray-scale and color Doppler sonography. *AJR Am J Roentgenol* 2006; **186**: 1240-1245 [PMID: 16632712]

58 **Wiesler ER**, Chloros GD, Cartwright MS, Smith BP, Rushing J, Walker FO. The use of diagnostic ultrasound in carpal tunnel syndrome. *J Hand Surg Am* 2006; **31**: 726-732 [PMID: 16713832]

59 **Naranjo A**, Ojeda S, Mendoza D, Francisco F, Quevedo JC, Erausquin C. What is the diagnostic value of ultrasonography compared to physical evaluation in patients with idiopathic carpal tunnel syndrome? *Clin Exp Rheumatol* 2007; **25**: 853-859 [PMID: 18173919]

60 **Kaymak B**, Ozçakar L, Cetin A, Candan Cetin M, Akinci A, Hasçelik Z. A comparison of the benefits of sonography and electrophysiologic measurements as predictors of symptom severity and functional status in patients with carpal tunnel syndrome. *Arch Phys Med Rehabil* 2008; **89**: 743-748 [PMID: 18374007 DOI: 10.1016/j.apmr.2007.09.041]

61 **Kwon BC**, Jung KI, Baek GH. Comparison of sonography and electrodiagnostic testing in the diagnosis of carpal tunnel syndrome. *J Hand Surg Am* 2008; **33**: 65-71 [PMID: 18261667 DOI: 10.1016/j.jhsa.2007.10.014]

62 **Pinilla I**, Martín-Hervás C, Sordo G, Santiago S. The usefulness of ultrasonography in the diagnosis of carpal tunnel syndrome. *J Hand Surg Eur Vol* 2008; **33**: 435-439 [PMID: 18687830 DOI: 10.1177/1753193408090396]

63 **Visser LH**, Smidt MH, Lee ML. High-resolution sonography versus EMG in the diagnosis of carpal tunnel syndrome. *J Neurol Neurosurg Psychiatry* 2008; **79**: 63-67 [PMID: 17470471]

64 **Ashraf AR**, Jali R, Moghtaderi AR, Yazdani AH. The diagnostic value of ultrasonography in patients with electrophysiologicaly confirmed carpal tunnel syndrome. *Electromyogr Clin Neurophysiol* 2009; **49**: 3-8 [PMID: 19280794]

65 **Pastare D**, Therimadasamy AK, Lee E, Wilder-Smith EP. Sonography versus nerve conduction studies in patients referred with a clinical diagnosis of carpal tunnel syndrome. *J Clin Ultrasound* 2009; **37**: 389-393 [PMID: 19479718 DOI: 10.1002/jcu.20601]

66 **Mohammadi A**, Afshar A, Etemadi A, Masoudi S, Baghizadeh A. Diagnostic value of cross-sectional area of median nerve in grading severity of carpal tunnel syndrome. *Arch Iran Med* 2010; **13**: 516-521 [PMID: 21039008]

67 **Ulaşli AM**, Duymuş M, Nacir B, Rana Erdem H, Koşar U. Reasons for using swelling ratio in sonographic diagnosis of carpal tunnel syndrome and a reliable method for its calculation. *Muscle Nerve* 2013; **47**: 396-402 [PMID: 23169554 DOI: 10.1002/mus.23528]

68 **Ooi CC**, Wong SK, Tan AB, Chin AY, Abu Bakar R, Goh SY, Mohan PC, Yap RT, Png MA. Diagnostic criteria of carpal tunnel syndrome using high-resolution ultrasonography: correlation with nerve conduction studies. *Skeletal Radiol* 2014; **43**: 1387-1394 [PMID: 24915739 DOI: 10.1007/s00256-014-1929-z]

P- Reviewer: Drampalos E, Mariano FF, Metzger PD **S- Editor**: Qi Y
L- Editor: A **E- Editor**: Lu YJ

World Journal of Radiology

Submit a Manuscript: http://www.wjgnet.com/esps/
Help Desk: http://www.wjgnet.com/esps/helpdesk.aspx
DOI: 10.4329/wjr.v8.i3.288

World J Radiol 2016 March 28; 8(3): 288-297
ISSN 1949-8470 (online)

MINIREVIEWS

Diffusion weighted imaging in gynecological malignancies - present and future

Dinesh Manoharan, Chandan J Das, Ankita Aggarwal, Arun K Gupta

Dinesh Manoharan, Chandan J Das, Ankita Aggarwal, Arun K Gupta, Department of Radiology Diagnosis, All India Institute of Medical Science, New Delhi 110029, Delhi, India

Author contributions: Manoharan D and Das CJ contributed equally to conception, article design, literature search, article drafting, critical revision and image preparation; Aggarwal A helped with the article concept and revision; Gupta AK helped in article preparation and final approval of version of article to be published.

Conflict-of-interest statement: There is no conflict of interest associated with any of the senior author or other coauthors contributed their efforts in this manuscript.

Correspondence to: Dr. Chandan J Das, MD, DNB, MNAMS, Assistant Professor, Department of Radiology Diagnosis, All India Institute of Medical Sciences, Ansari Nagar, New Delhi 110029, Delhi, India. docchandan17@gmail.com
Telephone: +91-11-26594889
Fax: +91-11-26588663

Received: May 24, 2015
Peer-review started: May 25, 2015
First decision: September 23, 2015
Revised: October 31, 2015
Accepted: December 3, 2015
Article in press: December 4, 2015
Published online: March 28, 2016

Abstract

The management of gynaecological malignancies has undergone a significant change in recent years with our improved understanding of cancer biogenetics, development of new treatment regimens and enhanced screening. Due to the rapid blooming of newer methods and techniques in gynaecology, surgery and oncology the scope and the role of imaging has also widened. Functional imaging in the form of diffusion weighted imaging (DWI) has been recently found to be very useful in assessing various tumours. Its ability to identify changes in the molecular level has dramatically changed the diagnostic approach of radiologists which was solely based on morphological criteria. It can improve the diagnostic accuracy of conventional magnetic resonance imaging, lend a hand in assessing tumour response to treatment regimens and detect tumour recurrence with better spatial resolution, negative radiation and diagnostic accuracy compared to positron emission tomography scan. The ability to quantify the diffusion has also lead to potential prediction of tumour aggressiveness and grade which directly correlate with the patient prognosis and management. Hence, it has become imperative for a radiologist to understand the concepts of DWI and its present and evolving role. In this article we present a brief description of the basics of DWI followed by its role in evaluation of female gynaecological malignancies.

Key words: Diffusion weighted imaging; Female pelvis; Magnetic resonance imaging; Gynaecology; Malignancy

Core tip: With rapidly evolving strategies in the management of the gynaecological malignancies today there is an increasing role of imaging to keep up with the pace of development and develop newer techniques which help in better management of the patient. Diffusion weighted imaging (DWI) is one such modality which helps in detecting changes at the molecular level and hence can help in better diagnosis of early cancers as well as in assessing response to treatment. The purpose

of this article is to make the reader familiar with the basic concepts of DWI and discuss the latest development in this field in evaluation of female gynaecological malignancies.

Manoharan D, Das CJ, Aggarwal A, Gupta AK. Diffusion weighted imaging in gynecological malignancies - present and future. *World J Radiol* 2016; 8(3): 288-297 Available from: URL: http://www.wjgnet.com/1949-8470/full/v8/i3/288.htm DOI: http://dx.doi.org/10.4329/wjr.v8.i3.288

INTRODUCTION

Diffusion weighted imaging (DWI) has become an integral part of neuroimaging since the 1980's. However its application in other areas apart from the brain has bloomed recently with the advent of faster imaging techniques and newer technologies like echo planar imaging, multichannel coils, parallel imaging and coils which can produce higher gradient amplitudes.

Its ability to assess changes in the molecular level in the brain has paved way for research in other areas such as oncologic imaging to try and further characterize these lesions and to augment morphological information derived from conventional imaging sequences. In this article we review briefly the basic principles of DWI and discuss its role in imaging of gynaecologic tumours.

Principle of diffusion weighted imaging

At molecular level in biologic tissues water molecules are in random motion called Brownian movement. When these water molecules are placed inside a magnetic field they acquire phase and precession frequency shift as time goes on when there is no restriction to their free movement.

However, the free movement of water molecules (Brownian movement) is dependent on various factors like cellular density, cell membrane integrity, intravascular space and the extracellular space. These factors may hinder or facilitate the movement of water molecules thus indirectly affecting their phase and precession frequencies.

DWI is basically a T2 weighted sequence in which we use two equal and opposite motion probing gradients before and after the 180 degree refocusing pulse. When the water molecules which are freely diffusing are exposed to the first pulse they acquire a phase shift which gradually changes and by the time the other equal and opposite gradient is applied they will not regain the signal; as because of free movement they are in different phases to time just after the first pulse hence no signal is produced at the time of acquisition, however water molecules which are static (diffusion restricted) regain signal as no significant phase shift has occurred by the time of second gradient and the signal loss from the first gradient is regained by the second opposite gradient.

The amplitude, duration and temporal spacing of the gradients are expressed as b value. At low b values back ground signal suppression is less due to T2 effects and at high b values there is good background signal suppression however at the expense of inherent signal loss.

Multiple b values images can be taken and the signal intensity at each value can be plotted on a graph and the log of the slope gives the Apparent Diffusion Coefficient (ADC) values. The ADC value is a quantitative measure of the diffusion in each pixel and it can also be represented as an image which can used in visual assessment of the diffusion value. The number of b values taken vary, generally more the b values more accurate is the calculated ADC value. In our institution we take three *b* values *viz*; 0, 400 and 800.

Protocol

DWI of the pelvis is usually single shot Echo Planar Imaging (EPI) sequence which gives excellent contrast to noise ratio (CNR) in spite of poor signal to noise ratio (SNR) due to very good background signal suppression and high tumour intensity. However they are very prone to spatial field distortions and susceptibility artefacts due to bowel movements. To minimize susceptibility artefacts a short TR and various parallel imaging techniques like sensitivity encoding, Generalized Autocalibrating Partial Parallelized Acquisitions are used. To increase the SNR; higher field strength MRI (3 T *vs* 1.5 T), reducing the echo time, increasing the signal averages, section thickness and a field of view can help. In our institution we perform scans using a 3 T system (Achieva 3T, Phillips Medical System); standard imaging parameters used are given in Table 1.

Cervical cancer

Cervical cancer is the second most common cancer in woman and most common gynaecologic cancer in women worldwide. At present the management of cervical cancer is based on International Federation of Gynaecology and obstetrics (FIGO) clinical staging system because most of the disease burden falls on the developing countries where advanced imaging facilities are sparse and most of the patients present in a locally advanced stage[1]. However, with improved healthcare facilities for screening of early cancer and advanced treatment options; more and more early cervical cancers are diagnosed and fertility preserving surgeries are being done[2,3].

Currently clinical FIGO staging is used to assess these tumours. The clinical FIGO staging has an error rate of 20%-64%. Size of tumor, parametrial involvement, pelvic side wall invasion, bowel and bladder involvement and distant metastases which form important prognostic factors are not adequately evaluated clinically[4,5]. Moreover assessing bowel and bladder involvement by rectosigmoidoscopy and cystoscopy respectively may prove fallacious as only mucosal involvement can be picked up by these methods. Hence there is a need for advanced imaging techniques to detect and stage them accurately.

Table 1 Parameters used for 3T magnetic resonance imaging

Parameters	Values
Coil	Six channel SENSE body coil
TR	3000 ms
TE	50 ms
Flip angle	90 deg
FOV	35 cm × 21 cm × 21 cm
Number of excitations	3
Slice thickness	5
Interstice gap	1
Matrix	128 × 128
Bandwidth	3018 Hz/pixel
Parallel imaging	SENSE (factor 2)

SENSE: Sensitivity encoding; FOV: Field of view.

Cervical cancer is a solid tumour and like many of the malignancies has atypical cells with high nuclear cytoplasmic ratio which are closely packed inhibiting the free movement of water molecules at the microscopic level[6]. Consequently, diffusion weighted imaging has been found to be very helping in detection of cervical cancer (Figure 1). A meta-analysis of the available studies conducted by Hou *et al*[7] shows that cervical cancer tissue shows restricted diffusion and lower ADC as compared to normal cervical tissue. Other studies have also shown that diffusion weighted MRI helps in precise demarcation of the tumour margins with reduced rates of overestimating the tumour volume (as in T2w in which both edema and mass are hyper intense)[8-15].

On conventional MRI the tumour is well delineated on T2 weighted sequence where it appears intermediate in signal intensity in the background T2 hypo intense cervical stroma. However in young patients where the cervical stroma is not very T2 hypo intense, the distinction is not very apparent. Also when there is diffusely infiltrating carcinoma or in early stages of tumour, conventional MRI fails to delineate the exact tumour extent[16,17]. Hence staging in such cases can be difficult and in such cases diffusion weighted MRI may help.

Diffusion weighted imaging is also being evaluated in trying to predict response to chemoradiotheraphy. Tumours with higher ADC at baseline are likely to be more necrotic and cystic and hence more hypoxic; due to these factors they may less responsive to chemoradiotherapy. A study by Liu *et al*[11] in 17 patients showed that pre-treatment ADC for complete response group was significantly lower than the partial response group (P = 0.005). Another study by Heo *et al*[18] showed mean ADC and 75th percentile ADC to be significantly higher in patients showing tumour recurrence (P = 0.043 and P = 0.008, respectively). The 75th percentile ADC was also a significant predictor of tumour recurrence in their study (P = 0.009; HR = 1.319). They also found that when the cut-off value of the 75th percentile ADC (0.936 × 10^{-3} mm^2/s) was used, the overall recurrence free survival rate above the cut-off value was significantly lower than that below the cut-off value (51.9% *vs* 91.7%, P = 0.003, log-rank test)[18]. However studies in this regard are very few and more studies are needed to define the exact ADC cut off.

Chemo radiotherapy induces cell necrosis, apoptosis which in turn leads to cell lysis and increase in extracellular space in turn leading to increased water diffusion[19,20]. Hence, Tumour response especially early post radiation/chemotherapy can be potentially assessed by diffusion weighted imaging even when there is no visible morphological change in size of the tumour. Currently the Response Evaluation Criteria In Solid Tumours (RECIST) criteria which is used for treatment response is based on the reduction in size which takes time and dear time could be wasted when there is a immediate need to change the chemotherapy regimen. Various studies have shown the same and in such cases higher values of ADC can be due to tumour lysis and necrosis which suggests response and lower values suggest incomplete response[10,11,17,21-24]. However, Therapies targeted against tumour vasculature will reduce ADC values as perfusion component of the DWI calculation at low b values may be significant in the tumour, also contribution of the inflammatory component which can increase ADC values is unaccounted for in the studies done so far.

In the post chemoradiotherapy setting the detection of recurrent or residual tumour is of pristine importance. It is very difficult to differentiate on conventional MRI as both edema/inflammation as well as tumour appears alike on convention MR sequences (T1 and T2). PET which is commonly used in post treatment setting can be fallacious as it shows activity in residual tumour as well as inflammatory tissue. However recurrent/residual tumour shows lower ADC values as compared to the edematous/inflammatory tissue and can be used to diagnose recurrence or residual tumour[25].

Endometrial carcinoma

Endometrial carcinoma is one of the common gynaecological malignancy and is the most common gynaecological malignancy in Western countries[26]. Depth of tumour invasion into the myometrium and lymph node spread are two important parameters determining the management and prognosis of the patient[17,27]. Patients having greater depth of myometrial invasion and lymph node metastases have a higher incidence of recurrence and worse prognosis.

They are staged as 1a when the tumour is limited to the endometrium with the intact junctional zone. When there is breech of the junctional zone and the tumour invades into less than 50% of the myometrium it is staged as 1b and 1c when the depth of penetration into myometrium is greater than 50% (Figure 2)[27]. This differentiation can also be done on MRI with T2W and post gadolinium T1 weighted sequences. A systematic review and metaanalysis of nine studies done by Andreano *et al*[28] showed that DWI and dynamic Contrast Enhanced (DCE) imaging showed similar high sensitivity of 86% in predicting the preoperative stage of the disease. In cases where junctional zone is indistinct or thinned out as in post-menopausal females or in cases of adenomyosis

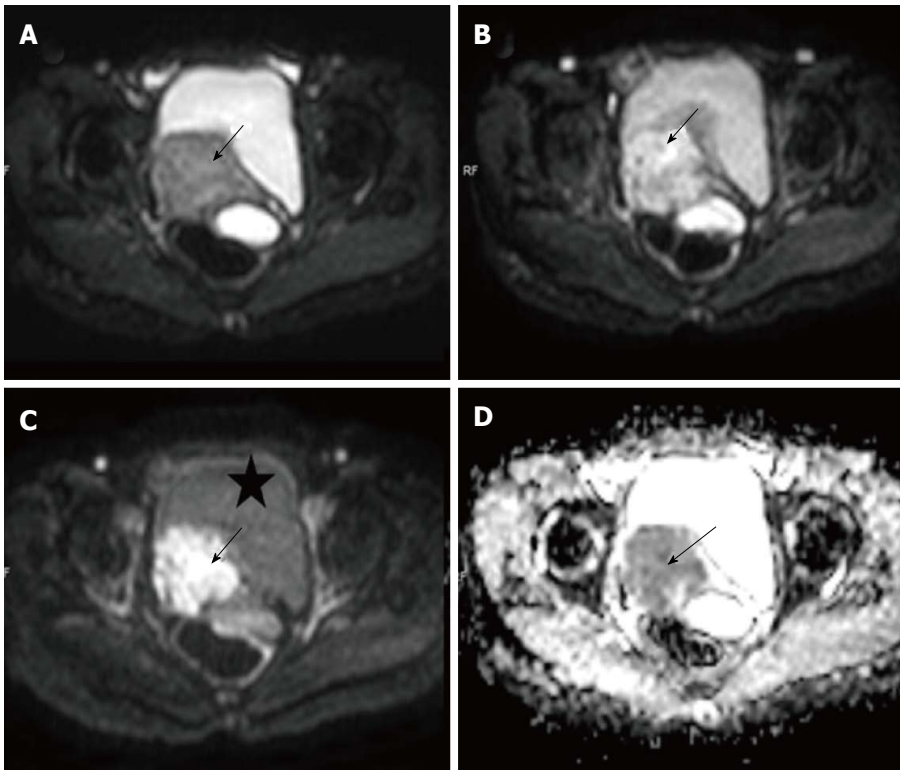

Figure 1 Carcinoma cervix. Axial diffusion weighted imagings of a biopsy proven case of carcinoma cervix show a mass (arrow) involving the cervix having hyper intense signal on b 0 (A), b 400 (B) and b 800 (C) images; Note the progressive loss of signal of the urinary bladder (marked as asterisk) as the B value increases; the mass is also hypointense on corresponding apparent diffusion coefficient image (D) confirming true diffusion restriction.

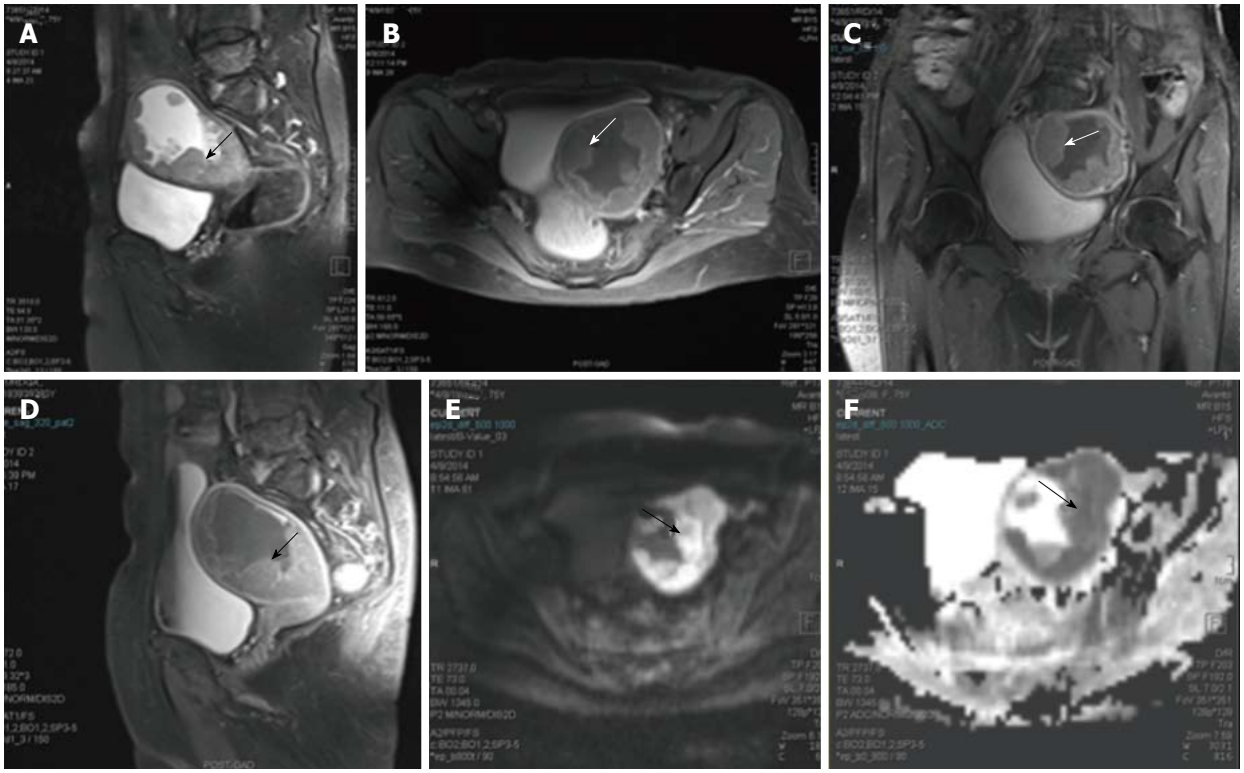

Figure 2 Endometrial carcinoma. Sagittal T2 weighted magnetic resonance image of a female who presented with menorrhagia. It shows irregular nodular thickening of the endometrial (arrow in A). The lesion on post contrast axial (B), coronal (C) and sagittal (D) images shows enhancement. On diffusion weighted imaging (E) and corresponding apparent diffusion coefficient (F) images, the lesion showed significant restriction of diffusion. The tumour is limited to the outer myometrium and no parametrial invasion noted suggesting a T1c disease. This lesion on biopsy turned out to be carcinoma endometrium.

when the size of the junctional zone is increased it may be difficult on DCE and T2W images alone to predict the depth of myometrial invasion. In such cases of diagnostic dilemma DWI can increase the diagnostic confidence[28,29].

In case of additional presence of benign lesions in myometrium, determining the depth of invasion is problem

due to heterogenous appearance of the myometrium. Also in cases when there are large polypoidal tumours there occurs stretching of the junctional zone leading to under staging of the carcinoma of endometrium. In all such cases DWI acts as an important ancillary study to correctly stage the tumour. Correct staging is important as it determines management [type of hysterectomy-Radical *vs* total abdominal hysterectomy (TAH)] and also in prognosis of the carcinoma[17,27-29].

Another role of DWI is to differentiate residual tumour or recurrence from post-surgical/radiotherapy changes which leads to distortion of the normal anatomy. Since both the residual tumour and post-operative inflammatory/post radiotherapy changes look alike on conventional imaging (both are T2 hyper intense), it is the diffusion weighted imaging which makes a distinction. Any tumour recurrence or residual tumour will show restriction of diffusion with lower ADC values whereas inflammatory tissue will not show any restriction.

Uterine sarcomas

Uterine sarcomas are broadly divided into two groups as non-epithelial and mixed epithelial - non epithelial neoplasms according to their histological characteristics. There are four types which fall into these broad groups; they are leiomyosarcoma, endometrial stromal tumour (ESS), undifferentiated endometrial sarcoma (UES) and adenosarcoma.

It is of pristine importance to differentiate these lesions from benign lesions as their management differs and they are often equal on clinical manifestations and on routine ultrasound imaging[30]. A study showed that the mean ADC value of sarcomas was lower than that of normal myometrium and degenerated leiomyomas; also sarcomas showed higher signal intensity on DWI images; however ordinary leiomyomas and cellular leiomyomas also showed overlapping ADC values and hyper intensity on DWI. This can be due by "T2 black out effect", since ordinary leiomyomas contain high hyalinized collagen they are hypointense on T2 weighted and DWI images leading to low ADC values.

Another study by Namimoto *et al*[31] showed similar findings however DWI combined with T2 weighted imaging showed improved diagnostic accuracy in their differentiation.

Thomassin-Naggara *et al*[32] in a retrospective study proposed a recursive partitioning model, using b 1000 signal intensity, T2 signal intensity, mean ADC, and patient age which correctly classified benign and malignant lesions in 92.4 % of cases.

Adenosarcomas are usually low grade tumours and typically present as polyps. They have been shown to have low ADC values in the limited studies available[33,34]. Overall studies trying to differentiate leiomyoma from sarcomas in terms of ADC values alone have been inconsistent with considerable overlap in values, ADC could be used as a adjuvant tool along with other parameters to increase the diagnostic confidence to characterize benign from malignant lesions[31-37].

Pelvic lymph node assessment

Pelvic lymph node involvement can also be easily assessed with diffusion weighted imaging. The most commonly used criteria for metastatic involvement on conventional MR sequences are morphology based which are node size > 10 mm, irregularly margins, contrast enhancement same as parent tumour tissue, extra nodal soft tissue and necrosis[17,21]. However various studies done shows that this is not an accurate method to detect metastasis[38-41]. Kitajima *et al*[41] found that in patients of endometrial and cervical cancer patients showed that DWI was better in detecting metastatic nodes compared to even PET CT ($P < 0.005$). However none were significantly adequate to replace lymphadenectomy. Hence DWI may serve as an important adjuvant method for diagnosis of lymph node involvement along with conventional imaging.

Ovarian cancer

Ovarian cancer is the fifth most common cancer in women worldwide. Very frequently women are diagnosed in late stages as it is most often asymptomatic in early stages[42]. Currently Ultrasound forms the initial imaging investigation of choice for the diagnosis of ovarian cancer; if the ultrasound is highly suspicious of ovarian cancer then patient directly undergoes abdominal CT scan followed by staging laprotomy. Features on ultrasound (US) that are suggestive of ovarian malignancy include an heteroechoic and irregular solid mass, an irregular multilocular cystic mass, presence of solid components or papillary projections in the cyst, high flow on colour doppler, ascitis, peritoneal nodules, and other evidence of metastatic disease in other organs[43]. However some of these masses remain indeterminate on USG and contrast enhanced MRI forms the investigation of choice in these patients. DWI can not only help in identifying the primary lesion (Figure 3) but also helps in identifying the deposits (Figures 3 and 4). Moreover, DWI can identify metastasis to ovary from other primaries (Figure 5).

Studies on the utility of DWI to differentiate benign from malignant ovarian lesions have been conflicting. Study done by Katayama *et al*[44] showed DWI provided no additional advantage over conventional MRI sequences. Another study by Moteki *et al*[45] showed that in small and medium sized lesions sized less than 12 cm ADC values were significantly lesser in malignant lesions($P < 0.03$). In this study the incorrectly higher ADC values in larger lesions > 12 cm were attributed to the sloshing effect intermittent compression of large ovarian lesions by abdominal breathing before the breath-hold scan[45]. In another study Nakayama *et al*[46] found that diffusion can be useful in fat poor teratomas as the keratinised content showed low ADC values. The problems in characterizing cystic lesions are further compounded by the susceptibility

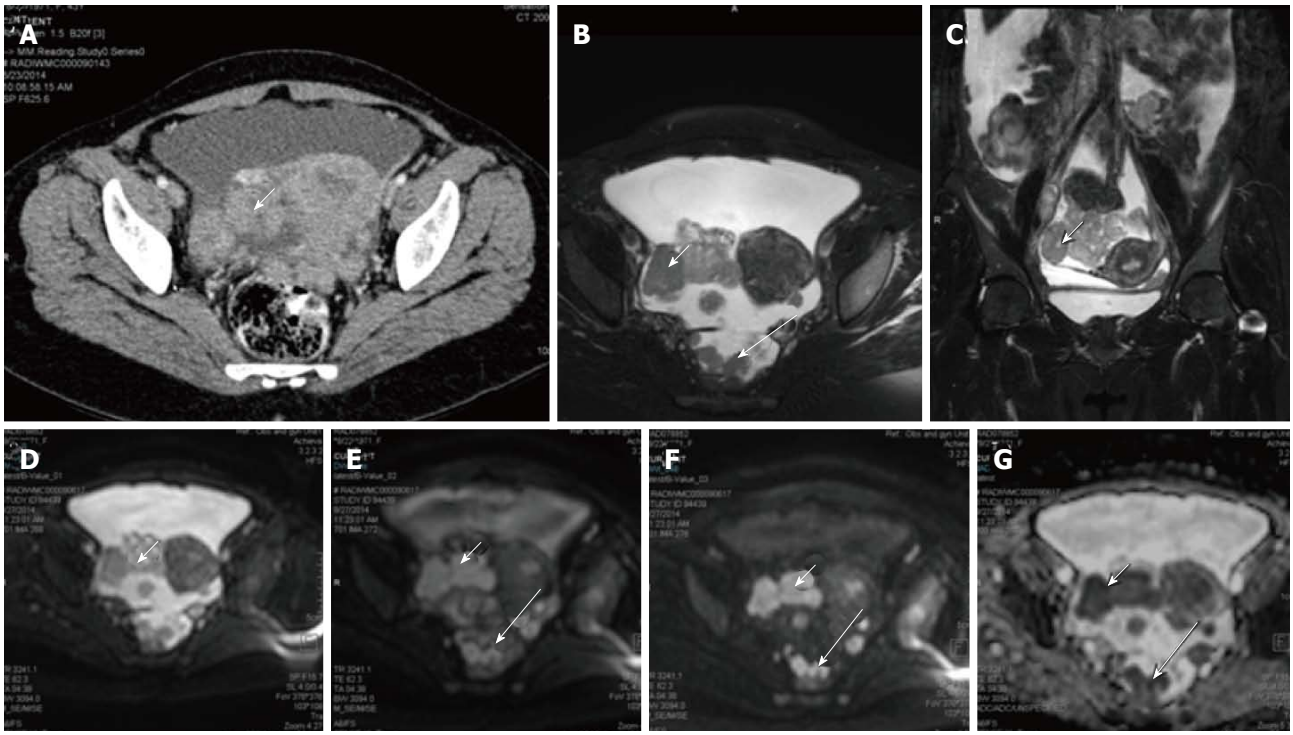

Figure 3 Carcinoma ovary. Axial contrast enhanced computed tomography image (A), T2 weighted axial (B) and coronal (C) images of a patient with known ovarian cancer shows right adnexal mass (arrows) multiple deposits in peritoneum of the pelvis (long arrows); On DWI, b 0 (D), b 400 (E), b 800 (F) and ADC (G) images show significant diffusion restriction in the primary (arrow) as well as peritoneal deposits (long arrow). These lesions were proven to be malignant deposits on fine needle aspiration cytology. ADC: Apparent diffusion coefficient; DWI: Diffusion weighted imaging.

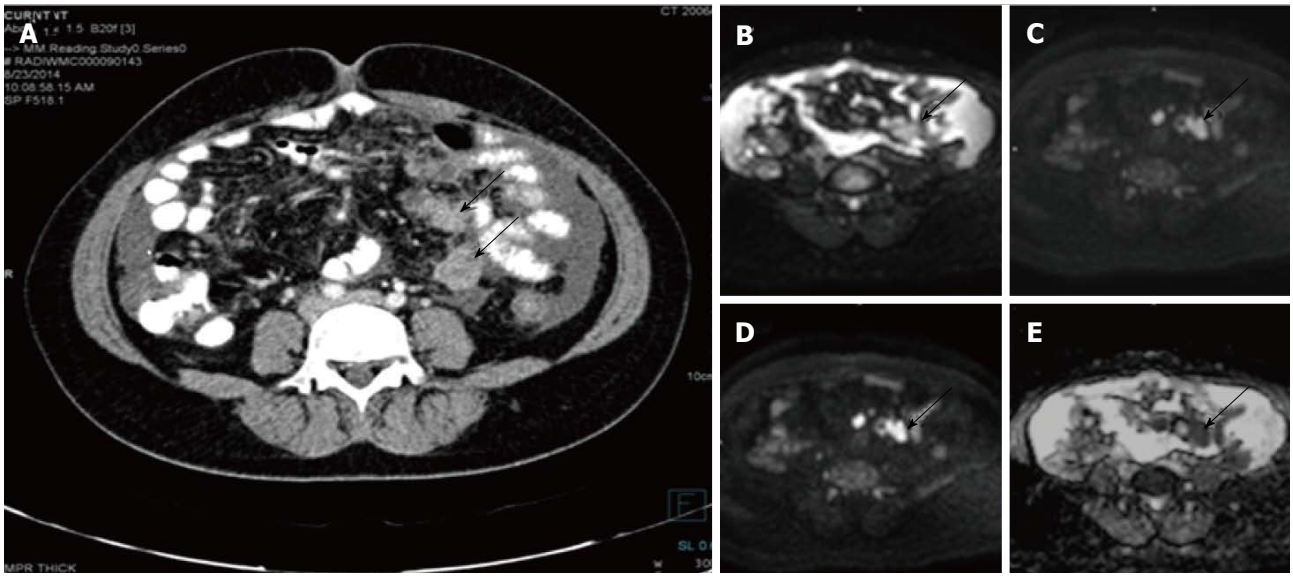

Figure 4 Serosal deposits in carcinoma ovary. Axial contrast enhanced computed tomography image (A) of a patient with known ovarian cancer shows enhancing soft tissues (arrows) over the surface of small bowel suggestive of serosal deposits. On diffusion weighted imaging, b 0 (B), b 400 (C), b 800 (D) and ADC (E) images show significant diffusion restriction in the serosal deposits. These lesions were proven to be malignant deposits on fine needle aspiration cytology. ADC: Apparent

artifacts induced by the blood products in the hemorrhagic cysts and the endometrial cysts[44,45].

Peritoneal deposits

Gynaecological malignancies especially ovarian cancer is known to present with peritoneal and serosal deposits (Figures 3 and 4). This transcoelomic spread of cancer is many of the times first presentation and presence of such implants determine further management. Fujii *et al*[47] showed sensitivity and specificity of 90% and 95.5% respectively for diffusion weighted imaging in detecting such deposits. In another study done by Low *et al*[48] combined conventional and DWI imaging showed better sensitivity and accuracy than DWI alone

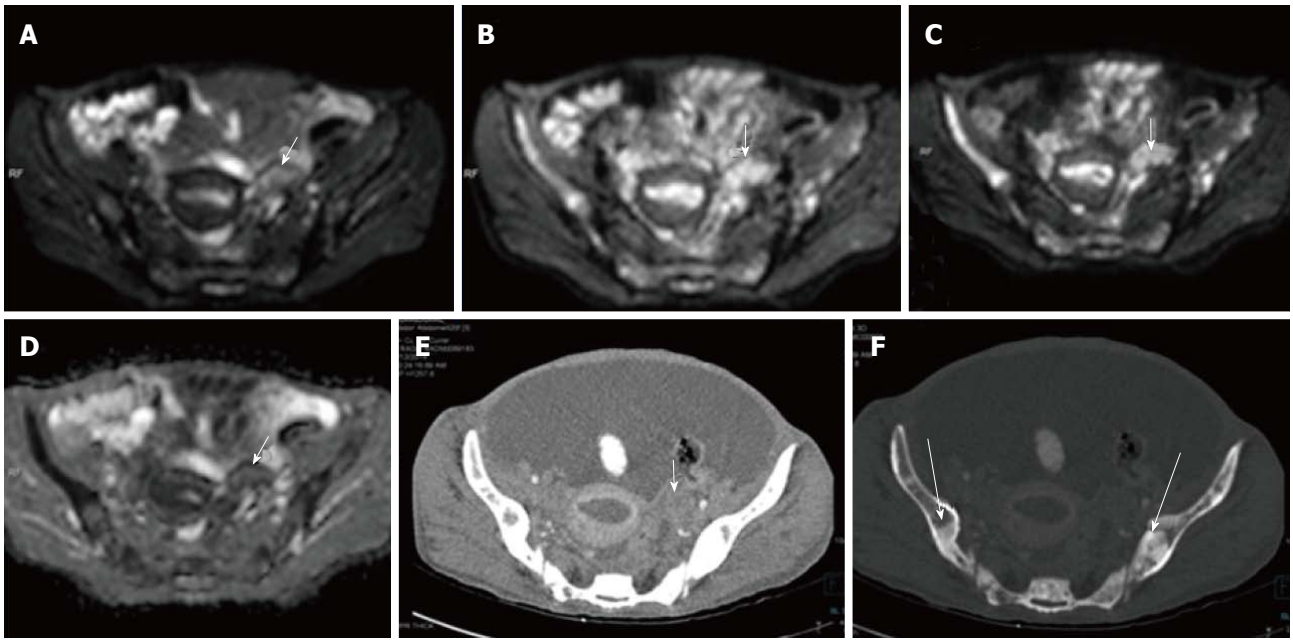

Figure 5 Left ovarian metastasis. Axial diffusion weighted imaging b 0 (A), b 400 (B), b 800 (C) and ADC (D) images of known case of carcinoma breast shows significant restricted diffusion of the left ovarian mass (arrow) suggesting left ovarian metastasis. Note is also made of multiple hypertense diffusion restricting lesions in the b/lilliac bone which were metastatic deposits. Axial contrast enhanced CT (E) showing the left adnexal mass (arrow) with multiple sclerotic metastases (thick arrows) in bilateral illiac bones better seen on CT bone window image (F). ADC: Apparent diffusion coefficient; CT: Computed tomography.

in detecting peritoneal implants. DWI significantly increases accuracy in detecting deposits and can be done routinely to detect the same.

Diffusion-weighted whole-body imaging with background body signal suppression

Whole body magnetic resonance diffusion-weighted imaging with background signal suppression (MR-DWIBS) background signal suppression (MR-DWIBS) is an exciting new technique that has come into vogue. This technique has the potential to detect distant metastasis and can be used as a part of staging work up, look for treatment response and detect recurrence[49,50]. Three-dimensional (3D) display of DWI can produce positron emission tomography (PET) like images.

In a study involving mixed cancer patients; Komori *et al*[51] found that a larger number of malignant tumors were detected visually with whole-body DWI than with PET/CT. However, it was difficult to differentiate between benign and malignant lesions. This has been one of the drawbacks of DWIBS, many benign lesions as well as normal structures such as abscesses, brain, salivary glands, tonsils, spleen, gallbladder, small intestine/small intestinal contents, colon, adrenal glands, prostate, testes etc may all exhibit high signal intensity showing diffusion restriction and is very difficult to differentiate from malignant involvement[50]. Sugita *et al*[52] found PET/CT to be more reliable than DWI and contrast-enhanced CT (CE-CT) in the detection of peritoneal dissemination. The sensitivity of PET/CT, DWI, and CE-CT were 94%, 85%, and 83% and the specificity were 94%, 89% and 87%, respectively. Current research in this area is largely limited to mixed tumour group; more studies in this area and research on individual gynaecological tumours are needed to determine the exact utility.

Pitfalls of DWI

Tissues with long relaxation time may have high signal intensity on DWI images especially on low b value images due to a phenomenon known as T2 shine through. If a lesion is bright on both DWI and ADC images, then it's likely due to shine through effect. This is a problem especially encountered in cystic lesions. In that situation, true diffusion can be found by correlating with the corresponding ADC map image to avoid T2 shine through[52].

On the other hand well-differentiated tumours may exhibit less restriction of diffusion due to their low cellularity. Other benign conditions such as blood (Figure 6), fat, abscesses, lymph nodes, and melanin may show restricted diffusion. Noting the baseline T1 and T2 images may help in arriving at the correct diagnosis.

The normal endometrium especially in secretory phase which is hyperplastic may show diffusion restriction due to very tightly packed cells and consequently will have low ADC values.

T2 shine-through effect may be produced by retained mucus and desmoplastic reaction post radiotheraphy may also show diffusion restriction however on high b value images (b1000 and above) they are no longer hyper intense.

Future direction

Although it has been used for evaluation of uterocervical as well as ovarian malignancies with inspiring results,

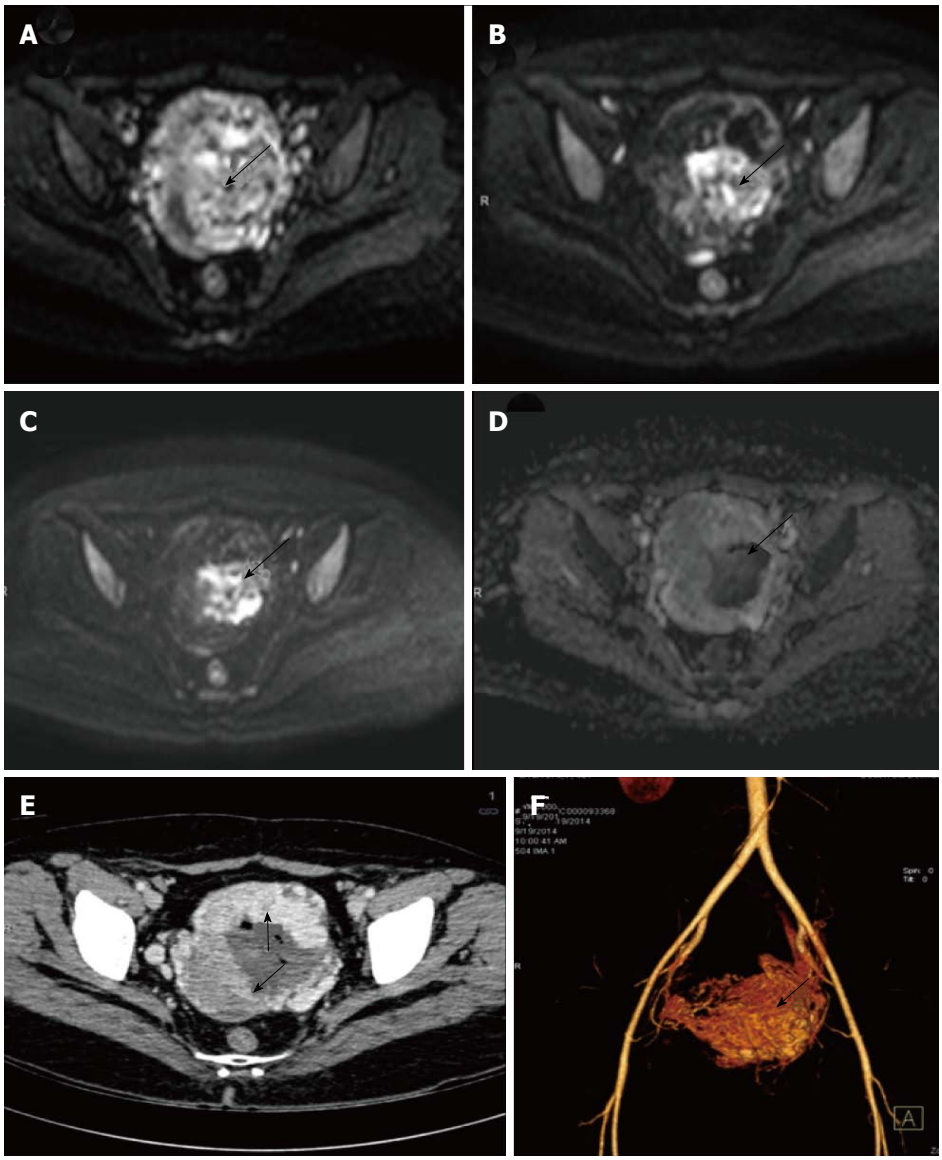

Figure 6 Gestational trophoblastic tumor. Axial diffusion weighted imaging b 0 (A), b 400 (B) and b 800 (C) and images of known case of gestational trophoblastic tumor shows significant restricted diffusion in the center of the mass (arrow). Note there is spurious restriction in ADC image (D). Axial contrast enhanced CT (E) showing the enhancing uterine mass (arrows) with nonenhancing central area likely hemorrhage which is responsible for the spurious diffusion restriction on DWI. CT angiography image (F) showing marked vascularity of the mass leading to intratumoral hemorrhage. ADC: Apparent diffusion coefficient; DWI: Diffusion weighted imaging; CT: Computed tomography.

paucity of studies is noted in the evaluation of vulvovaginal malignancies where deep spread can necessitate the need for cross sectional imaging. In ovarian cystic lesions haemorrhage often complicates the picture by causing susceptibility artifacts because of the EPI method used to acquire the DWI sequence. However with more and more advanced imaging techniques the artefacts can be reduced and it may pave the way for better characterization of ovarian cysts. The role of advanced diffusion imaging techniques such as diffusion tensor imaging, diffusion spectral imaging, diffusion weighted whole body imaging with background signal suppression (DWIBS) needs to be discovered in evaluating pelvic floor muscles and uterine musculatures before fertility preserving surgeries. These techniques have the potential to map the nerve fibre preoperatively which can guide the surgeons during surgery and thus can reduce post-operative complications.

CONCLUSION

In the last few years, DWI is gaining popularity and has been an important addition to the armamentarium of MRI. DWI has emerged as a robust tool for the evaluation of gynaecologic malignancies because of its ability to evaluate the functional status of the tumour similar to PET scan but without the risk of ionizing radiation. As the sequence takes very less time to acquire and is available in most of the 1.5 T and 3 T scanners, it is strongly recommended to be acquired along with routine MR sequences in evaluation of gynaecological malignancies.

REFERENCES

1 **Pecorelli S**, Zigliani L, Odicino F. Revised FIGO staging for carcinoma of the cervix. *Int J Gynaecol Obstet* 2009; **105**: 107-108 [PMID: 19342051 DOI: 10.1016/j.ijgo.2009.02.009]

2 **Sankaranarayanan R**, Esmy PO, Rajkumar R, Muwonge R, Swaminathan R, Shanthakumari S, Fayette JM, Cherian J. Effect of visual screening on cervical cancer incidence and mortality in Tamil Nadu, India: a cluster-randomised trial. *Lancet* 2007; **370**: 398-406 [PMID: 17679017 DOI: 10.1016/S0140-6736(07)61195-7]

3 **Thulaseedharan JV**, Malila N, Hakama M, Esmy PO, Cherian M, Swaminathan R, Muwonge R, Sankaranarayanan R. Effect of screening on the risk estimates of socio demographic factors on cervical cancer - a large cohort study from rural India. *Asian Pac J Cancer Prev* 2013; **14**: 589-594 [PMID: 23534800 DOI: 10.7314/APJCP.2013.14.1.589]

4 **Creasman WT**. New gynecologic cancer staging. *Gynecol Oncol* 1995; **58**: 157-158 [PMID: 7622099 DOI: 10.1006/gyno.1995.1203]

5 **Piver MS**, Chung WS. Prognostic significance of cervical lesion size and pelvic node metastases in cervical carcinoma. *Obstet Gynecol* 1975; **46**: 507-510 [PMID: 1196552]

6 **Saslow D**, Solomon D, Lawson HW, Killackey M, Kulasingam SL, Cain J, Garcia FA, Moriarty AT, Waxman AG, Wilbur DC, Wentzensen N, Downs LS, Spitzer M, Moscicki AB, Franco EL, Stoler MH, Schiffman M, Castle PE, Myers ER. American Cancer Society, American Society for Colposcopy and Cervical Pathology, and American Society for Clinical Pathology screening guidelines for the prevention and early detection of cervical cancer. *CA Cancer J Clin* 2012; **62**: 147-172 [PMID: 22422631 DOI: 10.3322/caac.21139]

7 **Hou B**, Xiang SF, Yao GD, Yang SJ, Wang YF, Zhang YX, Wang JW. Diagnostic significance of diffusion-weighted MRI in patients with cervical cancer: a meta-analysis. *Tumour Biol* 2014; **35**: 11761-11769 [PMID: 25168365 DOI: 10.1007/s13277-014-2290-5]

8 **Hoogendam JP**, Klerkx WM, de Kort GA, Bipat S, Zweemer RP, Sie-Go DM, Verheijen RH, Mali WP, Veldhuis WB. The influence of the b-value combination on apparent diffusion coefficient based differentiation between malignant and benign tissue in cervical cancer. *J Magn Reson Imaging* 2010; **32**: 376-382 [PMID: 20677265 DOI: 10.1002/jmri.22236]

9 **Charles-Edwards E**, Morgan V, Attygalle AD, Giles SL, Ind TE, Davis M, Shepherd J, McWhinney N, deSouza NM. Endovaginal magnetic resonance imaging of stage 1A/1B cervical cancer with A T2- and diffusion-weighted magnetic resonance technique: effect of lesion size and previous cone biopsy on tumor detectability. *Gynecol Oncol* 2011; **120**: 368-373 [PMID: 21093895 DOI: 10.1016/j.ygyno.2010.10.013]

10 **Chen J**, Zhang Y, Liang B, Yang Z. The utility of diffusion-weighted MR imaging in cervical cancer. *Eur J Radiol* 2010; **74**: e101-e106 [PMID: 19442466 DOI: 10.1016/j.ejrad.2009.04.025]

11 **Liu Y**, Bai R, Sun H, Liu H, Wang D. Diffusion-weighted magnetic resonance imaging of uterine cervical cancer. *J Comput Assist Tomogr* 2009; **33**: 858-862 [PMID: 19940650 DOI: 10.1097/RCT.0b013e31819e93af]

12 **Kilickesmez O**, Bayramoglu S, Inci E, Cimilli T, Kayhan A. Quantitative diffusion-weighted magnetic resonance imaging of normal and diseased uterine zones. *Acta Radiol* 2009; **50**: 340-347 [PMID: 19235579 DOI: 10.1080/02841850902735858]

13 **McVeigh PZ**, Syed AM, Milosevic M, Fyles A, Haider MA. Diffusion-weighted MRI in cervical cancer. *Eur Radiol* 2008; **18**: 1058-1064 [PMID: 18193428 DOI: 10.1007/s00330-007-0843-3]

14 **Naganawa S**, Sato C, Kumada H, Ishigaki T, Miura S, Takizawa O. Apparent diffusion coefficient in cervical cancer of the uterus: comparison with the normal uterine cervix. *Eur Radiol* 2005; **15**: 71-78 [PMID: 15538578 DOI: 10.1007/s00330-004-2529-4]

15 **Kuang F**, Yan Z, Li H, Feng H. Diagnostic accuracy of diffusion-weighted MRI for differentiation of cervical cancer and benign cervical lesions at 3.0T: Comparison with routine MRI and dynamic contrast-enhanced MRI. *J Magn Reson Imaging* 2015; **42**: 1094-1099 [PMID: 25824638 DOI: 10.1002/jmri.24894]

16 **Nougaret S**, Tirumani SH, Addley H, Pandey H, Sala E, Reinhold C. Pearls and pitfalls in MRI of gynecologic malignancy with diffusion-weighted technique. *AJR Am J Roentgenol* 2013; **200**: 261-276 [PMID: 23345345 DOI: 10.2214/AJR.12.9713]

17 **Sala E**, Rockall A, Rangarajan D, Kubik-Huch RA. The role of dynamic contrast-enhanced and diffusion weighted magnetic resonance imaging in the female pelvis. *Eur J Radiol* 2010; **76**: 367-385 [PMID: 20810230 DOI: 10.1016/j.ejrad.2010.01.026]

18 **Heo SH**, Shin SS, Kim JW, Lim HS, Jeong YY, Kang WD, Kim SM, Kang HK. Pre-treatment diffusion-weighted MR imaging for predicting tumor recurrence in uterine cervical cancer treated with concurrent chemoradiation: value of histogram analysis of apparent diffusion coefficients. *Korean J Radiol* 2013; **14**: 616-625 [PMID: 23901319 DOI: 10.3348/kjr.2013.14.4.616]

19 **Moffat BA**, Chenevert TL, Meyer CR, McKeever PE, Hall DE, Hoff BA, Johnson TD, Rehemtulla A, Ross BD. The functional diffusion map: an imaging biomarker for the early prediction of cancer treatment outcome. *Neoplasia* 2006; **8**: 259-267 [PMID: 16756718 DOI: 10.1593/neo.05844]

20 **Moffat BA**, Hall DE, Stojanovska J, McConville PJ, Moody JB, Chenevert TL, Rehemtulla A, Ross BD. Diffusion imaging for evaluation of tumor therapies in preclinical animal models. *MAGMA* 2004; **17**: 249-259 [PMID: 15580371 DOI: 10.1007/s10334-004-0079-z]

21 **Whittaker CS**, Coady A, Culver L, Rustin G, Padwick M, Padhani AR. Diffusion-weighted MR imaging of female pelvic tumors: a pictorial review. *Radiographics* 2009; **29**: 759-774; discussion 774-778 [PMID: 19448114 DOI: 10.1148/rg.293085130]

22 **Punwani S**. Diffusion weighted imaging of female pelvic cancers: concepts and clinical applications. *Eur J Radiol* 2011; **78**: 21-29 [PMID: 20801592 DOI: 10.1016/j.ejrad.2010.07.028]

23 **Harry VN**, Semple SI, Gilbert FJ, Parkin DE. Diffusion-weighted magnetic resonance imaging in the early detection of response to chemoradiation in cervical cancer. *Gynecol Oncol* 2008; **111**: 213-220 [PMID: 18774597 DOI: 10.1016/j.ygyno.2008.07.048]

24 **Schreuder SM**, Lensing R, Stoker J, Bipat S. Monitoring treatment response in patients undergoing chemoradiotherapy for locally advanced uterine cervical cancer by additional diffusion-weighted imaging: A systematic review. *J Magn Reson Imaging* 2015; **42**: 572-594 [PMID: 25346470 DOI: 10.1002/jmri.24784]

25 **Nicolet V**, Carignan L, Bourdon F, Prosmanne O. MR imaging of cervical carcinoma: a practical staging approach. *Radiographics* 2000; **20**: 1539-1549 [PMID: 11112809 DOI: 10.1148/radiographics.20.6.g00nv111539]

26 Cancer of the Endometrium. SEER Stat Fact Sheets online. Available from: URL: http//seer.cancer.gov/statfacts/html/corp.html

27 **Freeman SJ**, Aly AM, Kataoka MY, Addley HC, Reinhold C, Sala E. The revised FIGO staging system for uterine malignancies: implications for MR imaging. *Radiographics* 2012; **32**: 1805-1827 [PMID: 23065170 DOI: 10.1148/rg.326125519]

28 **Andreano A**, Rechichi G, Rebora P, Sironi S, Valsecchi MG, Galimberti S. MR diffusion imaging for preoperative staging of myometrial invasion in patients with endometrial cancer: a systematic review and meta-analysis. *Eur Radiol* 2014; **24**: 1327-1338 [PMID: 24668009 DOI: 10.1007/s00330-014-3139-4]

29 **Hori M**, Kim T, Onishi H, Imaoka I, Kagawa Y, Murakami T, Nakamoto A, Ueguchi T, Tatsumi M, Enomoto T, Kimura T, Tomiyama N. Endometrial cancer: preoperative staging using three-dimensional T2-weighted turbo spin-echo and diffusion-weighted MR imaging at 3.0 T: a prospective comparative study. *Eur Radiol* 2013; **23**: 2296-2305 [PMID: 23508278 DOI: 10.1007/s00330-013-2815-0]

30 **Wu TI**, Yen TC, Lai CH. Clinical presentation and diagnosis of uterine sarcoma, including imaging. *Best Pract Res Clin Obstet Gynaecol* 2011; **25**: 681-689 [PMID: 21816678 DOI: 10.1016/j.bpobgyn.2011.07.002]

31 **Namimoto T**, Yamashita Y, Awai K, Nakaura T, Yanaga Y, Hirai T, Saito T, Katabuchi H. Combined use of T2-weighted and diffusion-weighted 3-T MR imaging for differentiating uterine sarcomas from benign leiomyomas. *Eur Radiol* 2009; **19**: 2756-2764 [PMID:

19504102 DOI: 10.1007/s00330-009-1471-x]
32 **Thomassin-Naggara I**, Dechoux S, Bonneau C, Morel A, Rouzier R, Carette MF, Daraï E, Bazot M. How to differentiate benign from malignant myometrial tumours using MR imaging. *Eur Radiol* 2013; **23**: 2306-2314 [PMID: 23563602 DOI: 10.1007/s00330-013-2819-9]
33 **Takeuchi M**, Matsuzaki K, Yoshida S, Kudo E, Bando Y, Hasebe H, Kamada M, Nishitani H. Adenosarcoma of the uterus: magnetic resonance imaging characteristics. *Clin Imaging* 2009; **33**: 244-247 [PMID: 19411035 DOI: 10.1016/j.clinimag.2008.11.003]
34 **Yoshizako T**, Wada A, Kitagaki H, Ishikawa N, Miyazaki K. MR imaging of uterine adenosarcoma: case report and literature review. *Magn Reson Med Sci* 2011; **10**: 251-254 [PMID: 22214910]
35 **Saremi F**, Knoll AN, Bendavid OJ, Schultze-Haakh H, Narula N, Sarlati F. Characterization of genitourinary lesions with diffusion-weighted imaging. *Radiographics* 2009; **29**: 1295-1317 [PMID: 19755597 DOI: 10.1148/rg.295095003]
36 **Tamai K**, Koyama T, Saga T, Morisawa N, Fujimoto K, Mikami Y, Togashi K. The utility of diffusion-weighted MR imaging for differentiating uterine sarcomas from benign leiomyomas. *Eur Radiol* 2008; **18**: 723-730 [PMID: 17929022 DOI: 10.1007/s00330-007-0787-7]
37 **Zhang GF**, Zhang H, Tian XM, Zhang H. Magnetic resonance and diffusion-weighted imaging in categorization of uterine sarcomas: correlation with pathological findings. *Clin Imaging* 2014; **38**: 836-844 [PMID: 25027800 DOI: 10.1016/j.clinimag.2014.06.004]
38 **Chen YB**, Hu CM, Chen GL, Hu D, Liao J. Staging of uterine cervical carcinoma: whole-body diffusion-weighted magnetic resonance imaging. *Abdom Imaging* 2011; **36**: 619-626 [PMID: 20730423 DOI: 10.1007/s00261-010-9642-4]
39 **Klerkx WM**, Veldhuis WB, Spijkerboer AM, van den Bosch MA, Mali WP, Heintz AP, Bipat S, Sie-Go DM, van der Velden J, Schreuder HW, Stoker J, Peeters PH. The value of 3.0Tesla diffusion-weighted MRI for pelvic nodal staging in patients with early stage cervical cancer. *Eur J Cancer* 2012; **48**: 3414-3421 [PMID: 22835781 DOI: 10.1016/j.ejca.2012.06.022]
40 **Lee SI**, Catalano OA, Dehdashti F. Evaluation of gynecologic cancer with MR imaging, 18F-FDG PET/CT, and PET/MR imaging. *J Nucl Med* 2015; **56**: 436-443 [PMID: 25635136 DOI: 10.2967/jnumed.114.145011]
41 **Kitajima K**, Yamasaki E, Kaji Y, Murakami K, Sugimura K. Comparison of DWI and PET/CT in evaluation of lymph node metastasis in uterine cancer. *World J Radiol* 2012; **4**: 207-214 [PMID: 22761980 DOI: 10.4329/wjr.v4.i5.207]
42 **Trandafilovski P**. [The intensity of bronchial hyperreactivity and the evolution of pulmonary function]. *Plucne Bolesti* 2011; **42**: 36-37 [PMID: 2217630 DOI: 10.1136/bmj.d8009]
43 **Mohaghegh P**, Rockall AG. Imaging strategy for early ovarian cancer: characterization of adnexal masses with conventional and advanced imaging techniques. *Radiographics* 2012; **32**: 1751-1773 [PMID: 23065168 DOI: 10.1148/rg.326125520]
44 **Katayama M**, Masui T, Kobayashi S, Ito T, Sakahara H, Nozaki A, Kabasawa H. Diffusion-weighted echo planar imaging of ovarian tumors: is it useful to measure apparent diffusion coefficients? *J Comput Assist Tomogr* 2002; **26**: 250-256 [PMID: 11884782 DOI: 10.1097/00004728-200203000-00015]
45 **Moteki T**, Ishizaka H. Diffusion-weighted EPI of cystic ovarian lesions: evaluation of cystic contents using apparent diffusion coefficients. *J Magn Reson Imaging* 2000; **12**: 1014-1019 [PMID: 11105044 DOI: 10.1002/1522-2586(200012)12: 6<1014::AID-JMRI29>3.0.CO;2-T]
46 **Nakayama T**, Yoshimitsu K, Irie H, Aibe H, Tajima T, Nishie A, Asayama Y, Matake K, Kakihara D, Matsuura S, Nakano H, Honda H. Diffusion-weighted echo-planar MR imaging and ADC mapping in the differential diagnosis of ovarian cystic masses: usefulness of detecting keratinoid substances in mature cystic teratomas. *J Magn Reson Imaging* 2005; **22**: 271-278 [PMID: 16028258 DOI: 10.1002/jmri.20369]
47 **Fujii S**, Matsusue E, Kanasaki Y, Kanamori Y, Nakanishi J, Sugihara S, Kigawa J, Terakawa N, Ogawa T. Detection of peritoneal dissemination in gynecological malignancy: evaluation by diffusion-weighted MR imaging. *Eur Radiol* 2008; **18**: 18-23 [PMID: 17701040 DOI: 10.1007/s00330-007-0732-9]
48 **Low RN**, Sebrechts CP, Barone RM, Muller W. Diffusion-weighted MRI of peritoneal tumors: comparison with conventional MRI and surgical and histopathologic findings--a feasibility study. *AJR Am J Roentgenol* 2009; **193**: 461-470 [PMID: 19620444 DOI: 10.2214/AJR.08.1753]
49 **Ho KC**, Lin G, Wang JJ, Lai CH, Chang CJ, Yen TC. Correlation of apparent diffusion coefficients measured by 3T diffusion-weighted MRI and SUV from FDG PET/CT in primary cervical cancer. *Eur J Nucl Med Mol Imaging* 2009; **36**: 200-208 [PMID: 18779960 DOI: 10.1007/s00259-008-0936-5]
50 **Kwee TC**, Takahara T, Ochiai R, Nievelstein RA, Luijten PR. Diffusion-weighted whole-body imaging with background body signal suppression (DWIBS): features and potential applications in oncology. *Eur Radiol* 2008; **18**: 1937-1952 [PMID: 18446344 DOI: 10.1007/s00330-008-0968-z]
51 **Komori T**, Narabayashi I, Matsumura K, Matsuki M, Akagi H, Ogura Y, Aga F, Adachi I. 2-[Fluorine-18]-fluoro-2-deoxy-D-glucose positron emission tomography/computed tomography versus whole-body diffusion-weighted MRI for detection of malignant lesions: initial experience. *Ann Nucl Med* 2007; **21**: 209-215 [PMID: 17581719 DOI: 10.1007/s12149-007-0010-6]
52 **Sugita R**, Ito K, Fujita N, Takahashi S. Diffusion-weighted MRI in abdominal oncology: clinical applications. *World J Gastroenterol* 2010; **16**: 832-836 [PMID: 20143461 DOI: 10.3748/wjg.v16.i7.832]

P- Reviewer: Cuce F, Erich C **S- Editor**: Qiu S **L- Editor**: A
E- Editor: Lu YJ

World Journal of Radiology

Submit a Manuscript: http://www.wjgnet.com/esps/
Help Desk: http://www.wjgnet.com/esps/helpdesk.aspx
DOI: 10.4329/wjr.v8.i3.298

World J Radiol 2016 March 28; 8(3): 298-307
ISSN 1949-8470 (online)

ORIGINAL ARTICLE

Basic Study

Renal ablation using magnetic resonance-guided high intensity focused ultrasound: Magnetic resonance imaging and histopathology assessment

Maythem Saeed, Roland Krug, Loi Do, Steven W Hetts, Mark W Wilson

Maythem Saeed, Roland Krug, Loi Do, Steven W Hetts, Mark W Wilson, Department of Radiology and Biomedical Imaging, School of Medicine, University of California San Francisco, San Francisco, CA 94107-5705, United States

Author contributions: Saeed M designed the study, performed the experiments, analyzed MR images/histology and wrote the manuscript; Krug R performed the ablation and MR imaging and involved in manuscript editing; Do L achieved and analyzed the images, prepared the figures and involved in manuscript editing; Hetts SW and Wilson MW provided vital advices and were also involved in manuscript editing.

Institutional review board statement: Departmental Scientific Merit Approval.

Institutional animal care and use committee statement: This study received approval from Institutional Animal Care and Use Committee.

Conflict-of-interest statement: All investigators have no conflict-of-interest.

Data sharing statement: The authors are solely responsible for the data.

Correspondence to: Maythem Saeed, PhD, Professor, Department of Radiology and Biomedical Imaging, School of Medicine, University of California San Francisco, 185 Berry Street, Suite 350, Campus Box 0946, San Francisco, CA 94107-5705, United States. msaeed@ucsf.edu
Telephone: +1-415-5146221
Fax: +1-415-3539423

Received: June 26, 2015
Peer-review started: July 7, 2015
First decision: September 11, 2015
Revised: October 23, 2015
Accepted: November 13, 2015
Article in press: November 17, 2015
Published online: March 28, 2016

Abstract

AIM: To use magnetic resonance-guided high intensity focused ultrasound (MRg-HIFU), magnetic resonance imaging (MRI) and histopathology for noninvasively ablating, quantifying and characterizing ablated renal tissue.

METHODS: Six anesthetized/mechanically-ventilated pigs underwent single/double renal sonication (n = 24) using a 3T-MRg-HIFU (1.1 MHz frequency and 3000J-4400J energies). T2-weighted fast spin echo (T2-W), perfusion saturation recovery gradient echo and contrast enhanced (CE) T1-weighted (T1-W) sequences were used for treatment planning, temperature monitoring, lesion visualization, characterization and quantification, respectively. Histopathology was conducted in excised kidneys to quantify and characterize cellular and vascular changes. Paired Student's t-test was used and a P-value < 0.05 was considered statistically significant.

RESULTS: Ablated renal parenchyma could not be differentiated from normal parenchyma on T2-W or non-CE T1-W sequences. Ablated renal lesions were visible as hypoenhanced regions on perfusion and CE T1-W MRI sequences, suggesting perfusion deficits and necrosis. Volumes of ablated parenchyma on CE T1-W images *in*

vivo (0.12-0.36 cm^3 for single sonication 3000J, 0.50-0.84 cm^3, for double 3000J, 0.75-0.78 cm^3 for single 4400J and 0.12-2.65 cm^3 for double 4400J) and at postmortem (0.23-0.52 cm^3, 0.25-0.82 cm^3, 0.45-0.68 cm^3 and 0.29-1.80 cm^3, respectively) were comparable. The ablated volumes on 3000J and 4400J double sonication were significantly larger than single ($P < 0.01$), thus, the volume and depth of ablated tissue depends on the applied energy and number of sonication. Macroscopic and microscopic examinations confirmed the locations and presence of coagulation necrosis, vascular damage and interstitial hemorrhage, respectively.

CONCLUSION: Contrast enhanced MRI provides assessment of MRg-HIFU renal ablation. Histopathology demonstrated coagulation necrosis, vascular damage and confirmed the volume of damage seen on MRI.

Key words: Magnetic resonance-guided high intensity focused ultrasound; Renal ablation; Magnetic resonance imaging; Microscopy; High intensity focused ultrasound

Core tip: Renal carcinoma constitutes the majority of kidney malignancies. The gold standard procedure for treatment of renal carcinoma remains surgical excision. However, in a large number of patients, surgical excision is precluded by increased perioperative risk due to medical comorbidities. Recent innovations in the field of thermal ablation procedures and real-time imaging have accelerated the development of magnetic resonance-guided high intensity focused ultrasound (MRg-HIFU). This study showed that contrast enhanced magnetic resonance imaging (MRI) provides good assessment of renal ablation created noninvasively by MRg-HIFU. The volume and depth of ablated tissue depends on the applied energy and number of sonications. Histopathology demonstrated coagulation necrosis and vascular damage in the ablated tissue and confirmed the volume of damage seen on contrast enhanced MRI.

Saeed M, Krug R, Do L, Hetts SW, Wilson MW. Renal ablation using magnetic resonance-guided high intensity focused ultrasound: Magnetic resonance imaging and histopathology assessment. *World J Radiol* 2016; 8(3): 298-307 Available from: URL: http://www.wjgnet.com/1949-8470/full/v8/i3/298.htm DOI: http://dx.doi.org/10.4329/wjr.v8.i3.298

INTRODUCTION

The number of renal cell carcinoma cases increases with approximately 65000 new cases diagnosed each year in the United States[1]. The increased use of high-resolution diagnostic imaging has led to the serendipitous detection of small renal tumors in asymptomatic patients with small masses of renal carcinoma[2,3]. The gold standard procedure for treatment of localized renal carcinoma remains surgical excision. However, in a large number of patients, surgical excision is precluded by increased perioperative risk due to medical comorbidities[4,5]. In early 1990, radiofrequency ablation has emerged as a treatment option for this population, with the aim of achieving local oncologic control in a nephron-sparing manner while avoiding the potential morbidity associated with surgical extirpation and general anesthesia. Ritchie *et al*[6] showed that magnetic resonance-guided high intensity focused ultrasound (MRg-HIFU) was effective in two-third of the renal cell carcinoma cases. They suggested that advancement in ablation speed, respiratory navigation and treatment monitoring will improve outcomes and accurate histological analyses are essential in determining treatment efficacy. Innovations in the field of thermal ablation procedures and imaging in the last decade have accelerated the development of MRg-HIFU[7].

There are great differences in heat sensitivity between different cell types and tissues. In order to exploit the use of hyperthermia in the clinic, investigators need a better understanding of heating effects on various cell types and tissues[8]. MRg-HIFU has been used for treating uterine fibroids[9,10], palliation of bone metastases[11], ablation in the brain tumor through the skull[12], breast cancer[13,14], prostate[15] and hepatocellular carcinoma[16]. The safety and feasibility of using extracorporeal HIFU in treating patients with kidney tumor has been demonstrated[17,18]. The objective of this study was to use magnetic resonance imaging (MRI) and histopathology for assessing non-tumor renal ablation in swine model created by MRg-HIFU.

MATERIALS AND METHODS

Animal model

This investigation conformed to National Institutes of Health guidelines for the care and use of laboratory animals and was approved by the Institutional Animal Care and Use Committee. Six farm pigs (mean weight 31.0 ± 1.7 kg) (Pork Power Farms, Turlock, CA) were premedicated with 0.5 mg/kg acepromazine (Fort Dodge Animal Health, Fort Dodge, IA) and 25 mg/kg ketamine (Fort Dodge Animal Health). Animals were anesthetized with a mixture of isoflurane 2%-5% (Abbot Lab., North Chicago, IL) and oxygen and mechanically ventilated. Saline (10 mL/kg per hour) (Abbot Lab., North Chicago, IL) was IV infused. Heart rate, O2-saturation and core body temperature were monitored. Rocuronium bromide (Hospira Inc, Lake Forest, IL) was IV administered prior to ablation to minimize twitching and diaphragm motion during ablation.

MRg-HIFU setting

An MRg-HIFU system (ExAblate 2000, Insightec Ltd, Tirat Carmel, Israel) with a phased array transducer of 208 elements embedded in an MR table was used to create renal ablations. The table was connected to a 3T wide-bore MRI scanner (Discovery MR750w,

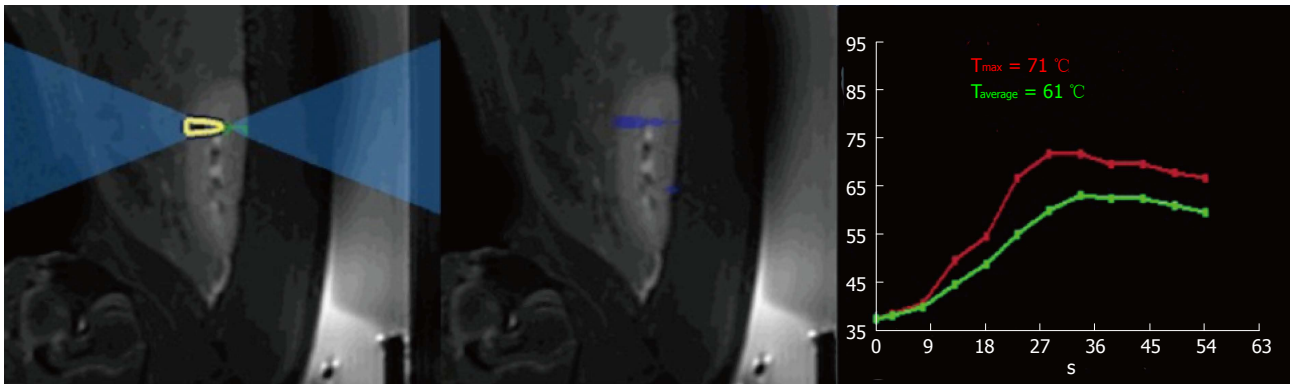

Figure 1 A localizer was performed to verify the position of the kidneys relative to the transducer. Coronal T2-weighted (T2-W) magnetic resonance images show the result of added T2-W treatment planning sequence, which was transferred to the high intensity focused ultrasound software (left and center). The right plot shows the temperature rise during ablation in the renal parenchyma. The red temperature curve represents the maximum temperature measured at the point of focus, while the green curve represents the average temperature in the region of interest.

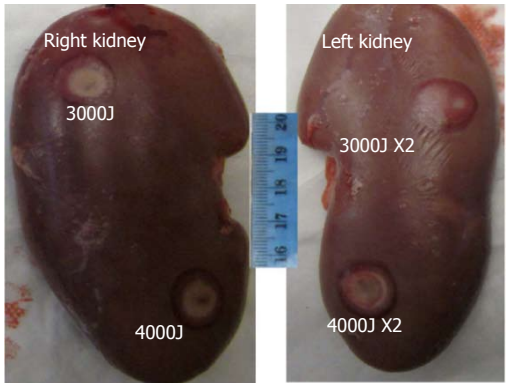

Figure 2 Macroscopic dorsal lesions in the right (single sonication) and left (double sonication) kidney are shown after high intensity focused ultrasound. Note the doughnut-shape hemorrhage (dark red) is surrounding coagulation necrosis (pale). Double sonication at 4400J produced larger lesions compared with the others.

GE, Milwaukee, WI). The back hair was shaved and closely examined for any defects or scars, which might impede the propagation of acoustic energy from the transducer. The pigs were then placed onto the scanner table in a supine position, inside a shallow bath filled with degassed water, so both non-tumor kidneys were centered above the transducer.

Increases in temperature were monitored using phase-differences in fast spoiled gradient-echo sequences (proton resonant frequency shift method) in renal parenchyma. A low-energy test sonication was performed in the para-vertebral muscles to confirm accuracy of the system set-up, calibrate the HIFU beam location and the path of the sound waves. All prescribed targets in the kidneys were 1 cm of the proximal and distal poles based on sagittal plane (Figure 1). A total of 24 lesions (4 per animal and 2 per kidney) were created at 2-3 mm from the renal capsule. The energies used in this study were determined in a pilot study (n = 1 pig), where lower energy (< 2000J) showed no visible renal ablation. The used focal spots were similar in size and geometry. In all animals one single sonication of 3000J at the upper (or proximal) pole of the right kidney and one single sonication of 4400J at the lower (or distal) pole of the right kidney were performed. Double sonication at the respective poles of the left kidney was performed. Unlike single sonication in the right kidney, each target in the left kidney was treated with double overlapping sonication of 3000J lasted for 30 s or 4400J lasted for 40 s (Figure 2). In the double sonication, the second sonication was performed in the exact same location as the first. The frequency was constant (1.1 MHz) in all cases, but the cooling times between sonication were 90 s and 132 s for 3000J and 4400J, respectively. The cooling time was determined by the HIFU software and was sufficient to prevent thermal damage related to heat accumulation in non-targeted tissues. Relatively high energies (3000J to 4400J) and low power (100-110W) were needed to produce visible lesions compared with other soft tissue like in the pancreas (1000J and 500-1350W)[19].

MR imaging and analysis

The default body coil and a 64-channel receiver cardiac coil (GE Healthcare, Waukesha, WI) were used in the current study. Axial, coronal and sagittal planes to the kidney were acquired to verify proper position of the transducer and to plan the ablation treatment. Axial and sagittal T2-W fast spin echo (FSE) (T2-W) sequence with fat saturation was used and the acquired images transferred to the HIFU software. MR thermometry was performed, using 3D segmented-EPI during each sonication with multiphase multi-slice echo planar imaging[20,21].

Post-ablation imaging without contrast was performed 60 min after sonication and with contrast media after 90 min. Table 1 shows the used imaging sequences and their parameters. Two-dimensional T2-W, 2D CE T1-weighted (T1-W) FSE and 3D liver acquisition with volume acquisition (LAVA) images were performed before and after ablation. Signal intensity (SI) ratios (ablated lesion SI/normal parenchyma SI) on T2-W and non-enhanced T1-W images were determined to demonstrate the SI differences prior to contrast media administration. Furthermore, perfusion imaging was conducted during

Table 1 Multiple magnetic resonance imaging sequences used for temperature monitoring, characterization and quantification of ablated kidneys

Pulse sequence	TR (ms)	TE (ms)	ETL	rBW (kHz)	Flip angle (degree)	Slice thickness	Matrix size	NEX	Acquisition time (s)
T2-W thermometry	210	18.3	12	15.63	35	4	256 × 192	1	100
2D T2-W FSE (pre and post ablation)	7300	68	12	15.63	11	4	256 × 192	3	400
Perfusion (post ablation)	3.7	1.5	NA	62.5	9	5	96 × 96	1	120
2D T1-W FSE (pre and post ablation[1])	985	7.2	6	31.25	120	5	192 × 192	1	16
3D LAVA (pre and post ablation[1])	3.9	1.5	NA	62.5	15	5	192 × 192	3	240

[1]Both 2-dimensional T1-weighted fast spin echo and 3-dimentional LAVA images. TR: Repetition time; TE: Echo time; ETL: Echo train length; rBW: Receiver bandwidth; NEX: Number of excitation per step; LAVA: Liver acquisitions with volume acquisition.

bolus injection of 0.2 mmol/kg Gd-DTPA (Bayer, Wayne, NJ). Saturation recovery gradient echo sequence was acquired after ablation to monitor regional perfusion in normal and ablated renal parenchyma. Imaging was performed before and during contrast injection. Regional signal intensity was monitored for 2 min after bolus injection of MR contrast media. Signal intensities were measured in the aortic blood (arterial input function), ablated and normal renal parenchyma.

Post-contrast administration, 2D CE T1-W and 3D LAVA images were repeated. LAVA is based on a 3 dimensional spoiled gradient echo pulse sequence. The 3D volumes (cm^3) of ablated renal parenchyma on only CE MRI (showed best delineation) were determined by multiplying the cranial-caudal, transverse and anterior-posterior lengths of each lesion and presented as means ± standard error of the means. On histopathology, each slice (both faces) was digitally photographed and weighed and the volumes (cm^3) of ablated renal parenchyma were measured using planemetric method.

Histopathology

The skin and tissues adjacent to the kidneys were macroscopically examined after each procedure. More than four hours after sonication the animals were heparinized, terminated and perfused *in situ* with 4% formalin to ensure proper tissue fixation. At postmortem, both kidneys and surrounding organs were macroscopically examined *in situ*. The kidneys were excised, transversely sliced, examined and weighed then fixed in buffered formalin for 48 h to delineate ablated lesions. The lesions were measured using planemetric method. For histopathology the slices from the ablated lesions were embedded in paraffin, sectioned (5 μm) and stained with hematoxylin-eosin (H and E) and examined microscopically.

Statistical analysis

Paired Student's *t*-test was performed to compare lesion volumes after different sonication energies. Regional signal intensity on perfusion imaging and lesion masses were presented as means ± standard error of the mean. Kruskal-Wallis test was used as a non-parametric test to compare the extents of ablated lesions measured on MRI and postmortem. The relationship between MRI *in situ* and postmortem data was assessed using Pearson's correlation coefficient. A *P* value of less than 0.05 was considered statistically significant.

RESULTS

MR imaging-guided HIFU was successfully used to create 24 focal renal lesions in 6 animals (4 per animal and 2 per kidney). The duration of renal planning and sonication was between 50-60 min. The sonication caused no change in average core body temperature, heart rate or O_2 saturation (Table 2). Breath-hold, with the use of muscle relaxant, rocuronium bromide, minimized muscle twitching and diaphragm movement motion during sonication and imaging. During ablation, the temperature rise (58 ℃-63 ℃) in the targeted region was monitored (Figure 1).

MRI characterization and quantification

The ablated lesions were not visible (isointense compared with surrounding renal parenchyma) on fat-suppressed T2-W and non-enhanced T1-W images. SI ratios on T2-W and non-enhanced T1-W images were 1.02 ± 0.02 and 1.03 ± 0.01, respectively, suggesting that there was no evidence of edema four hours after treatment.

On the other hand, perfusion imaging during injection of Gd-DTPA demonstrated hypoperfused ablated lesions as wedged-shaped zones (Figure 3). The changes in SI as a function of time were demonstrated in aortic blood, normal and ablated renal parenchyma. The perfusion deficits persisted for 2 min after contrast administration regardless of the sonication energies. Severe ischemia was observed in ablated lesions (Figure 4). We were unable to monitor the first passage indices (max upslope, max SI and time to the peak) of MR contrast media in the kidneys, because there was a trade-off between temporal resolution, spatial resolution and coverage related to the anatomical locations of the left and right kidneys and the lesions in a single kidney being created far from each other.

Furthermore, 2D CE T1-W FSE and 3D LAVA demonstrated the locations of the lesions in the proximal and distal poles of the kidneys (Figure 5). The locations of lesions on these images matched lesions seen on perfusion

Table 2 Regional, core body temperatures, heart rate and oxygen tension monitored during each sonication

Energy dose (Joules)	Temp (max) (℃)	Temp (avg) (℃)	Core body temp (℃)	HR (bpm)	O_2-saturation (%)
Single 3000	57 ± 3	56 ± 3	38.3 ± 0.6	89 ± 5	99 ± 1
Double 3000	61 ± 4	59 ± 4	38.1 ± 0.5	87 ± 4	99 ± 1
Single 4400	63 ± 6	61 ± 6	38.4 ± 0.4	86 ± 5	99 ± 1
Double 4400	63 ± 4	62 ± 5	38.5 ± 0.3	88 ± 4	99 ± 1

bpm: Beat/min. O_2: Oxygen; HR: Heart rate; Temp: Temperature.

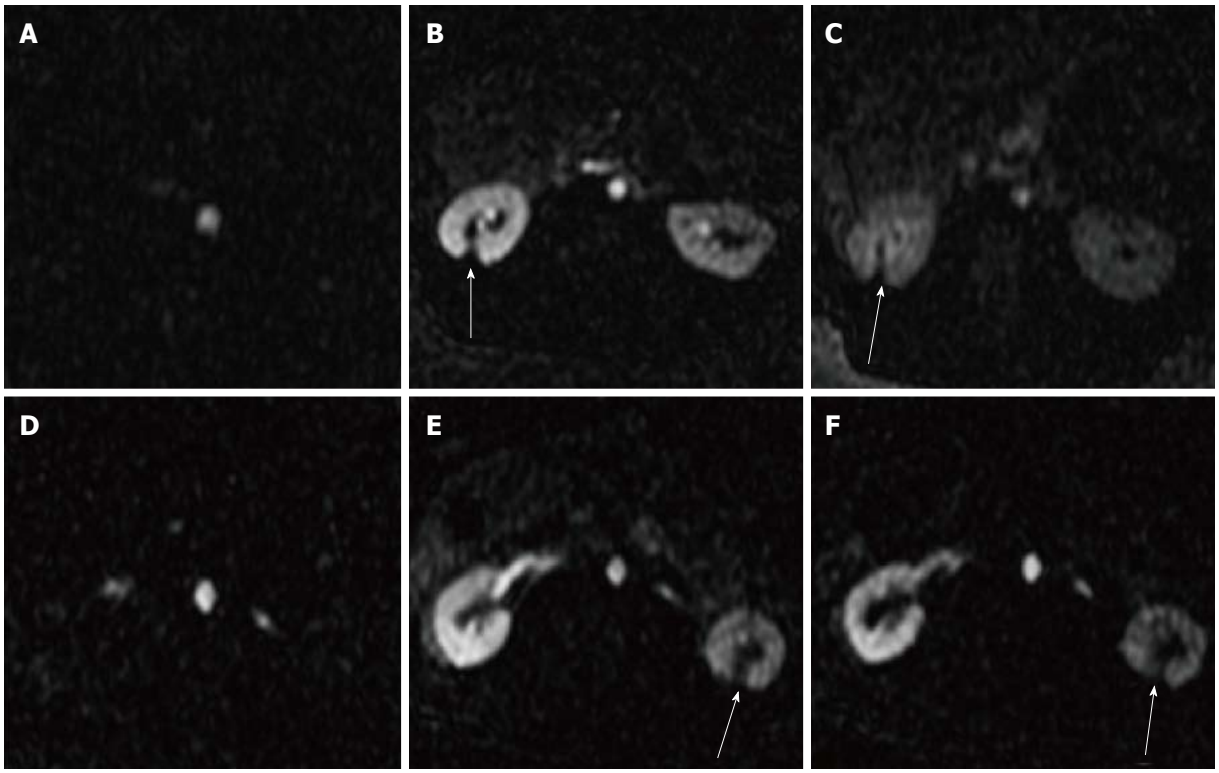

Figure 3 Selected 2D perfusion magnetic resonance images acquired from two representative animals. The images show the arrival of Gd-DTPA bolus (A, D) in the aorta and 20-120 s (B, E and C, F) in the kidneys. Arrows denote the hypoperfused ablated lesions.

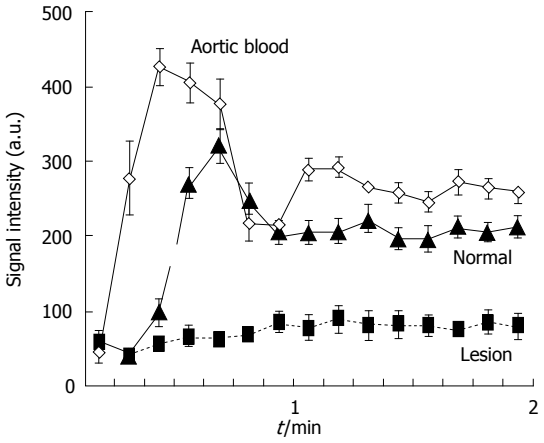

Figure 4 2D magnetic resonance perfusion demonstrates severely hypoperfused ablated lesions after magnetic resonance-guided high intensity focused ultrasound compared to remote non-ablated tissue. Diamond: Aortic blood; Triangle: Viable renal tissue; Square: Ablated lesion. a.u.: Arbitrary units.

MRI. Furthermore, both CE 2D T1-W FSE and 3D LAVA pulse sequences provided good contrast (T1 weighted). On both sequences, a thin hyperenhanced rim was visible around the ablated region on both MRI sequences. Figure 6 shows the wedged-shaped lesions on delayed CE 3D LAVA and 2D T1-W FSE images and macroscopic slices with close correspondence between ablated lesions *in vivo* on MRI and *in vitro* sections.

The average of each lesion dimension and volumes as a function of energy (joules) and sonication number are summarized in Table 3. The lesion volumes within each of the energies varied between animals (0.12-0.36 cm^3 for single sonication 3000J, 0.50-0.84 cm^3 for double 3000J, 0.75-0.784 cm^3 for single 4400J and 0.12-2.65 cm^3 for double 4400J). The ablated volumes on 3000J and 4400J double sonication were significantly larger than single ($P < 0.01$). The ablated volumes on 4400J double sonication were significantly larger than 3000J double sonication ($P < 0.01$).

Table 3 Lesions dimensions and volumes using single and double overlapping rectangular focal sonication

Energy dose (Joules)	CC (mm)	Transverse (mm)	AP (mm)	MRI volume (mm^3)	Postmortem volume (mm^3)
Single 3000	7.3 ± 0.07	7.8 ± 1.0	5.6 ± 0.1	317 ± 54	380 ± 111
Double 3000	7.9 ± 1.1	11.4 ± 1.6	7.5 ± 0.7	675 ± 41[a,c]	587 ± 28[a]
Single 4400	7.5 ± 0.7	7.8 ± 1.6	5.6 ± 0.7	354 ± 143	517 ± 52
Double 4400	11.4 ± 1.7	12.8 ± 3.0	10 ± 1.4	1450 ± 458[a,e,h]	1280 ± 238[a,e,h]

[a]$P < 0.05$ 2 × 3000J overlapping sonication *vs* single 3000J sonication; [c]$P < 0.05$ 2 × 3000J overlapping sonication *vs* single 4400J sonication; [e]$P < 0.05$ 2 × 4000J sonication *vs* single 3000J sonication; and [h]$P < 0.01$ 2 × 4000J overlapping sonication *vs* 2 × 3000J overlapping sonication. CC: Cranial-caudal; AP: Anterio-posterior; MRI: Magnetic resonance imaging.

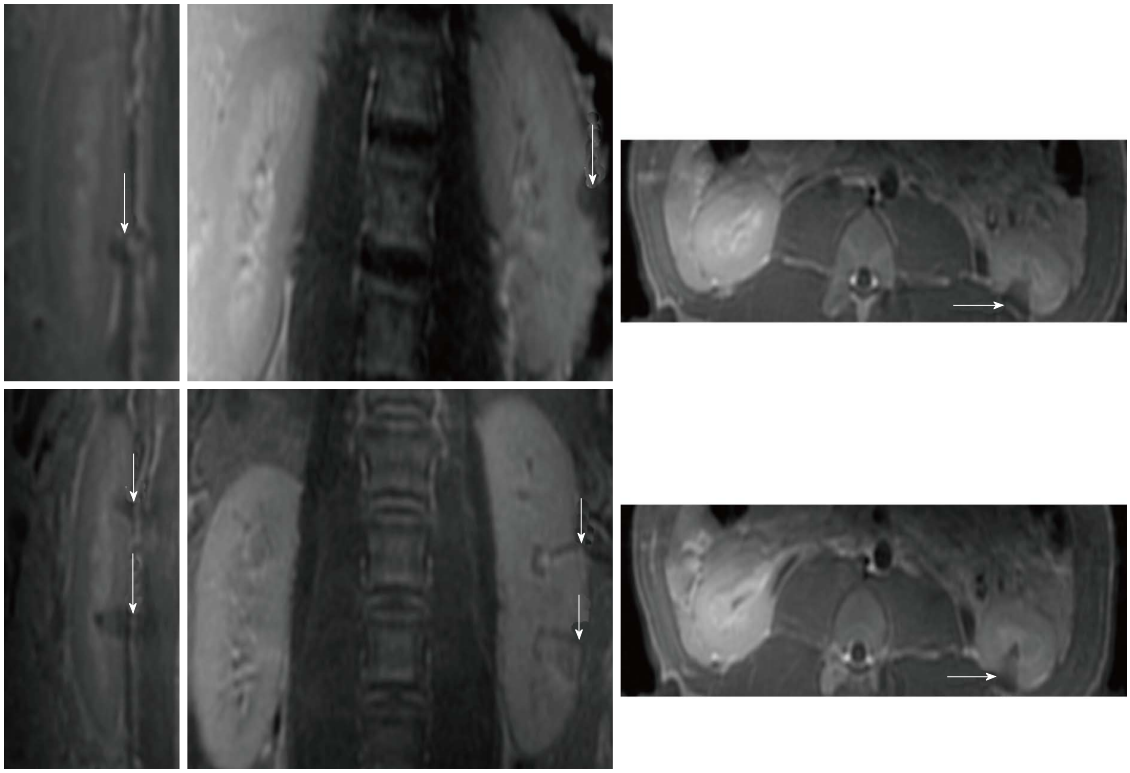

Figure 5 Renal lesions on three magnetic resonance imaging views acquired 3 h after sonication using single 4400J (top row, animal 1) and double 4400J (bottom row, animal 2). The wedge-shape hypoenhanced lesions are seen on contrast enhanced T1-weighted fast spin echo images in sagittal (left images), coronal (center images) and axial (right images) views.

On CE T1-W MRI, the transverse and anterio-posterior dimensions were significantly larger on double sonication (3000J or 4400J) compared with single. Cranial-caudal dimension was significantly larger on double 4400J compared with all other energies and number of sonication. Single sonication of 3000J compared with 4400J produced no significant difference. Paired Student's *t*-test revealed no significant difference in the lesion volumes measured *in situ* on MRI and postmortem (Table 3).

Histopathology characterization and quantification

At postmortem, minor skin burns were observed in two animals and one in the adjacent intestine at double 4400J energy. During postmortem laparotomy no bleeding was found in the peritoneal cavity. In the kidneys, the ablated lesions and surrounding hemorrhage were visible by the naked eye (Figure 2). Renal axial slices showed predominantly wedged-shaped confluent necrotic renal parenchyma (pale) surrounded by hemorrhagic zone (dark red) (Figure 6).

Quantitative analysis of the volumes of ablated parenchyma revealed significant difference between double sonication at 3000J and 4400J and single. Single 3000J and 4400J sonication caused no significant difference in the volumes of ablated parenchyma (Table 3). The data indicate that two overlapping sonication of 4400J are required to produce large lesions > 1.4 cm^3. The lesion volumes within each energies varied between animals (0.23-0.52 cm^3 for single sonication 3000J, 0.25-0.82 cm^3 for double 3000J, 0.45-0.68 cm^3 for single 4400J and 0.29-1.80 cm^3 for double 4400J. Pearson's test showed close correlation between *in situ* MRI and postmortem analysis of ablated parenchyma ($r = 0.98$, $y = -0.19 + 0.13x$, $P < 0.001$) (Figure 7).

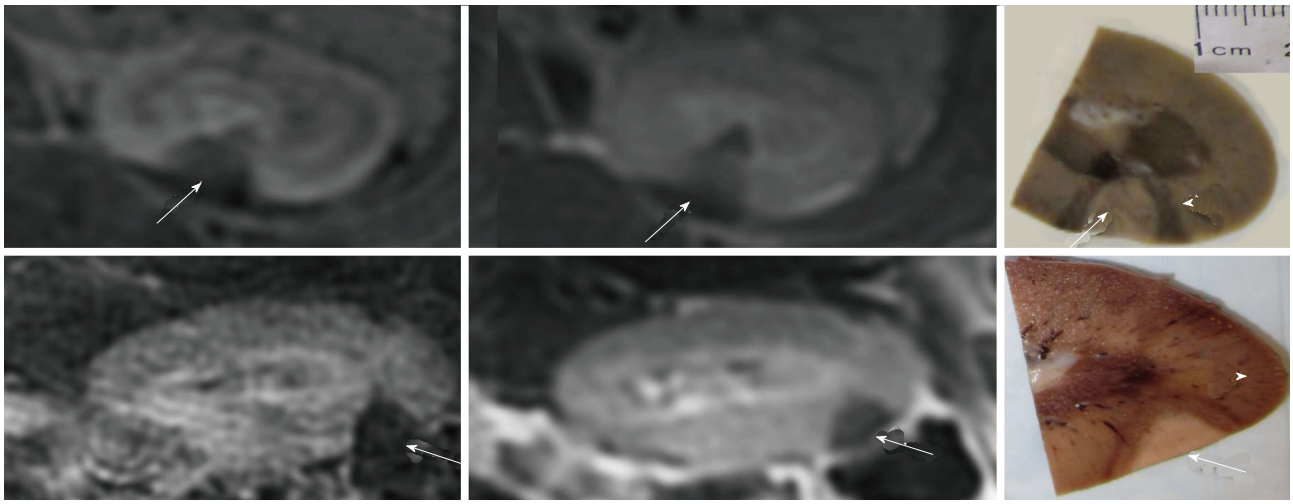

Figure 6 The wedge-shape lesions on contrast enhanced liver acquisitions with volume acquisition (left) and T1-weighted fast spin echo (center) images and gold-standard macroscopic slices (white arrows) from 2 animals (top and bottom rows). Note the close correspondence of ablated lesions *in situ* and *in vitro*. Coagulation necrosis (white arrows) is surrounded by hemorrhagic zone (arrowheads) as shown macroscopically.

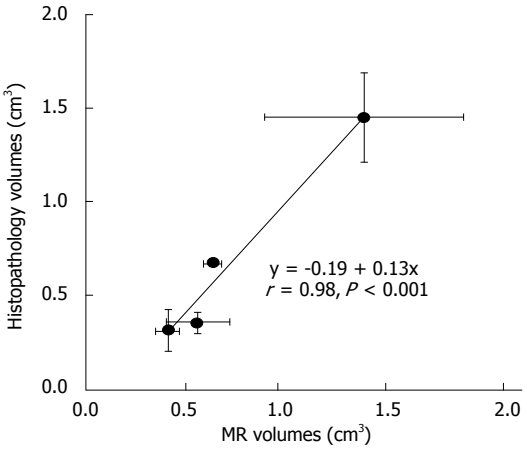

Figure 7 A close correlation was found between *in situ* magnetic resonance imaging and postmortem renal ablation volumes. The bars in the x- and y-axes represent the standard error of the means. The ablated volumes after single sonication at 3000J and 4400J were not significantly different, while volumes at double sonications were significantly larger on both 4400J than 3000J. Furthermore, the effect of double sonications at 4400J was significantly larger than the other energies.

At the cellular level, ablated parenchyma showed necrotic cells in the core of the lesion, hemorrhage at the rim and vascular damage. The necrotic renal parenchyma was without nuclei, opaque and eosinophilic, due to the denaturation of proteins. Intracellular details were lost, which is typical of coagulation necrosis containing outlines of enucleated cells. No evidence of inflammation or peri-renal parenchyma injury was found (Figure 8).

DISCUSSION

The major findings are that (1) noninvasive MRI provided an instant sense of temperature elevation and quantification of renal ablated lesions demonstrated by focal perfusion deficits and necrosis in order to monitor the effects of a range of energies on MRg-HIFU; (2) volumes of renal damage on MRg-HIFU are energy (Joules) dependent; (3) lesion volumes measured *in situ* on MRI and postmortem specimens showed good correlation, despite the difference in the methods of measurement; and (4) macroscopic examination confirmed lesion location and wedged-shape necrosis, while microscopic examination revealed coagulation necrosis, microvascular damage and hemorrhage in the ablated target.

We found that the best contrast between the ablated lesion and normal renal parenchyma is on perfusion, CE 2D T1-W FSE and CE 3D LAVA in a clinically feasible scan time. Although T2-W FSE provides better anatomical information within the kidney, the contrast between the lesion and normal renal parenchyma was poor on T2-W and non-enhanced T1-W images (1.02 ± 0.02 and 1.03 ± 0.01, respectively). The capsules were not visible on T2-W MRI to determine the degree of damage because of the use of fat saturation sequence, but microscopy confirmed the lack of damage in peri-renal renal parenchyma (Figure 8). Wile *et al*[22] found that the ablated lesions become difficult to visualize on fat-suppressed T2-W, since the lesion is isointense relative to surrounding suppressed fat.

MRI and computed tomography (CT) play important roles in guiding renal tumor ablation[22]. However, CE CT was limited in detecting post-ablation (12 mo) lesions. Furthermore, given the need for ionizing radiation on CT, multiple ablation procedures and follow-up imaging, it is likely that MRI will assume an increased role in longitudinal monitoring after renal ablation[23]. The 3T MR-guided system satisfies the requirements of HIFU ablation by providing temperature mapping, high spatial resolution images of target soft tissues and perfusion data. It also provides better features, such as twice the SNR/CNR and uniform fat suppression compared with 1.5T system[24].

This noninvasive study used a 3T MR-guided HIFU and energies (Joules, InSightec) as units of ablation

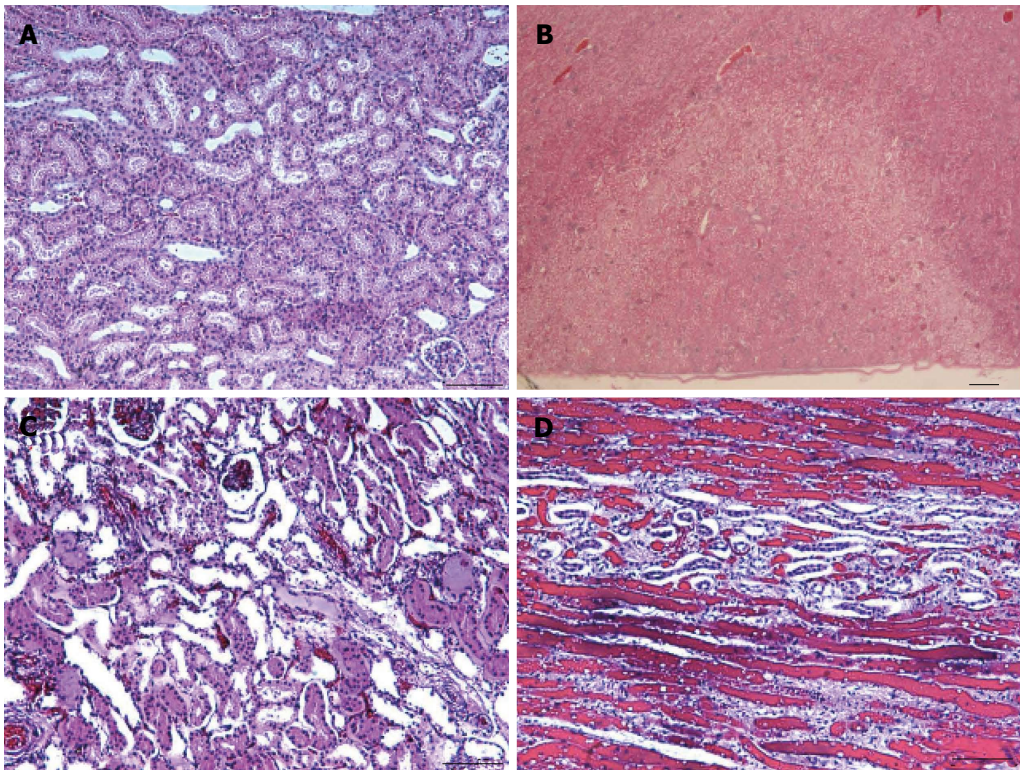

Figure 8 Microscopic sections (hematoxylin-eosin) of a normal renal tissue (A, × 40), the territory of both ablated (pale) and normal renal tissue (B, × 10) and ablated lesion (C, × 40) with damaged nephrons in a haphazard array and hemorrhage (D, × 100). Note the close agreement in the triangular infarct territory on microscopy and microscopy lesions in Figure 6 and magnetic resonance imaging in Figure 6. There was no evidence of peri-renal tissue injury (B).

rather than power (Watts, Philips Systems) used in previous studies[25,26]. Recent experimental studies showed the effectiveness of both power (Watts) and energy (Joules) units in ablating tissues[20,21,25-27]. The relationship between energy dose and lesion depth must be considered[20,21], especially in deep-seated tumors, because this relation depends on the type/density/size of targets and microenvironment factors, such as vascularity/perfusion. Other biologic factors, such as different organs or pathologies with variable structures and perfusions, may dictate the variable with greater utility in generating thermal lesions, thus further comparative studies are necessary.

Our histological study indicated that not only renal parenchyma showed coagulation necrosis but also vessels were severely damaged by HIFU treatment. The damaged vessels with coagulated blood most likely played a critical role in abolishing blood perfusion. Wu *et al*[28] suggested that the cause of perfusion deficits after MR-HIFU ablation is vascular damage, while Shaw *et al*[29] presented an integrated multi-stage mechanism through which HIFU-mediated vascular occlusion could occur.

Study limitations

The main limitations of this feasibility study were: (1) the use of non-tumor kidney model to determine the suitable energies, frequency and duration, which may have different acoustic response from the microenvironment of renal cell carcinoma tissue; (2) the renal motion related to the breathing was not navigated, but minimized by a muscle relaxant and breath holding during sonication. The effects of respiratory motion, boney obstacles and/or shallow angle of focused spots on the variability of ablated volumes and depth cannot be excluded; and (3) the used energy for the kidneys caused minor collateral damage in the skin, subcutaneous muscles and intestine in two animals. Similar cutaneous and subcutaneous tissue burning was previously observed in patients[9].

In conclusion, this MRI and histopathology study provided good assessment of non-tumor renal ablation created by MRg-HIFU. The volume of renal damage is energy and number of sonication dependent on MRg-HIFU. Contrast enhanced MRI is a good tool for visualization and quantification of ablated tissues.

ACKNOWLEDGMENTS

We would like to thank Carol Stillson for her technical support in the experimentation.

COMMENTS

Background

Renal carcinoma constitutes the majority of kidney malignancies. The increased use of high-resolution diagnostic imaging has led to the serendipitous detection of small renal tumors in asymptomatic patients with small masses of renal carcinoma. The gold standard procedure for treatment of localized renal carcinoma remains surgical excision, however, in a large number of patients, surgical excision is precluded by increased perioperative risk due to medical

comorbidities.

Research frontiers

The combination of 3T magnetic resonance imaging (MRI) and MR-guided high intensity focused ultrasound (MRg-HIFU) is suited for noninvasive renal and other tissues ablation. Ablated tissue is well defined on MRI and reflects macro and micro-anatomic changes observed at autopsy and microscopy. Furthermore, the volumes of ablated tissue measured on MRI after MRg-HIFU are energy (Joules) dependent and comparable with autopsy.

Innovations and breakthroughs

Radiofrequency ablation has emerged as a treatment option for renal carcinoma population, with the aim of achieving local oncologic control in a nephron-sparing manner, while avoiding the potential morbidity associated with surgical extirpation and general anesthesia. Innovations in the field of thermal ablation procedures and real-time imaging in the last decade have accelerated the development of non-invasive MRg-HIFU.

Applications

Noninvasive MRg-HIFU with MRI may be utilized for diagnostic and therapeutic purposes in cases of renal masses. It reduces morbidity and health care cost.

Terminology

MRg-HIFU is a new noninvasive technique used for treating tumors. Currently, it is used for treating some cases of uterine fibroids, palliation of bone metastases, brain tumor through the skull, breast cancer, prostate and hepatocellular carcinoma. MRI is another noninvasive imaging technique that has the potential to detect and monitor tumor treatment.

Peer-review

The study is well-performed and the results are interesting.

REFERENCES

1 **Siegel R**, Naishadham D, Jemal A. Cancer statistics, 2013. *CA Cancer J Clin* 2013; **63**: 11-30 [PMID: 23335087 DOI: 10.3322/caac.21166]

2 **Campbell SC**, Novick AC, Belldegrun A, Blute ML, Chow GK, Derweesh IH, Faraday MM, Kaouk JH, Leveillee RJ, Matin SF, Russo P, Uzzo RG. Guideline for management of the clinical T1 renal mass. *J Urol* 2009; **182**: 1271-1279 [PMID: 19683266 DOI: 10.1016/j.juro.2009.07.004]

3 **Ljungberg B**, Cowan NC, Hanbury DC, Hora M, Kuczyk MA, Merseburger AS, Patard JJ, Mulders PF, Sinescu IC. EAU guidelines on renal cell carcinoma: the 2010 update. *Eur Urol* 2010; **58**: 398-406 [PMID: 20633979 DOI: 10.1016/j.eururo.2010.06.032]

4 **Huang WC**, Elkin EB, Levey AS, Jang TL, Russo P. Partial nephrectomy versus radical nephrectomy in patients with small renal tumors--is there a difference in mortality and cardiovascular outcomes? *J Urol* 2009; **181**: 55-61; discussion 61-62 [PMID: 19012918 DOI: 10.1016/j.juro.2008.09.017]

5 **Miller DC**, Schonlau M, Litwin MS, Lai J, Saigal CS; Urologic Diseases in America Project. Renal and cardiovascular morbidity after partial or radical nephrectomy. *Cancer* 2008; **112**: 511-520 [PMID: 18072263 DOI: 10.1002/cncr.23218]

6 **Ritchie RW**, Leslie T, Phillips R, Wu F, Illing R, ter Haar G, Protheroe A, Cranston D. Extracorporeal high intensity focused ultrasound for renal tumours: a 3-year follow-up. *BJU Int* 2010; **106**: 1004-1009 [PMID: 20230379 DOI: 10.1111/j.1464-410X.2010.09289.x]

7 **Hynynen K**, Freund WR, Cline HE, Chung AH, Watkins RD, Vetro JP, Jolesz FA. A clinical, noninvasive, MR imaging-monitored ultrasound surgery method. *Radiographics* 1996; **16**: 185-195 [PMID: 10946699]

8 **Dewey WC**. Arrhenius relationships from the molecule and cell to the clinic. *Int J Hyperthermia* 2009; **25**: 3-20 [PMID: 19219695 DOI: 10.1080/02656730902747919]

9 **Trumm CG**, Stahl R, Clevert DA, Herzog P, Mindjuk I, Kornprobst S, Schwarz C, Hoffmann RT, Reiser MF, Matzko M. Magnetic resonance imaging-guided focused ultrasound treatment of symptomatic uterine fibroids: impact of technology advancement on ablation volumes in 115 patients. *Invest Radiol* 2013; **48**: 359-365 [PMID: 23385396 DOI: 10.1097/RLI.0b013e3182806904]

10 **Voogt MJ**, Trillaud H, Kim YS, Mali WP, Barkhausen J, Bartels LW, Deckers R, Frulio N, Rhim H, Lim HK, Eckey T, Nieminen HJ, Mougenot C, Keserci B, Soini J, Vaara T, Köhler MO, Sokka S, van den Bosch MA. Volumetric feedback ablation of uterine fibroids using magnetic resonance-guided high intensity focused ultrasound therapy. *Eur Radiol* 2012; **22**: 411-417 [PMID: 21901565 DOI: 10.1007/s00330-011-2262-8]

11 **Catane R**, Beck A, Inbar Y, Rabin T, Shabshin N, Hengst S, Pfeffer RM, Hanannel A, Dogadkin O, Liberman B, Kopelman D. MR-guided focused ultrasound surgery (MRgFUS) for the palliation of pain in patients with bone metastases--preliminary clinical experience. *Ann Oncol* 2007; **18**: 163-167 [PMID: 17030549 DOI: 10.1093/annonc/mdl335]

12 **Hynynen K**, McDannold N, Clement G, Jolesz FA, Zadicario E, Killiany R, Moore T, Rosen D. Pre-clinical testing of a phased array ultrasound system for MRI-guided noninvasive surgery of the brain--a primate study. *Eur J Radiol* 2006; **59**: 149-156 [PMID: 16716552 DOI: 10.1016/j.ejrad.2006.04.007]

13 **Zippel DB**, Papa MZ. The use of MR imaging guided focused ultrasound in breast cancer patients; a preliminary phase one study and review. *Breast Cancer* 2005; **12**: 32-38 [PMID: 15657521]

14 **Wu F**, Wang ZB, Zhu H, Chen WZ, Zou JZ, Bai J, Li KQ, Jin CB, Xie FL, Su HB. Extracorporeal high intensity focused ultrasound treatment for patients with breast cancer. *Breast Cancer Res Treat* 2005; **92**: 51-60 [PMID: 15980991 DOI: 10.1007/s10549-004-5778-7]

15 **Napoli A**, Anzidei M, Ciolina F, Marotta E, Cavallo Marincola B, Brachetti G, Di Mare L, Cartocci G, Boni F, Noce V, Bertaccini L, Catalano C. MR-guided high-intensity focused ultrasound: current status of an emerging technology. *Cardiovasc Intervent Radiol* 2013; **36**: 1190-1203 [PMID: 23474917 DOI: 10.1007/s00270-013-0592-4]

16 **Okada A**, Murakami T, Mikami K, Onishi H, Tanigawa N, Marukawa T, Nakamura H. A case of hepatocellular carcinoma treated by MR-guided focused ultrasound ablation with respiratory gating. *Magn Reson Med Sci* 2006; **5**: 167-171 [PMID: 17139143]

17 **Illing RO**, Kennedy JE, Wu F, ter Haar GR, Protheroe AS, Friend PJ, Gleeson FV, Cranston DW, Phillips RR, Middleton MR. The safety and feasibility of extracorporeal high-intensity focused ultrasound (HIFU) for the treatment of liver and kidney tumours in a Western population. *Br J Cancer* 2005; **93**: 890-895 [PMID: 16189519 DOI: 10.1038/sj.bjc.6602803]

18 **Wu F**, Wang ZB, Chen WZ, Bai J, Zhu H, Qiao TY. Preliminary experience using high intensity focused ultrasound for the treatment of patients with advanced stage renal malignancy. *J Urol* 2003; **170**: 2237-2240 [PMID: 14634387]

19 **Sofuni A**, Moriyasu F, Sano T, Itokawa F, Tsuchiya T, Kurihara T, Ishii K, Tsuji S, Ikeuchi N, Tanaka R, Umeda J, Tonozuka R, Honjo M, Mukai S, Fujita M, Itoi T. Safety trial of high-intensity focused ultrasound therapy for pancreatic cancer. *World J Gastroenterol* 2014; **20**: 9570-9577 [PMID: 25071354 DOI: 10.3748/wjg.v20.i28.9570]

20 **Bucknor MD**, Rieke V, Do L, Majumdar S, Link TM, Saeed M. MRI-guided high-intensity focused ultrasound ablation of bone: evaluation of acute findings with MR and CT imaging in a swine model. *J Magn Reson Imaging* 2014; **40**: 1174-1180 [PMID: 24925593 DOI: 10.1002/jmri.24451]

21 **Bucknor MD**, Rieke V, Seo Y, Horvai AE, Hawkins RA, Majumdar S, Link TM, Saeed M. Bone remodeling after MR imaging-guided high-intensity focused ultrasound ablation: evaluation with MR imaging, CT, Na(18)F-PET, and histopathologic examination in a swine model. *Radiology* 2015; **274**: 387-394 [PMID: 25302829 DOI: 10.1148/radiol.14132605]

22 **Wile GE**, Leyendecker JR, Krehbiel KA, Dyer RB, Zagoria RJ. CT and MR imaging after imaging-guided thermal ablation of renal neoplasms. *Radiographics* 2007; **27**: 325-339; discussion 339-340 [PMID: 17374856]
23 **Davenport MS**, Caoili EM, Cohan RH, Ellis JH, Higgins EJ, Willatt J, Fox GA. MRI and CT characteristics of successfully ablated renal masses: Imaging surveillance after radiofrequency ablation. *AJR Am J Roentgenol* 2009; **192**: 1571-1578 [PMID: 19457820 DOI: 10.2214/AJR.08.1303]
24 **Fukatsu H**. 3T MR for clinical use: update. *Magn Reson Med Sci* 2003; **2**: 37-45 [PMID: 16210818]
25 **Wijlemans JW**, de Greef M, Schubert G, Bartels LW, Moonen CT, van den Bosch MA, Ries M. A clinically feasible treatment protocol for magnetic resonance-guided high-intensity focused ultrasound ablation in the liver. *Invest Radiol* 2015; **50**: 24-31 [PMID: 25198833 DOI: 10.1097/RLI.0000000000000091]
26 **Wijlemans JW**, Deckers R, van den Bosch MA, Seinstra BA, van Stralen M, van Diest PJ, Moonen CT, Bartels LW. Evolution of the ablation region after magnetic resonance-guided high-intensity focused ultrasound ablation in a Vx2 tumor model. *Invest Radiol* 2013; **48**: 381-386 [PMID: 23399810 DOI: 10.1097/RLI.0b013e3182820257]
27 **Zibly Z**, Graves CA, Harnof S, Hadani M, Cohen ZR. Sonoablation and application of MRI guided focused ultrasound in a preclinical model. *J Clin Neurosci* 2014; **21**: 1808-1814 [PMID: 25012486 DOI: 10.1016/j.jocn.2014.04.008]
28 **Wu F**, Chen WZ, Bai J, Zou JZ, Wang ZL, Zhu H, Wang ZB. Tumor vessel destruction resulting from high-intensity focused ultrasound in patients with solid malignancies. *Ultrasound Med Biol* 2002; **28**: 535-542 [PMID: 12049967 DOI: 10.1016/S0301-5629(01)00515-4]
29 **Shaw CJ**, ter Haar GR, Rivens IH, Giussani DA, Lees CC. Pathophysiological mechanisms of high-intensity focused ultrasound-mediated vascular occlusion and relevance to non-invasive fetal surgery. *J R Soc Interface* 2014; **11**: 20140029 [PMID: 24671935 DOI: 10.1098/rsif.2014.0029]

P- Reviewer: Stavroulopoulos A **S- Editor**: Gong XM **L- Editor**: A
E- Editor: Lu YJ

World Journal of Radiology

Submit a Manuscript: http://www.wjgnet.com/esps/
Help Desk: http://www.wjgnet.com/esps/helpdesk.aspx
DOI: 10.4329/wjr.v8.i3.308

World J Radiol 2016 March 28; 8(3): 308-315
ISSN 1949-8470 (online)

ORIGINAL ARTICLE

Retrospective Study

Angiographic and volumetric effects of mammalian target of rapamycin inhibitors on angiomyolipomas in tuberous sclerosis

Rahul A Sheth, Adam S Feldman, Elahna Paul, Elizabeth A Thiele, T Gregory Walker

Rahul A Sheth, Department of Interventional Radiology, MD Anderson Cancer Center, Houston, TX 77030, United States

Adam S Feldman, Department of Urology, Massachusetts General Hospital, Boston, MA 02114, United States

Elahna Paul, Department of Pediatric Nephrology, Massachusetts General Hospital, Boston, MA 02114, United States

Elizabeth A Thiele, Department of Neurology, Massachusetts General Hospital, Boston, MA 02114, United States

T Gregory Walker, Division of Interventional Radiology, Department of Radiology, Massachusetts General Hospital, Boston, MA 02114, United States

Author contributions: Sheth RA collected and analyzed the data and drafted the manuscript; Feldman AS, Paul E, Thiele EA and Walker TG provided analytical oversight; Walker TG designed and supervised the study; Feldman AS, Paul E, Thiele EA and Walker TG revised the manuscript for important intellectual content; all authors have read and approved the final version to be published.

Institutional review board statement: The study was reviewed and approved by the Massachusetts General Hospital Institutional Review Board.

Informed consent statement: Informed consent was waved in this retrospective study.

Conflict-of-interest statement: All authors declare no conflicts of interest.

Data sharing statement: No additional data are available.

Correspondence to: Rahul A Sheth, MD, Assistant Professor, Department of Interventional Radiology, MD Anderson Cancer Center, 1400 Pressler St., FCT14.6000, Houston, TX 77030, United States. rasheth@mdanderson.org
Telephone: +1-713-7450652
Fax: +1-713-7924098

Received: September 29, 2015
Peer-review started: October 2, 2015
First decision: November 4, 2015
Revised: November 26, 2015
Accepted: January 8, 2016
Article in press: January 11, 2016
Published online: March 28, 2016

Abstract

AIM: To investigate the angiographic and volumetric effects of mammalian target of rapamycin (mTOR) inhibitors on angiomyolipomas (AMLs) in a case series of patients with tuberous sclerosis complex.

METHODS: All patients who underwent catheter angiography prior to and following mTOR inhibitor therapy (n = 3) were evaluated. All cross-sectional imaging studies were analyzed with three-dimensional volumetrics, and tumor volume curves for all three tissue compartments (soft tissue, vascular, and fat) were generated. Segmentation analysis tools were used to automatically create a region of interest (ROI) circumscribing the AML. On magnetic resonance images, the "fat only" map calculated from the in- and opposed-phase gradient recalled echo sequences was used to quantify fat volume within tumors. Tumor vascularity was measured by applying a thresholding tool

within the ROI on post-contrast subtraction images. On computed tomography images, volume histogram analysis of Hounsfield unit was performed to quantify tumor tissue composition. The angiography procedures were also reviewed, and tumor vascularity based on pre-embolization angiography was characterized in a semi-quantitative manner.

RESULTS: Patient 1 presented at the age of 15 with a 6.8 cm right lower pole AML and a 4.0 cm right upper pole AML. Embolization was performed of both tumors, and after a few years of size control, the tumors began to grow, and the patient was initiated on mTOR inhibitor therapy. There was an immediate reduction in the size of both lesions. The patient then underwent repeat embolization and discontinuation of mTOR inhibition, after which point there was a substantial regrowth in both tumors across all tissue compartments. Patient 2 presented at the age of 18 with a right renal AML. Following a brief period of tumor reduction after embolization, she was initiated on mTOR inhibitor therapy, with successful reduction in tumor size across all tissue compartments. As with patient 1, however, there was immediate rebound growth following discontinuation of inhibitor therapy, without sustained control despite repeat embolization. patient 3 presented at the age of 5 with a left renal AML and underwent two embolization procedures without lasting effect prior to starting mTOR inhibition. As with patients 1 and 2, following discontinuation of therapy, there was immediate rebound growth of the tumor. Repeat embolization, however, was notable for a substantial reduction in intratumoral aneurysms and vascularity.

CONCLUSION: AML volume reduction as well as post-treatment rebound growth due to mTOR inhibitors involves all three tissue components of the tumor.

Key words: Tuberous sclerosis; Angiomyolipoma; Sirolimus; Angiography; Transcatheter embolization; Interventional radiology; Mammalian target of rapamycin inhibition; Everolimus; Volumetrics

Core tip: Pharmacologic management of tuberous sclerosis complex-associated angiomyolipomas with mammalian target of rapamycin inhibitors can provide substantial tumor volume reduction for the duration of the therapeutic course. This volume reduction impacts all three tissue compartments of the tumor. Unfortunately rebound growth involving all tissue compartments follows shortly after discontinuation of mammalian target of rapamycin (mTOR) inhibitor therapy. The addition of transarterial embolization to mTOR inhibition did not curtail the occurrence of rebound growth.

Sheth RA, Feldman AS, Paul E, Thiele EA, Walker TG. Angiographic and volumetric effects of mammalian target of rapamycin inhibitors on angiomyolipomas in tuberous sclerosis. *World J Radiol* 2016; 8(3): 308-315 Available from: URL: http://www.wjgnet.com/1949-8470/full/v8/i3/308.htm DOI: http://dx.doi.org/10.4329/wjr.v8.i3.308

INTRODUCTION

Tuberous sclerosis complex (TSC) is an autosomal dominant genetic disorder affecting approximately 2 million people globally. Mutations in the *TSC1* and *TSC2* genes, important regulators of the mammalian target of rapamycin (mTOR) signaling pathway, result in the development of tumors involving multiple organ systems. As many as 80% of patients with TSC develop renal angiomyolipomas (AMLs), which are soft tissue hamartomatous tumors containing multiple soft tissue components including fat, smooth muscle, and blood vessels. Although they are not malignant, AMLs can lead to a variety of complications, the most significant of which is spontaneous hemorrhage. While the risk of bleeding is actually relatively low, the morbidity and mortality rates for such events are high; as a result, AMLs represent the most common cause of death in adults with TSC[1].

Lesion size is the traditional biomarker for prognosticating the risk of spontaneous AML hemorrhage, with tumors greater than 4 cm considered to be at risk[2]. AMLs in patients with TSC tend to continuously increase in size[3,4]. As a result, methods to abrogate or at least control tumor growth are crucial for this patient population. Treatment options range from invasive, such as nephrectomy or partial nephrectomy, to minimally invasive, such as transcatheter arterial embolization. The latter technique is a nephron-sparing procedure that has been used to treat AMLs for both emergent and prophylactic indications[4-6].

Recently, new medical therapies for TSC-associated AMLs have been developed. Sirolimus and everolimus, a sirolimus derivative, are immunosuppressants that operate by inhibiting the mTOR signaling pathway, thus interrupting the molecular pathway that is dysregulated in TSC patients. In a Phase Ⅰ/Ⅱ study, sirolimus reduced AML volume to 53% of baseline over a 12 mo period[7]. Likewise, 42% of patients achieved at least 50% AML volume reduction with everolimus[8]. The effect, however, is not sustained, as following cessation of drug administration, only 5% of patients maintain the volume reduction[9].

mTOR inhibitors represent an intriguing new option for the management of TSC-associated AMLs, but questions remain regarding their appropriate use. Specifically, because of the rebound growth following discontinuation, should patients be prescribed a lifelong regimen, despite the lack of data regarding long term risks? Moreover, while mTOR inhibitors are known to reduce tumor volume, it is unknown how these medications impact tumoral composition, including tumor vascularity, and by extension, the risk for tumoral bleeding. Furthermore,

possible synergies between mTOR inhibitors and minimally invasive interventions such as transarterial embolization have not been explored. In this case series, we present the angiographic and volumetric effects of mTOR inhibitors on AMLs in patients who underwent transcatheter arterial embolization prior to and following a course of mTOR inhibitor therapy. We characterize the impact of mTOR inhibition on tumoral tissue compartments through volumetric cross sectional imaging analysis and on tumor vascularity by angiography. We additionally report on the outcomes of mTOR inhibition and arterial embolization combination therapy.

MATERIALS AND METHODS

Study population

Institutional review board (IRB) approval was obtained for this single institution, retrospective study. Thirty-nine TSC patients who underwent transcatheter arterial embolization procedures for renal AMLs between 2000 and 2014 were identified. Of these patients, 11 received mTOR inhibitors for management of their AMLs, and 3 patients underwent angiography and transcatheter embolization of their AMLs prior to and following a course of mTOR inhibitor therapy. These three patients comprise the study group for this case series.

Cross sectional imaging

All patients underwent routine cross-sectional imaging of their kidneys on at least an annual basis. All patients underwent MR imaging, and one patient additionally underwent CT imaging. MR imaging was performed on a Signa 1.5-T system (GE Healthcare, Waukesha, WI) or a Magnetom 3.0-T system (Siemens, Malvern, PA). All MR examinations were monitored by a pediatric radiologist, and imaging protocols were individually tailored. Commonly, protocols included a tri-phase localizer, coronal T2-weighted HASTE, axial T1-weighted in- and opposed-phase gradient recalled echo (GRE), pre-contrast coronal or axial T1-weighted 3D GRE, and contrast-enhanced coronal or axial T1-weighted 3D GRE obtained at 30, 70, and 180 s after contrast administration. In- and opposed-phase imaging data were used to calculate "fat only" image maps of the kidneys *via* the Dixon method[10]. The T1 pre-contrast mask images were subtracted from the post-contrast images to generate contrast maps; the arterial phase subtraction map (difference between post-contrast images obtained at 30 s following contrast administration and the pre-contrast mask) was used as the vascularity map for the AMLs. Intravenous gadopentetate dimeglumine was used as the contrast agent.

CT scanning was performed by a 64-detector row CT scanner (GE Discovery CT 750 HD; GE Healthcare, Waukesha, WI). Pre-contrast imaging of the abdomen was obtained, followed by contrast injection at 2-3 cc/s with a total volume of 2 cc/kg. Post-contrast imaging at 30 s (arterial phase) and at 100 s (nephrographic phase) were obtained.

Embolization technique

Transcatheter arterial embolization was performed prophylactically in all 3 patients by attending interventional radiologists. Selective renal angiography was performed using a 4 or 5 Fr selective catheter (Cook, Bloomington, IN). Superselective catheterization of arterial pedicles supplying the targeted AML was performed using a coaxial microcatheter (Renegade; Boston Scientific, Natick, MA) over a microwire (Transcend; Boston Scientific, Natick, MA). Once satisfactory microcatheter positioning was confirmed with digital subtraction angiography (DSA), embolization was performed under continuous fluoroscopy using calibrated 300-500 micron microspheres (Embosphere; Merit Medical, South Jordan, UT). Achievement of stasis within the target artery and absence of inadvertent non-target embolization of adjacent normal renal parenchyma were monitored during the embolization portion of the procedure. Stasis within the target artery was considered the standardized embolization endpoint and was confirmed with post-embolization DSA imaging. This endpoint was achieved in all embolization procedures.

Image analysis

Volumetric analysis of MR and CT images was performed using a standard clinical three-dimensional image analysis software package (iNtuition; TeraRecon, Foster City, CA). Segmentation analysis tools were used to automatically create a region of interest (ROI) circumscribing the AML; minor adjustments were then made manually in three orthogonal planes. The ROI was then used to calculate tumor volumes. On MR images, the "fat only" map calculated from the in- and opposed-phase GRE sequences was used to quantify fat volume within tumors (Figure 1A). Tumor vascularity was measured by applying a thresholding tool within the ROI to semi-automatically segment areas of vascular enhancement on post-contrast subtraction images (Figure 1B). On CT images, volume histogram analysis of Hounsfield unit (HU) was performed to quantify tumor tissue composition (Figure 1C). Pixels with HU ranging from -100 to -20 HU were considered to represent macroscopic fat, and pixels with HU ranging from 100 to 200 were considered to represent blood vessels; selection of these thresholds represents an adaptation from a previously published technique[11].

Tumor vascularity that was based on angiographic imaging was analyzed in a semi-quantitative manner using a previously published grading scale[12]. The lesions were characterized based upon several parameters: Mean vessel density, size, the absence or presence of a parasitized arterial supply, and the number and size of any pseudoaneurysms. Based on these observations, lesions were then classified into 3 grades of vascularity. Grade 1 lesions demonstrated small caliber peripheral arteries without significant central vascularity. Lesions with microaneurysms less than 2 mm in size were also

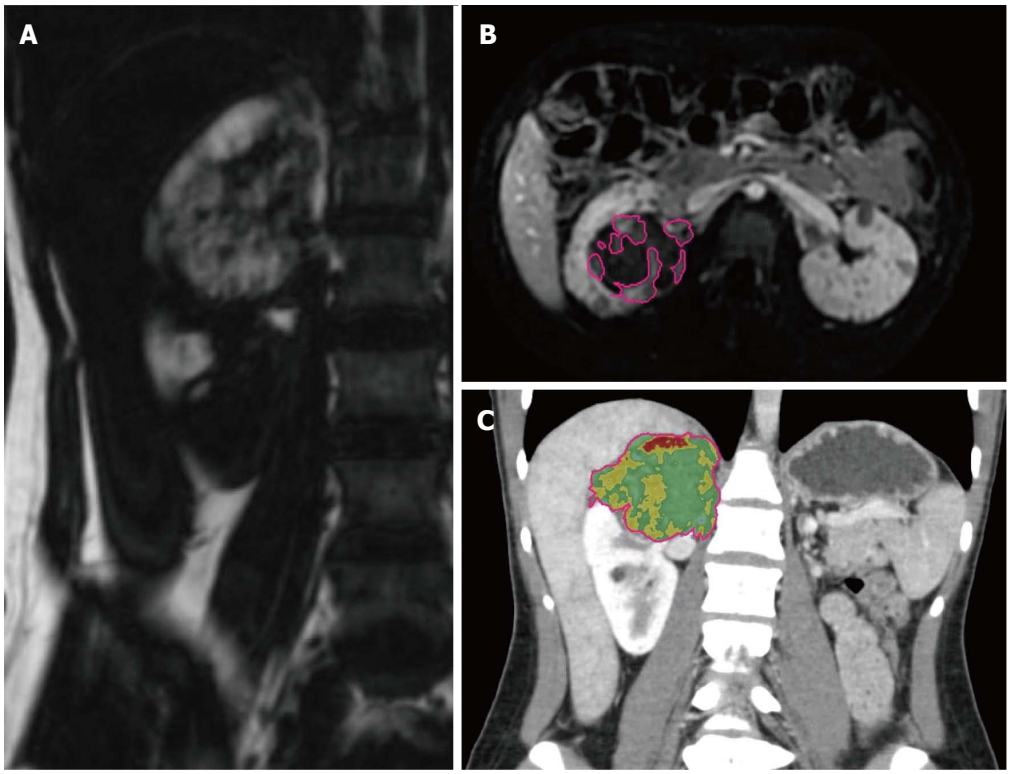

Figure 1 Examples of volumetric analysis on computed tomography and magnetic resonance imaging. A: Coronal "fat-only" maps created from in- and opposed-phase gradient recalled imaging were used to measure macroscopic fat volumes within AMLs; B: Segmentation of tumoral vascularity (automatically generated regions of interest demarcated by pink line) from post-contrast subtraction imaging was used to calculate tumor vascular volumes; C: Histogram analysis from CT was used to calculate tumoral fat and vascular content (pseudocoloring depicts fatty tissue as red and vascular tissue as yellow). CT: Computed tomography; AML: Angiomyolipoma.

Table 1 Timeline for patient 1

Time (d)	Event
0	MRI
76	Angiogram with embolization of right upper and lower pole AMLs
189	MRI
560	MRI
924	MRI
1660	MRI
1793	Initiation of mTOR inhibitor
2017	MRI
2381	MRI
2382	Angiogram with embolization of right lower pole AML
2383	Cessation of mTOR inhibitor
2542	MRI
2752	MRI

MRI: Magnetic resonance imaging; AML: Angiomyolipoma; mTOR: Mammalian target of rapamycin.

considered grade 1. Grade 2 lesions demonstrated medium-sized and/or abundant arteries with or without a parasitized arterial supply. Additionally lesions with pseudoaneurysms between 2 and 5 mm were considered grade 2. Grade 3 lesions contained large, tortuous vessels and/or pseudoaneurysms greater than 5 mm in size.

RESULTS

Patient 1

At the time of initial presentation, patient 1 was a 15-year-old female with a history of TSC-associated seizure disorder, developmental delay, autism and bilateral renal AMLs (Table 1). During several years of serial surveillance imaging she was noted to have a gradual increase in the size and number of her renal lesions. Specifically, there was a 6.8 cm right lower pole AML, a 4.0 cm right upper pole AML, and a 3.8 cm left upper pole AML, none of which had a substantial fatty component. There was no evidence of hydronephrosis, and there were no mass-related symptoms such as flank pain. Given the tumoral size, prophylactic embolization of the right upper and lower pole AMLs was performed in 2007 in order to reduce the risk of hemorrhage. Angiographically the right upper pole lesion demonstrated grade 3 vascularity, while the right lower pole lesion demonstrated grade 2 vascularity. Despite initial control of tumoral size, both lesions began enlarging approximately 2 years after embolization (right lower pole, Figure 2A; right upper pole, Figure 2B). As a result, mTOR therapy with everolimus 10 mg daily was initiated in 2011, which resulted in a dramatic decrease in tumor volume of both the soft tissue [-521% (upper pole) and -943% (lower pole)] and vascular compartments

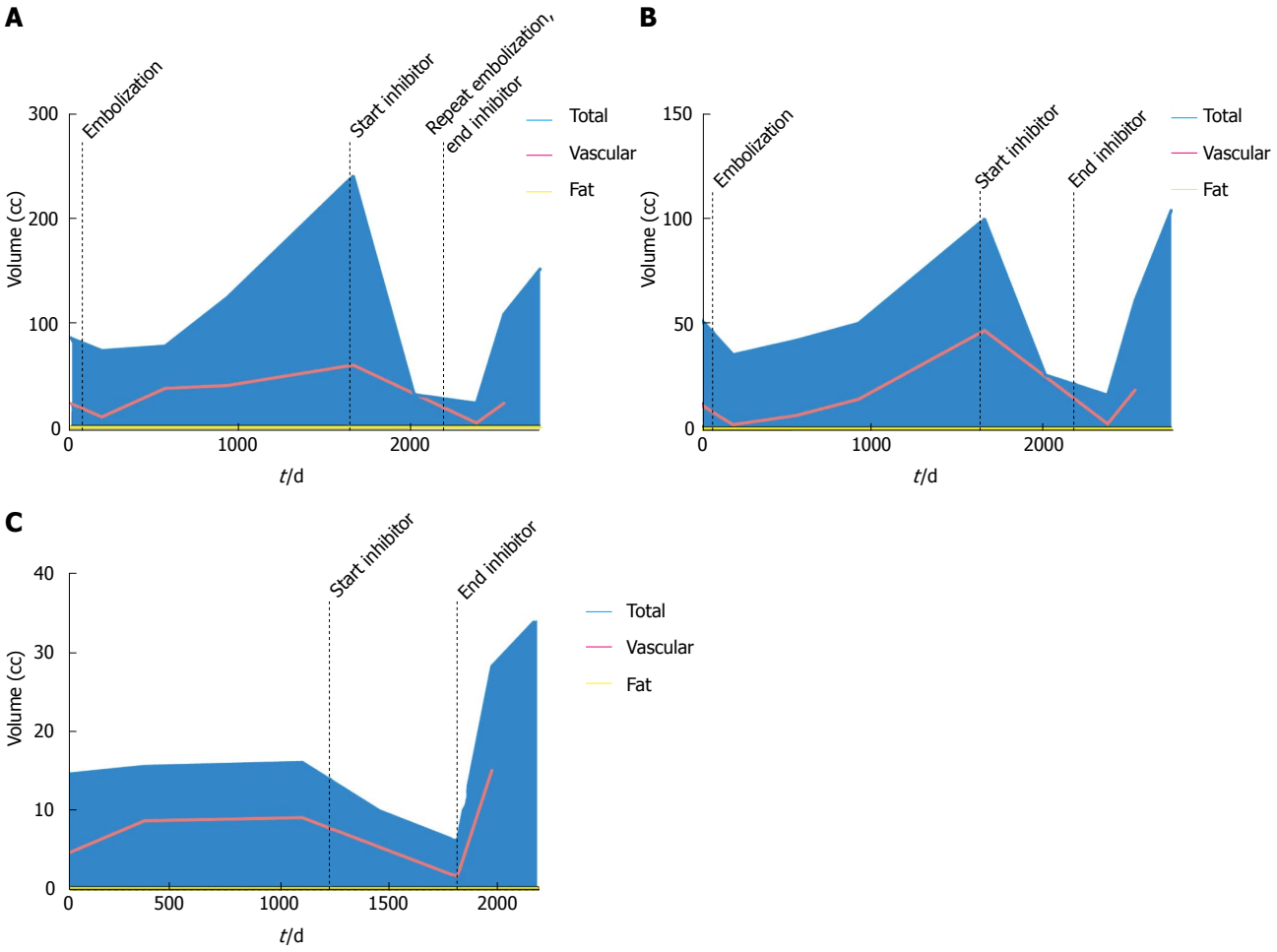

Figure 2 Volumetric analysis of patient 1 angiomyolipomas. Both the right lower pole (A) and right upper pole (B) AMLs demonstrated growth several years following transarterial embolization and immediate response to mTOR inhibitor therapy. The performance of a second embolization did not prevent rebound growth following discontinuation of mTOR inhibitor; C: The left renal AML which did not undergo embolization demonstrated slow sustained growth prior to mTOR inhibitor, with a rapid increase in volume following discontinuation. AML: Angiomyolipoma; mTOR: Mammalian target of rapamycin.

[-1791% (upper pole) and -1257% (lower pole)]. The left upper pole AML, which was not embolized, also demonstrated a significant decrease in size (-166.7%) (Figure 2C). The patient experienced mild side effects from mTOR inhibitor therapy such as oral ulcers. In 2013, mTOR inhibitor therapy was stopped, as diminishing returns were expected with regards to further decreases in tumor size. In an effort to consolidate the gains made by mTOR inhibition, repeat embolization of the right lower pole AML was performed; at this time, grade 2 vascularity was again seen in the lesion. Upon termination of mTOR inhibitor therapy, there was immediate rebound growth of the left upper pole AML (82.5%). The two right renal AMLs which had undergone embolization demonstrated a brief period of tumoral size control, but within a year both lesions demonstrated substantial rebound growth [84.5% (upper pole) and 84.7% (lower pole) from nadir].

Patient 2

At the time of initial presentation, patient 2 was an 18-year-old female with a history of TSC-associated seizure disorder, facial angiofibromas, a right renal AML, and an atrophic left kidney (Table 2). She underwent serial cross sectional CT imaging of the right renal AML for several years, which demonstrated sizeable fat and vascular compartments within the tumor (Figure 3). In 2006 transcatheter embolization of the AML was performed because of lesion size, at which time the tumor vascularity was grade 2. Despite an initial volume response, the tumor began to grow, and as a result she was enrolled in an mTOR inhibitor phase II clinical trial with sirolimus 4 mg daily for one year. The patient did not experience any major side effects from this therapy. During the treatment course there was a significant decrease in tumoral volume (-52%) mirrored across the fat (-61.5%), soft tissue (-32%), and vascular (-496%) compartments. Upon discontinuation of mTOR inhibition there was rebound tumoral growth, once again across all three tissue compartments. The patient subsequently underwent repeat embolization of the AML, at which time the tumor vascularity was grade 1. This procedure, however, was not able to provide sustained control of tumor size, as continued growth of the AML occurred despite the repeat embolization.

Table 2 Timeline for patient 2

Time (d)	Event
0	CT
399	CT
1322	CT
1411	Angiogram with embolization of right upper pole AML
1600	CT
1680	MRI
1658	Initiation of mTOR inhibitor
1799	MRI
1908	MRI
2093	MRI
2094	Cessation of mTOR inhibitor
2280	MRI
3192	MRI
3951	MRI
4039	Angiogram with embolization of right upper pole AML
4270	MRI
4624	MRI

MRI: Magnetic resonance imaging; AML: Angiomyolipoma; mTOR: Mammalian target of rapamycin; CT: Computed tomography.

Table 3 Timeline for patient 3

Time (d)	Event
0	MRI
30	Angiogram with embolization of left renal AML
105	MRI
338	MRI
625	MRI
750	Angiogram with embolization of left renal AML
861	MRI
1434	MRI
2157	MRI
2158	Initiation of mTOR inhibitor
2437	MRI
2897	MRI
2897	Angiogram with embolization of left renal AML
2898	Cessation of mTOR inhibitor
3108	MRI

MRI: Magnetic resonance imaging; AML: Angiomyolipoma; mTOR: Mammalian target of rapamycin.

Patient 3

At the time of initial presentation, patient 3 was a 5-year-old male with a history of TSC-associated seizure disorder, developmental delay, and a left renal AML (Table 3). Cross sectional imaging demonstrated no significant fatty component to the renal lesion. He underwent prophylactic embolization of the tumor in 2004. The tumor demonstrated grade 1 vascularity on initial angiography. After embolization, initial tumor response was quickly followed by continued growth of the tumor (54.8%) (Figure 4), necessitating repeat embolization in 2006; angiography during this repeat embolization was notable for a significant increase in tumor vascularity since the initial embolization, with the development of multiple large pseudoaneurysms that were consistent with grade 3 vascularity (Figure 5). After the repeat embolization, a short period of tumor regression was

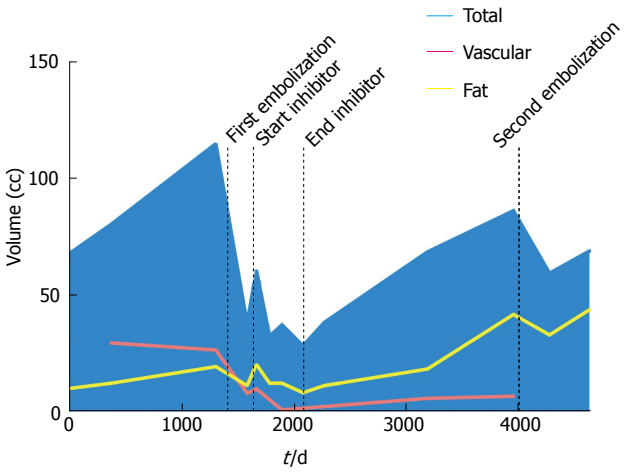

Figure 3 Volumetric analysis of patient 2 angiomyolipoma. A right renal AML underwent embolization prior a course of mTOR inhibitor therapy. Following this course, there was rebound growth involving the lipid, soft tissue, and vascular components of the tumor. Performance of a second embolization only temporarily curtailed tumoral growth. AML: Angiomyolipoma; mTOR: Mammalian target of rapamycin.

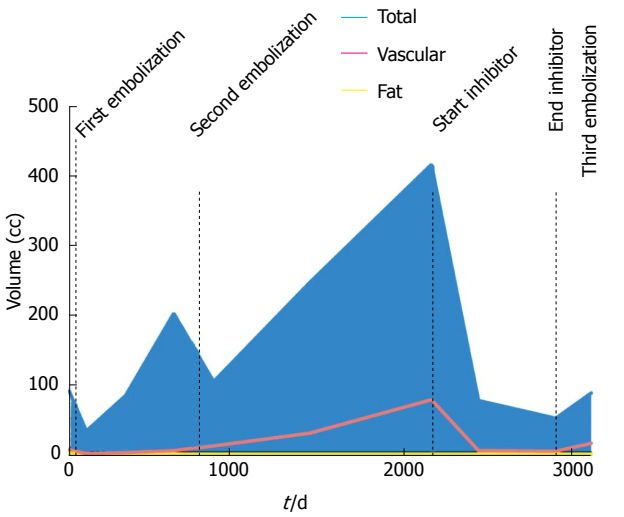

Figure 4 Volumetric analysis of patient 3 angiomyolipoma. A left renal AML was treated with two embolization procedures prior to mTOR inhibitor therapy. Reduction in tumor volume with mTOR inhibitor affected both the soft tissue and vascular components of the tumor. However, discontinuation resulted in rebound growth, including tumor vascularity. AML: Angiomyolipoma; mTOR: Mammalian target of rapamycin.

again followed by steady tumor growth. mTOR inhibitor therapy was initiated in 2010 with sirolimus 2.5 mg twice daily, and for the subsequent 2 years, there was excellent control of tumor volume. The patient did not experience any major side effects from this therapy. In 2012, mTOR inhibitor therapy was stopped, as diminishing returns were expected with regards to further decreases in tumor size. In an effort to consolidate the gains made by mTOR inhibition, the patient underwent a third embolization. Tumor vascularity was notably decreased as compared to the second embolization procedure (Figure 5C). Following the third embolization, however, the tumor demonstrated immediate rebound growth (41%).

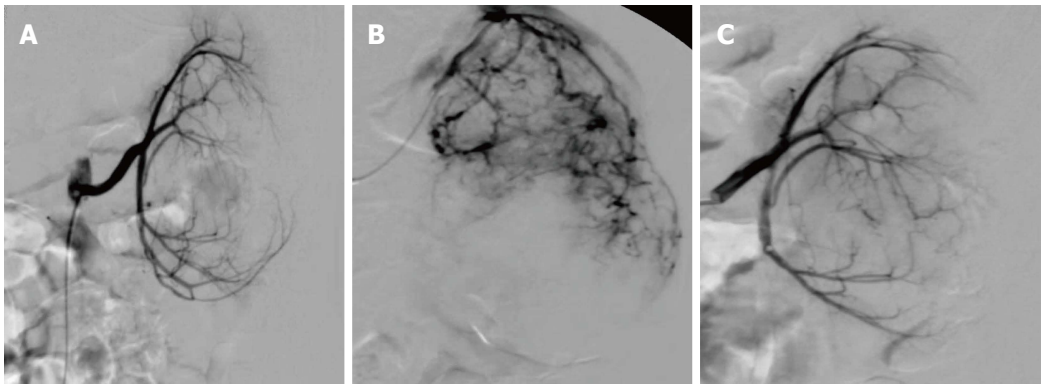

Figure 5 Angiographic analysis of patient 3 angiomyolipomas. A: At the time of the patient's first embolization, initial angiography demonstrated low overall tumoral vasculature (grade 1); B: The second embolization, however, revealed interval significant expansion of tumor vascularity including development of multiple aneurysms (grade 3); C: Following a course of mTOR inhibitor, tumor vascularity was reduced to grade 1 at the third embolization. mTOR: Mammalian target of rapamycin.

DISCUSSION

AMLs are the most commonly encountered benign renal tumor[13], and while they most frequently arise sporadically in the general population, approximately 80% of patients with TSC develop these tumors. The most devastating complication of AMLs is hemorrhage. Tumor size is the most commonly used predictor for hemorrhagic risk, although such decision algorithms are based upon data gathered primarily from sporadic AMLs. TSC-associated AMLs, however, are likely biologically distinct from their sporadic counterparts, and while some studies have corroborated the use of 4 cm diameter as a threshold for intervention in the setting of TSC as at-risk for hemorrhage[14], other reports have found no size association until the AMLs are on the order of 10 cm[4].

Alternative biomarkers have therefore been sought to prognosticate risk of hemorrhage. Rimon *et al*[12] established a semiquantitative vascular grading system for AMLs and found that tumors with more extensive vascularity were more likely to bleed. Planché *et al*[11] performed composition analyses of AMLs prior to and following embolization using CT histograms and demonstrated that tumors with a dominant angiomyogenic composition were better responders to transarterial embolization than tumors that were predominantly lipid containing.

By applying the same vascular grading scale as Rimon *et al*[12] we demonstrate that mTOR inhibitor therapy may reduce tumor vascularity, though given the concomitant performance of intra-arterial embolization, segregating the effects of the two treatment methods based on these data is limited. The reduction in tumor volume is paralleled across the lipid and angiomyogenic components of the lesions. Moreover, rebound growth following discontinuation of mTOR inhibitor therapy is also paralleled across all tissue compartments, including tumor vascularity. This corroborates the hypothesis that any hemorrhage risk reduction achieved by mTOR inhibition is lost once therapy is stopped.

The impact of transcatheter arterial embolization on tumor volume in this case series is remarkable for its transience. All three patients demonstrated regrowth soon after embolization. Previously published reports have demonstrated a far better success rate with TSC-associated AML embolization. For example, Kothary *et al*[5] found a 43% treatment failure rate among 10 TSC patients treated for 21 AMLs. Others have reported even greater success rates: Ewalt *et al*[6] described essentially no regrowth in all 16 TSC patients following AML embolization, and Harabayashi *et al*[4] reported a decrease in tumor size in 10 of 11 TSC-associated AMLs following embolization. While the reasons for these discrepancies are unclear, patient selection and duration of follow up may contribute. For example, the majority of patients reported by Ewalt *et al*[6] were followed for only 3 mo, while embolization for prophylaxis was considered to be an exclusion criterion by Harabayashi *et al*[4] and thus patients with asymptomatic AMLs were not included.

We acknowledge several limitations to this study. Firstly, the small sample size limits the generalizability of the conclusions. However, AMLs with a variety of initial tissue compositions, including lipomatous and non-lipomatous as well as highly vascular and poorly vascular tumors, were included, and the findings of volume reduction in all three tissue compartments were seen in all lesions. Moreover, given the study design, the independent effect of mTOR inhibitors cannot be purely isolated, as all patients underwent embolization as well.

The addition of transcatheter arterial embolization to mTOR inhibitor therapy did not provide sustained abrogation of tumor growth. Although it would be highly desirable to consolidate the gains in tumor volume control from mTOR inhibition by embolizing the residual tumor and thereby prevent rebound growth, this synergy unfortunately did not occur in our series.

Pharmacologic management of TSC-associated AMLs with mTOR inhibitors can provide substantial tumor volume reduction for the duration of the therapeutic course. In this case series, we illustrate that this volume reduction impacts all three tissue compartments of

the tumor. Tumor vascularity tended to be lower grade following mTOR inhibition, suggesting that mTOR inhibitors may reduce risk of tumoral rupture. Unfortunately rebound growth involving all tissue compartments follows shortly after discontinuation of mTOR inhibitor therapy, suggesting that the risk reductions are lost. The addition of transarterial embolization to mTOR inhibitors did not curtail the occurrence of rebound growth.

COMMENTS

Background

Tuberous sclerosis complex (TSC) is an autosomal dominant genetic disorder affecting approximately 2 million people globally. Mutations in the *TSC1* and *TSC2* genes, important regulators of the mammalian target of rapamycin signaling pathway, result in the development of tumors involving multiple organ systems. As many as 80% of patients with TSC develop renal angiomyolipomas, which are soft tissue hamartomatous tumors containing multiple soft tissue components including fat, smooth muscle, and blood vessels.

Research frontiers

Segmentation analysis tools were used to automatically create a region of interest circumscribing the angiomyolipomas. On magnetic resonance images, the "fat only" map calculated from the in- and opposed-phase gradient recalled echo sequences was used to quantify fat volume within tumors. Tumor vascularity was measured by applying a thresholding tool within the region of interest on post-contrast subtraction images.

Innovations and breakthroughs

Transcatheter arterial embolization was performed prophylactically in all 3 patients by attending interventional radiologists.

Applications

Stasis within the target artery was considered the standardized embolization endpoint and was confirmed with post-embolization digital subtraction angiography imaging. This endpoint was achieved in all embolization procedures.

Terminology

Transcatheter arterial embolization.

Peer-review

The authors have performed a good study, the manuscript is interesting.

REFERENCES

1 **Shepherd CW**, Gomez MR, Lie JT, Crowson CS. Causes of death in patients with tuberous sclerosis. *Mayo Clin Proc* 1991; **66**: 792-796 [PMID: 1861550 DOI: 10.1016/S0025-6196(12)61196-3]

2 **Yamakado K**, Tanaka N, Nakagawa T, Kobayashi S, Yanagawa M, Takeda K. Renal angiomyolipoma: relationships between tumor size, aneurysm formation, and rupture. *Radiology* 2002; **225**: 78-82 [PMID: 12354988 DOI: 10.1148/radiol.2251011477]

3 **Steiner MS**, Goldman SM, Fishman EK, Marshall FF. The natural history of renal angiomyolipoma. *J Urol* 1993; **150**: 1782-1786 [PMID: 8230504]

4 **Harabayashi T**, Shinohara N, Katano H, Nonomura K, Shimizu T, Koyanagi T. Management of renal angiomyolipomas associated with tuberous sclerosis complex. *J Urol* 2004; **171**: 102-105 [PMID: 14665854 DOI: 10.1097/01.ju.0000100100.36354.61]

5 **Kothary N**, Soulen MC, Clark TW, Wein AJ, Shlansky-Goldberg RD, Crino PB, Stavropoulos SW. Renal angiomyolipoma: long-term results after arterial embolization. *J Vasc Interv Radiol* 2005; **16**: 45-50 [PMID: 15640409 DOI: 10.1097/01.RVI.0000143769.79774.70]

6 **Ewalt DH**, Diamond N, Rees C, Sparagana SP, Delgado M, Batchelor L, Roach ES. Long-term outcome of transcatheter embolization of renal angiomyolipomas due to tuberous sclerosis complex. *J Urol* 2005; **174**: 1764-1766 [PMID: 16217279 DOI: 10.1097/01.ju.0000177497.31986.64]

7 **Bissler JJ**, McCormack FX, Young LR, Elwing JM, Chuck G, Leonard JM, Schmithorst VJ, Laor T, Brody AS, Bean J, Salisbury S, Franz DN. Sirolimus for angiomyolipoma in tuberous sclerosis complex or lymphangioleiomyomatosis. *N Engl J Med* 2008; **358**: 140-151 [PMID: 18184959 DOI: 10.1056/NEJMoa063564]

8 **Bissler JJ**, Kingswood JC, Radzikowska E, Zonnenberg BA, Frost M, Belousova E, Sauter M, Nonomura N, Brakemeier S, de Vries PJ, Whittemore VH, Chen D, Sahmoud T, Shah G, Lincy J, Lebwohl D, Budde K. Everolimus for angiomyolipoma associated with tuberous sclerosis complex or sporadic lymphangioleiomyomatosis (EXIST-2): a multicentre, randomised, double-blind, placebo-controlled trial. *Lancet* 2013; **381**: 817-824 [PMID: 23312829 DOI: 10.1016/S0140-6736(12)61767-X]

9 **Peng ZF**, Yang L, Wang TT, Han P, Liu ZH, Wei Q. Efficacy and safety of sirolimus for renal angiomyolipoma in patients with tuberous sclerosis complex or sporadic lymphangioleiomyomatosis: a systematic review. *J Urol* 2014; **192**: 1424-1430 [PMID: 24813310 DOI: 10.1016/j.juro.2014.04.096]

10 **Glover GH**. Multipoint Dixon technique for water and fat proton and susceptibility imaging. *J Magn Reson Imaging* 1991; **1**: 521-530 [PMID: 1790376 DOI: 10.1002/jmri.1880010504]

11 **Planché O**, Correas JM, Mader B, Joly D, Méjean A, Hélénon O. Prophylactic embolization of renal angiomyolipomas: evaluation of therapeutic response using CT 3D volume calculation and density histograms. *J Vasc Interv Radiol* 2011; **22**: 1388-1395 [PMID: 21757371 DOI: 10.1016/j.jvir.2011.05.016]

12 **Rimon U**, Duvdevani M, Garniek A, Golan G, Bensaid P, Ramon J, Morag B. Large renal angiomyolipomas: digital subtraction angiographic grading and presentation with bleeding. *Clin Radiol* 2006; **61**: 520-526 [PMID: 16713423 DOI: 10.1016/j.crad.2006.02.003]

13 **Chan CK**, Yu S, Yip S, Lee P. The efficacy, safety and durability of selective renal arterial embolization in treating symptomatic and asymptomatic renal angiomyolipoma. *Urology* 2011; **77**: 642-648 [PMID: 21131030 DOI: 10.1016/j.urology.2010.08.040]

14 **van Baal JG**, Smits NJ, Keeman JN, Lindhout D, Verhoef S. The evolution of renal angiomyolipomas in patients with tuberous sclerosis. *J Urol* 1994; **152**: 35-38 [PMID: 8201681]

P- Reviewer: Andersen PE, Kambadakone A, Tarazov PG
S- Editor: Qiu S **L- Editor**: A **E- Editor**: Lu YJ

World Journal of Radiology

Submit a Manuscript: http://www.wjgnet.com/esps/
Help Desk: http://www.wjgnet.com/esps/helpdesk.aspx
DOI: 10.4329/wjr.v8.i3.316

World J Radiol 2016 March 28; 8(3): 316-321
ISSN 1949-8470 (online)

ORIGINAL ARTICLE

Retrospective Study

Multidetector computed tomography features of pancreatic metastases from leiomyosarcoma: Experience at a tertiary cancer center

Chong Hyun Suh, Abhishek Keraliya, Atul B Shinagare, Kyung Won Kim, Nikhil H Ramaiya, Sree Harsha Tirumani

Chong Hyun Suh, Kyung Won Kim, Department of Radiology and Research Institute of Radiology, University of Ulsan College of Medicine, Asan Medical Center, Seoul 138-736, South Korea

Chong Hyun Suh, Department of Radiology, Namwon Medical Center, Jeollabuk-Do 590-702, South Korea

Abhishek Keraliya, Atul B Shinagare, Nikhil H Ramaiya, Sree Harsha Tirumani, Department of Imaging, Dana Farber Cancer Institute, Harvard Medical School, Boston, MA 02115, United States

Abhishek Keraliya, Atul B Shinagare, Nikhil H Ramaiya, Sree Harsha Tirumani, Department of Radiology, Brigham and Women's Hospital, Harvard Medical School, Boston, MA 02115, United States

Author contributions: Shinagare AB and Ramaiya NH designed the research; Suh CH, Keraliya A and Tirumani SH performed the research; Shinagare AB and Kim KW contributed new reagents/analytic tools; Suh CH, Kim KW and Tirumani SH analyzed the data; Suh CH and Tirumani SH wrote the paper.

Institutional review board statement: The study was approved by the institutional review board.

Informed consent statement: Informed consent was waived by the institutional review board.

Conflict-of-interest statement: None of the authors have any conflicts of interest pertaining to the content in the manuscript. Dr. Shinagare is a recipient of RSNA research grant unrelated to the current study.

Data sharing statement: No additional data available.

Correspondence to: Sree Harsha Tirumani, MD, Department of Imaging, Dana Farber Cancer Institute, Harvard Medical School, 450 Brookline Avenue, Boston, MA 02115, United States. stirumani@partners.org
Telephone: +1-617-6326312
Fax: +1-617-5828574

Received: August 20, 2015
Peer-review started: August 22, 2015
First decision: November 6, 2015
Revised: November 15, 2015
Accepted: January 5, 2016
Article in press: January 7, 2016
Published online: March 28, 2016

Abstract

AIM: To describe the multidetector computed tomography features of pancreatic metastasis from leiomyosarcoma (LMS).

METHODS: Between January 1995 and December 2012, 13 consecutive patients (11 women, 2 men; mean age of 57 years; range, 38-78 years) with pancreatic metastases from LMS were included in our study. Imaging features including location, number, largest dimension, tumor attenuation and enhancement characteristics, presence of necrosis, pancreatic ductal dilatation, common bile duct (CBD) dilatation, presence of pancreatitis, and atrophy were documented.

RESULTS: The most common site of origin of the pancreatic metastases from LMS was uterus (38.5%), followed by retroperitoneum (30.8%) and extremity

(23.1%). None of the patients in our study had pancreas as the first site of metastasis. All patients developed pancreatic metastases at a median interval of 24 mo. Pancreatic metastases from LMS were solitary in 8/13 patients and multiple in 5/13 patients, had no predilection for any part of the pancreas, were hypovascular on arterial phase in 10/13 patients and associated with pancreatic duct dilatation in 3/13 patients. None had CBD dilatation. None of the pancreatic metastases in LMS cohort caused pancreatitis, and atrophy. Median duration of follow-up was 19 mo for LMS cohort during which two patients underwent resection of metastasis (median survival 45 mo) while the remaining underwent systemic therapy (median survival 13 mo).

CONCLUSION: Pancreatic metastases from LMS are often solitary and hypovascular masses and less commonly associated with pancreatic ductal dilatation, CBD dilatation, pancreatitis or pancreatic atrophy. Surgical resection of solitary LMS pancreatic metastasis can be considered due to the long survival of these patients.

Key words: Pancreatic metastasis; Hypovascular; Renal cell carcinoma; Leiomyosarcoma; Multidetector computed tomography

Core tip: Pancreatic metastases from leiomyosarcoma (LMS) commonly arise in the uterus and are characterized by a long latency period after the diagnosis of primary tumor. Although the imaging features of the pancreatic metastases from LMS are nonspecific, pancreatic metastases from LMS should be considered in the differential diagnosis of solitary or multiple hypovascular masses without pancreatic ductal dilatation, common bile duct dilatation, pancreatitis, atrophy in the pancreas in patients with history of LMS. Surgical resection of solitary LMS pancreatic metastasis can be considered due to the long survival of these patients after detection of pancreatic metastasis.

Suh CH, Keraliya A, Shinagare AB, Kim KW, Ramaiya NH, Tirumani SH. Multidetector computed tomography features of pancreatic metastases from leiomyosarcoma: Experience at a tertiary cancer center. *World J Radiol* 2016; 8(3): 316-321 Available from: URL: http://www.wjgnet.com/1949-8470/full/v8/i3/316.htm DOI: http://dx.doi.org/10.4329/wjr.v8.i3.316

INTRODUCTION

Pancreatic metastases are rare accounting for approximately 2%-5% of all malignant pancreatic neoplasms[1-3]. Metastatic spread to pancreas can occur from a variety of primary malignancies with the most common primaries being renal cell carcinoma (RCC), lung cancer, breast cancer, colorectal cancer, and malignant melanoma[2,4]. The overall incidence of pancreatic metastasis in patients with diffuse metastatic disease varies between 3% and 12% in various autopsy series. Leiomyosarcoma (LMS) is a rare and aggressive malignant tumor composed of cells of smooth muscle origin. The most common primary sites of LMS include genitourinary tract, usually the uterus, retroperitoneum and gastrointestinal tract[5]. The common sites of distant metastases from LMS are lungs, kidney, and liver[6,7]. Pancreatic metastasis from LMS is extremely rare[8-10].

Pancreatic metastases are often asymptomatic and can come to clinical attention on imaging either at the time of initial work or post-operative surveillance of non-pancreatic primary neoplasm. Less commonly, they can present with symptoms due to biliary obstruction. Characterization of pancreatic metastasis on imaging studies can be challenging as well as crucial because they can mimic primary pancreatic malignancy and determine the prognosis and management[11]. Most of the radiology literature has been focused on the imaging features of pancreatic metastasis from RCC. Being a rare disease entity, the imaging features of pancreatic metastasis from LMS have not been reported so far. The available literature focuses on management[12,13] and are small series of case reports[8-10]. Accordingly, the purpose of this article is to describe the multidetector computed tomography (MDCT) features of pancreatic metastasis from LMS.

MATERIALS AND METHODS

Subjects

This study was a Health Insurance Portability and Accountability Act (HIPAA) compliant, institutional review board-approved retrospective study with waiver for informed consent. Between January 2000 and December 2012, 323 patients with LMS arising in uterus (n = 116), extremities (n = 55), retroperitoneum (n = 36), skin (n = 25), inferior vena cava (n = 23), mesentery (n = 15), bowel (n = 1) and other sites (n = 42) were either primarily treated or referred to our institute. The radiology reports of all these 323 patients were searched electronically to identify patients with pancreatic metastases which returned 13 patients (11 women, 2 men; mean age of 57 years; range, 38-78 years). These 13 consecutive patients with pancreatic metastases from LMS on MDCT scans were included in our study and the remaining 310 patients were excluded. The histopathology of the primary tumor was confirmed as LMS in all the patients as part of the routine oncology care.

Imaging

Pretreatment contrast-enhanced CT scan and follow-up imaging were available in all 13 patients. In total we reviewed 148 CT examinations. The CT scans of were performed at our institute on multidetector scanners [four-slice (GE Healthcare, Barrington, IL, United States), 16-row (Siemens Medical Solutions, Forchheim, Germany), and 64-row (Toshiba America Medical Systems, Tustin, CA,

Table 1 Distribution of primary leiomyosarcoma

Site	*n* (%)
Uterus	5 (38.5)
Retroperitoneum	4 (30.8)
Extremity	3 (23.1)
Inferior vena cava	1 (7.7)

United States) MDCT systems with 0.5 mm collimation, 120 kVp, 500 mA (max), gantry rotation time 0.5 s, table speed of 26.5 mm/rotation. The anatomic coverage extended from the clavicles to the pubic symphysis according to the standard department protocol. After intravenous contrast administration, the images of the chest and upper abdomen were acquired after a delay of 25-30 s followed by images of the abdomen and pelvis after 60-70 s. Oral contrast was administered in all the patients.

The imaging was reviewed in consensus by two oncoradiology fellowship trained radiologists (SHT and NHR) with 9 and 16 years of experience each. Imaging features of pancreatic metastases from LMS including location, number, largest dimension, tumor attenuation and enhancement characteristics on CT with respect to the paraspinal muscles (less than, similar to or greater than skeletal muscles) in the portal venous phase, presence of necrosis, pancreatic ductal dilatation, common bile duct (CBD) dilatation, presence of pancreatitis, atrophy, peripancreatic soft tissue infiltration, peripancreatic lymphadenopathy, and vessel involvement were recorded. For determining hypervascularity, the arterial phase images of chest CT which included the upper sections of the abdomen were used. On follow-up imaging, the number of metastasis and size of metastasis were recorded. The metastatic disease was confirmed either by histopathology or by serial imaging demonstrating interval change in the index lesions.

Clinical data

The clinical information for all the 13 patients including demographic data, site of primary tumor, first site of metastases, the date of pancreatic metastasis, duration of follow-up and outcome were documented from the electronic medical record. The time from diagnosis of metastasis to diagnosis of pancreatic metastasis and overall survival were calculated from the clinical data.

Statistical analysis

Statistical analysis was performed with SPSS software (SPSS, version 21; IBM, Armonk, NY) by one of the authors (CHS). $P < 0.05$ was considered to indicate a significant difference.

RESULTS

The distribution of the primary tumor in our study is shown in Table 1. In 11 (84.6%) patients, first site of metastases was lung. Other sites of first metastasis were right paracolic gutter, subcutaneous tissue, spine, and bones. None of the patients had pancreas as the first site of metastases. All patients developed pancreatic metastases at a median interval of 24 mo (range, 1-77 mo).

Imaging of pancreatic metastases in our study

The mean size of pancreatic metastasis in our study was 2.0 cm (range, 1.0-3.5 cm). Table 2 summarizes the imaging characteristic of pancreatic metastasis from LMS. The location of pancreatic metastasis from LMS was the head in six patients (46.2%), body in two patients, tail in one patient, head and body in three patients, and body and tail in one patient. Pancreatic metastases from LMS were solitary in eight patients (61.5%) and multiple in five patients (38.5%). The pancreatic metastasis were hypovascular on the arterial phase in 10/13 (76.9%) patients and hypervascular in the remaining patients. On the venous phase, the enhancement was homogeneous in seven patients (53.8%), and heterogeneous in 6 patients (46.2%). CT evidence of necrosis was present in six tumors. Pancreatic ductal dilatation (mean, 4.7 mm; range, 3-8 mm) was noted in 3 patients (23.1%). None of the patients had CBD dilatation, CT evidence of pancreatitis, atrophy, peripancreatic lymphadenopathy, or vascular invasion.

Follow-up imaging

Of the 13 patients in our study, two patients with solitary pancreatic metastasis underwent Whipple's resection. The remaining eleven patients received systemic treatment. In addition, prophylactic CBD stenting was performed in three patients with metastasis in the head/uncinate process. The median duration of follow-up after detection of pancreatic metastasis in our study was 19 mo (range, 1-48 mo). During follow-up, the two patients who underwent resection of the pancreatic metastasis remained free of pancreatic metastasis on the last follow-up scan. The remaining patients showed increase in mean tumor size from 2.0 cm to 3.9 cm (range, 1.0-7.3 cm). The number of pancreatic metastasis increased in four patients during follow-up (Figure 1).

Outcome

In patients with pancreatic metastasis from LMS at the time of last follow-up, 12 out of the 13 patients have died at a median interval of 48 mo (interquartile range, 30-61 mo) after the diagnosis of metastases. The median survival after the diagnosis of pancreatic metastasis in these 13 patients was 19 mo (interquartile range, 8-34 mo). In two patients who underwent surgical resection, while one patient died 45 mo after the diagnosis of pancreatic metastasis, another patient was alive at the time of last follow-up. In 11 patients who underwent systemic chemotherapy, the median survival was 13 mo (interquartile range, 8-25 mo).

DISCUSSION

In our study, the most common site of origin of LMS in patients with pancreatic metastases was uterus (38.5%),

Table 2 Imaging characteristic of pancreatic metastasis from leiomyosarcoma *n* (%)

Imaging characteristic	Pancreatic metastasis from LMS (*n* = 13)
Age (yr)	57
Sex (male: female)	2:11
Size of largest (cm)	2.0 ± 0.8
Location	
Head	6 (46.2)
Body	2 (15.4)
Tail	1 (7.7)
Head and body	3 (23.1)
Body and tail	1 (7.7)
Head and tail	0
Head, body, and tail	0
Solitary	8 (61.5)
Multiple	5 (38.5)
Tumor attenuation on arterial phase	
Hypovascular	10 (76.9)
Hypervascular	3 (23.1)
Homogeneity	
Homogeneous enhancement	7 (54.8)
Heterogeneous enhancement	6 (46.2)
Necrosis	6 (46.2)
Pancreatic ductal dilatation	3 (23.1)
Common bile duct dilatation	0 (0)
Pancreatitis	0 (0)
Atrophy	0 (0)

LMS: Leiomyosarcoma.

followed by retroperitoneum (30.8%) and extremity (23.1%). There was no specific predilection of the metastasis for any part of the pancreas in our study. We found that metastasis to pancreas occurs later in the disease course in LMS at a median interval of 24 mo after the diagnosis of primary and was always preceded by metastasis to other sites like lungs. In a literature review of 333 pancreatic metastases, Minni *et al*[14] demonstrated that 77.6% of patients developed pancreatic metastasis metachronously at an interval of 9.2 years after the diagnosis of primary tumor. Awareness of late occurrence of pancreatic metastasis in LMS may justify long-term follow-up of these patients and necessitate caution while interpreting images. Pancreas as the first site of metastasis was not seen in any of the patients in our cohort and identification of a pancreatic mass in a patient with LMS who has no other sites of metastasis should raise the suspicion of alternate pathology like primary pancreatic malignancy.

Metastasis to pancreas can be solitary or multiple/diffuse. Pancreatic metastases from LMS in our study were more often solitary at the time of detection. This is in agreement with previous reports[14,15]. Solitary pancreatic metastasis can be difficult to differentiate from primary pancreatic malignancy. However in contrast to primary pancreatic cancer, pancreatic ductal dilatation, pancreatic atrophy, vascular invasion and peripancreatic adenopathy were uncommon in pancreatic metastasis from LMS which can help differentiate the two entities.

LMS can cause widespread hematogenous metastases,

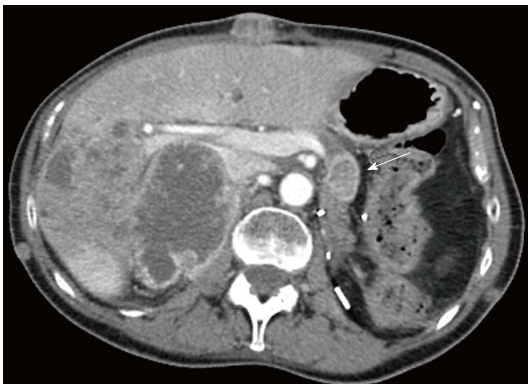

Figure 1 Fifty-four-year-old woman with pancreatic metastasis from retroperitoneal leiomyosarcoma. Axial contrast-enhanced computed tomography image of the upper abdomen in the arterial phase demonstrates a hypovascular metastasis with central necrosis in the pancreatic body (arrow). Note the hepatic, right adrenal and subcutaneous metastasis.

particularly to the lungs, liver, soft tissues and bones. Hepatic metastases from LMS are frequently hypervascular[16]. However, in contrast to hepatic metastasis, pancreatic metastases in 10 of 13 (76.9%) patients in our study were hypovascular on arterial phase. This may be explained by relative hypervascularity of the normal pancreatic parenchyma. Pancreatic metastases from RCC, which is the most common primary tumor to metastasize to the pancreas[2,4], are usually hypervasuclar[17].

Surgical resection of pancreatic metastasis is a relatively safe and useful procedure. Pancreatic resections can be performed with low mortality and morbidity rates[4,18,19]. Minni *et al*[14] in their study reviewed all cases of pancreatic metastasis reported in literature including 5 cases of LMS metastasis and found that 150 of 234 pancreatic metastases underwent pancreatic resection and concluded that surgical resection should be considered in patients with pancreatic metastasis as they tend to have prolonged survival. In our study, two patients with single metastasis underwent Whipple's operation for pancreatic metastasis and the median survival after the diagnosis of pancreatic metastasis was 45 mo compared to the median survival was 13 mo in the 11 patients who underwent systemic chemotherapy. Therefore, surgical resection of solitary pancreas metastasis could be considered as a treatment option in the patients with pancreatic metastases from LMS.

Our study had several limitations. First, the number of study patients was small and this was retrospective study. Second, limitations of this study include a referral bias of the study populations that may confound our imaging findings. However, these limitations appear unavoidable when dealing with a disease as rare as pancreatic metastasis from LMS at a large referral center. Given the rare nature of this disease process and the lack of other large studies, we believe that our study adds to the existing knowledge about pancreatic metastasis from LMS.

To conclude, we present the MDCT features of pancreatic metastases from LMS. Pancreatic metastases from LMS

commonly arise in the uterus and are characterized by a long latency period after the diagnosis of primary tumor. Although the imaging features of the pancreatic metastases from LMS are nonspecific, pancreatic metastases from LMS should be considered in the differential diagnosis of solitary or multiple hypovascular masses without pancreatic ductal dilatation, CBD dilatation, pancreatitis, atrophy in the pancreas in patients with history of LMS. Surgical resection of solitary LMS pancreatic metastasis can be considered due to the long survival of these patients after detection of pancreatic metastasis.

COMMENTS

Background

Pancreatic metastases are rare accounting for approximately 2%-5% of all malignant pancreatic neoplasms. The overall incidence of pancreatic metastasis in patients with diffuse metastatic disease varies between 3% and 12% in various autopsy series. The most common primary sites of leiomyosarcoma (LMS) include genitourinary tract, usually the uterus, retroperitoneum and gastrointestinal tract. The common sites of distant metastases from LMS are lungs, kidney, and liver. Pancreatic metastasis from LMS is extremely rare. Pancreatic metastases are often asymptomatic and can come to clinical attention on imaging either at the time of initial work or post-operative surveillance of non-pancreatic primary neoplasm. Less commonly, they can present with symptoms due to biliary obstruction. Characterization of pancreatic metastasis on imaging studies can be challenging as well as crucial because they can mimic primary pancreatic malignancy and determine the prognosis and management. Accordingly, the purpose of this article is to describe the multidetector computed tomography features of pancreatic metastasis from LMS.

Research frontiers

Most of the radiology literature has been focused on the imaging features of pancreatic metastasis from renal cell carcinoma. Being a rare disease entity, the imaging features of pancreatic metastasis from LMS have not been reported so far. The available literature focuses on management and are small series of case reports.

Innovations and breakthroughs

In this study, the most common site of origin of LMS in patients with pancreatic metastases was uterus (38.5%), followed by retroperitoneum (30.8%) and extremity (23.1%). There was no specific predilection of the metastasis for any part of the pancreas in this study. The authors found that metastasis to pancreas occurs later in the disease course in LMS at a median interval of 24 mo after the diagnosis of primary and was always preceded by metastasis to other sites like lungs. In a literature review of 333 pancreatic metastases, Minni *et al* demonstrated that 77.6% of patients developed pancreatic metastasis metachronously at an interval of 9.2 years after the diagnosis of primary tumor. Awareness of late occurrence of pancreatic metastasis in LMS may justify long-term follow-up of these patients and necessitate caution while interpreting images. Pancreas as the first site of metastasis was not seen in any of the patients in this cohort and identification of a pancreatic mass in a patient with LMS who has no other sites of metastasis should raise the suspicion of alternate pathology like primary pancreatic malignancy.

Applications

Pancreatic metastases from LMS commonly arise in the uterus and are characterized by a long latency period after the diagnosis of primary tumor. Although the imaging features of the pancreatic metastases from LMS are nonspecific, pancreatic metastases from LMS should be considered in the differential diagnosis of solitary or multiple hypovascular masses without pancreatic ductal dilatation, common bile duct (CBD) dilatation, pancreatitis, atrophy in the pancreas in patients with history of LMS. Surgical resection of solitary LMS pancreatic metastasis can be considered due to the long survival of these patients after detection of pancreatic metastasis.

Terminology

LMS is a rare and aggressive malignant tumor composed of cells of smooth muscle origin.

Peer-review

The author of this paper evaluated the MDCT features of pancreatic metastases from LMS. Pancreatic metastases from LMS should be considered in the differential diagnosis of solitary or multiple hypovascular masses without pancreatic ductal dilatation, CBD dilatation, pancreatitis, atrophy in the pancreas in patients with history of LMS.

REFERENCES

1 **Ascenti G**, Visalli C, Genitori A, Certo A, Pitrone A, Mazziotti S. Multiple hypervascular pancreatic metastases from renal cell carcinoma: dynamic MR and spiral CT in three cases. *Clin Imaging* 2004; **28**: 349-352 [PMID: 15471667 DOI: 10.1016/s0899-7071(03)00198-0]

2 **Crippa S**, Angelini C, Mussi C, Bonardi C, Romano F, Sartori P, Uggeri F, Bovo G. Surgical treatment of metastatic tumors to the pancreas: a single center experience and review of the literature. *World J Surg* 2006; **30**: 1536-1542 [PMID: 16847716 DOI: 10.1007/s00268-005-0464-4]

3 **Kassabian A**, Stein J, Jabbour N, Parsa K, Skinner D, Parekh D, Cosenza C, Selby R. Renal cell carcinoma metastatic to the pancreas: a single-institution series and review of the literature. *Urology* 2000; **56**: 211-215 [PMID: 10925080 DOI: 10.1016/S0090-4295(00)00639-7]

4 **Sohn TA**, Yeo CJ, Cameron JL, Nakeeb A, Lillemoe KD. Renal cell carcinoma metastatic to the pancreas: results of surgical management. *J Gastrointest Surg* 2001; **5**: 346-351 [PMID: 11985973 DOI: 10.1016/S1091-255X(01)80060-3]

5 **Rossi CR**, Casali P, Kusamura S, Baratti D, Deraco M. The consensus statement on the locoregional treatment of abdominal sarcomatosis. *J Surg Oncol* 2008; **98**: 291-294 [PMID: 18726899 DOI: 10.1002/jso.21067]

6 **Rose PG**, Piver MS, Tsukada Y, Lau T. Patterns of metastasis in uterine sarcoma. An autopsy study. *Cancer* 1989; **63**: 935-938 [PMID: 2914299 DOI: 10.1002/1097-0142(19890301)63]

7 **Taylor HB**, Norris HJ. Mesenchymal tumors of the uterus. IV. Diagnosis and prognosis of leiomyosarcomas. *Arch Pathol* 1966; **82**: 40-44 [PMID: 5938448]

8 **Alonso Gómez J**, Arjona Sánchez Á, Martínez Cecilia D, Díaz Nieto R, Roldán de la Rúa J, Valverde Martínez A, Lizárraga Febres E, Padillo Ruiz J, Rufián Peña S. Uterine leiomyosarcoma metastasis to the pancreas: report of a case and review of the literature. *J Gastrointest Cancer* 2012; **43**: 361-363 [PMID: 20549388 DOI: 10.1007/s12029-010-9172-x]

9 **Iwamoto I**, Fujino T, Higashi Y, Tsuji T, Nakamura N, Komokata T, Douchi T. Metastasis of uterine leiomyosarcoma to the pancreas. *J Obstet Gynaecol Res* 2005; **31**: 531-534 [PMID: 16343254 DOI: 10.1111/j.1447-0756.2005.00344.x]

10 **Ozturk S**, Unver M, Ozturk BK, Bozbıyık O, Erol V, Kebabcı E, Olmez M, Zalluhoglu N, Bayol U. Isolated metastasis of uterine leiomyosarcoma to the pancreas: Report of a case and review of the literature. *Int J Surg Case Rep* 2014; **5**: 350-353 [PMID: 24858977 DOI: 10.1016/j.ijscr.2014.04.016]

11 **Wente MN**, Kleeff J, Esposito I, Hartel M, Müller MW, Fröhlich BE, Büchler MW, Friess H. Renal cancer cell metastasis into the pancreas: a single-center experience and overview of the literature. *Pancreas* 2005; **30**: 218-222 [PMID: 15782097 DOI: 10.1097/01.mpa.0000153337.58105.47]

12 **Hernández S**, Martín-Fernández J, Lasa I, Busteros I, García-Moreno F. Pancreaticoduodenectomy for metastasis of uterine leiomyosarcoma to the pancreas. *Clin Transl Oncol* 2010; **12**: 643-645 [PMID: 20851807 DOI: 10.1007/s12094-010-0571-z]

13 **Tan CH**, Tamm EP, Marcal L, Balachandran A, Charnsangavej C, Vikram R, Bhosale P. Imaging features of hematogenous metastases to the pancreas: pictorial essay. *Cancer Imaging* 2011; **11**: 9-15 [PMID: 21367687 DOI: 10.1102/1470-7330.2011.0002]

14 **Minni F**, Casadei R, Perenze B, Greco VM, Marrano N, Margiotta A, Marrano D. Pancreatic metastases: observations of three cases and review of the literature. *Pancreatology* 2004; **4**: 509-520 [PMID: 15316227 DOI: 10.1159/000080248]
15 **Tsitouridis I**, Diamantopoulou A, Michaelides M, Arvanity M, Papaioannou S. Pancreatic metastases: CT and MRI findings. *Diagn Interv Radiol* 2010; **16**: 45-51 [PMID: 20027546 DOI: 10.4261/1305-3825.dir.1996-08.1]
16 **Shah SH**, Jagannathan JP, Krajewski K, O'Regan KN, George S, Ramaiya NH. Uterine sarcomas: then and now. *AJR Am J Roentgenol* 2012; **199**: 213-223 [PMID: 22733915 DOI: 10.2214/ajr.11.7287]
17 **Palmowski M**, Hacke N, Satzl S, Klauss M, Wente MN, Neukamm M, Kleeff J, Hallscheidt P. Metastasis to the pancreas: characterization by morphology and contrast enhancement features on CT and MRI. *Pancreatology* 2008; **8**: 199-203 [PMID: 18434757 DOI: 10.1159/000128556]
18 **Büchler MW**, Wagner M, Schmied BM, Uhl W, Friess H, Z'graggen K. Changes in morbidity after pancreatic resection: toward the end of completion pancreatectomy. *Arch Surg* 2003; **138**: 1310-1314; discussion 1315 [PMID: 14662530 DOI: 10.1001/archsurg.138.12.1310]
19 **Reddy S**, Edil BH, Cameron JL, Pawlik TM, Herman JM, Gilson MM, Campbell KA, Schulick RD, Ahuja N, Wolfgang CL. Pancreatic resection of isolated metastases from nonpancreatic primary cancers. *Ann Surg Oncol* 2008; **15**: 3199-3206 [PMID: 18784960 DOI: 10.1245/s10434-008-0140-7]

P- Reviewer: Takebayashi S **S- Editor**: Qi Y **L- Editor**: A
E- Editor: Lu YJ

World Journal of Radiology

Submit a Manuscript: http://www.wjgnet.com/esps/
Help Desk: http://www.wjgnet.com/esps/helpdesk.aspx
DOI: 10.4329/wjr.v8.i3.322

World J Radiol 2016 March 28; 8(3): 322-330
ISSN 1949-8470 (online)

ORIGINAL ARTICLE

Observational Study

Simultaneous whole body ^{18}F-fluorodeoxyglucose positron emission tomography magnetic resonance imaging for evaluation of pediatric cancer: Preliminary experience and comparison with ^{18}F-fluorodeoxyglucose positron emission tomography computed tomography

Brian S Pugmire, Alexander R Guimaraes, Ruth Lim, Alison M Friedmann, Mary Huang, David Ebb, Howard Weinstein, Onofrio A Catalano, Umar Mahmood, Ciprian Catana, Michael S Gee

Brian S Pugmire, Department of Radiology, Cincinnati Children's Hospital Medical Center, Cincinnati, OH 45229, United States

Alexander R Guimaraes, Division of Body Imaging, Oregon Health Sciences University, Portland, OR 97239, United States

Alexander R Guimaraes, Onofrio A Catalano, Michael S Gee, Division of Abdominal Imaging, Massachusetts General Hospital, Boston, MA 02114, United States

Alexander R Guimaraes, Umar Mahmood, Ciprian Catana, Martinos Center for Biomedical Imaging, Charlestown, MA 02129, United States

Ruth Lim, Umar Mahmood, Division of Nuclear Medicine and Molecular Imaging, Massachusetts General Hospital, Boston, MA 02114, United States

Ruth Lim, Michael S Gee, Division of Pediatric Imaging, MassGeneral Hospital for Children, Boston, MA 02114, United States

Alison M Friedmann, Mary Huang, David Ebb, Howard Weinstein, Division of Pediatric Hematology-Oncology, MassGeneral Hospital for Children, Boston, MA 02114, United States

Author contributions: Gee MS was the principal investigator and designed the study; Pugmire BS and Gee MS participated in the acquisition, analysis, and interpretation of the data, and drafted the initial manuscript; Guimaraes AR, Lim R, Catalano OA, Mahmood U and Catana C were involved in revising the intellectual content of the data; Friedmann AM, Huang M, Ebb D, Weinstein H participated in patient recruitment.

Institutional review board statement: This study was reviewed and approved by the Dana Farber Cancer Institute Institutional Review Board.

Informed consent statement: All study participants, or their legal guardian, provided informed written consent prior to study enrollment.

Conflict-of-interest statement: The authors have no relevant financial interests to disclose.

Data sharing statement: No additional data are available.

Correspondence to: Michael S Gee, MD, Division of Pediatric Imaging, MassGeneral Hospital for Children, 55 Fruit St, Boston, MA 02114, United States. msgee@partners.org
Telephone: +1-61-77244207
Fax: +1-61-77268360

Received: September 30, 2015
Peer-review started: October 1, 2015
First decision: November 4, 2015
Revised: November 18, 2015
Accepted: January 5, 2016
Article in press: January 7, 2016
Published online: March 28, 2016

Abstract

AIM: To describe our preliminary experience with simultaneous whole body ^{18}F-fluorodeoxyglucose (^{18}F-FDG)

positron emission tomography and magnetic resonance imaging (PET-MRI) in the evaluation of pediatric oncology patients.

METHODS: This prospective, observational, single-center study was Health Insurance Portability and Accountability Act-compliant, and institutional review board approved. To be eligible, a patient was required to: (1) have a known or suspected cancer diagnosis; (2) be under the care of a pediatric hematologist/oncologist; and (3) be scheduled for clinically indicated ^{18}F-FDG PET-CT examination at our institution. Patients underwent PET-CT followed by PET-MRI on the same day. PET-CT examinations were performed using standard department protocols. PET-MRI studies were acquired with an integrated 3 Tesla PET-MRI scanner using whole body T1 Dixon, T2 HASTE, EPI diffusion-weighted imaging (DWI) and STIR sequences. No additional radiotracer was given for the PET-MRI examination. Both PET-CT and PET-MRI examinations were reviewed by consensus by two study personnel. Test performance characteristics of PET-MRI, for the detection of malignant lesions, including FDG maximum standardized uptake value (SUVmax) and minimum apparent diffusion coefficient (ADCmin), were calculated on a per lesion basis using PET-CT as a reference standard.

RESULTS: A total of 10 whole body PET-MRI exams were performed in 7 pediatric oncology patients. The mean patient age was 16.1 years (range 12-19 years) including 6 males and 1 female. A total of 20 malignant and 21 benign lesions were identified on PET-CT. PET-MRI SUVmax had excellent correlation with PET-CT SUVmax for both benign and malignant lesions (R = 0.93). PET-MRI SUVmax > 2.5 had 100% accuracy for discriminating benign from malignant lesions using PET-computed tomography (CT) reference. Whole body DWI was also evaluated: the mean ADCmin of malignant lesions (780.2 + 326.6) was significantly lower than that of benign lesions (1246.2 + 417.3; P = 0.0003; Student's t test). A range of ADCmin thresholds for malignancy were evaluated, from 0.5-1.5 × 10^{-3} mm^2/s. The 1.0 × 10^{-3} ADCmin threshold performed best compared with PET-CT reference (68.3% accuracy). However, the accuracy of PET-MRI SUVmax was significantly better than ADCmin for detecting malignant lesions compared with PET-CT reference (P < 0.0001; two-tailed McNemar's test).

CONCLUSION: These results suggest a clinical role for simultaneous whole body PET-MRI in evaluating pediatric cancer patients.

Key words: Positron emission tomography; Radiology; Pediatric imaging; Oncology; Cancer; Magnetic resonance imaging

Core tip: Combined positron emission tomography and magnetic resonance imaging (PET-MRI) is an exciting new imaging modality; however, its clinical role remains undefined. PET-MRI has distinct potential advantages for pediatric patients, but the data regarding PET-MRI in children remains limited. We report our experience using PET-MRI in pediatric oncology patients. We found excellent correlation between PET-MRI and PET-computed tomography (CT) maximum standardized uptake values as well as excellent test performance characteristics for PET-MRI using PET-CT as a reference. We also include an evaluation of MRI diffusion weighted imaging in comparison to PET-MRI and PET-CT, which has not been reported previously in the literature.

Pugmire BS, Guimaraes AR, Lim R, Friedmann AM, Huang M, Ebb D, Weinstein H, Catalano OA, Mahmood U, Catana C, Gee MS. Simultaneous whole body ^{18}F-fluorodeoxyglucose positron emission tomography magnetic resonance imaging for evaluation of pediatric cancer: Preliminary experience and comparison with ^{18}F-fluorodeoxyglucose positron emission tomography computed tomography. *World J Radiol* 2016; 8(3): 322-330 Available from: URL: http://www.wjgnet.com/1949-8470/full/v8/i3/322.htm DOI: http://dx.doi.org/10.4329/wjr.v8.i3.322

INTRODUCTION

Combined 18-fluorodeoxyglucose (FDG) positron emission tomography-magnetic resonance imaging (PET-MRI) is a promising new imaging modality. Early results in adult patients have shown that PET-MRI is technically feasible and demonstrates excellent concordance with positron emission tomography-computed tomography (PET-CT) findings[1-9]. PET-MRI has several potential benefits in pediatric cancer patients. First, it holds the promise of improved evaluation of neoplastic disease by combining the superior soft tissue contrast and tissue characterization abilities of MRI, including diffusion-weighted imaging (DWI), with PET metabolic information. This combination is particularly helpful in the evaluation of primary and metastatic malignancies involving the central nervous system, bone marrow, mediastinum, pelvis, and extremities, all of which are relatively common in the pediatric population. Current imaging protocols for these malignancies typically involve separate MRI and PET-CT examinations. The availability of whole body integrated PET-MRI scanners is advantageous both in terms of reducing overall scan times, which would lead to shorter exposure to sedation and anesthesia, as well as improved anatomic registration of PET and MR images due to simultaneous data acquisition[10]. Additionally, by substituting MRI for CT, PET-MRI promises substantially reduced ionizing radiation doses compared to PET-CT. Finally, the superior soft tissue contrast of MRI compared to CT is likely to improve the characterization of incidental indeterminate findings seen on whole body imaging[2], potentially decreasing the need for additional follow-up examinations and/or invasive procedures.

Evidence regarding the performance of integrated

PET-MRI in the pediatric oncology population is relatively sparse compared with adults, with a total of 42 patients included in three published studies[11-13]. The purpose of this study is to evaluate the performance of whole body integrated PET-MRI using ^{18}F-FDG for the detection of malignant lesions in pediatric patients using PET-CT performed earlier on the same day as a reference standard. We compared ^{18}F-FDG standardized uptake values derived from PET-MR with MR-based attenuation correction to those obtained derived from PET-CT with CT attenuation correction. In addition, we evaluated the performance of whole body DWI, which has been shown to be useful for lymphoma staging in both pediatric and adult patients[14,15], for malignant lesion detection compared with PET-CT reference.

MATERIALS AND METHODS

The Institutional Review Board (IRB) of our hospital approved this prospective study, which was Health Insurance Portability and Accountability Act (HIPAA) compliant. Informed consent was obtained from all patients 18 or more years of age and from the parents or legal guardians of all patients under 18 years of age. All patients under the age of the 18 also gave their assent to participation in this study.

Patient selection

In order to be eligible for this study a patient was required to: (1) have a known or suspected cancer diagnosis; (2) be under the care of a pediatric hematologist/oncologist; and (3) be scheduled for clinically indicated ^{18}F-FDG PET-CT examination at our institution. Patients were not eligible to participate if they would require sedation or general anesthesia in order to undergo the PET-MRI examination, were inpatients at the time of their PETCT, had any contraindications to MRI (*e.g.*, non-MRI compatible implants), or were not able to follow directions and hold still for the MRI examination. Patients who underwent additional clinically indicated follow-up PET-CT examinations during the study time period were eligible to undergo an accompanying PET-MRI with each subsequent PET-CT.

Imaging technique

PET-CT: All patients underwent PET-CT examinations prior to PET-MRI, which were performed with a 64-slice PET-CT scanner (Siemens Biograph, Siemens Medical Solutions, Knoxville, TN) on our institution's main hospital campus. While data from the PET-CT were collected for comparison to PET-MRI, the PET-CT was performed based on clinical indications and the decision to obtain the PET-CT scan and the image acquisition protocol of the PET-CT were explicitly not under the control of this study. Therefore, the PET-CT examinations were performed according to standard departmental protocols which include (1) a low-dose attenuation-correction CT (120 kVp, 11 mAs) without intravenous contrast acquired during shallow free breathing from the base of skull to the mid-thigh, followed by (2) PET image acquisition, followed by (3) a diagnostic-quality CT of varying anatomic coverage with or without intravenous contrast (depending on the clinical indication). PET-CT imaging began a mean of 59 min (range 48-78 min) after intravenous FDG administration. PET data underwent automatic attenuation correction using attenuation maps generated from the attenuation-correction CT. The diagnostic CT portion of the examination was performed using standardized, weight-adjusted protocols, including dose modulation, as this is the standard protocol for pediatric patients at our institution.

PET-MRI: Immediately following the PET-CT examinations patients were transported a short distance to an off-campus research facility where the PET-MRI scanner is located. No additional 18-FDG was administered. PET-MRI studies were acquired with a 3 Tesla Biograph mMR scanner (Siemens Medical Solutions, Knoxville, TN) with a 16-channel head and neck surface coil and three or four 12-channel body coils (the number of body coils used was dependent on the height of the patient). These coils were combined to form a multichannel whole-body coil. The PET-MRI acquisitions began a mean of 170 min (range 131-222 min) after FDG injection.

PET acquisition was performed with a 26 cm z-axis field of view and 30% overlap between adjacent table stations. Four to five table positions were acquired based on patient height. The pulse sequences comprising the MRI portion of the PET-MR protocol are summarized in Table 1. MRI acquisitions were simultaneously with PET acquisition starting from the level of the mid-thigh and moving toward the head. Images of the thighs, pelvis, and neck were acquired during shallow free breathing and images of the upper abdomen and thorax were acquired during expiration breath holding. PET data underwent automatic attenuation correction with attenuation maps generated from the two-point Dixon sequence. The FDG administration time was used as the reference time for decay correction. Diffusion weighted imaging was performed using B-values of 50, 400, and 800 s/mm^2.

Statistical analysis

Both PET-CT and PET-MRI examinations were reviewed by consensus by two study personnel (one board certified pediatric radiologist and one radiology resident) using a Syngo workstation (Version 2.00.0000.0014, Siemens Healthcare, Erlangen, Germany). Lesions were identified based on anatomic CT images as abnormally enlarged (> 10 mm diameter) lymph nodes or soft tissue lesions in visceral solid organs or bones. Additional non-enlarged, normal-appearing lymph nodes were included as lesions in the study as control nonmalignant lesions. A maximum standardized uptake value (SUVmax) > 2.5 based on PET-CT imaging was defined as being positive for malignancy. SUVmax values for each lesion on both the PET-CT and PET-MRI were obtained using three-dimensional (3-D) regions of interest (ROIs). The correlation between the SUVmax values obtained

Table 1 Magnetic resonance imaging pulse sequences in pediatric whole body positron emission tomography-magnetic resonance imaging protocol

Pulse sequence	Plane	TR (ms)	TE (ms)	Thk/sp (mm)	Flip angle (°)	BW (Hz/Px)	FOV (cm)	Matrix	TA
T1 Dixon VIBE AC	Coronal	3.6	1.2	3/0	10	965	40-50	192 × 121	0:19
T1 VIBE	Axial	3.9	2.5	3/0	9	720	35-45	288 × 288	0:24
T2 HASTE FS	Axial	1600	95	5/0	9	710	30-40	320 × 260	1:08
EPI DWI	Axial	11000	70	6/0	N/A	2084	30-40	160 × 120	3:51
STIR	Coronal	4000	48	4/0	120	200	35-40	320 × 192	4:54

AC: Attenuation correction; TR: Repetition time; TE: Echo time; BW: Bandwidth; FOV: Field of view; TA: Acquisition time (per table position); VIBE: Volumetric interpolated breath hold examination; HASTE: Half-fourier acquisition single-shot turbo spin echo; FS: Fat suppression; EPI: Echo planar imaging; DWI: Diffusion weighted imaging; STIR: Short tau inversion recovery.

Table 2 Patients and diagnoses

Age at time of diagnosis	Sex	Diagnosis	Total number of PET-MRI examinations
13	Male	Gastrointestinal stromal tumor	3
19	Male	Undifferentiated small round cell sarcoma	1
12	Male	Rhabdomyosarcoma	1
18	Male	Non-Hodgkin's lymphoma (follicular)	1
18	Male	Hodgkin's lymphoma	1
19	Male	Non-Hodgkin's lymphoma (large B-cell)	2
14	Female	Paraganglioma	1

PET-MRI: Positron emission tomography-magnetic resonance imaging.

for each lesion with PET-CT and PET-MR was analyzed using the Pearson correlation coefficient with a statistical significance threshold of $P < 0.05$. Minimum apparent diffusion coefficient (ADCmin) values were also obtained for each lesion based on the lowest value obtained for a voxel on ADC maps within the lesion, and the correlation between the ADCmin and the PET-CT SUVmax values was analyzed using the Pearson correlation method.

Test performance characteristics of PET-MRI, for the detection of malignant lesions, including FDG SUVmax and ADCmin, was calculated on a per lesion basis using PET-CT as a reference standard. Radiation dose estimates for the CT portion of the PET-CT examinations were obtained by converting the dose length product to effective dose (mSv) using standard conversion factors. The effective dose for the PET portion of the PET-CT examinations was calculated using age specific conversion factors previously published by Chawla *et al*[16]. The mean imaging time (total time of image acquisition) was calculated for both PET-CT and PET-MRI and these means were compared using Student's *t*-test.

RESULTS

A total of 10 PET-CT and 10 PET-MRI examinations were performed and evaluated from 7 patients. The mean patient age was 16.1 years (range 12-19 years) including 6 males and 1 female. Their diagnoses included gastrointestinal stromal tumor (GIST), lymphoma (both Hodgkin and non-Hodgkin lymphoma), rhabdomyosarcoma, paraganglioma, and undifferentiated malignant small round cell sarcoma (Table 2), (Figures 1-5). The mean PET-CT image acquisition time was 28.8 min (range 27-31 min) and the mean PET-MRI acquisition time was 75.4 min (range 51-115 min). The mean effective dose imparted by the PET-CT examinations was 12.18 mSv (range 6.1-17.9), whereas the mean effective dose of the PET portion alone was 4.05 mSv (range 3.39-4.9). This difference was statistically significant ($P = 0.004$, Student's *t* test). The mean effective dose for the CT portion of the PET-CT examination was 8.12 mSv (range 2.1-13.0), accounting for 66.7% of the total effective dose for all PET-CT examinations. PET-MRI, by extension, would be associated with an approximately 67% reduction in total effective ionizing radiation dose compared with PET-CT in our pediatric study population.

A total of 20 FDG-avid malignant lesions and 21 non-FDG-avid benign lesions were detected by PET-CT and PET-MRI and included in our analysis. The most common malignant lesion locations were lymph nodes (10), solid abdominal organs (3), lung (3), and bone (2). The correlation between the PET-CT and PET-MRI SUVmax values based on CT attenuation corrected PET-CT and MR attenuation corrected PET-MR imaging was excellent ($R = 0.93$; $P < 0.0001$) (Figure 6A). Using an SUVmax threshold of > 2.5, PET-MRI SUVmax categorized benign and malignant lesions perfectly compared with PET-CT reference, with an accuracy, sensitivity, and specificity values all of 100% (Table 3). We also evaluated whole-body DWI as an independent biomarker of malignancy compared with PET-CT reference. There was a negative correlation between lesion ADCmin as assessed on DWI and PET-CT SUVmax values, as expected, that was less robust compared with PET-MRI SUVmax (Figure 6B; $R = -0.39$, $P > 0.05$). The mean ADCmin of malignant lesions (780.2 + 326.6) was significantly lower than that of benign lesions (1246.2 + 417.3; $P = 0.0003$ Student's *t* test). We evaluated the performance of a range of ADCmin thresholds for malignancy, from 0.5-1.5 × 10^{-3} mm^2/s. The 1.0 × 10^{-3} ADCmin threshold performed best compared with PET-CT reference (68.3% accuracy; Table 3). However, the accuracy of PET-MRI SUVmax was significantly better than ADCmin for detecting malignant lesions

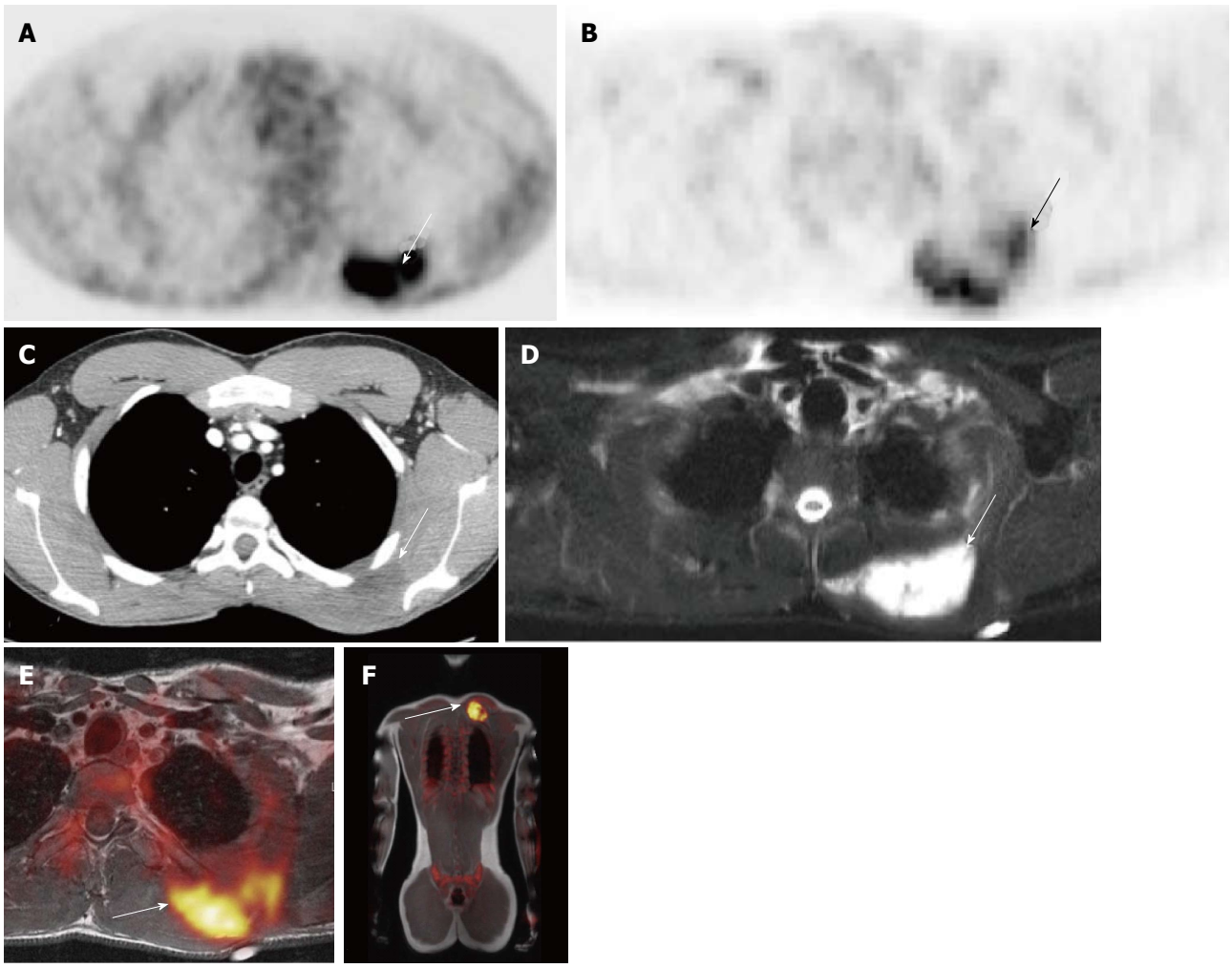

Figure 1 19-year-old male with undifferentiated malignant small round cell sarcoma. Axial image from the PET-CT examination (A) shows intense uptake in mass in the left upper back (white arrow); axial image from the PET-MRI examination (B) shows similar FDG uptake in this region (white arrow); axial CT image from the PET-CT (C) shows a slightly hypodense mass in this region (white arrow). This mass is much better seen on the axial T2 fat suppressed image from the PET-MRI (D) (white arrow). Fused PET-MRI images [T1-weighted axial (E) and whole body coronal (F) MR sequences] again show intense FDG uptake associated with the mass in the left upper back (white arrows). PET-MRI: Positron emission tomography-magnetic resonance imaging; CT: Computed tomography; FDG: Fluorodeoxyglucose.

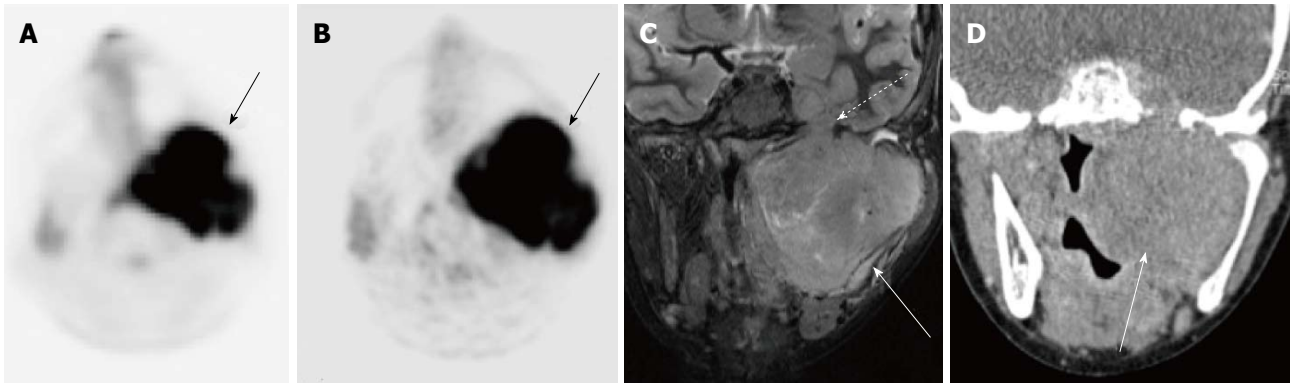

Figure 2 12-year-old male with rhabdomyosarcoma. Axial PET image from PET-MRI (A) shows intense FDG uptake in the left parapharyngeal region (black arrow). Axial PET image from PET-CT (B) shows similar uptake in the same region (black arrow). Coronal T2-weighted fat suppressed image from the MRI portion of the examination (C) clearly shows extent of tumor (white arrow) including perineural spread through foramen rotundum (white dashed arrow). Tumor is not as well delineated on this coronal CT image from the PET-CT examination (D) (white arrow). PET-MRI: Positron emission tomography-magnetic resonance imaging; CT: Computed tomography; FDG: Fluorodeoxyglucose.

compared with PET-CT reference ($P < 0.0001$; two-tailed McNemar's test).

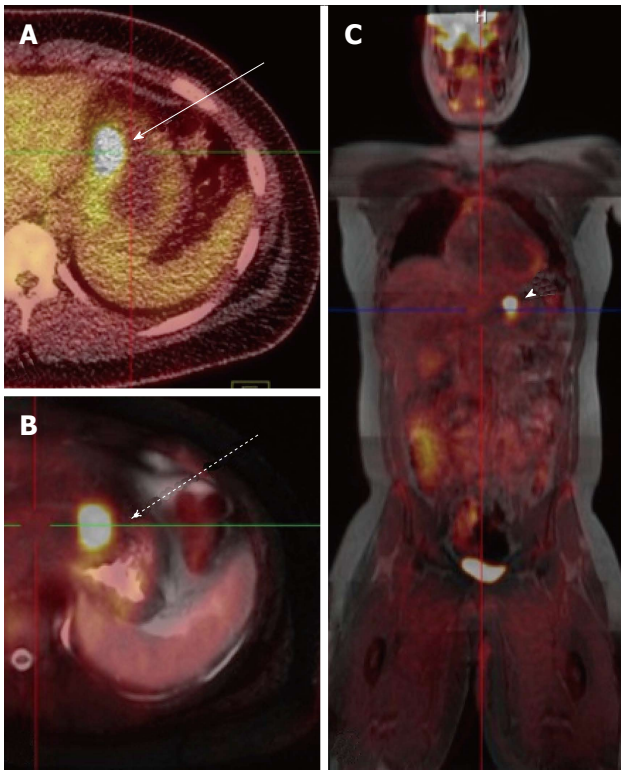

Figure 3 14-year-old male with gastrointestinal stromal tumor. Axial fused PET-CT image (A) shows intense uptake along the lesser curvature of the stomach (white arrow). Axial fused PET-MRI image (B) (T2-weighed HASTE sequence) shows similar intense uptake along the lesser curvature (dashed arrow). Coronal whole body fused PET-MRI image (C) (T1 VIBE sequence) shows intense uptake in the same region (arrowhead). PET-MRI: Positron emission tomography-magnetic resonance imaging; CT: Computed tomography.

DISCUSSION

In this study, we present our initial experience using simultaneous whole body integrated PET-MRI for the evaluation of pediatric oncology patients. Our results demonstrate very good correlation between lesion PET-MRI and PET-CT SUVmax values, which confirms previous results reported by our group and others[7,11,13]. A PET-MRI SUVmax threshold of > 2.5 demonstrated 100% accuracy for detecting malignant lesions seen on PET-CT obtained the same visit. Importantly, PET-MRI was able to accurately detect lesions in both bone and lung, two tissues that can sometimes be associated with segmentation and attenuation correction artifacts on PET-MRI[17,18]. Our results suggest that the Dixon-based MR attenuation correction technique provides accurate whole body tissue attenuation maps across a broad spectrum of tissue types. In addition, the use of 3D ROIs to calculate lesion volumetric SUVmax values may help mitigate small variations in SUV values within a lesion.

We also evaluated the performance of the whole body DWI component of the simultaneous whole body PET-MRI protocol as an independent biomarker of malignancy compared with PET-CT reference. Malignant lesions (defined by PET-CT SUVmax) as a group exhibited a significantly lower ADCmin compared with benign lesions. An ADCmin threshold < 1.0×10^{-3} mm^2/s was the best

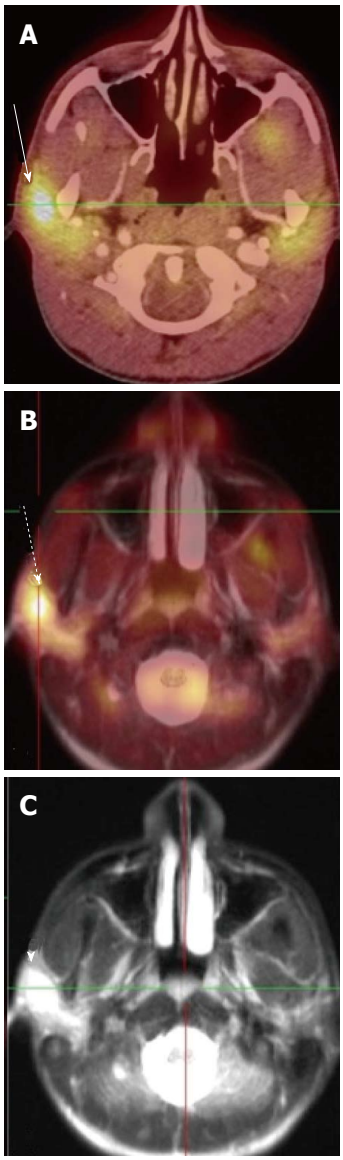

Figure 4 18-year-old male with follicular lymphoma of the right parotid gland. Axial fused PET-CT image (A) shows intense uptake in the region of the right parotid gland (white arrow). Axial fused PET-MRI image (B) (T2 HASTE sequence) shows similar intense uptake in the right parotid (yellow image). Axial T2 HASTE image (C) shows a focal T2-hyperintense mass in the right parotid. This mass was not well seen on CT. PET-MRI: Positron emission tomography-magnetic resonance imaging; CT: Computed tomography.

DWI biomarker of malignancy, with an accuracy of 68.3% and a positive predictive value of 66.7%. Of note, the accuracy of ADCmin was significantly lower than that of PET-MRI SUVmax, suggesting that the PET portion of a combined PET-MRI examination remains a critical component of cancer imaging. Our results are similar to those observed in adult lymphoma patients undergoing PET-MRI[19] and are in keeping with other recent studies suggesting there is no single ADC quantitative threshold that can reliably distinguish benign from malignant lesions in pediatric oncology patients[14,20]. To our knowledge, this is the first study to directly compare DWI ADC and PET-MRI SUV for cancer detection in pediatric patients.

Our results also show that PET-MRI would result in substantial radiation dose savings compared to PET-

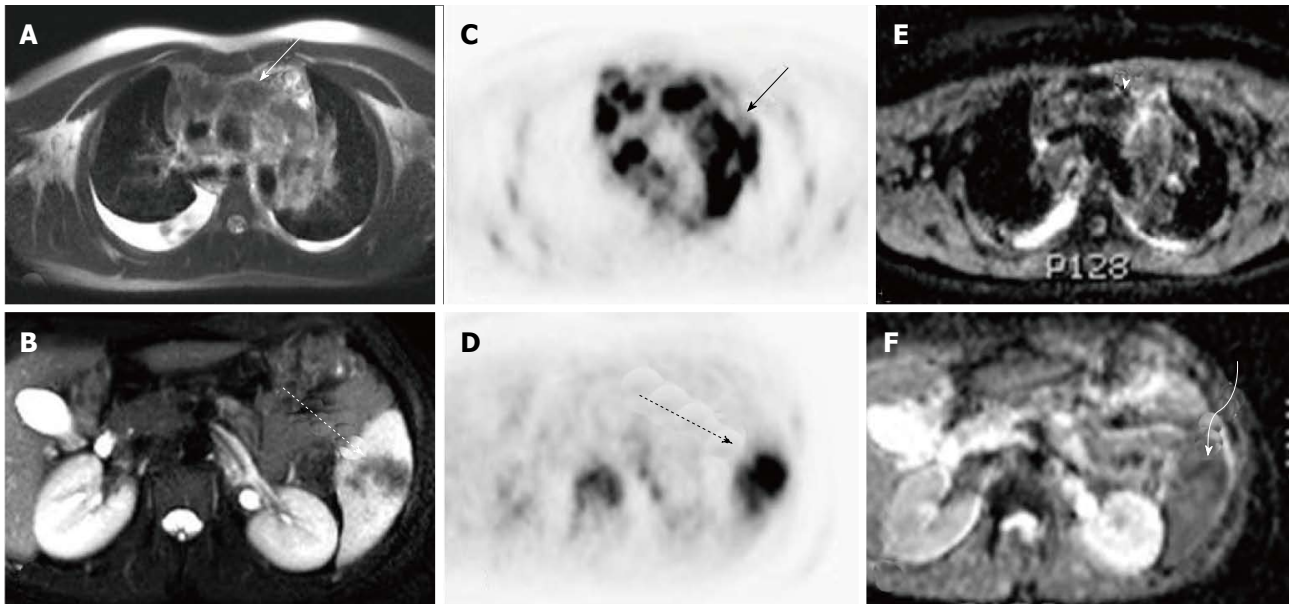

Figure 5 18-year-old male with nodular sclerosing Hodgkin's lymphoma. Axial T2-weighted MRI images of the chest (A) and abdomen (B) demonstrate enlarged mediastinal lymph nodes (white solid arrow) and a region of hypointensity within the spleen (white dashed arrow). Axial images from the concurrently obtained PET examination (C and D) demonstrate intense radiotracer uptake within the mediastinal lymph nodes (solid black arrow) and spleen (dashed black arrow). Axial ADC map images through the same regions (E and F) show areas of decreased signal intensity corresponding to the areas of radiotracer uptake (arrowhead and curve arrow). PET: Positron emission tomography; MRI: Magnetic resonance imaging; ADC: Apparent diffusion coefficient.

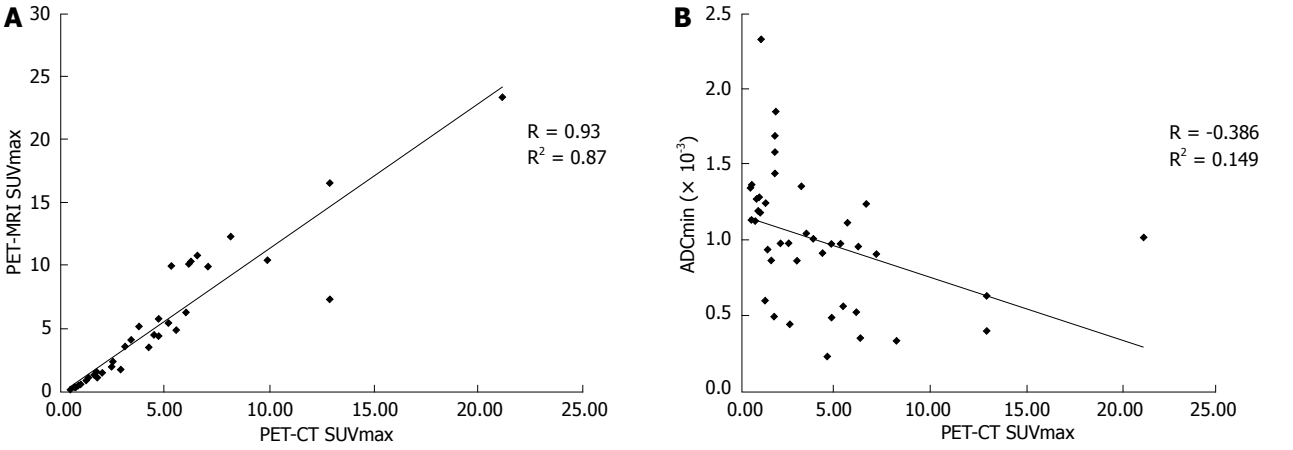

Figure 6 Correlation between positron emission tomography-magnetic resonance imaging biomarkers and positron emission tomography-computed tomography and ADCmin values with positron emission tomography-computed tomography SUVmax. A: PET-MRI SUVmax as a function of PET-CT SUVmax; B: PET-MRI ADCmin as a function of PET-CT SUVmax. PET-MRI: Positron emission tomography-magnetic resonance imaging; CT: Computed tomography; ADCmin: Minimum apparent diffusion coefficient; SUVmax: Maximum standardized uptake value.

CT, with a 67% total reduction in total effective dose. Our results are comparable with those observed in other studies[11-13]. The radiation exposure reduction in this population is predominantly due to the fact that contrast-enhanced diagnostic CT imaging is typically performed as part of the PET-CT exam in the pediatric oncology population at our institution and many others. The substitution of MRI for CT would have a significant impact on radiation reduction in this vulnerable population, especially considering that many of these patients will undergo serial PET-CT imaging for staging and evaluation of treatment response. It should be noted that, while MRI does not use ionizing radiation, it is not without risks, including the theoretical risk of tissue heating as well as known risks of interactions with implanted material and potential reactions to intravenous contrast material. Additionally, in younger patients MRI frequently requires the use of sedatives or anesthetics, which also carry their own associated risks. PET-CT in very young patients also frequently requires sedation or anesthesia, so the substitution of PET-MRI does not entail an increased risk in this regard.

One issue that may impact routine clinical implementation of PET-MRI is the relatively long scan time compared with PET-CT. However, when considering that many pediatric oncology patients would also routinely require separately-acquired PET-CT and diagnostic MR imaging for local tumor staging, the simultaneous whole

Table 3 Comparative performance of positron emission tomography-magnetic resonance imaging maximum standardized uptake value and minimum apparent diffusion coefficient for lesion detection compared with positron emission tomography-computed tomography reference

Test characteristic	SUVmax > 2.5	ADCmin < 0.5 mm^2/s	ADCmin < 1.0 mm^2/s	ADCmin < 1.5 mm^2/s
Accuracy	100%[1]	61.0%	68.3%	58.5%
Sensitivity	100%	28.6%	70.0%	100.0%
Specificity	100%	95.0%	66.7%	19.0%
Positive predictive value	100%	85.7%	66.7%	54.1%

[1]Indicates statistical significance ($P < 0.001$, two-tailed McNemar's test). ADCmin: Minimum apparent diffusion coefficient; SUVmax: Maximum standardized uptake value.

body PET-MRI acquisition may not increase overall imaging time. The simultaneous whole body PET-MRI acquisition may be an issue for small children who may not be able to tolerate awake scanning without the need for sedation or anesthesia. However, as these children would ordinarily require sedation or anesthesia for PET-CT, PET-MRI would not likely increase their overall exposure to anesthesia related risks. Future research is being directed at developing shorter whole body PET-MRI protocols.

Limitations of our study include the small sample size, relatively older adolescent population, the wide range of tumor types included, and the fact that the research PET-MRI scans were consistently performed after the clinical PET-CT exams. In addition, histologic confirmation was not available for all of the lesions included in the study and we utilized PET-CT as the reference standard. However, all of these patients had histologic confirmation of disease prior to imaging and PET-CT would be considered the imaging standard for detection of malignant lesions in this patient population. Future studies will be needed to evaluate PET-MRI as a sole imaging modality in specific tumor types.

In summary, we present our preliminary results of simultaneous whole body PET-MRI for evaluation of pediatric oncology patients. Our results suggest that PET-MRI has high accuracy for detecting malignant lesions across a wide range of tumor types and anatomic locations, and is associated with a substantial reduction in patient ionizing radiation exposure compared with PET-CT. PET-MRI will likely be increasingly utilized for imaging evaluation of pediatric oncology patients in the near future.

COMMENTS

Background

Positron emission tomography-magnetic resonance imaging (PET-MRI) is a novel imaging technique that combines the spatial and contrast resolution of MRI with the physiologic information provided by PET into one integrated examination. It holds significant promise as a new imaging modality, however the literature regarding this technique in children remains limited.

Research frontiers

While a few early studies have provided preliminary evidence that PET-MRI is a safe and accurate technique for the evaluation of malignant disease in the pediatric population, further research is needed to confirm these early findings and elucidate the appropriate clinical role for PET-MRI in these patients. Potential areas where PET-MRI may provide added benefit are soft-tissue sarcomas, lymphoma, and brain tumors.

Innovations and breakthroughs

The findings of this prospective observational study confirm the high accuracy of PET-MRI for the detection of malignant lesions, using PET-computed tomography (CT) as a reference. This study is the first to compare PET directly with diffusion weighted imaging in the detection of such lesions and demonstrates the superiority of PET in this application.

Applications

These data provide greater evidence that PET-MRI is an imaging technique which is ready for clinical use as well as more detailed investigation to further define its clinical role.

Terminology

Combined PET-MRI is an imaging technique which allows for the simultaneous acquisition of PET and MRI images. The PET attenuation correction is accomplished through the use of MRI sequences rather than CT images. The PET-MRI images can be fused and viewed simultaneous providing a more complete imaging evaluation of the patient.

Peer-review

This paper describes a research study meant to assess the feasibility and accuracy of PET-MRI in the evaluation of pediatric cancer. The focus of the work is to compare the performance of PET-MRI in its ability, accuracy and utility to detect and characterize cancerous tumors using PET-CT as a reference standard on pediatric oncology patients during the same visit. Obtained results suggest that PET-MRI has high accuracy for detecting malignant lesions across a wide range of tumor types and anatomic locations, and it is associated with a substantial reduction in patient ionizing radiation exposure compared with PET-CT.

REFERENCES

1 **Catalano OA**, Nicolai E, Rosen BR, Luongo A, Catalano M, Iannace C, Guimaraes A, Vangel MG, Mahmood U, Soricelli A, Salvatore M. Comparison of CE-FDG-PET/CT with CE-FDG-PET/MR in the evaluation of osseous metastases in breast cancer patients. *Br J Cancer* 2015; **112**: 1452-1460 [PMID: 25871331 DOI: 10.1038/bjc.2015.112]

2 **Catalano OA**, Rosen BR, Sahani DV, Hahn PF, Guimaraes AR, Vangel MG, Nicolai E, Soricelli A, Salvatore M. Clinical impact of PET/MR imaging in patients with cancer undergoing same-day PET/CT: initial experience in 134 patients--a hypothesis-generating exploratory study. *Radiology* 2013; **269**: 857-869 [PMID: 24009348 DOI: 10.1148/radiol.13131306]

3 **Partovi S**, Robbin MR, Steinbach OC, Kohan A, Rubbert C, Vercher-Conejero JL, Kolthammer JA, Faulhaber P, Paspulati RM, Ros PR. Initial experience of MR/PET in a clinical cancer center. *J Magn Reson Imaging* 2014; **39**: 768-780 [PMID: 24006287 DOI: 10.1002/jmri.24334]

4 **Gaertner FC**, Fürst S, Schwaiger M. PET/MR: a paradigm shift. *Cancer Imaging* 2013; **13**: 36-52 [PMID: 23446110 DOI: 10.1102/1470-7330.2013.0005]

5 **Quick HH**, von Gall C, Zeilinger M, Wiesmüller M, Braun H, Ziegler S, Kuwert T, Uder M, Dörfler A, Kalender WA, Lell M. Integrated whole-body PET/MR hybrid imaging: clinical experience. *Invest Radiol* 2013; **48**: 280-289 [PMID: 23442775 DOI: 10.1097/RLI.0b013e3182845a08]

6 **Schwenzer NF**, Schraml C, Müller M, Brendle C, Sauter A, Spengler W, Pfannenberg AC, Claussen CD, Schmidt H. Pulmonary lesion assessment: comparison of whole-body hybrid MR/PET and PET/CT imaging--pilot study. *Radiology* 2012; **264**: 551-558 [PMID: 22653189 DOI: 10.1148/radiol.12111942]

7 **Drzezga A**, Souvatzoglou M, Eiber M, Beer AJ, Fürst S, Martinez-

Möller A, Nekolla SG, Ziegler S, Ganter C, Rummeny EJ, Schwaiger M. First clinical experience with integrated whole-body PET/MR: comparison to PET/CT in patients with oncologic diagnoses. *J Nucl Med* 2012; **53**: 845-855 [PMID: 22534830 DOI: 10.2967/jnumed.111.098608]

8 **Delso G**, Fürst S, Jakoby B, Ladebeck R, Ganter C, Nekolla SG, Schwaiger M, Ziegler SI. Performance measurements of the Siemens mMR integrated whole-body PET/MR scanner. *J Nucl Med* 2011; **52**: 1914-1922 [PMID: 22080447 DOI: 10.2967/jnumed.111.092726]

9 **Eiber M**, Takei T, Souvatzoglou M, Mayerhoefer ME, Fürst S, Gaertner FC, Loeffelbein DJ, Rummeny EJ, Ziegler SI, Schwaiger M, Beer AJ. Performance of whole-body integrated 18F-FDG PET/MR in comparison to PET/CT for evaluation of malignant bone lesions. *J Nucl Med* 2014; **55**: 191-197 [PMID: 24309383 DOI: 10.2967/jnumed.113.123646]

10 **Rakheja R**, Chandarana H, DeMello L, Jackson K, Geppert C, Faul D, Glielmi C, Friedman KP. Correlation between standardized uptake value and apparent diffusion coefficient of neoplastic lesions evaluated with whole-body simultaneous hybrid PET/MRI. *AJR Am J Roentgenol* 2013; **201**: 1115-1119 [PMID: 24147485 DOI: 10.2214/AJR.13.11304]

11 **Schäfer JF**, Gatidis S, Schmidt H, Gückel B, Bezrukov I, Pfannenberg CA, Reimold M, Ebinger M, Fuchs J, Claussen CD, Schwenzer NF. Simultaneous whole-body PET/MR imaging in comparison to PET/CT in pediatric oncology: initial results. *Radiology* 2014; **273**: 220-231 [PMID: 24877983 DOI: 10.1148/radiol.14131732]

12 **Hirsch FW**, Sattler B, Sorge I, Kurch L, Viehweger A, Ritter L, Werner P, Jochimsen T, Barthel H, Bierbach U, Till H, Sabri O, Kluge R. PET/MR in children. Initial clinical experience in paediatric oncology using an integrated PET/MR scanner. *Pediatr Radiol* 2013; **43**: 860-875 [PMID: 23306377 DOI: 10.1007/s00247-012-2570-4]

13 **Gatidis S**, Schmidt H, Gücke B, Bezrukov I, Seitz G, Ebinger M, Reimold M, Pfannenberg CA, Nikolaou K, Schwenzer NF, Schäfer JF. Comprehensive Oncologic Imaging in Infants and Preschool Children With Substantially Reduced Radiation Exposure Using Combined Simultaneous 18F-Fluorodeoxyglucose Positron Emission Tomography/Magnetic Resonance Imaging: A Direct Comparison to 18F-Fluorodeoxyglucose Positron Emission Tomography/Computed Tomography. *Invest Radiol* 2016; **51**: 7-14 [PMID: 26309185]

14 **Littooij AS**, Kwee TC, Barber I, Granata C, Vermoolen MA, Enríquez G, Zsíros J, Soh SY, de Keizer B, Beek FJ, Hobbelink MG, Bierings MB, Stoker J, Nievelstein RA. Whole-body MRI for initial staging of paediatric lymphoma: prospective comparison to an FDG-PET/CT-based reference standard. *Eur Radiol* 2014; **24**: 1153-1165 [PMID: 24563179 DOI: 10.1007/s00330-014-3114-0]

15 **Siegel MJ**, Jokerst CE, Rajderkar D, Hildebolt CF, Goyal S, Dehdashti F, Wagner Johnston N, Siegel BA. Diffusion-weighted MRI for staging and evaluation of response in diffuse large B-cell lymphoma: a pilot study. *NMR Biomed* 2014; **27**: 681-691 [PMID: 24700565 DOI: 10.1002/nbm.3105]

16 **Chawla SC**, Federman N, Zhang D, Nagata K, Nuthakki S, McNitt-Gray M, Boechat MI. Estimated cumulative radiation dose from PET/CT in children with malignancies: a 5-year retrospective review. *Pediatr Radiol* 2010; **40**: 681-686 [PMID: 19967534 DOI: 10.1007/s00247-009-1434-z]

17 **Attenberger U**, Catana C, Chandarana H, Catalano OA, Friedman K, Schonberg SA, Thrall J, Salvatore M, Rosen BR, Guimaraes AR. Whole-body FDG PET-MR oncologic imaging: pitfalls in clinical interpretation related to inaccurate MR-based attenuation correction. *Abdom Imaging* 2015; **40**: 1374-1386 [PMID: 26025348 DOI: 10.1007/s00261-015-0455-3]

18 **Lyons K**, Seghers V, Williams JL, Sorensen JI, Paldino MJ, Krishnamurthy R, Rohren EM. Qualitative FDG PET Image Assessment Using Automated Three-Segment MR Attenuation Correction Versus CT Attenuation Correction in a Tertiary Pediatric Hospital: A Prospective Study. *AJR Am J Roentgenol* 2015; **205**: 652-658 [PMID: 26295654 DOI: 10.2214/AJR.14.14231]

19 **Heacock L**, Weissbrot J, Raad R, Campbell N, Friedman KP, Ponzo F, Chandarana H. PET/MRI for the evaluation of patients with lymphoma: initial observations. *AJR Am J Roentgenol* 2015; **204**: 842-848 [PMID: 25794075 DOI: 10.2214/AJR.14.13181]

20 **Klenk C**, Gawande R, Uslu L, Khurana A, Qiu D, Quon A, Donig J, Rosenberg J, Luna-Fineman S, Moseley M, Daldrup-Link HE. Ionising radiation-free whole-body MRI versus (18)F-fluorodeoxyglucose PET/CT scans for children and young adults with cancer: a prospective, non-randomised, single-centre study. *Lancet Oncol* 2014; **15**: 275-285 [PMID: 24559803 DOI: 10.1016/S1470-2045(14)70021-X]

P- Reviewer: Assadi M, Casciaro S, Rokni Yazdi H **S- Editor**: Qiu S
L- Editor: A **E- Editor**: Lu YJ

Published by **Baishideng Publishing Group Inc**
8226 Regency Drive, Pleasanton, CA 94588, USA
Telephone: +1-925-223-8242
Fax: +1-925-223-8243
E-mail: bpgoffice@wjgnet.com
Help Desk: http://www.wjgnet.com/esps/helpdesk.aspx
http://www.wjgnet.com